The orientation dynamics of anisotropic particles in shearing flows

A Thesis
Submitted for the Degree of
DOCTOR OF PHILOSOPHY

by

NAVANEETH KIZHAKKE MARATH

ENGINEERING MECHANICS UNIT
JAWAHARLAL NEHRU CENTRE FOR ADVANCED SCIENTIFIC RESEARCH
(A Deemed University)
Bangalore – 560 064

January 2017

DECLARATION

I hereby declare that the matter embodied in the thesis entitled “ **The orientation dynamics of anisotropic particles in shearing flows** ” is the result of investigations carried out by me at the Engineering Mechanics Unit, Jawaharlal Nehru Centre for Advanced Scientific Research, Bangalore, India under the supervision of **Prof. Ganesh Subramanian**, and that it has not been submitted elsewhere for the award of any degree or diploma.

In keeping with the general practice in reporting scientific observations, due acknowledgment has been made whenever the work described is based on the findings of other investigators.

Navaneeth Kizhakke Marath

CERTIFICATE

I hereby certify that the matter embodied in this thesis entitled “ **The orientation dynamics of anisotropic particles in shearing flows** ” has been carried out by **Mr. Navaneeth Kizhakke Marath** at the Engineering Mechanics Unit, Jawaharlal Nehru Centre for Advanced Scientific Research, Bangalore, India under my supervision and that it has not been submitted elsewhere for the award of any degree or diploma.

Prof. Ganesh Subramanian
(Research Supervisor)

Acknowledgements

I would like to thank my advisor Dr. Ganesh Subramanian for being an extraordinary mentor. His physical intution in fluid mechanics has helped me tremendously while working on my thesis problem. I thank him for being extremely patient with me and for always finding time for discussions.

I thank Vivek, whose notes and Mathematica workbooks were extremely useful while solving the planar linear flow problem. I am grateful to Ruchir, for carrying out the simulations in the rheology problem. I thank all the faculty members of EMU for their courses. I thank JNCASR and DST for financial support. I thank all the past and present members of EMU, especially, the 2010 batch, for making life in JNCASR enjoyable. I would also like to thank the administration and other support staff of JNCASR. I am indebted to all my friends and family members who have supported me throughout the course of Ph.D.

I am fortunate to have three awesome women in my life: my mother, sister, and ’partner in crime’ Pavi. I am grateful to them for their emotional and unconditional support.

Abstract

The thesis investigates the first effects of micro-scale inertia and stochastic orientation fluctuations on the orientation dynamics of spheroids in shearing flows. The first chapter of the thesis focuses on a single spheroid in a planar linear flow and the long-time orientation dynamics of the spheroid set up by weak inertial effects is identified. The second chapter of the thesis focuses on estimating the viscosity of a dilute suspension of spheroids in a simple shear flow. It turns out that the inertia sets up a unique steady state orientation distribution, and therefore a unique viscosity, for a dilute suspension of prolate spheroids of all aspect ratios, and of oblate spheroids with aspect ratios greater than 0.14. A stochastic orientational decorrelation mechanism is needed to render the viscosity unique for a dilute suspension of (oblate) spheroids with aspect ratios smaller than 0.14. Rotary Brownian motion is considered as a canonical example for the decorrelation mechanism. Interestingly, the steady state orientation distribution in the presence of both inertia and rotary Brownian motion lends itself to a novel thermodynamic interpretation and leads to the identification of the 'Tumbling-spinning transition' in an anisotropic particle suspension. The 'Tumbling-spinning transition' has striking similarities to the coil-stretch transition of high molecular weight polymers in extension-dominated flows. This interpretation is also explained in the second chapter of thesis. In the third chapter the long-time orientation dynamics of a spheroid sedimenting in a simple shear flow is analyzed. The fourth chapter investigates the effect of inertia on the time period of rotation of a spheroid in a simple shear flow, a canonical rheological flow, and a specific instance of a planar linear flow, is also quantified.

The first chapter is concerned with understanding the effect of inertia on the motion of spheroidal particles in a planar linear flow. A spheroid can be characterized by its orientation (as specified by a pair of angles) and its aspect ratio (κ); with $0 < \kappa < 1$ for an oblate spheroid and $\kappa > 1$ for a prolate spheroid. The planar linear flow can be defined in terms of a single parameter λ, with $-1 \leq \lambda \leq 1$, and as λ increases from -1, one obtains different flows starting from a solid-body rotation at $\lambda = -1$, the elliptic linear flows for $-1 < \lambda < 0$, a simple shear flow at $\lambda = 0$, the hyperbolic linear flows for $0 < \lambda < 1$, finally terminating in a planar extensional flow at $\lambda = 1$. The motion of the spheroid in a planar linear flow is well understood in the

Stokes limit, that is, when there is no inertia either in the particle or the fluid phase. In the Stokes limit, a spheroid rotates indefinitely in any of a single parameter family of periodic orbits, named Jeffery orbits (after the original discoverer) provided λ is less than a critical value that is a function of the particle aspect ratio, approaching zero in the limit of extreme aspect ratios ($\kappa = 0$ and ∞). An investigation is carried out to find the effect of weak particle inertia at O(*St*) and weak fluid inertia at O(*Re*), where *St* and *Re* are respectively the Stokes number and Reynolds number based on the length of the major axis of the spheroid. The expressions for the O(*Re*) and the O(*St*) corrections to the angular velocity in the Stokes limit are obtained in terms of a volume integral using a reciprocal theorem. A novel analytical framework based on a vector spheroidal harmonics formalism is used to obtain the Stokes disturbance velocity fields entering the reciprocal theorem integral, and the evaluation of the resulting integral in spheroidal coordinates yields closed-form expressions for the inertial corrections. The motion of the spheroid is characterized in terms of an inertial drift defined as the change in the orbit constant (C, defined in such a way that it is constant for a particular Jeffery orbit) in a single Jeffery period. Based on the inertial drift, the λ and κ values for which the final orientation of the spheroid is uniquely determined by inertial effects alone, independent of initial conditions, are identified. For these λ and κ's, the final orientation of the spheroid is restricted to two orbits; the tumbling orbit, where the orientation vector rotates in the flow-gradient plane and the spinning orbit, where the orientation vector is always aligned to the vorticity axis, regardless of initial orientation. For the λ and κ values other than those identified above, inertia does not stabilize a unique orbit. A repeller orbit exists separating the unit hemisphere into two distinct basins of attraction; with the attractor being the tumbling orbit for one basin and the spinning orbit for the other. Thus, depending on the basin in which the initial orientation of the spheroid lies, the final orientation can either be the tumbling orbit or the spinning orbit.

The second chapter is concerned with estimating the effect of inertia on the viscosity of a dilute suspension of spheroids in a simple shear flow. The suspension viscosity is a function of the spheroid orientation distribution. It is well known that in the Stokes limit there is no unique steady state orientation distribution and therefore the viscosity is indeterminate. The analysis in chapter 1 of the thesis shows that in a simple shear flow inertia leads to a unique steady state orientation distribution for prolate spheroids and oblate spheroids of aspect ratio larger than 0.14. In the absence of stochastic orientation fluctuations, this distribution is singular, being localized at either the tumbling or spinning orbits. The viscosity is estimated for this suspension using this singular distribution. For a suspension of spheroids with aspect ratio less than 0.14 the steady state viscosity continues to depend on the initial orientation distribution via the fractions of initial orientations in the basins of attraction of the tumbling and spinning

orbits. Therefore, an additional stochastic orientation decorrelation mechanism in the form of rotary Brownian motion, characterized by the Peclet number (Pe_r), is included to obtain the unique steady state orientation distribution. The orientation distribution in the presence of the inertia and the rotary Brownian motion is formulated as the solution of a one-dimensional drift-diffusion equation in the orbital coordinate (C) with the combined inertial and Brownian drift arising as the gradient of a potential. Regarding this potential as an effective free energy, the steady state orientation distribution lends itself to a novel thermodynamic interpretation in $\kappa - C - RePe_r$ space; $RePe_r$ plays the role of a inverse (non-equilibrium) temperature. The minima of the potentials are identified as phases with the small-C and large-C minima respectively named the spinning and the tumbling phases and a phase diagram is constructed in the $\kappa - C - RePe_r$ space. The transition between the tumbling and spinning phases with changing $RePe_r$ is regarded as a phase transition with an associated coexistence region. Interestingly, this coexistence region continues to exist for other planar linear flows with λ's close to 0, although the region rapidly shrinks with increasing $|\lambda|$. The evolution in the two-phase region is characterized by a pronounced hysteresis and experiments where the hysteresis may be observable are proposed. The viscosity is estimated based on the steady state distribution and remarkably, there exists a transition from a shear-thinning behavior to a shear-thickening behavior for the viscosity with increasing aspect ratio, with the transition leading to a discontinuous jump in viscosity at an aspect ratio of about 0.013 in the athermal limit ($RePe_r \to \infty$).

The third chapter is concerned with understanding the effect of inertia on the orientation of a spheroid sedimenting(due to gravity) in a simple shear flow. Three canonical situations with gravity along the flow, gradient and vorticity axes of a simple shear flow are analyzed. The attractors and repellers in the orientation space are identified for these three cases.

The fourth chapter is concerned with understanding the effect of inertia on the time period of rotation of spheroids in a simple shear flow. A deficiency of the O(St/Re) analysis above is that it does not predict a change in the time period (relative to the Jeffery value) in the asymptotically stable orientation states - the tumbling and spinning orbits. On the other hand, simulations have consistently observed a decrease (increase) in the time period with increasing particle (fluid) inertia, respectively. To account for this discrepancy, the effect of particle and fluid inertia to O(St^2) and O($Re^{3/2}$) respectively, is analyzed, again based on a generalized reciprocal theorem formulation. The particle inertia at O(St^2) results in a decrease in the particle time period as well as in the maximum angular velocity and an increase in the minimum angular velocity; all of these being in agreement with the aforementioned simulations. The fluid inertial calculation is considerably more involved since the O($Re^{3/2}$) correction to the

Jeffery period arises from the outer region (distances from the spheroid greater than the inertial screening length of O($Re^{-1/2}$)). Since inertia arises in the far field, the spheroid is treated as a time-dependent force-dipole singularity, and the calculation of the period alteration at O($Re^{3/2}$) is performed in reciprocal space. The fluid inertia results in an increase the time period, again consistent with simulation results.

Table of contents

List of figures

List of tables

Chapter 1

Introduction

Suspensions of anisotropic particles are ubiquitous in nature (Mueller *et al.* 2011; Caro *et al.* 2012) as well as in industrial systems (Lundell *et al.* 2011; Amini *et al.* 2014), with the particle shape varying between extremes of disk and fiber-shaped morphologies (van Olphen 1963; Mueller *et al.* 2011; Lundell *et al.* 2011; Derakhshandeh *et al.* 2011; Caro *et al.* 2012). It is important to understand the orientation dynamics of the suspended particles, subjected to a flow, in order to estimate the transport characteristics of the suspension. For instance, blood, is a concentrated suspension of deformable cells in plasma, and its rheology is sensitively dependent on the orientation distribution of the dominant suspended constituent - red blood cells (Caro *et al.* (2012)). Red blood cells are shaped like biconcave disks with a diameter of about $8\mu m$, and to estimate the rheological properties of blood, one must understand the orientation dynamics of the disks in a pulsatile flow, the typical flow in the cardiovascular system. Another example of an anisotropic suspension is magma, which is a three phase mixture of inorganic silicate melt, gas bubbles and anisotropic mineral crystals. The viscosity of magma determines the nature of the volcanic eruption (Mueller *et al.* (2011)). While the effect of bubbles on magma rheology is known (Manga *et al.* (1998);Llewellin *et al.* (2002)), the importance of suspended crystals on magma rheology has only been recognized recently (Mueller *et al.* (2011)). In a paper manufacturing process, one needs to understand the orientation dynamics of cellulose fibres in the pulp suspension, subjected to a flow, in order to predict and control the properties of the final product (Lundell *et al.* 2011). Reflective flakes are often used for flow visualization purposes (Thoroddsen & Bauer (1999);Goto *et al.* (2011)), and to interpret the scattered intensity patterns that arise from the suspended flakes, it is crucial that one have a knowledge of their orientation dynamics in the local shearing flow (Savas (1985);Gauthier *et al.* (1998)). These flakes have sizes of the order micro meters and often have extreme aspect ratios. In contrast to suspensions of spheres, anisotropic particle suspensions exhibit a rich array of equilibrium and non-equilibrium phases owing to the additional orientational degree of freedom at the microstructural level (Vroege & Lekkerkerker 1992; Brown & Rennie 2001; Michot *et al.* 2006; Lekkerkerker & Vroege 2012). As shown originally by Onsager (Larson (1988)), this can lead to non-trivial transitions in orientational order (isotropic to nematic phases), in turn leading to abrupt changes in transport properties with changes in volume fraction.

As a first step to understand the rheology of, and orientation dynamics in, suspensions of anisotropic particles, a detailed investigation of the orientation dynamics of a spheroid in a planar linear flow is presented in this thesis. A spheroid is a canonical anisotropic particle, its aspect ratio (κ) being the microstructural parameter. Although characterized by a single microstructural parameter, the shape of the spheroid changes from a flat disk to a slender fibre, as its κ varies from 0 to ∞, with $\kappa = 1$ being a sphere. Thus, understanding the orientation dynamics of a spheroid of an arbitrary aspect ratio in a suspension, subjected to a flow, might bring insights into the behaviour of particles, whose anistoropy can vary over a large range. The particles encountered in the physical examples above, are small in size (order of microns). So one would expect fluid inertia characterized by Reynolds number(Re), and particle inertia characterized by Stokes number(St), to be weak at the length scale of the particle. For a spheroid with a semi-major axis of length 'L', one can define $Re = \rho\dot{\gamma}L^2/\mu$ and $St = \rho_p\dot{\gamma}L^2/\mu$, where ρ and ρ_p are the fluid and particle densities, μ is the fluid viscosity and $\dot{\gamma}$, a measure of the magnitude of the velocity gradient, characterizes the strength of the flow. In accordance with the small particle sizes encountered in the above applications, the thesis explores in detail the first effects of inertia in the limit of small but finite Re and St. The flow, on the length scale of the small particle may be approximated as a linear flow, and planar linear flow is the most general two-dimensional flow. Planar linear flow is characterized by a parameter λ, and depending on λ, it can be any of a solid-body rotation, an elliptic linear flow, a simple shear flow, a hyperbolic linear flow or a planar extensional flow. The parameter λ takes values from -1 to 1, with $\lambda = -1$, $\lambda = 0$ and $\lambda = 1$, corresponding to a solid body rotation, a simple shear flow and a planar extensional flow, respectively. The suspension is assumed to be dilute in order to eliminate the non-trivial effects of hydrodynamic interaction, and therefore the hydrodynamic volume fraction, $nL^3 << 1$, where n is the number density of the spheroids in the suspension. The neglect of hydrodynamic interaction, allows one to focus on understanding the orientation dynamics of a single particle, a spheroid here, in a flowing suspension.

A fundamental result of Stokesian hydrodynamics, is that an isolated non-Brownian spheroid in planar linear flow, rotates indefinitely along any of a one-parameter family of spherical ellipses provided λ is less than a critical value, say λ_{crit} (Hinch & Leal 1972). The parameter is the orbital coordinate C, which takes values between 0 and ∞. These orbits are originally derived for a spheroid rotating in a simple shear flow by Jeffery (Jeffery 1922), and are eponymously called the Jeffery orbits. The indefinite rotation of a spheroid along a particular Jeffery orbit, in this limit, makes its orientation distribution at any time, depend on its initial orientation. As a result, the viscosity of a dilute suspension of spheroids, which is a function of the orientation distribution of a single spheroid, becomes indeterminate in the infinitely dilute limit corresponding to $O(nL^3)$, nL^3 being the aforementioned hydrodynamic volume.This is unlike the case of a dilute suspension of rigid spheres, where the orientation is a degenerate degree of freedom (in not affecting the velocity field); the $O(\phi)$[1] correction to the viscosity can determined and is given by $5\phi/2$, where 5/2 is the well known Einstein coefficient (Leal 1992). The indeterminacy mentioned above for a spheroid is a consequence of Stokes flow reversibility which leads to closed streamlines or pathlines in other situations, with profound implications for the relevant micro-scale transport processes (Batchelor & Green 1972*a*,*b*; Kao *et al.* 1977*b*; Subramanian & Brady 2006; Subramanian & Koch 2006*a*,*c*, 2007; Krishnamurthy 2014).

The primary question that this thesis tries to address is as follows: Can weak inertial effects at $O(Re)$ and $O(St)$ eliminate the indeterminacy associated with the Stokes limit? To answer this question, one has to understand the orientation dynamics of a spheroid in planar linear flows (with $\lambda<\lambda_{crit}$), in the presence of inertia. The corrections to the leading order Jeffrey angular velocity at $O(Re)$ and $O(St)$, for an arbitrary aspect ratio spheroid, rotating in a planar linear flow, are derived in chapter 2, using a generalized reciprocal theorem formulation (Leal (1979);Subramanian & Koch (2005);Subramanian & Koch (2006*b*)). To evaluate the integral in the generalized reciprocal theorem, one needs the Stokesian disturbance velocity field around a spheroid in a planar linear flow. While this velocity field may be obtained using earlier results based on the method of singularities (Chwang & Wu (1974);Chwang & Wu (1975)), herein the vector spheroidal harmonics formalism developed by Kushch and coworkers (Kushch (1997);Kushch (1998)) is used. The formalism is based on expressing the general solution of the Stokes equations, around an arbitrary number of spheroidal particles, as a superposition of growing and decaying vector harmonics in local spheroidal coordinates defined with respect to a Cartesian system centered at each particle, and aligned with the particle axis of symmetry. This formalism was already used for understanding the inertial and viscoelastic effects on a single sedimenting particle in an otherwise quiescent fluid (Dabade *et al.* 2015). Inertia results in a drift across the closed trajectories in Stokes flow, and the drift

---

[1] ϕ and nL^3 are the physical and hydrodynamic volume fractions, and that there is no distinction between the two in the case of spheres.

is characterized using a multiple time scale analysis. The orbits stabilized by the inertial drift are identified in the $\lambda - \kappa$ plane. For the majority of (λ, κ) combinations, the stabilized orbit is either one confined to the flow-gradient plane of the ambient planar linear flow (the tumbling orbit), or one where the spheroid orientation vector is aligned with the vorticity vector of the ambient flow (the spinning orbit). However, for some (λ, κ) combinations, depending on the initial orientation of the spheroid, the orbit stabilized can be either the spinning or the tumbling orbit, since both these orbits have non-trivial basins of attraction, separated by an unstable (repeller) limit cycle, on the unit sphere of orientation. Therefore, for these combinations, inertia alone cannot eliminate the dependency on the initial orientation.

In chapter 3 the question that is addressed is finding the viscosity of a dilute suspension of neutrally buoyant spheroids in simple shear flow. As mentioned earlier, in the Stokes limit the viscosity is indeterminate. The analysis in chapter 2 indicates that weak inertial effects, in a simple shear flow, stabilize the tumbling orbit for neutrally buoyant prolate spheroids ($\kappa > 1$) of any aspect ratio, and the spinning orbit for neutrally buoyant oblate spheroids($\kappa < 1$) whose aspect ratios are larger than 0.137. For these spheroids, the viscosity is calculated based on the steady state orientation distribution localized at these stable orbits (as is the case in the athermal non-interacting limit). For neutrally buoyant oblate spheroids whose aspect ratios are smaller than 0.137, inertia stabilizes either the spinning or the tumbling orbit, depending on the spheroid's initial orientation. It is shown that if an additional decorrelation mechanism in the form of rotary Brownian motion, characterized by $Pe_r (Pe_r = \dot{\gamma}/D_r)$, where D_r is the rotary Brownian diffusivity, is included, the dependence on the initial orientation is eliminated. The unique steady state orientation distribution determined by the combined effect of the Brownian motion and inertia is obtained by solving a convection-diffusion equation. The steady state Jeffery-orbit distribution arising from a balance of inertia and thermal fluctuations is shown to be of the Boltzmann equilibrium form, with a potential that depends on C, particle aspect ratio (κ), and a dimensionless shear rate ($RePe_r$), and therefore lends itself to a novel thermodynamic interpretation in $C - \kappa - RePe_r$ space. In particular, the transition of the potential from a single to a double-well structure, below a critical κ, is interpreted as a phase transition, and the small-C and large-C minima identified with spinning and tumbling phases. The tumbling-spinning phase diagrams are characterized for a range of flows bracketing simple shear flow, and the tumbling-spinning envelope is found to be maximum in extent for simple shear. The hysteretic dynamics within the two-phase tumbling-spinning envelope renders the rheology sensitively dependent on the precise shear rate history; the signature in simple shear flow being a multi-valued viscosity at a given shear rate. The tumbling-spinning transition identified here is analogous to the coil-stretch transition in the polymer physics literature (De Gennes

1974; Hinch 1974). It should persist under more general circumstances, and has implications for the suspension stress response in inhomogeneous shearing flows.

In chapter 4, the question that is addressed is the effect of inertia on the orientation dynamics of a spheroid, sedimenting in simple shear flow. The effect of inertia on a spheroid sedimenting in a quiescent fluid is already analyzed in Dabade *et al.* (2015). The sedimentation torque at O(Re_{sed}), where $Re_{sed} = \rho U_{sed} L/\mu$, is the Reynolds number in sedimentation, with U_{sed} being the sedimentation velocity, makes the spheroid sediment in a broadside-on configuration. In the broadside-on configuration, the prolate spheroid orientation will be perpendicular to the translational velocity, and the oblate spheroid orientation will be aligned to the translational velocity. The angular velocity of a spheroid sedimenting in a simple shear flow is obtained again using a reciprocal theorem. The strength of the sedimentation to that due to inertial drift is characterized by the non-dimensional numbers Re_{sed}/Re and St/Re. The orientation dynamics of a spheroid is analyzed in detail for three canonical cases, where the sedimenting force is aligned with any of the gradient, vorticity and flow axes of the simple shear flow .

In chapter 5, the question that is addressed is the effect of inertia, on the time period of rotation of a spheroid rotating in the orbits that are stabilized by the O(Re) and O(St) drifts in simple shear flow. It turns out that in the stabilized orbits, the O(Re) and O(St) corrections to the angular velocity derived in chapter 2, do not alter the time period of rotation from its leading order Jeffery value. Mao & Alexeev (2014) have investigated the effect of inertia on the time period of rotation of spheroids of different aspect ratios using the lattice Boltzmann method, and concluded that the effect of fluid inertia is to increase the time period from its leading order value, and that of particle inertia is to decrease it; this numerical investigation is, however, restricted to Re's of order unity, and the scalings for small Re and St are unclear. The O($Re^{3/2}$) and O(St^2) corrections to the time period of rotation are calculated in this chapter for a spheroid of an arbitrary aspect ratio, rotating in its long-time orbit (either the tumbling or spinning mode) in simple shear flow. The calculation of the O(St^2) correction is straightforward since it is regular in nature. The time period correction at O($Re^{3/2}$) has a singular origin, and arises from fluid inertial effects in the outer region (distances from the spheroid of order the inertial screening length of O($LRe^{-\frac{1}{2}}$)) where the leading order Stokes approximation ceases to be valid. Since the correction comes from the effects of inertia in the far field, the rotating spheroid is approximated as a time-dependent point-force-dipole singularity. This allows for the relevant reciprocal theorem integral to be evaluated in Fourier space. It is shown that fluid inertia at O($Re^{3/2}$) leads to an increase in the time period of rotation compared to that in the Stokes limit, and particle inertia at O(St^2) leads to a decrease of the same, consistent with the results of recent numerical simulations.

Chapter 2

The orientation dynamics of a spheroid in planar linear flow

2.1 Introduction

In this chapter we investigate the effect of inertia on the orientation dynamics of a spheroid in planar linear flow. A spheroid is the simplest shape that can be used to model anisotropic particles, and is characterized by its orientation ($\boldsymbol{p}$) and aspect ratio (κ). As the aspect ratio of the spheroid increases from 0 to ∞ its shape changes from thin disk to slender fiber. Planar linear flows form a one-parameter family characterized by a parameter λ, and depending on λ, the flow can be any of a solid body rotation, the elliptic linear flows, a simple shear flow, the hyperbolic linear flows or an extensional flow. The parameter λ can take any value from -1 to 1, and with increasing λ, the streamlines of the planar linear flow transition from being closed for solid body rotation and the elliptic linear flows, to straight lines for the simple shear flow, and to open streamlines for the hyperbolic linear and extensional flows (Bentley & Leal 1986; Subramanian & Koch 2006*c*). The effect of inertia on the streamline topology plays a significant role in determining the transport properties of many disperse multiphase systems (Subramanian & Koch 2006*a*,*c*, 2007; Krishnamurthy 2014). Planar linear flows can be easily generated in an experiment(Bentley & Leal 1986; Lee *et al.* 2007), the device used being a four roll mill, developed originally by G.I Taylor. The orientation dynamics of a non-Brownian spheroid in planar linear flow is well known in the Stokes limit, that is, when there is no inertia in the particle as well as the surrounding fluid. In this limit, the spheroid rotates in any of a one parameter family of closed orbits, when λ is less than a critical value, say λ_{crit},(Hinch & Leal 1972), and the orbit in which the spheroid rotates is determined by its initial orientation. The orbits are spherical ellipses, as shown by Jeffery (1922), and are eponymously known as

Jeffery orbits. When $\lambda \geq \lambda_{crit}$, the trajectories are not closed; the open trajectories connect a network of six fixed points on the unit sphere. The first effects of fluid and particle inertia at O(Re) and O(St) on the orientation dynamics of the spheroid rotating in a planar linear flow is analyzed in detail in this chapter. Here Re is the Reynolds number, $Re = \rho_f \dot{\gamma} L^2/\mu$, and St is the Stokes number, $St = \rho_p \dot{\gamma} L^2/\mu$, where ρ_p and ρ_f are the particle and the fluid densities, $\dot{\gamma}$ is the shear rate characterizing the ambient planar linear flow, μ is the fluid viscosity and L is the the length of the semi-major axis of the spheroid.

Jeffery (1922) himself had hypothesized that in simple shear flow, weak inertial effects would eventually move the particle to an orbit of minimum dissipation. These correspond to the log-rolling and tumbling orbits for prolate and oblate spheroids, respectively. Initial experimental investigations (Taylor (1923),Trevelyan & Mason (1951)) were inconclusive. The earliest analytical investigation which studied the effect of weak fluid inertia on a nearly spherical particle in simple shear flow was that of Saffman (1956), and appeared to confirm Jeffery's hypothesis, although no details of the analysis were given. In the same paper, the author concluded that particle inertia does not lead to any drift. In contrast, Karnis *et al.* (1966), in experiments with disks and rods in Couette flow, observed the particles to migrate towards orbits of maximum energy dissipation. Later, Harper & Chang (1968) analyzed the motion of a dumbbell-shaped particle, in simple shear flow, in the limit when the inter- sphere separation is much greater than the inertial screening length (of $O(aRe^{-\frac{1}{2}})$, a being the sphere radius). The torque leading to the drift was regarded as arising from inertial lift forces (Saffman (1965)) acting independently on the each sphere, and as a result, the dumbbell was found to move towards a tumbling mode. However, as argued in Subramanian & Koch (2005), use of the Saffman lift-force is inconsistent with the limit considered by the authors. There have been more recent investigations for the inertial drift in simple shear flow, based on a reciprocal theorem formulation, that are either limited to particles with large aspect ratios (Subramanian & Koch (2005)), with the attendant simplifications arising from viscous slender body theory (Batchelor (1970*a*)), or to particles with aspect ratios near unity which allow for a regular perturbation expansion about a sphere (Subramanian & Koch (2006*b*)). For nearly spherical axisymmetric particles, Subramanian & Koch (2006*b*) conclude that the effect of fluid inertia is in accordance with Jeffery's hypothesis. Particle inertia was found to cause prolate and oblate near-spheres to drift towards tumbling and spinning modes, respectively. For slender fibers, Subramanian & Koch (2005) found a fluid inertial drift towards the tumbling mode, a decrease in the speed of rotation with increasing Re, and a relatively modest critical Re above which the particle ceases to rotate. It was also argued therein that the effects of particle inertia would be asymptotically small for large aspect ratios. Recently, the effect of particle inertia on the orientation of axisymmetric particles of arbitrary aspect ratios in planar linear flow, to O(*St*), has been examined by Einarsson *et al.* (2014). In this work, the O(*St*) correction to the leading order Jeffery angular velocity in a general linear flow is presented in an invariant form, and it concludes that in the particular case of simple shear flow, prolate and oblate spheroids drift towards the tumbling and spinning modes, respectively, consistent with the near-sphere analysis of Subramanian & Koch (2006*b*). However, they do not do a detailed investigation of the effect of particle inertia on the orientation of a spheroid in a planar linear flow. In Candelier *et al.* (2015) the effect of fluid inertia on the orientation dynamics of a nearly spherical axisymmetric particle in a planar linear flow is investigated. The angular velocity at O(*Re*) is derived for the nearly spherical axisymmetric particle therein. However they do not examine the orientation dynamics of the particle for all λ's. They focus only on the orientation dynamics in three cases, that is the solid body rotation, simple shear flow and extensional flow. In the particular case of extensional flow, the inertia does not alter the location of the fixed points. However, it alters the rate of approach to or divergence from a fixed points. Einarsson *et al.* (2015*a*) and Einarsson *et al.* (2015*b*) have looked at the effect of both particle and fluid inertia, respectively, on spheroids of an arbitrary aspect ratio in a simple shear flow, and we comment on this effort in the conclusions section.

There have been several recent numerical investigations that examine the orientation dynamics of anisotropic particles for the specific case of simple shear flow. These may be conveniently divided into those that analyze the orientational motion of neutrally buoyant spheroids (*Re*= *St*), over a wide range of *Re*, via (mainly) Lattice Boltzmann simulations (Aidun *et al.* (1998);Ding & Aidun (2000);Qi & Luo (2003);Huang *et al.* (2012);Mao & Alexeev (2014)) and via the distributed Lagrangian multiplier based fictitious domain method (Yu *et al.* (2007)), and those that examine the orientation dynamics of massive spheroids and triaxial ellipsoids in shear flow in the absence of fluid inertia, but over a wide range of *St*, via a numerical integration of the governing ODE's (Lundell & Carlsson (2010);Lundell & Carlsson (2011);Challabotla *et al.* (2015)). One of the main conclusions of the second group of investigations is a rather sharp transition, across a narrow range in *St*, from a small-*St* to a large-*St* dynamics. In the former regime, as would be expected, the inertial drift leads to a spiraling trajectory for the orientation vector with each turn of the spiral closely resembling a Jeffery orbit. In the latter regime, the drift is again asymptotically slow but has a very different character, akin to the classical Euler top (Goldstein (1962)) with a superposed secular drift, that is outside the scope of the current investigation. The first group of investigations above, culminating in the recent effort of Huang *et al.* (2012), has identified a series of transitions in the rotation mode as a function of *Re* for both prolate and oblate spheroids. With increasing *Re*, the sequence of rotation modes are tumbling, log-rolling, inclined rolling, precession and nutation around an inclined axis, and finally, a stationary state at the highest *Re*'s (Huang *et al.* (2012)), for a prolate spheroid. For an oblate spheroid, this sequence is simpler, consisting of a low-*Re*, spinning mode followed by an inclined spinning mode, and a stationary state at the highest *Rey*'s. The general focus of these simulation efforts has been more on the transition in rotations, and less on the dependence of the period of rotation on *Re*; although, it is clear that, over the lower range of *Re*'s, the period increases monotonically due to the onset of fluid inertial effects. The work by Mao & Alexeev (2014) is an exception in this regard, and the authors find that the effects of particle and fluid inertia are, respectively, to decrease and increase the time period of rotation from the inertialess Jeffrey value. Note that, in two dimensions, increasing *Re* had already been shown to eventually arrest rotation of an elliptic cylinder (Ding & Aidun (2000)). In three dimensions, for sufficiently slender bodies, such an arrest has been predicted to occur at a fairly modest *Re* of $O(\kappa^{-1}\ln\kappa)$, κ being the large aspect ratio (Subramanian & Koch (2005)). As is the case for numerical investigations, the above efforts for neutrally buoyant spheroids (and, to a lesser extent, those for massive spheroids) are limited in the number of aspect ratios examined and in terms of analyzing the detailed dependence of the nature of the final steady or time-periodic state on the particular initial orientation. For instance, excepting Mao & Alexeev (2014), all other efforts only look at prolate and oblate spheroids with aspect ratios of 2 and 0.5, respectively. Further, the numerical simulations of neutrally buoyant spheroids are necessarily limited to wall-bounded domains with periodic boundary conditions in the flow and vorticity directions. The effect of the wall confinement on the aforementioned transitions is not small, and the effects of periodicity are uncertain. There is also some disagreement, between different efforts, with regard to the detailed sequence of transitions, and the precise estimates of the associated critical *Re*'s. This appears partly due to the differing nature of the numerical methods, and partly due to the different initial orientations examined in different investigations. The analysis given here will serve as a very useful point of validation for any numerical effort. Although restricted to $Re, St \ll 1$, the qualitative nature of the orientation dynamics is expected to conform to predictions even when $Re, St \sim O(1)$. In sharp contrast to the above numerical investigations and the earlier theoretical efforts, we cover the entire range of aspect ratios for both prolate and oblate spheroids, and show that in simple shear flow, for sufficiently thin oblate spheroids (aspect ratios smaller than about 0.14 which have not been examined in any of the above simulations), the long-time orientation dynamics is a function of the initial orientation, with the unit sphere being divided into distinct basins of attraction corresponding to the tumbling and spinning modes. For the dilute regime of relevance here, the dependence on initial conditions for the said aspect ratios is expected to be eliminated, over much longer times, on account of weak thermal or hydrodynamically induced orientation fluctuations. The case of weak Brownian motion is analyzed here in some detail.

Very recently, there have been a pair of numerical investigations of both neutrally and non-neutrally buoyant prolate spheroids, again using variants of the Lattice Boltzmann method. Rosen *et al.* (2014) examined a neutrally buoyant prolate spheroid with aspect ratio 4 (in contrast to the aspect ratio of 2 considered in virtually all of the aforementioned numerical efforts) in simple shear flow with increasing *Re*. A sequence of rotational states, similar to that found earlier by Huang *et al.* (2012) for a prolate spheroid of aspect ratio 2, was found, although the transition Reynolds numbers differed in magnitude (lower for the higher aspect ratio). Importantly, the authors interpreted the transitions from one rotational state to the other in terms of the analogous bifurcations of the fixed points of a model two-dimensional two-parameter vector field. This dynamical systems perspective is crucial to understand the underlying system symmetries. For instance, the analogy with the model dynamical system naturally explains the presence of two possible inclined log-rolling and precessing modes, symmetrically disposed about the ambient vorticity axis; as to which one is actually observed in a simulation depends on the initial orientation. The authors also observed the tumbling mode of the spheroid to co-exist with other rotational states at higher *Re*, until the tumbling period diverged at a critical Reynolds number, via a saddle-node bifurcation, in a manner similar to that found earlier by one of the authors for two-dimensional elliptic cylinders (Ding & Aidun (2000)). Rosen *et al.* (2015) have extended the study of Rosen *et al.* (2014) to non-neutrally buoyant spheroids, and examine in detail the effects of varying particle inertia and aspect ratio (prolate spheroids with aspect ratios ranging from 2 to 6) on the different transition Reynolds numbers (tumbling → tumbling/log-rolling, tumbling/log-rolling → tumbling/inclined log-rolling, etc).

The chapter is organized as follows. In section 2.2, a reciprocal theorem formulation (Leal (1979);Subramanian & Koch (2005);Subramanian & Koch (2006*b*)) is used to obtain the expression for the angular velocity of a spheroid in planar linear flow, accounting for both fluid and particle inertia. The analysis of particle inertia is a fairly straightforward exercise, involving a regular expansion of the angular velocity for small *St* with the leading-order term being the Jeffery angular velocity. The analysis of even weak fluid inertia is a difficult exercise in general, but it is shown that the $O(Re)$ correction has a regular character with its calculation requiring only a knowledge of the Stokes velocity fields. Thus, in section 2.3, we derive an analytical expression for the disturbance velocity field due to a freely rotating spheroid in planar linear flow, at $Re = 0$, based on a vector spheroidal harmonics formalism developed originally by Kushch and co-workers in the context of elastic composites (Kushch & Sangani

(2003);Kushch (1997);Kushch (1998)). The general velocity field is expressed in spheroidal coordinates as a sum of five contributions, each corresponding to a simpler canonical linear flow, the relative amplitudes of these component flows being determined by the instantaneous orientation of the spheroid. In section 2.4 the orientation dynamics of spheroid in the Stokes limit is discussed. Sections 2.5 and 2.6, respectively, analyze the $O(St)$ and the $O(Re)$ inertial drift for prolate and oblate spheroids with a detailed characterization of the bifurcation in the orientation dynamics in a $\lambda - \kappa$ plane. In these sections, we use an analytical approximation to investigate the orientation dynamics, based on an orbital drift interpretation, thereby eliminating the need to numerically integrate the differential equations corresponding to the angular velocities. Section 2.7 examines the drift, arising from both particle and fluid inertia, for neutrally buoyant prolate and oblate spheroids. The formal derivation of the analytical approximation mentioned above using a multiple time scale analysis is presented in section 2.8. Further, we also discuss the limitation of the drift analysis for extreme aspect ratio particles (slender fibres and flat disks) in this section. In section 2.9, we summarize the results.

2.2 Formulation for the inertial drift: The generalized reciprocal theorem

The velocity and stress fields in two different problems, the problem of interest and a test problem, corresponding to two different flow configurations, past the same particle can be related through a generalized reciprocal theorem (Leal (1979);Subramanian & Koch (2005);Subramanian & Koch (2006*b*)). The two problems are defined based on a dynamical quantity that needs to be evaluated, which is an unknown in the problem of interest. The test problem is usually chosen to be one in which the velocity and stress fields are known a priori. In the present case, the quantity of interest is the correction to the angular velocity of a neutrally buoyant spheroid suspended in a Newtonian fluid undergoing a planar linear flow with the inertial acceleration, both of the particle and that of the fluid, being taken into account. The disturbance velocity and stress fields in the aforementioned problem of interest are denoted by $\boldsymbol{u}'^{(1)}$ and $\boldsymbol{\sigma}'^{(1)}$. The disturbance fields are related to the total velocity and stress fields in the problem by $\boldsymbol{u}'^{(1)} = \boldsymbol{u}^{(1)} - \boldsymbol{\Gamma}\cdot\boldsymbol{x}$ and $\boldsymbol{\sigma}'^{(1)} = \boldsymbol{\sigma}^{(1)} - \boldsymbol{\sigma}^{(\infty)} = \boldsymbol{\sigma}^{(1)} + p^{\infty}\boldsymbol{I} - 2\boldsymbol{E}$. Here, $\boldsymbol{\Gamma}\cdot\boldsymbol{x}$ is the ambient planar linear flow in non-dimensional form defined with the origin at the center of the spheroid. The transpose of the non-dimensional velocity (ambient) gradient tensor and the rate-of strain tensor in a space-fixed coordinate system ($X'Y'Z'$, with unit vector triplet $\mathbf{1}'_x$,$\mathbf{1}'_y$ and $\mathbf{1}'_z$) are given by $\boldsymbol{\Gamma} = \mathbf{1}'_x\mathbf{1}'_y + \lambda\mathbf{1}'_y\mathbf{1}'_x$ and $\boldsymbol{E} = (\mathbf{1}'_x\mathbf{1}'_y + \mathbf{1}'_y\mathbf{1}'_x)(\lambda+1)/2$ respectively. The parameter λ characterizes the family of planar linear flows with (1-λ)/(1+λ) denoting the rate

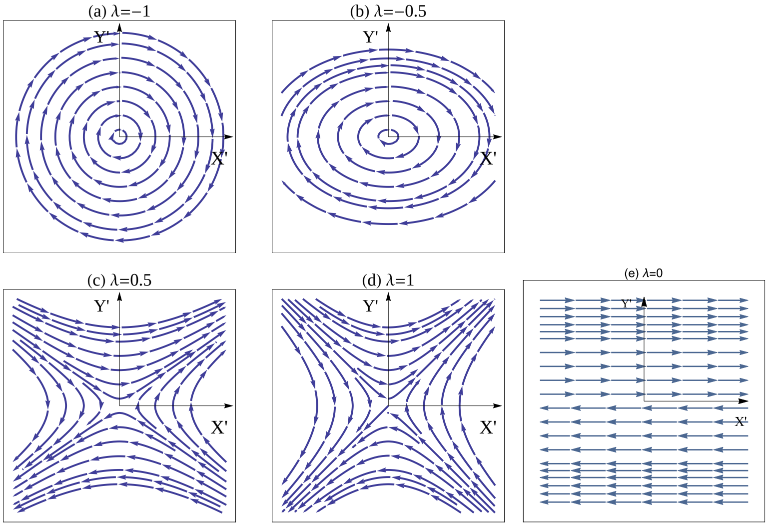

Fig. 2.1 The stream lines in the spaced-fixed coordinate system for (a) solid body rotation (b) elliptic flow (c) hyperbolic flow (d) extensional flow and (e) simple shear flow.

of vorticity to extension in the flow. As λ increases from -1, one obtains different flows starting from a solid-body rotation at $\lambda = -1$, the elliptic linear flows for $-1 < \lambda < 0$, a simple shear flow at $\lambda = 0$, the hyperbolic linear flows for $0 < \lambda < 1$, finally terminating in a planar extensional flow at λ=1. The ambient streamline patterns for these flows are shown in figure 2.1. As λ increases from -1 to 1, there is a transition from a closed (figure 2.1(a) and (b)) to an open streamline pattern (figure 2.1(c) and (d)) with the streamlines for $\lambda = 0$ alone (figure 2.1(e)) being straight lines. The axes of the space-fixed coordinate system X', Y' and Z' are defined such that they coincide with the flow, the gradient and the vorticity directions of the simple shear flow ($\lambda = 0$), respectively (figure 2.2). Above, p^∞ is the pressure field required to maintain the ambient linear flow for finite Re. The ambient pressure (p^∞) is obtained by equating its gradient to the inertial acceleration, whence one finds $p^\infty = -Re\,\boldsymbol{x}\cdot\boldsymbol{\Gamma}\cdot\boldsymbol{\Gamma}\cdot\boldsymbol{x}/2$. Note that p^∞=0 for simple shear flow. The test problem, with its velocity and stress fields denoted by $\boldsymbol{u}^{(2)}$ and $\boldsymbol{\sigma}^{(2)}$ respectively, corresponds to the Stokesian rotation of a spheroid, with the same instantaneous orientation as that in the problem of interest, in an otherwise quiescent ambient. The reciprocal theorem then yields the following identity:

$$\int_S \boldsymbol{u}'^{(1)}\cdot\boldsymbol{\sigma}^{(2)}\cdot\boldsymbol{n}\,dS - \int_S \boldsymbol{u}^{(2)}\cdot\boldsymbol{\sigma}'^{(1)}\cdot\boldsymbol{n}\,dS = Re\int_V \boldsymbol{\nabla}\cdot\boldsymbol{\sigma}'^{(1)}\cdot\boldsymbol{u}^{(2)}\,dV, \qquad (2.1)$$

where $\boldsymbol{n}$ is the unit normal into the fluid domain V and S includes all bounding surfaces. Here, Re is a non-dimensional measure of fluid inertia in relation to viscous forces, and is defined as $Re = \dot{\gamma}L^2/\nu$, where $\dot{\gamma}$ is the ambient shear rate, L is taken to be the spheroid semi-major axis,

$\nu = \mu/\rho_f$ is the kinematic viscosity of the suspending fluid with μ and ρ_f being its viscosity and density, respectively. The velocity fields $\boldsymbol{u}'^{(1)}$ and $\boldsymbol{u}^{(2)}$ decay sufficiently rapidly for the surface integrals at infinity to be neglected, and the bounding surface S in (2.1) reduces to that of the spheroid (S_p). The divergence of the stress $\boldsymbol{\nabla}\cdot\boldsymbol{\sigma}'^{(1)}$ in (2.1) is equal to the inertial acceleration $\frac{D\boldsymbol{u}'^{(1)}}{Dt}$, and may be written in terms of $\boldsymbol{\Gamma}$ and $\boldsymbol{u}'^{(1)}$. The no-slip boundary conditions in the two problems imply that, on S_p, $\boldsymbol{u}'^{(1)} = \boldsymbol{\Omega}_1 \wedge \boldsymbol{x} - \boldsymbol{\Gamma}\cdot\boldsymbol{x}$ and $\boldsymbol{u}^{(2)} = \boldsymbol{\Omega}_2 \wedge \boldsymbol{x}$. In this chapter, we determine $\boldsymbol{\Omega}_1$ to $O(Re)$, and to $O(St)$, where $St = \rho_p\dot{\gamma}L^2/\mu$ is a dimensionless measure of particle inertia, ρ_p being the particle density. The relative importance of particle and fluid inertia is determined by the ratio $St/Re = \rho_p/\rho_f$. Thus, for a gas-solid system we have $St \gg Re$, but for solid-liquid systems $St \approx Re$; for neutrally buoyant particles in particular, $St = Re$.

Accounting for the boundary conditions above, the surface integrals in (2.1) may now be expressed as:

$$\int_{S_p} \boldsymbol{u}^{(2)}\cdot\boldsymbol{\sigma}'^{(1)}\cdot\boldsymbol{n}\,dS = \boldsymbol{\Omega}_2\cdot\mathscr{L}_1 - \boldsymbol{\Omega}_2\cdot\int_{S_p}\boldsymbol{x}\times(\boldsymbol{\sigma}^{\infty}\cdot\boldsymbol{n})\,dS, \tag{2.2}$$

$$= St\,\boldsymbol{\Omega}_2\cdot\frac{d}{dt}(\boldsymbol{I}_p\cdot\boldsymbol{\Omega}_1) - \boldsymbol{\Omega}_2\cdot\int_{S_p}\boldsymbol{x}\times(\boldsymbol{\sigma}^{\infty}\cdot\boldsymbol{n})\,dS, \tag{2.3}$$

$$= St\,\boldsymbol{\Omega}_2\cdot\frac{d}{dt}(\boldsymbol{I}_p\cdot\boldsymbol{\Omega}_1) + \boldsymbol{\Omega}_2\cdot\int_{S_p}(\boldsymbol{x}\times\boldsymbol{n})\,p^{\infty}\,dS, \tag{2.4}$$

$$\int_{S_p} \boldsymbol{u}'^{(1)}\cdot\boldsymbol{\sigma}^{(2)}\cdot\boldsymbol{n}\,dS = \int_{S_p}\boldsymbol{n}\cdot(\boldsymbol{\Omega}_1\wedge\boldsymbol{x} - \boldsymbol{\Gamma}\cdot\boldsymbol{x})\cdot\boldsymbol{\sigma}^{(2)}dS, \tag{2.5}$$

$$= \boldsymbol{\Omega}_1\cdot\mathscr{L}_2 - \boldsymbol{\Gamma} : \int_{S_p}\boldsymbol{x}(\boldsymbol{\sigma}^{(2)}\cdot\boldsymbol{n})dS, \tag{2.6}$$

where we have assumed the absence of any external torque in the problem of interest. As a result, the hydrodynamic torque ($\mathscr{L}_1$) must equal the angular acceleration, and $\boldsymbol{I}_p$ above is the moment of inertia tensor of the spheroid. For an inertialess particle, the torque-free condition would mean $\mathscr{L}_1 = 0$. In (2.6), $\mathscr{L}_2$ is the hydrodynamic torque acting on the spheroid in the test problem. The identity (2.1) now takes the form:

$$\begin{aligned}\boldsymbol{\Omega}_1\cdot\mathscr{L}_2 =& \boldsymbol{\Gamma} : \int_{S_p}\boldsymbol{x}(\boldsymbol{\sigma}^{(2)}\cdot\boldsymbol{n})dS + St\left[\frac{d}{dt}(\boldsymbol{I}_p\cdot\boldsymbol{\Omega}_1)\right]\cdot\boldsymbol{\Omega}_2 + Re\int_V \boldsymbol{\nabla}\cdot\boldsymbol{\sigma}'^{(1)}\cdot\boldsymbol{u}^{(2)}dV \\ &+ \boldsymbol{\Omega}_2\cdot\int_{S_p}(\boldsymbol{x}\times\boldsymbol{n})\,p^{\infty}\,dS.\end{aligned} \tag{2.7}$$

The non-dimensional equations of motion and the continuity equation for the problem of interest, $(\boldsymbol{\sigma}^{(1)}, \boldsymbol{u}^{(1)})$, are given by:

$$Re\left[\frac{\partial \boldsymbol{u}^{(1)}}{\partial t} + \boldsymbol{u}^{(1)} \cdot \boldsymbol{\nabla} \boldsymbol{u}^{(1)}\right] = -\boldsymbol{\nabla} p^{(1)} + \nabla^2 \boldsymbol{u}^{(1)}, \tag{2.8}$$

$$\boldsymbol{\nabla} \cdot \boldsymbol{u}^{(1)} = 0. \tag{2.9}$$

with

$$\boldsymbol{u}^{(1)} = \boldsymbol{\Omega}_1 \wedge \boldsymbol{x} \qquad \text{for} \qquad \boldsymbol{x} \,\varepsilon\, S_p, \tag{2.10}$$

$$\boldsymbol{u}^{(1)} \rightarrow \boldsymbol{\Gamma} \cdot \boldsymbol{x} \qquad \text{for} \qquad \boldsymbol{x} \rightarrow \infty. \tag{2.11}$$

In terms of the disturbance field used in the reciprocal theorem formulation above, we have:

$$Re\left[\frac{\partial \boldsymbol{u}'^{(1)}}{\partial t} + (\boldsymbol{\Gamma} \cdot \boldsymbol{x}) \cdot \boldsymbol{\nabla} \boldsymbol{u}'^{(1)} + \boldsymbol{\Gamma} \cdot \boldsymbol{u}'^{(1)} + \boldsymbol{u}'^{(1)} \cdot \boldsymbol{\nabla} \boldsymbol{u}'^{(1)}\right] = -\boldsymbol{\nabla} p'^{(1)} + \nabla^2 \boldsymbol{u}'^{(1)}, \tag{2.12}$$

$$\boldsymbol{\nabla} \cdot \boldsymbol{u}'^{(1)} = 0, \tag{2.13}$$

with

$$\boldsymbol{u}'^{(1)} = \boldsymbol{\Omega}_1 \wedge \boldsymbol{x} - \boldsymbol{\Gamma} \cdot \boldsymbol{x} \qquad \text{for} \qquad \boldsymbol{x} \,\varepsilon\, S_p, \tag{2.14}$$

$$\boldsymbol{u}'^{(1)} \rightarrow 0 \qquad \text{for} \qquad \boldsymbol{x} \rightarrow \infty. \tag{2.15}$$

The test problem, $(\boldsymbol{\sigma}^{(2)}, \boldsymbol{u}^{(2)})$, in (2.1), is defined by

$$-\boldsymbol{\nabla} p^{(2)} + \nabla^2 \boldsymbol{u}^{(2)} = 0, \tag{2.16}$$

$$\boldsymbol{\nabla} \cdot \boldsymbol{u}^{(2)} = 0, \tag{2.17}$$

with

$$\boldsymbol{u}^{(2)} = \boldsymbol{\Omega}_2 \wedge \boldsymbol{x} \qquad \text{for} \qquad \boldsymbol{x} \,\varepsilon\, S_p, \tag{2.18}$$

$$\boldsymbol{u}^{(2)} \rightarrow 0 \qquad \text{for} \qquad \boldsymbol{x} \rightarrow \infty. \tag{2.19}$$

For $St = 0$, $\boldsymbol{\Omega}_2$ may be chosen orthogonal to the spheroidal symmetry axis since the axial rotation of the spheroid does not couple to a change in its orientation. An inertialess spheroid, as it rotates along a Jeffery orbit, spins at a rate commensurate with the ambient vorticity vector projected along its axis. However, with particle inertia, the presence of gyroscopic forces implies that orientation and spin dynamics are coupled, and the test problem must therefore include both the axial and transverse rotation problems (Subramanian & Koch 2006*b*).

Using the form of the inertial acceleration in (2.12) and the ambient pressure given above (2.1), (2.7) may be rewritten as:

$$\begin{aligned}\boldsymbol{\Omega}_1\cdot\mathscr{L}_2=\boldsymbol{\Gamma}:\int_{S_p}\boldsymbol{x}(\boldsymbol{\sigma}^{(2)}\cdot\boldsymbol{n})dS+St\left[\frac{d}{dt}(\boldsymbol{I}_p\cdot\boldsymbol{\Omega}_1)\right]\cdot\boldsymbol{\Omega}_2-Re\,\boldsymbol{\Omega}_2\cdot\int_{S_p}(\boldsymbol{x}\times\boldsymbol{n})\frac{\boldsymbol{x}\cdot\boldsymbol{\Gamma}\cdot\boldsymbol{\Gamma}\cdot\boldsymbol{x}}{2}dS\\+Re\int_V\left[\frac{\partial\boldsymbol{u}'^{(1)}}{\partial t}+(\boldsymbol{\Gamma}\cdot\boldsymbol{x})\cdot\nabla\boldsymbol{u}'^{(1)}+\boldsymbol{\Gamma}\cdot\boldsymbol{u}'^{(1)}+\boldsymbol{u}'^{(1)}\cdot\nabla\boldsymbol{u}'^{(1)}\right]\cdot\boldsymbol{u}^{(2)}dV.\end{aligned}\tag{2.20}$$

Further, noting that the velocity field in the test problem is linear in $\boldsymbol{\Omega}_2$, one may write $\boldsymbol{u}^{(2)}=\boldsymbol{U}^{(2)}\cdot\boldsymbol{\Omega}_2$, $\mathscr{L}_2=\boldsymbol{L}^{(2)}\cdot\boldsymbol{\Omega}_2$ and $\boldsymbol{\sigma}^{(2)}=\boldsymbol{\Sigma}^{(2)}\cdot\boldsymbol{\Omega}_2$, where $\boldsymbol{U}^{(2)}$ and $\boldsymbol{L}^{(2)}$ are second-order tensors, and $\boldsymbol{\Sigma}^{(2)}$ is a third-order tensor, only dependent only on the geometry of the spheroidal particle, and are known in closed form as a function of the aspect ratio (see section 2.3; also see Dabade *et al.* (2015)). Accounting for $\boldsymbol{\Omega}_2$ being arbitrary, (2.20) takes the form:

$$\begin{aligned}\boldsymbol{\Omega}_1\cdot\boldsymbol{L}^{(2)}=\boldsymbol{\Gamma}:\int_{S_p}\boldsymbol{x}(\boldsymbol{\Sigma}^{(2)}\cdot\boldsymbol{n})dS+St\frac{d}{dt}(\boldsymbol{I}_p\cdot\boldsymbol{\Omega}_1)-Re\int_{S_p}(\boldsymbol{x}\times\boldsymbol{n})\frac{\boldsymbol{x}\cdot\boldsymbol{\Gamma}\cdot\boldsymbol{\Gamma}\cdot\boldsymbol{x}}{2}dS\\+Re\int_V\left[\frac{\partial\boldsymbol{u}'^{(1)}}{\partial t}+(\boldsymbol{\Gamma}\cdot\boldsymbol{x})\cdot\nabla\boldsymbol{u}'^{(1)}+\boldsymbol{\Gamma}\cdot\boldsymbol{u}'^{(1)}+\boldsymbol{u}'^{(1)}\cdot\nabla\boldsymbol{u}'^{(1)}\right]\cdot\boldsymbol{U}^{(2)}dV,\end{aligned}\tag{2.21}$$

valid for arbitrary Re and St. In section 2.3, we obtain expressions for the disturbance fields that appear in (2.21), using a spheroidal harmonics formalism, in a body-fixed coordinate system aligned with the spheroid symmetry axis. As a result, it becomes convenient to evaluate the unsteady acceleration involved in the last integral in the right-hand side of (2.21) in a coordinate system that rotates with the spheroid (XYZ in figure 2.2), but with the Y axis constrained to lie in the flow-gradient plane. The constraint implies that while the axes of this coordinate system section rotate with the spheroid, the resulting spin about the spheroid axis (Z) differs from the actual rate of spin. Using the relation between the time derivatives in the two coordinate systems, we have:

$$\begin{aligned}
\frac{\partial \boldsymbol{u}'^{(1)}}{\partial t} + \boldsymbol{u}'^{(1)} \cdot \boldsymbol{\nabla} \boldsymbol{u}'^{(1)} &= \frac{d\boldsymbol{u}'^{(1)}}{dt} && (2.22)\\
&= \left(\frac{d\boldsymbol{u}'^{(1)}}{dt}\right)_r + \boldsymbol{\Omega}_b \wedge \boldsymbol{u}'^{(1)}, && (2.23)\\
&= \left(\frac{\partial \boldsymbol{u}'^{(1)}}{\partial t}\right)_r + \boldsymbol{u}_r^{(1)} \cdot \boldsymbol{\nabla} \boldsymbol{u}'^{(1)} + \boldsymbol{\Omega}_b \wedge \boldsymbol{u}'^{(1)}, && (2.24)
\end{aligned}$$

where $\boldsymbol{\Omega}_b$ is the angular velocity of the body-fixed coordinate system, and we have used that the total time derivative in the rotating coordinate system involves calculating the rate of change for an element that moves with the velocity in the rotating coordinate system, which is given in terms of the original disturbance field as $\boldsymbol{u}_r^{(1)} = \boldsymbol{u}'^{(1)} - \boldsymbol{\Omega}_b \wedge \boldsymbol{x}$. Using this relation, (2.24) takes the form:

$$\frac{\partial \boldsymbol{u}'^{(1)}}{\partial t} + \boldsymbol{u}'^{(1)} \cdot \boldsymbol{\nabla} \boldsymbol{u}'^{(1)} = \left(\frac{\partial \boldsymbol{u}'^{(1)}}{\partial t}\right)_r + \boldsymbol{u}'^{(1)} \cdot \boldsymbol{\nabla} \boldsymbol{u}'^{(1)} + \boldsymbol{\Omega}_b \wedge \boldsymbol{u}'^{(1)} - (\boldsymbol{\Omega}_b \wedge \boldsymbol{x}) \cdot \boldsymbol{\nabla} \boldsymbol{u}'^{(1)}, \qquad (2.25)$$

where the third term arises from the usual rate of change of the rotating unit vector triad relative to a space-fixed coordinate system, while the fourth term denotes the rate of change due to the spatially inhomogeneous disturbance velocity field being swept past a space-fixed point with velocity $\boldsymbol{\Omega}_b \wedge \boldsymbol{x}$. Using (2.25) in (2.21), we have the following form for the reciprocal theorem identity:

$$\begin{aligned}
\boldsymbol{\Omega}_1 \cdot \boldsymbol{L}^{(2)} = \boldsymbol{\Gamma} : \int_{S_p} \boldsymbol{x} (\boldsymbol{\Sigma}^{(2)} \cdot \boldsymbol{n}) dS + St \frac{d}{dt} (\boldsymbol{I}_p \cdot \boldsymbol{\Omega}_1) - Re \int_{S_p} (\boldsymbol{x} \times \boldsymbol{n}) \frac{\boldsymbol{x} \cdot \boldsymbol{\Gamma} \cdot \boldsymbol{\Gamma} \cdot \boldsymbol{x}}{2} dS \\
+ Re \int_V \left[\left(\frac{\partial \boldsymbol{u}'^{(1)}}{\partial t}\right)_r + (\boldsymbol{\Gamma} \cdot \boldsymbol{x}) \cdot \boldsymbol{\nabla} \boldsymbol{u}'^{(1)} + \boldsymbol{\Gamma} \cdot \boldsymbol{u}'^{(1)} + \boldsymbol{u}'^{(1)} \cdot \boldsymbol{\nabla} \boldsymbol{u}'^{(1)} + \boldsymbol{\Omega}_b \wedge \boldsymbol{u}'^{(1)} \right. \\
\left. - (\boldsymbol{\Omega}_b \wedge \boldsymbol{x}) . \boldsymbol{\nabla} \boldsymbol{u}'^{(1)} \right] \cdot \boldsymbol{U}^{(2)} dV, \qquad (2.26)
\end{aligned}$$

which will be used in conjunction with the expressions for the disturbance velocity fields derived in section 2.3.

In order to estimate the $O(Re)$ correction to $\boldsymbol{\Omega}_1$, it is sufficient to use the leading-order Jeffery approximation for $\boldsymbol{\Omega}_b$ in the volume integral in (2.26), since the neglected terms of $O(ReSt)$ and $O(Re^2)$ are asymptotically smaller than those retained. This leading-order angular velocity, obtained from neglecting the inertial contributions in (2.26), is given by:

$$\boldsymbol{\Omega}_{jeff}\cdot\boldsymbol{L}^{(2)}=\boldsymbol{\Gamma}:\int_{S_p}\boldsymbol{x}(\boldsymbol{\Sigma}^{(2)}\cdot\boldsymbol{n})dS. \tag{2.27}$$

The components of $\boldsymbol{\Omega}_{jeff}$ orthogonal to $\boldsymbol{p}$, obtained from (2.27), lead to the well-known Jeffery orbit equations for a spheroid which, in non-dimensional form, are given by (Kim & Karrila (1991);Leal & Hinch (1971),Hinch & Leal (1972)):

$$\dot{\boldsymbol{p}}_{jeff}=\boldsymbol{\omega}\wedge\boldsymbol{p}+\frac{\kappa^2-1}{\kappa^2+1}[\boldsymbol{E}\cdot\boldsymbol{p}-\boldsymbol{p}(\boldsymbol{E}:\boldsymbol{p}\boldsymbol{p})], \tag{2.28}$$

where $\dot{\boldsymbol{p}}_{jeff}=\boldsymbol{\Omega}_{jeff}\wedge\boldsymbol{p}$, $\boldsymbol{\omega}=\frac{1}{2}\boldsymbol{\varepsilon}:(\boldsymbol{\Gamma}-\boldsymbol{\Gamma}^{\dagger})$, with $\boldsymbol{\Gamma}$ as defined before, is the ambient vorticity vector and κ is the spheroid aspect ratio; if b be the semi-minor axis, $\kappa=L/b$ and b/L for prolate and oblate spheroids, respectively. Since the spheroid spins at a rate commensurate with the projected ambient vorticity, we have $\boldsymbol{\Omega}_{jeff}\cdot\boldsymbol{p}=\frac{1}{2}\boldsymbol{\omega}\cdot\boldsymbol{p}$. The angular velocity in (2.28) may be written in terms of spherical coordinates (with the ambient vorticity direction as the polar axis) as:

$$\dot{\phi}_j=-\left(\frac{1-\lambda}{2}\right)+\left(\frac{1+\lambda}{2}\right)\frac{\kappa^2-1}{\kappa^2+1}\cos 2\phi_j, \tag{2.29}$$

$$\dot{\theta}_j=\left(\frac{1+\lambda}{4}\right)\frac{\kappa^2-1}{\kappa^2+1}\sin 2\theta_j\sin 2\phi_j, \tag{2.30}$$

where θ_j is the angle between the symmetry axis of the spheroid and the direction (Z') of ambient vorticity and ϕ_j is the dihedral angle between the flow-vorticity plane $(X'Z')$ and the orientation-vorticity plane (ZZ') - see figure 2.2. As mentioned earlier, for simplifying the calculation, we restrict the Y axis of the body-aligned coordinate system to the flow-gradient plane. The unit vectors of the body-aligned coordinate system XYZ can be expressed in terms of the unit vectors of the space-fixed coordinate system $X'Y'Z'$ (see figure 2.2) as $\mathbf{1}_x$ = $\cos\theta_j\cos\phi_j\mathbf{1}'_x$ + $\cos\theta_j\sin\phi_j\mathbf{1}'_y$ -$\sin\theta_j\mathbf{1}'_z$, $\mathbf{1}_y$ = $-\sin\phi_j\mathbf{1}'_x$ + $\cos\phi_j\mathbf{1}'_y$ and $\mathbf{1}_z$ = $\sin\theta_j\cos\phi_j\mathbf{1}'_x$ + $\sin\theta_j\sin\phi_j\mathbf{1}'_y$ +$\cos\theta_j\mathbf{1}'_z$. Thus, $\boldsymbol{\Omega}_b=\boldsymbol{\Omega}^t_{jeff}=-\dot{\phi}_j\sin\theta_j\,\mathbf{1}_x+\dot{\theta}_j\,\mathbf{1}_y+\dot{\phi}_j\cos\theta_j\,\mathbf{1}_z$ with ϕ_j and θ_j satisfying the Jeffery equations above; the subscript $'t'$ emphasizes the difference in the spin component of $\boldsymbol{\Omega}_b$ compared to $\boldsymbol{\Omega}_{jeff}\cdot\boldsymbol{p}$.

To determine $\boldsymbol{\Omega}_1$ to $O(Re)$, one may also use the Stokes approximation $(\boldsymbol{u}'^{(1)}_s)$ for the velocity field $\boldsymbol{u}'^{(1)}$ in (2.26). That this approximation leads to a convergent integral may be seen by noting that, for a linear flow at $Re=0$, we have $\boldsymbol{u}'^{(1)}_s\sim O(1/r^2)$ for $r\gg L$, and from (2.8), it is then seen that $\frac{D\boldsymbol{u}'^{(1)}_s}{Dt}\sim O(1/r^2)$ for large r. Since $\boldsymbol{u}^{(2)}\sim O(1/r^2)$ for $r\gg L$, the $O(Re)$

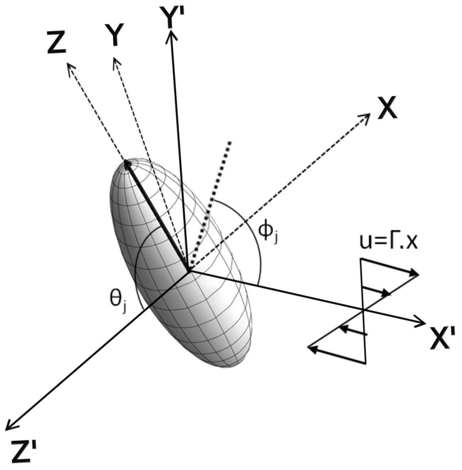

Fig. 2.2 The body-fixed and space-fixed coordinate systems.

integrand based on the Stokes approximation is $O(1/r^4)$ for $r \gg L$, implying convergence. As for the case of sedimentation in a quiescent fluid (Dabade *et al.* 2015), this points to the regular nature of the $O(Re)$ correction with the dominant contribution to the $O(Re)$ torque arising due to fluid inertial forces acting within a volume of order the size of the particle itself. It may be shown that the next correction to the angular velocity is $O(Re^{\frac{3}{2}})$, and is singular in character, arising from the effects of inertia acting on length scales of $O(Re^{-\frac{1}{2}})$. The non-uniformity of the Stokes approximation must be accounted for at this order (Subramanian *et al.* 2011). As will be seen later, while the $O(Re)$ correction evaluated here is sufficient to account for an inertial drift across Jeffery orbits, the effects of inertia on the Jeffery period, observed in recent simulations (Mao & Alexeev 2014), where the spheroid rotation in either the tumbling or spinning mode is observed to slow down with increasing Re, requires an analysis of the next correction at $O(Re^{\frac{3}{2}})$, and this is reported in chapter 5.

To $O(Re)$, (2.26) may now be written as:

$$\begin{aligned}\boldsymbol{\Omega}_1 \cdot \boldsymbol{L}^{(2)} - St\frac{d}{dt}(\boldsymbol{I}_p \cdot \boldsymbol{\Omega}_1) = \boldsymbol{\Gamma} : \int_{S_p} \boldsymbol{x}(\boldsymbol{\Sigma}^{(2)} \cdot \boldsymbol{n})dS - Re\int_{S_p}(\boldsymbol{x} \times \boldsymbol{n})\frac{\boldsymbol{x} \cdot \boldsymbol{\Gamma} \cdot \boldsymbol{\Gamma} \cdot \boldsymbol{x}}{2}dS \\ + Re\int_V \left[\frac{\partial \boldsymbol{u}'^{(1)}_s}{\partial t} + (\boldsymbol{\Gamma} \cdot \boldsymbol{x}) \cdot \boldsymbol{\nabla}\boldsymbol{u}'^{(1)}_s + \boldsymbol{\Gamma} \cdot \boldsymbol{u}'^{(1)}_s + \boldsymbol{u}'^{(1)}_s \cdot \boldsymbol{\nabla}\boldsymbol{u}'^{(1)}_s + \boldsymbol{\Omega}^t_{jeff} \wedge \boldsymbol{u}'^{(1)}_s - \right. \\ \left. (\boldsymbol{\Omega}^t_{jeff} \wedge \boldsymbol{x}).\boldsymbol{\nabla}\boldsymbol{u}'^{(1)}_s\right] \cdot \boldsymbol{U}^{(2)}dV,\end{aligned} \tag{2.31}$$

which is the final form on which subsequent calculations are based on. Note that St in (2.31) is still arbitrary. The operator on the left-hand-side, when considered alone, governs the rotations of an axisymmetric free body arising from a balance of centrifugal and gyroscopic forces. These are known from classical mechanics (the *Euler* top), and correspond to the limit $St \to \infty$ (Goldstein 1962). Herein, we assume St to be small, and only consider the effects of weak particle inertia to $O(St)$ and to $O(St^2)$ in chapter 5. The surface integral on the right-hand-side must lead to the well-known Jeffery orbits (Jeffery 1922) in the inertialess limit, while the second term, is the contribution from the ambient pressure, and the third term, the volume integral, captures fluid inertial effects to $O(Re)$. The analysis of the leading-order effects of fluid inertia therefore requires the Stokes disturbance velocity field ($\boldsymbol{u}'^{(1)}_s$) due to a torque-free spheroid, of an arbitrary orientation, in an ambient linear shear flow.

2.3 Solutions to the Stokes equation in spheroidal coordinates

The reciprocal theorem formulation in its final form, (2.31), requires the Stokes disturbance velocity field due to a torque-free spheroidal particle in a planar linear flow ($\boldsymbol{u}'^{(s)}$) and that due to a rotating spheroid in a quiescent fluid ($\boldsymbol{u}^{(2)}$). The integral in the reciprocal theorem is evaluated in a body-aligned coordinate system (XYZ). The transpose of the ambient velocity gradient tensor, $\boldsymbol{\Gamma}$, when expressed in the body-aligned coordinate system, becomes:

$$\begin{aligned}\boldsymbol{\Gamma} = {} & (1+\lambda)\cos^2\theta_j \sin\phi_j \cos\phi_j \mathbf{1}_x\mathbf{1}_x + \cos\theta_j(\cos^2\phi_j - \lambda\sin^2\phi_j)\mathbf{1}_x\mathbf{1}_y \\ & + (1+\lambda)\sin\theta_j\cos\theta_j\sin\phi_j\cos\phi_j(\mathbf{1}_x\mathbf{1}_z + \mathbf{1}_z\mathbf{1}_x) + \cos\theta_j(\lambda\cos^2\phi_j - \sin^2\phi_j)\mathbf{1}_y\mathbf{1}_x \\ & - (1+\lambda)\cos\phi_j\sin\phi_j\mathbf{1}_y\mathbf{1}_y + \sin\theta_j(\lambda\cos^2\phi_j - \sin^2\phi_j)\mathbf{1}_y\mathbf{1}_z \\ & + \sin\theta_j(\cos^2\phi_j - \lambda\sin^2\phi_j)\mathbf{1}_z\mathbf{1}_y + (1+\lambda)\sin^2\theta_j\sin\phi_j\cos\phi_j\mathbf{1}_z\mathbf{1}_z. \qquad (2.32)\end{aligned}$$

The velocity gradient tensor can be split into a rate-of-strain tensor and vorticity tensor. In the Stokes limit, a torque-free spheroid does not generate a disturbance velocity field in response to the ambient vorticity. The disturbance field in response to the flow is driven by the rate-of-strain tensor (denoted by $\boldsymbol{E}$) alone, which is given by :

$$\begin{aligned}\boldsymbol{E} = (1+\lambda)\Big(&\cos^2\theta_j\sin\phi_j\cos\phi_j\mathbf{1}_x\mathbf{1}_x + \frac{1}{2}\cos\theta_j(\cos^2\phi_j - \sin^2\phi_j)(\mathbf{1}_x\mathbf{1}_y + \mathbf{1}_y\mathbf{1}_x)\\ &+\sin\theta_j\cos\theta_j\sin\phi_j\cos\phi_j(\mathbf{1}_x\mathbf{1}_z + \mathbf{1}_z\mathbf{1}_x) - \cos\phi_j\sin\phi_j\mathbf{1}_y\mathbf{1}_y + \frac{1}{2}\sin\theta_j(\cos^2\phi_j - \sin^2\phi_j)\\ &(\mathbf{1}_y\mathbf{1}_z + \mathbf{1}_z\mathbf{1}_y) + \sin^2\theta_j\sin\phi_j\cos\phi_j\mathbf{1}_z\mathbf{1}_z\Big),\end{aligned} \tag{2.33}$$

in the body-aligned coordinate system. Note that $\boldsymbol{E}$ for a planar linear flow is simply $(1+\lambda)$ times $\boldsymbol{E}$ for the simple shear flow ($\lambda = 0$). The velocity disturbance field for an arbitrarily oriented spheroid in response to the ambient rate of strain tensor can be written as a response to five canonical component linear flows, whose matrix representation is given by:

$$(1+\lambda)\begin{bmatrix} \cos^2\theta_j\sin\phi_j\cos\phi_j & \frac{1}{2}\cos\theta_j(\cos^2\phi_j-\sin^2\phi_j) & \sin\theta_j\cos\theta_j\sin\phi_j\cos\phi_j \\ \frac{1}{2}\cos\theta_j(\cos^2\phi_j-\sin^2\phi_j) & -\cos\phi_j\sin\phi_j & \frac{1}{2}\sin\theta_j(\cos^2\phi_j-\sin^2\phi_j) \\ \sin\theta_j\cos\theta_j\sin\phi_j\cos\phi_j & \frac{1}{2}\sin\theta_j(\cos^2\phi_j-\sin^2\phi_j) & \sin^2\theta_j\sin\phi_j\cos\phi_j \end{bmatrix}$$

$$=(1+\lambda)\begin{bmatrix} -\frac{1}{2}\sin^2\theta_j\sin\phi_j\cos\phi_j & 0 & 0 \\ 0 & -\frac{1}{2}\sin^2\theta_j\sin\phi_j\cos\phi_j & 0 \\ 0 & 0 & \sin^2\theta_j\sin\phi_j\cos\phi_j \end{bmatrix}$$

$$+(1+\lambda)\begin{bmatrix} \frac{1}{2}(\cos^2\theta_j+1)\sin\phi_j\cos\phi_j & 0 & 0 \\ 0 & -\frac{1}{2}(\cos^2\theta_j+1)\sin\phi_j\cos\phi_j & 0 \\ 0 & 0 & 0 \end{bmatrix}$$

$$+(1+\lambda)\begin{bmatrix} 0 & \frac{1}{2}\cos\theta_j(\cos^2\phi_j-\sin^2\phi_j) & 0 \\ \frac{1}{2}\cos\theta_j(\cos^2\phi_j-\sin^2\phi_j) & 0 & 0 \\ 0 & 0 & 0 \end{bmatrix}$$

$$+(1+\lambda)\begin{bmatrix} 0 & 0 & \sin\theta_j\cos\theta_j\sin\phi_j\cos\phi_j \\ 0 & 0 & 0 \\ \sin\theta_j\cos\theta_j\sin\phi_j\cos\phi_j & 0 & 0 \end{bmatrix}$$

$$+(1+\lambda)\begin{bmatrix} 0 & 0 & 0 \\ 0 & 0 & \frac{1}{2}\sin^2\theta_j(\cos^2\phi_j-\sin^2\phi_j) \\ 0 & \frac{1}{2}\sin^2\theta_j(\cos^2\phi_j-\sin^2\phi_j) & 0 \end{bmatrix}. \tag{2.34}$$

The five component matrices above correspond, respectively, to an axisymmetric extensional flow (uni-axial or bi-axial depending on the sign of $\sin\phi_j\cos\phi_j$) along the spheroidal axis (Z) of symmetry with an amplitude proportional to $\sin^2\theta_j\cos\phi_j\sin\phi_j$; a pair of extensional flows in the plane (XY) transverse to the axis of symmetry, one of them being obtained from the other via a 45^o rotation about the symmetry axis, and with amplitudes proportional to $\frac{1}{2}(\cos^2\theta_j+1)\sin\phi_j\cos\phi_j$ and $\frac{1}{2}\cos\theta_j(\cos^2\phi_j-\sin^2\phi_j)$; and a pair of longitudinal extensional flows in planes containing the axis of symmetry (the XZ and YZ planes) and with amplitudes proportional to $\sin\theta_j\cos\theta_j\sin\phi_j\cos\phi_j$ and $\frac{1}{2}\sin^2\theta_j(\cos^2\phi_j-\sin^2\phi_j)$.

Denoting the disturbance fields corresponding to the five component linear flows as $\boldsymbol{u}_{1s}-\boldsymbol{u}_{5s}$, we have $\boldsymbol{u}'^{(1)}_s=\sum_{i=1}^{5}\boldsymbol{u}_{is}$, with $\boldsymbol{u}_{1s}$ corresponding to the axisymmetric extension, $\boldsymbol{u}_{2s},\boldsymbol{u}_{3s}$ corresponding to the two planar extensions, and $\boldsymbol{u}_{4s},\boldsymbol{u}_{5s}$ corresponding to the pair of longitudinal extensions above. While the expressions for these component Stokesian velocity fields may be obtained using earlier results based on the method of singularities (Chwang & Wu 1974, 1975), herein we use the vector spheroidal harmonics formalism developed by Kushch and co-workers (Kushch 1997, 1998). The reasons for this choice have been outlined in Dabade *et al.* (2015), where the formalism was used for a single sedimenting particle in an otherwise quiescent fluid. Since the structure of the formalism, and a comparison with a similar expansion of the velocity field in terms of spherical harmonics, originally given by Lamb [for instance, see Chapter 4 Kim & Karrila (1991)], has already been explained in some detail in Dabade *et al.* (2015), we will be brief here. The formalism is based on expressing the general solution of the Stokes equations, around an arbitrary number of spheroidal particles, as a superposition of growing and decaying vector harmonics in local spheroidal coordinates defined with respect to a Cartesian system centered at each particle, and aligned with the particle axis of symmetry. For a prolate spheroid, the spheroidal coordinates (ξ,η,ϕ) are related to Cartesian coordinates (x,y,z) as $x+iy=d\bar{\xi}\bar{\eta}\exp(i\phi)$ and $z=d\xi\eta$, with $\bar{\xi}=\sqrt{(\xi^2-1)}$ and $\bar{\eta}=\sqrt{(1-\eta^2)}$, where d is the inter focal distance. Here, the constant ξ-surfaces denote a family of con-focal prolate spheroids with the inter-foci distance being equal to $2d$; ξ_0 denotes the surface of the particle and is also equal to the inverse of the eccentricity of the spheroid. The constant η-surfaces represent a family of confocal two-sheeted hyperboloids, while the constant ϕ-surfaces are planes passing through the axis of symmetry. The disturbance field due to a single particle in an infinite viscous ambient must involve only decaying spheroidal harmonics, and may therefore be written in the form:

$$\boldsymbol{u}(\boldsymbol{x}) = \sum_{i=1}^{3}\sum_{t=0}^{\infty}\sum_{s=-t}^{t} A_{ts}^{(i)} \boldsymbol{S}_{ts}^{(i)}(\boldsymbol{r}, d), \tag{2.35}$$

where the decaying (singular) partial vectorial solutions are given by:

$$\mathbf{S}_{ts}^{(1)} = \mathbf{e}_1 F_{t+1}^{s-1} - \mathbf{e}_2 F_{t+1}^{s+1} + \mathbf{1}_z F_{t+1}^{s}, \tag{2.36}$$

$$\mathbf{S}_{ts}^{(2)} = \frac{1}{t}\left[\mathbf{e}_1 (t+s) F_t^{s-1} + \mathbf{e}_2 (t-s) F_t^{s+1} + \mathbf{1}_z s F_t^{s}\right], \tag{2.37}$$

$$\begin{aligned}\mathbf{S}_{ts}^{(3)} = {} & \mathbf{e}_1 \left\{-(x-iy)\mathrm{D}_2 F_{t-1}^{s-1} - (\xi_0^2-1) d\mathrm{D}_1 F_t^{s} + (t+s-1)(t+s)\beta_{-(t+1)} F_{t-1}^{s-1}\right\} \\ & + \mathbf{e}_2 \left\{(x+iy)\mathrm{D}_1 F_{t-1}^{s+1} - (\xi_0^2-1) d\mathrm{D}_2 F_t^{s} - (t-s-1)(t-s)\beta_{-(t+1)} F_{t-1}^{s+1}\right\} \\ & + \mathbf{1}_z \left[z\mathrm{D}_3 F_{t-1}^{s} - \xi_0^2 d\mathrm{D}_3 F_t^{s} - C_{-(t+1),s} F_{t-1}^{s}\right],\end{aligned} \tag{2.38}$$

with $\mathbf{S}_{ts}^{(i)} \to \mathbf{0}$ for $\boldsymbol{r} \to \infty$. Here, $\beta_t = \frac{t+3}{(t+1)(2t+3)}$, $C_{t,s} = (t+s+1)(t-s+1)\beta_t$ with $t = 0, 1, \ldots;\ |s| \le t$; further, $\mathbf{e}_1 = (\mathbf{1}_x + i\mathbf{1}_y)/2$, $\mathbf{e}_2 = (\mathbf{1}_x - i\mathbf{1}_y)/2$, with $\mathbf{1}_z$, as before, being directed along the axis of symmetry of the spheroidal coordinate system. The D_i's denote differential operators with $D_1 = (\partial/\partial x - i\partial/\partial y)$, $D_2 = (\partial/\partial x + i\partial/\partial y)$, and $D_3 = (\partial/\partial z)$. In (2.36)-(2.38), the functions $F_t^s \equiv F_t^s(\mathbf{r}, d)$ are the singular solid spheroidal harmonics of the form $F_t^s = Q_t^s(\xi) Y_t^s(\eta, \phi)$ with $Y_t^s(\eta, \phi) = P_t^s(\eta)\exp(is\phi)$ being the familiar scalar surface harmonics, and P_t^s and Q_t^s being the associated Legendre functions of the first and second kind, respectively (Morse & Feshbach 1953). The analogs of all of the above expressions, for an oblate spheroid, can be derived from using the transformation $\xi \leftrightarrow \mathrm{i}\bar{\xi}$ and $d \leftrightarrow -id$ (Dabade *et al.* (2015)). The aspect ratio can be expressed in terms of ξ_0 as $\kappa = \xi_0/\sqrt{\xi_0^2 - 1}$ $(= \sqrt{\xi_0^2 - 1}/\xi_0)$ for prolate (oblate) spheroid.

Now, the $\boldsymbol{S}_{ts}^{(1)}$'s and $\boldsymbol{S}_{ts}^{(2)}$'s are harmonic functions, while the $\boldsymbol{S}_{ts}^{(3)}$'s satisfy the biharmonic equation, and are therefore the only vectorial solutions associated with a non-trivial pressure field. The index t in $\boldsymbol{S}_{ts}^{(i)}$ is a measure of the rapidity of decay of the velocity disturbance field for large r, with $\lim_{r\to\infty} \boldsymbol{u}(\boldsymbol{x}) \propto r^{-t}$, this arising from the large-ξ behavior of the Q_t^s's. Since the $\boldsymbol{S}_{ts}^{(3)}$'s alone include the fundamental singularities of the Stokes equations, in light of the large-r behavior indicated above, one expects the $\boldsymbol{S}_{1s}^{(3)}$'s to be relevant to the translation problem where $\boldsymbol{u}(\boldsymbol{x}) \propto 1/r$; and the $\boldsymbol{S}_{2s}^{(3)}$'s to come into play for both transverse rotations and the disturbance fields in an ambient linear flow, for all of which $\boldsymbol{u}(\boldsymbol{x}) \propto 1/r^2$ - see (2.39)-(2.47) and (2.59)-(2.61) below. Note that axial rotation is an exception in that it does not generate a pressure field and the velocity disturbance in this case is harmonic, being proportional to $\boldsymbol{S}_{20}^{(2)}$ (see (2.68)). The second index s in all these cases denotes the variation of the velocity field as a function of the azimuthal angle in the plane transverse to the symmetry axis, with $s = 0$ corresponding to an axisymmetric exterior field; for instance, the disturbance velocity field in an ambient axisymmetric extensional flow must involve $\boldsymbol{S}_{20}^{(3)}$.

For a prolate spheroid, use of the surface boundary condition at $\xi = \xi_0$ leads to the following expressions, in terms of the $\boldsymbol{S}_{ts}^{(3)}$'s, for the disturbance velocity and pressure fields corresponding to the five canonical linear flows above:

$$\boldsymbol{u}_{1s} = \frac{-d\bar{\xi}_0(1+\lambda)}{(Q_1^1(\xi_0) - \xi_0 Q_2^1(\xi_0))}(\sin^2\theta_j \sin\phi_j \cos\phi_j)\boldsymbol{S}_{20}^{(3)}, \tag{2.39}$$

$$p_{1s} =, \frac{-2d\bar{\xi}_0(1+\lambda)}{(Q_1^1(\xi_0) - \xi_0 Q_2^1(\xi_0))}(\sin^2\theta_j \sin\phi_j \cos\phi_j)D_3F_1^0, \tag{2.40}$$

$$\boldsymbol{u}_{2s} = -\frac{d\bar{\xi}_0(1+\lambda)}{(3Q_1^1(\xi_0) - \xi_0 Q_2^1(\xi_0))}[\sin\phi_j \cos\phi_j(1+\cos^2\theta_j)](\boldsymbol{S}_{22}^{(3)} + \boldsymbol{S}_{2,-2}^{(3)}), \tag{2.41}$$

$$p_{2s} = -\frac{2d\bar{\xi}_0(1+\lambda)}{(3Q_1^1(\xi_0) - \xi_0 Q_2^1(\xi_0))}[\sin\phi_j \cos\phi_j(1+\cos^2\theta_j)](D_3F_1^2 + D_3F_1^{-2}), \tag{2.42}$$

$$\boldsymbol{u}_{3s} = \frac{\mathrm{i}d\bar{\xi}_0(1+\lambda)}{(3Q_1^1(\xi_0) - \xi_0 Q_2^1(\xi_0))}[\cos\theta_j \cos 2\phi_j](\boldsymbol{S}_{22}^{(3)} - \boldsymbol{S}_{2,-2}^{(3)}), \tag{2.43}$$

$$p_{3s} = \frac{2\mathrm{i}d\bar{\xi}_0(1+\lambda)}{(3Q_1^1(\xi_0) - \xi_0 Q_2^1(\xi_0))}[\cos\theta_j \cos 2\phi_j](D_3F_1^2 - D_3F_1^{-2}), \tag{2.44}$$

$$\boldsymbol{u}_{4s} = \frac{2d\xi_0\bar{\xi}_0(1+\lambda)}{Q_2^1(\xi_0)(2\xi_0^2-1)}(\sin\theta_j \cos\theta_j \sin\phi_j \cos\phi_j)(\boldsymbol{S}_{21}^{(3)} - \boldsymbol{S}_{2,-1}^{(3)}), \tag{2.45}$$

$$p_{4s} = \frac{4d\xi_0\bar{\xi}_0(1+\lambda)}{Q_2^1(\xi_0)(2\xi_0^2-1)}(\sin\theta_j \cos\theta_j \sin\phi_j \cos\phi_j)(D_3F_1^1 - D_3F_1^{-1}), \tag{2.46}$$

$$\boldsymbol{u}_{5s} = -\frac{\mathrm{i}d\xi_0\bar{\xi}_0(1+\lambda)}{Q_2^1(\xi_0)(2\xi_0^2-1)}[\sin\theta_j(\cos^2\phi_j - \sin^2\phi_j)](\boldsymbol{S}_{21}^{(3)} + \boldsymbol{S}_{2,-1}^{(3)}), \tag{2.47}$$

$$p_{5s} = -\frac{2\mathrm{i}d\xi_0\bar{\xi}_0(1+\lambda)}{Q_2^1(\xi_0)(2\xi_0^2-1)}[\sin\theta_j(\cos^2\phi_j - \sin^2\phi_j)](D_3F_1^1 + D_3F_1^{-1}). \tag{2.48}$$

On substitution of the expressions for the $\boldsymbol{S}_{ts}^{(3)}$'s and F_t^s's, given in (2.38), the disturbance velocity fields take the following forms:

$$
\begin{aligned}
\boldsymbol{u}_{1s} = &-\frac{d\bar{\xi}_0(1+\lambda)}{(Q_1^1(\xi_0)-\xi_0 Q_2^1(\xi_0))}(\sin^2\theta_j \sin\phi_j \cos\phi_j)\Bigg[\boldsymbol{x}\frac{\partial}{\partial z}(P_1^0 Q_1^0) - \mathbf{1}_z d\xi_0^2 \frac{\partial}{\partial z}(P_2^0 Q_2^0) \\
&- d\bar{\xi}_0^2\left(\mathbf{1}_x\frac{\partial}{\partial x}+\mathbf{1}_y\frac{\partial}{\partial y}\right)(P_2^0 Q_2^0)\Bigg], \qquad (2.49)\\
p_{1s} = &-\frac{2d\bar{\xi}_0(1+\lambda)}{(Q_1^1(\xi_0)-\xi_0 Q_2^1(\xi_0))}(\sin^2\theta_j \sin\phi_j \cos\phi_j)\frac{\partial}{\partial z}(P_1^0 Q_1^0), \qquad (2.50)
\end{aligned}
$$

$$
\begin{aligned}
\boldsymbol{u}_{2s} = &\frac{d\bar{\xi}_0(1+\lambda)}{(\xi_0 Q_2^1(\xi_0)-3Q_1^1(\xi_0))}(1+\cos^2\theta_j)\sin\phi_j\cos\phi_j\left[\boldsymbol{x}\left\{\frac{\partial}{\partial y}(P_1^1 Q_1^1 \sin\phi) - \frac{\partial}{\partial x}(P_1^1 Q_1^1\cos\phi)\right\}\right.\\
&\left.-\frac{d\bar{\xi}_0^2}{12}\left(\mathbf{1}_x\frac{\partial}{\partial x}+\mathbf{1}_y\frac{\partial}{\partial y}\right)(P_2^2 Q_2^2\cos 2\phi) - \frac{d\xi_0^2}{12}\mathbf{1}_z\frac{\partial}{\partial z}(P_2^2 Q_2^2 \cos 2\phi)\right], \qquad (2.51)
\end{aligned}
$$

$$
p_{2s} = \frac{2d\bar{\xi}_0(1+\lambda)}{(\xi_0 Q_2^1(\xi_0)-3Q_1^1(\xi_0))}(1+\cos^2\theta_j)\sin\phi_j\cos\phi_j\left[\frac{\partial}{\partial y}(P_1^1 Q_1^1\sin\phi) - \frac{\partial}{\partial x}(P_1^1 Q_1^1 \cos\phi)\right], \qquad (2.52)
$$

$$
\begin{aligned}
\boldsymbol{u}_{3s} = &\frac{d\bar{\xi}_0(1+\lambda)}{(3Q_1^1(\xi_0)-\xi_0 Q_2^1(\xi_0))}\cos\theta_j(\cos^2\phi_j - \sin^2\phi_j)\left[\boldsymbol{x}\left\{\frac{\partial}{\partial x}(P_1^1 Q_1^1\sin\phi) + \frac{\partial}{\partial y}(P_1^1 Q_1^1 \cos\phi)\right\}\right.\\
&\left.+\frac{d\bar{\xi}_0^2}{12}\left(\mathbf{1}_x\frac{\partial}{\partial x}+\mathbf{1}_y\frac{\partial}{\partial y}\right)(P_2^2 Q_2^2 \sin 2\phi) + \frac{d\xi_0^2}{12}\mathbf{1}_z\frac{\partial}{\partial z}(P_2^2 Q_2^2\sin 2\phi)\right], \qquad (2.53)\\
p_{3s} = &\frac{2d\bar{\xi}_0(1+\lambda)}{(3Q_1^1(\xi_0)-\xi_0 Q_2^1(\xi_0))}\cos\theta_j(\cos^2\phi_j-\sin^2\phi_j)\left[\frac{\partial}{\partial x}(P_1^1 Q_1^1 \sin\phi) + \frac{\partial}{\partial y}(P_1^1 Q_1^1\cos\phi)\right], \qquad (2.54)
\end{aligned}
$$

$$
\begin{aligned}
\boldsymbol{u}_{4s} = &\frac{2d\xi_0\bar{\xi}_0(1+\lambda)}{Q_2^1(\xi_0)(2\xi_0^2-1)}(\sin\theta_j\cos\theta_j\sin\phi_j\cos\phi_j)\left[\boldsymbol{r}\frac{\partial}{\partial z}(P_1^1 Q_1^1\cos\phi) - \frac{d\xi_0^2}{3}\mathbf{1}_z\frac{\partial}{\partial z}(P_2^1 Q_2^1\cos\phi)\right.\\
&\left.-\frac{d\bar{\xi}_0^2}{3}\left(\mathbf{1}_x\frac{\partial}{\partial x}+\mathbf{1}_y\frac{\partial}{\partial y}\right)(P_2^1 Q_2^1 \cos\phi)\right], \qquad (2.55)\\
p_{4s} = &\frac{4d\xi_0\bar{\xi}_0(1+\lambda)}{Q_2^1(\xi_0)(2\xi_0^2-1)}(\sin\theta_j\cos\theta_j\sin\phi_j\cos\phi_j)\frac{\partial}{\partial z}(P_1^1 Q_1^1\cos\phi), \qquad (2.56)
\end{aligned}
$$

$$\boldsymbol{u}_{5s} = \frac{d\xi_0\bar{\xi}_0(1+\lambda)}{Q_2^1(\xi_0)(2\xi_0^2-1)}\sin\theta_j(\cos^2\phi_j - \sin^2\phi_j)\left[\boldsymbol{r}\frac{\partial}{\partial z}(P_1^1 Q_1^1 \sin\phi) - \frac{d\xi_0^2}{3}\mathbf{1}_z\frac{\partial}{\partial z}(P_2^1 Q_2^1\sin\phi) \right.$$
$$\left. -\frac{d\bar{\xi}_0^2}{3}\left(\mathbf{1}_x\frac{\partial}{\partial x} + \mathbf{1}_y\frac{\partial}{\partial y}\right)(P_2^1 Q_2^1 \sin\phi)\right], \tag{2.57}$$

$$p_{5s} = \frac{2d\xi_0\bar{\xi}_0(1+\lambda)}{Q_2^1(\xi_0)(2\xi_0^2-1)}\sin\theta_j(\cos^2\phi_j - \sin^2\phi_j)\frac{\partial}{\partial z}(P_1^1 Q_1^1\sin\phi). \tag{2.58}$$

As shown by Dabade *et al.* (2015), the test velocity fields in (2.31), corresponding to transverse rotations about the x and y axes, are given by:

$$\boldsymbol{u}_{sx}^{(2)} = \frac{id(2\xi_0^2-1)}{2Q_1^0(\xi_0)\xi_0 - \xi_0 Q_1^1(\xi_0)}\left(\mathbf{S}_{1,1}^{(2)} - \mathbf{S}_{1,-1}^{(2)}\right) + \frac{id(\xi_0 Q_1^1(\xi_0) + 2\bar{\xi}_0 Q_1^0(\xi_0))}{Q_2^1(\xi_0)(2Q_1^0(\xi_0)\xi_0 - \xi_0 Q_1^1(\xi_0))}\left(\mathbf{S}_{2,1}^{(3)} + \mathbf{S}_{2,-1}^{(3)}\right), \tag{2.59}$$

$$= -\frac{d(2\xi_0^2-1)}{(2\xi_0 Q_1^0(\xi_0) - \xi_0 Q_1^1(\xi_0))}(2P_1^0 Q_1^0\mathbf{1}_y + P_1^1 Q_1^1\sin\phi\,\mathbf{1}_z)$$
$$-\frac{d}{(2\xi_0 Q_1^0(\xi_0) - \xi_0 Q_1^1(\xi_0))}\left[\boldsymbol{r}\frac{\partial}{\partial z}(P_1^1 Q_1^1\sin\phi) - \frac{d\xi_0^2}{3}\mathbf{1}_z\frac{\partial}{\partial z}(P_2^1 Q_2^1\sin\phi)\right.$$
$$\left.-\frac{d\bar{\xi}_0^2}{3}\left(\mathbf{1}_x\frac{\partial}{\partial x} + \mathbf{1}_y\frac{\partial}{\partial y}\right)(P_2^1 Q_2^1\sin\phi)\right], \tag{2.60}$$

$$\boldsymbol{u}_{sy}^{(2)} = \frac{d(2\xi_0^2-1)}{(2\xi_0 Q_1^0(\xi_0) - \xi_0 Q_1^1(\xi_0))}\left(\mathbf{S}_{1,1}^{(2)} + \mathbf{S}_{1,-1}^{(2)}\right) + \frac{d(\xi_0 Q_1^1(\xi_0) + 2\bar{\xi}_0 Q_1^0(\xi_0))}{Q_2^1(\xi_0)(2\xi_0 Q_1^0(\xi_0) - \xi_0 Q_1^1(\xi_0))}\left(\mathbf{S}_{2,1}^{(3)} - \mathbf{S}_{2,-1}^{(3)}\right), \tag{2.61}$$

$$= \frac{d(2\xi_0^2-1)}{(2\xi_0 Q_1^0(\xi_0) - \xi_0 Q_1^1(\xi_0))}(2P_1^0 Q_1^0\mathbf{1}_x + P_1^1 Q_1^1\cos\phi\,\mathbf{1}_z)$$
$$+\frac{d}{(2\xi_0 Q_1^0(\xi_0) - \xi_0 Q_1^1(\xi_0))}\left[\boldsymbol{r}\frac{\partial}{\partial z}(P_1^1 Q_1^1\cos\phi) - \frac{d\xi_0^2}{3}\mathbf{1}_z\frac{\partial}{\partial z}(P_2^1 Q_2^1\cos\phi)\right.$$
$$\left.-\frac{d\bar{\xi}_0^2}{3}\left(\mathbf{1}_x\frac{\partial}{\partial x} + \mathbf{1}_y\frac{\partial}{\partial y}\right)(P_2^1 Q_2^1\cos\phi)\right], \tag{2.62}$$

respectively, with the corresponding pressure fields being given by:

$$p_{sx}^{(2)} = \frac{2\mathrm{i}d(\xi_0 Q_1^1(\xi_0) + 2\bar{\xi}_0 Q_1^0(\xi_0))}{Q_2^1(\xi_0)(2\xi_0 Q_1^0(\xi_0) - \xi_0 Q_1^1(\xi_0))}(D_2^1 + D_2^{-1}), \tag{2.63}$$

$$= -\frac{2d(\xi_0 Q_1^1(\xi_0) + 2\bar{\xi}_0 Q_1^0(\xi_0))}{Q_2^1(\xi_0)(2\xi_0 Q_1^0(\xi_0) - \xi_0 Q_1^1(\xi_0))}\frac{\partial}{\partial z}(P_1^1 Q_1^1 \sin\phi), \tag{2.64}$$

$$p_{sy}^{(2)} = \frac{2(\xi_0 Q_1^1(\xi_0) + 2\bar{\xi}_0 Q_1^0(\xi_0))}{Q_2^1(\xi_0)(2\xi_0 Q_1^0(\xi_0) - \xi_0 Q_1^1(\xi_0))}(D_2^1 - D_2^{-1}), \tag{2.65}$$

$$= \frac{2d(\xi_0 Q_1^1(\xi_0) + 2\bar{\xi}_0 Q_1^0(\xi_0))}{Q_2^1(\xi_0)(2\xi_0 Q_1^0(\xi_0) - \xi_0 Q_1^1(\xi_0))}\frac{\partial}{\partial z}(P_1^1 Q_1^1 \cos\phi), \tag{2.66}$$

where $D_t^s = dD_3 F_t^s$. The test velocity field corresponding to rotation about the z axis is given by:

$$\boldsymbol{u}_{sz}^{(2)} = \frac{2\mathrm{i}d\bar{\xi}_0}{Q_1^1(\xi_0)}\boldsymbol{S}_{10}^{(2)}, \tag{2.67}$$

$$= \frac{d\bar{\xi}_0}{Q_1^1(\xi_0)}(-\sin\phi\,\mathbf{1}_x + \cos\phi\,\mathbf{1}_y)(P_1^1 Q_1^1), \tag{2.68}$$

with $p_{sz}^{(2)} = 0$, there being no associated pressure field with axial rotation. The magnitudes of the torque for axial and transverse rotations are given by $8\pi X_C$ and $8\pi Y_C$ respectively, with $X_C = \frac{4\left(\xi_0^2-1\right)}{3\xi_0^3\left(2\xi_0-2\left(\xi_0^2-1\right)\coth^{-1}\xi_0\right)}$ and $Y_C = \frac{4\left(2\xi_0^2-1\right)}{3\xi_0^3\left(2\left(\xi_0^2+1\right)\coth^{-1}\xi_0-2\xi_0\right)}$. The second-order tensors characterizing the test problem that appear in (2.31) are therefore given by $\boldsymbol{U}^{(2)} = \boldsymbol{u}_{sx}^{(2)}\mathbf{1}_x + \boldsymbol{u}_{sy}^{(2)}\mathbf{1}_y + \boldsymbol{u}_{sz}^{(2)}\mathbf{1}_z$ and $\boldsymbol{L}^{(2)} = -8\pi(X_C\boldsymbol{pp} + Y_C(\boldsymbol{I} - \boldsymbol{pp}))$ with $\boldsymbol{p} = \mathbf{1}_z$. The test torque tensor, $\boldsymbol{L}^{(2)}$ in (2.76), is defined in the end of section 2.3. The non-dimensional moment of inertia tensor, $\boldsymbol{I}_p$, is given by $\frac{4\pi}{15}\bar{\xi}_0^2\left[\frac{2\xi_0^2}{\xi_0^4}\boldsymbol{pp} + \frac{(2\xi_0^2-1)}{\xi_0^4}(\boldsymbol{I}-\boldsymbol{pp})\right]$ and $\frac{4\pi}{15}\bar{\xi}_0\left[\frac{2}{\xi_0}\boldsymbol{pp} + \frac{(2\xi_0^2-1)}{\xi_0^3}(\boldsymbol{I}-\boldsymbol{pp})\right]$ for prolate and oblate spheroids, respectively.

2.4 Stokes limit and the equivalent aspect ratio

In this section we will focus on the trajectories of the orientation of a spheroid in a planar linear flow in the Stokes limit. The rate of change of angles θ_j and ϕ_j in this limit are given in (2.29) and (2.30). These angular velocities can be recovered from (2.31) by evaluating the integral in the limit of $Re = 0$ and $St = 0$, and noting that $\boldsymbol{\Sigma}^{(2)} \cdot \mathbf{1}_\xi = -\boldsymbol{P}^{(2)}\mathbf{1}_\xi + 2\left[\frac{\bar{\xi}}{d(\xi^2-\eta^2)^{\frac{1}{2}}}\frac{\partial}{\partial\xi}\boldsymbol{U}^{(2)} + \frac{1}{2}\mathbf{1}_\xi \wedge (\boldsymbol{\nabla} \wedge \boldsymbol{U}^{(2)})\right]$, where $\boldsymbol{P}^{(2)}$ is the pressure corresponding to the transverse rotations. It can be shown that for a given aspect ratio, the trajectories are closed orbits on a unit sphere only till a particular λ say λ_{crit}(see Hinch & Leal (1972)). This is expected because the vortical component of the flow responsible for the existence of closed orbits decreases with increasing λ (figure 2.1 (a)-(e)) and at $\lambda = \lambda_{crit}$, becomes sufficiently small compared to the extensional component, and as a result closed orbits ceases to exist for $\lambda > \lambda_{crit}$. It can be noted that λ_{crit} is always positive implying that the critical flow separating open and closed trajectories on the unit sphere is always a hyperbolic linear flow. One finds $\lambda_{crit} = 1/\kappa^2$ and κ^2 respectively for prolate and oblate spheroids of aspect ratio κ. Note that $\lambda_{crit} \rightarrow 0$ for infinitely thin fibers and disks, implying that the critical flow asymptotes to a simple shear for extreme aspect ratios. This is consistent with the fact that the orientation of an infinitely slender fibre and the normal to a flat disk evolve in an affine manner, merely following the ambient streamlines (projected onto the unit sphere). In figure 2.3, λ_{crit} is plotted as a function of κ. As indicated, the trajectories for the spheroid orientation are closed, when (λ, κ) is below λ_{crit} curve. There are six fixed points on the unit sphere for $\lambda > \lambda_{crit}$; pairs of unstable and stable nodes, and a third pair of saddle points on the Z' axis (the indices of these fixed points add to the Euler characteristic, as must be the case). Almost all the trajectories end in the two stable fixed points. The stable fixed points and the closed orbits for both prolate and oblate spheroids are also shown in the relevant regions of figure 2.3. As will be shown in later sections, in the region below the λ_{crit} curve in figure 2.3, weak inertia will result in a drift across the closed orbits, and the long-time orientation distribution can be drastically different from that implied by Stokesian dynamics which predicts a continued dependence on the initial orientation distribution for all times. For the region above the λ_{crit} curve, weak inertia can only alter the location of the fixed points by O(Re) or O(St). Therefore this region in the $\lambda - \kappa$ plane is not analyzed in detail. Note that the correction to the angular velocities at O(Re) and O(St) presented in the next two sections are, however, valid for all regions in the $\lambda - \kappa$ plane.

It has been shown that in the Stokes limit, the closed trajectories of the spheroid orientation vector in a planar linear flow ($\lambda < \lambda_{crit}$), are the same as the trajectories (Jeffery (1922)) of an equivalent spheroid in a simple shear flow of strength $(1-\lambda)$ (Hinch & Leal 1972; Prager 1957; Bretherton 1962). The aspect ratio of this latter spheroid is a function of λ and κ, and is given by:

$$\kappa_{eq} = \sqrt{\frac{(\kappa^2+1)(1-\lambda)+(\kappa^2-1)(1+\lambda)}{(\kappa^2+1)(1-\lambda)-(\kappa^2-1)(1+\lambda)}}. \tag{2.69}$$

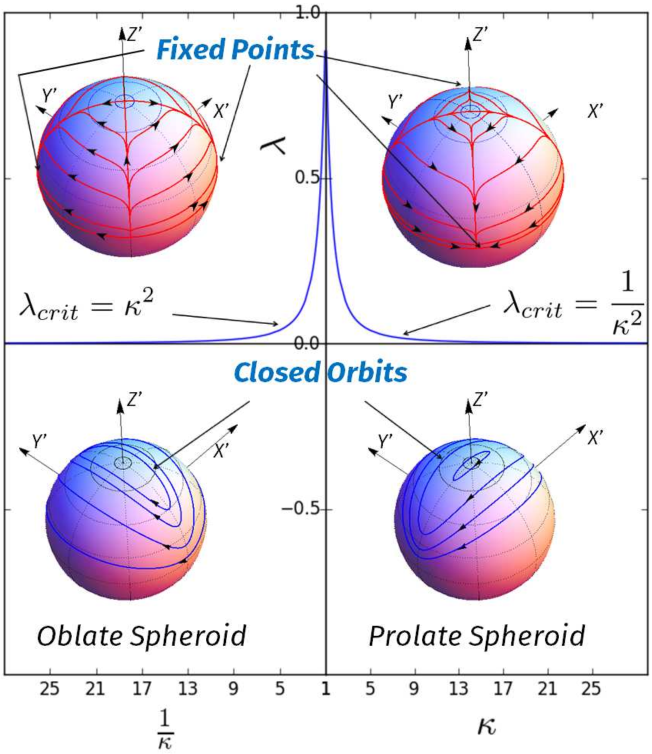

Fig. 2.3 The critical λ curve in the $\lambda - \kappa$ plane. The blue curve corresponds to the critical λ curve which separates the region of closed orbits from the region of open trajectories in the $\lambda - \kappa$ plane. Typical trajectory topologies, that is the trace of the orientation vector on a unit sphere centered at the origin starting from various initial conditions, are shown in the inset plots as blue (closed) and red (open and moving towards fixed point) curves for regions above and below the λ_{crit} curve. The two stable fixed points for both prolate and oblate spheroids in the open trajectory region are also indicated.

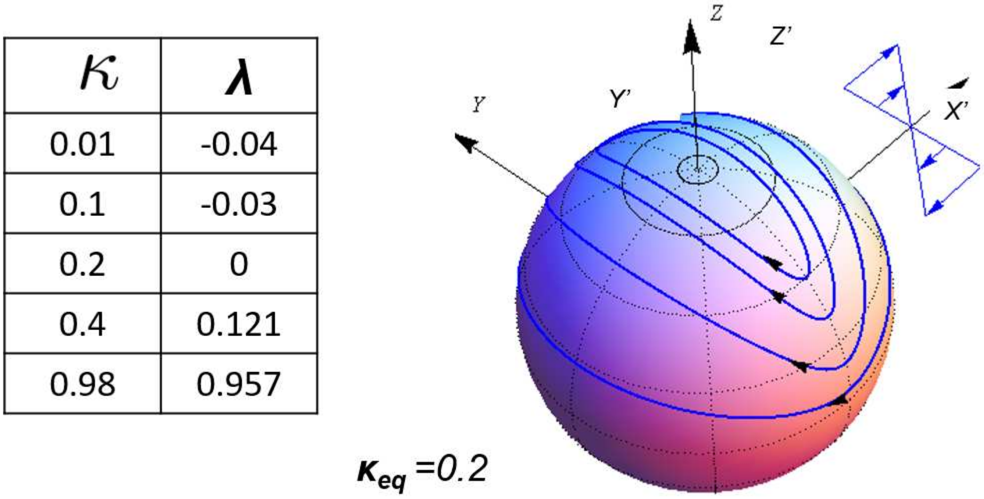

κ	λ
0.01	-0.04
0.1	-0.03
0.2	0
0.4	0.121
0.98	0.957

Fig. 2.4 The trajectories of a spheroid of aspect ratio 0.2 in a simple shear flow. The table shows some combinations of κ and λ for which the equivalent aspect ratio is 0.2

This means that the angular velocities of a spheroid in a planar linear flow given in (2.29) and (2.30) are (1-λ) times the angular velocities of a spheroid of $\kappa = \kappa_{eq}$ in simple shear flow. For simple shear flow (λ=0), of course, κ_{eq} is same as κ. From (2.69), κ_{eq} varies from 1 to ∞(0) for prolate(oblate) as the λ increases from -1 to λ_{crit}. In figure 2.4 we have shown the orbits of a spheroid with aspect ratio $\kappa_{eq} = 0.2$ in a simple shear flow and have listed some combinations of κ and λ which results in an equivalent aspect ratio of 0.2. Thus, the closed trajectories in a planar linear flow are Jeffery orbits of the aforementioned equivalent spheroid. This would also mean that spheroids of different aspect ratios can have the same trajectories for different flows. In particular, a spheroid of an arbitrary aspect ratio describes the nearly meridional trajectories similar to a slender fibre (for prolate) or a flat disk (for oblate) for $\lambda \rightarrow \lambda_{crit}$.

In the following sections, we interpret the weak inertial effects in terms of a drift across the trajectories described above in a non-orthogonal orbital coordinate system (C,τ)(Leal & Hinch (1971)). The constant C lines coincide with the Jeffery orbits of the planar linear flow for the spheroid under consideration, while the constant τ lines are same as the constant-ϕ contours (on the unit sphere). The orbital coordinates are related to θ_j and ϕ_j in terms of the equivalent aspect ratio κ_{eq}:

$$C = \tan\theta_j \frac{\sqrt{(\kappa_{eq}^2 \sin^2\phi_j + \cos^2\phi_j)}}{\kappa_{eq}}, \tag{2.70}$$

$$\tau = \tan^{-1}\left(\frac{1}{\kappa_{eq}\tan\phi_j}\right). \tag{2.71}$$

Here, C varies from 0 to ∞, with $C = 0$ (called a spinning orbit) being the trajectory where the spheroid is aligned with Z' axis (vorticity axis) and $C = \infty$ (called a tumbling orbit) being the trajectory where the spheroid orientation vector traverses a unit circle in the X'-Y' plane (flow-gradient plane). The angular velocities of the spheroid in the tumbling and spinning orbits are respectively, perpendicular and parallel to the orientation vector. The intermediate finite-C orbits are three-dimensional precessional orbits. For any fixed C, the orbit phase τ varies from 0 to 2π and is defined such that the rate of change of orientation in the τ coordinate is constant (despite ϕ_j changing at a variable rate). The equations for the rates of change take a simple form in the orbital coordinate system, and are given by:

$$\frac{dC}{dt} = 0, \tag{2.72}$$

$$\frac{d\tau}{dt} = \frac{(1-\lambda)\kappa_{eq}}{(\kappa_{eq}^2+1)}. \tag{2.73}$$

Evidently, the orbital coordinate C of the spheroid does not change in the Stokes limit. Note that the above equations are valid for $-1 < \lambda < \lambda_{crit}$. In the limit of $\lambda \to -1$, that is the trivial case of solid-body rotation, κ_{eq} is 1, and the orbits are merely circles transverse to the ambient vorticity. In the limit of $\lambda \to \lambda_{crit}$, $\kappa_{eq} \to \infty$ (0) for prolate (oblate) spheroid, and the angular velocity $d\tau/dt \to 0$, consistent with the fact that the rotation of the spheroid has to arrest at $\lambda = \lambda_{crit}$.

2.5 The effect of particle inertia: massive spheroids (*Re*=0 and *St* $\ll 1$)

In this section we investigate the effect of the particle inertia on the orientation dynamics of a spheroid in a planar linear flow. We calculate the O(St) correction to the angular velocity using (2.31) by setting $Re = 0$, whence (2.31) reduces to:

$$\boldsymbol{\Omega}_1 \cdot \boldsymbol{L}_2 = \boldsymbol{\Gamma} : \int_{S_p} \boldsymbol{x}(\boldsymbol{\Sigma}^{(2)} \cdot \boldsymbol{n}) dS + St \frac{d}{dt}(\boldsymbol{I}_p \cdot \boldsymbol{\Omega}_1). \tag{2.74}$$

The second term on the right-hand side above gives the correction due to the particle angular acceleration. As mentioned earlier, it is convenient to evaluate the correction in the body-aligned coordinate system (XYZ in figure 2.2), which rotates with $\boldsymbol{\Omega}^{\boldsymbol{t}}_{jeff}$. The rate of change in the space-fixed coordinate system is related to the rate of change in XYZ as $\frac{d}{dt}(.) = \left(\frac{d}{dt}(.)\right)_b + \boldsymbol{\Omega}^{\boldsymbol{t}}_{jeff} \wedge (.)$, the subscript 'b' denoting the XYZ system. Noting that the moment of inertia tensor is a constant in XYZ, (2.74) takes the form:

$$\boldsymbol{\Omega}_1 \cdot \boldsymbol{L}^{(2)} = \boldsymbol{\Gamma} : \int_{S_p} \boldsymbol{x}(\boldsymbol{\Sigma}^{(2)} \cdot \boldsymbol{n}) dS + St \left[\boldsymbol{I}_p \cdot \left(\frac{d\boldsymbol{\Omega}_1}{dt} \right)_b + \boldsymbol{\Omega}^{\boldsymbol{t}}_{jeff} \wedge (\boldsymbol{I}_p \cdot \boldsymbol{\Omega}_1) \right]. \tag{2.75}$$

Using a regular expansion of the form $\boldsymbol{\Omega}_1 = \boldsymbol{\Omega}_{jeff} + St\, \boldsymbol{\Omega}^{(1)}_{1St} + O(St^2)$ for the particle angular velocity, one obtains:

$$\boldsymbol{\Omega}^{(1)}_{1St} \cdot \boldsymbol{L}^{(2)} = \boldsymbol{I}_p \cdot \frac{d\boldsymbol{\Omega}_{jeff}}{dt_{jeff}} + \boldsymbol{\Omega}^{\boldsymbol{t}}_{jeff} \wedge (\boldsymbol{I}_p \cdot \boldsymbol{\Omega}_{jeff}), \tag{2.76}$$

at $O(St)$. In (2.76), to leading order, $(d/dt)_b$ is replaced by $(d/dt)_{jeff}$, where the latter denotes the rate of change along the closed orbit in the Stokes limit, given by (2.29) and (2.30) in terms of θ_j and ϕ_j. The rates of change of ϕ_j and θ_j, at $O(St)$, can be obtained from (2.76), $\dot{\phi}_{jSt} = -\Omega^{(1)x}_{1St} / \sin\theta_j$ and $\dot{\theta}_{jSt} = \Omega^{(1)y}_{1St}$ and are given by:

$$\begin{aligned} \left(\frac{d\theta_j}{dt}\right)_{St} &= \sin\theta_j \cos\theta_j \left[F^p_1(\xi_0,\lambda) + F^p_2(\xi_0,\lambda)\cos 2\phi_j + F^p_3(\xi_0,\lambda)\cos 2\theta_j + F^p_4(\xi_0,\lambda)\cos 4\phi_j \right. \\ &\quad \left. + F^p_5(\xi_0,\lambda)\cos(2\theta_j - 4\phi_j) + F^p_6(\xi_0,\lambda)\cos(2\theta_j + 4\phi_j) \right], \end{aligned} \tag{2.77}$$

$$\begin{aligned} \left(\frac{d\phi_j}{dt}\right)_{St} &= \sin\phi_j \cos\phi_j \left[G^p_1(\xi_0,\lambda) + G^p_2(\xi_0,\lambda)\cos 2\theta_j + G^p_3(\xi_0,\lambda)\cos 2\phi_j \right. \\ &\quad \left. + G^p_4(\xi_0,\lambda)\cos 2\theta_j \cos 2\phi_j \right]. \end{aligned} \tag{2.78}$$

The functions of κ and λ that appear above for a prolate spheroid are given by:

$$F_1^p(\xi_0,\lambda) = \frac{\left(-1+\xi_0^2\right)\left(-3+2\lambda-3\lambda^2+4(-1+\lambda)^2\xi_0^2\right)\left(-\xi_0+\coth^{-1}\xi_0\left(1+\xi_0^2\right)\right)}{160\xi_0\left(1-2\xi_0^2\right)^2}, \tag{2.79}$$

$$F_2^p(\xi_0,\lambda) = -\frac{\left(-1+\lambda^2\right)\left(-1+\xi_0^2\right)^2\left(-\xi_0+\coth^{-1}\xi_0\left(1+\xi_0^2\right)\right)}{40\xi_0\left(1-2\xi_0^2\right)^2}, \tag{2.80}$$

$$F_3^p(\xi_0,\lambda) = F_4^p(\xi_0,\lambda) = -\frac{(1+\lambda)^2\left(-1+\xi_0^2\right)\left(-\xi_0+\coth^{-1}\xi_0\left(1+\xi_0^2\right)\right)}{160\xi_0\left(1-2\xi_0^2\right)^2}, \tag{2.81}$$

$$F_5^p(\xi_0,\lambda) = F_6^p(\xi_0,\lambda) = \frac{(1+\lambda)^2\left(-1+\xi_0^2\right)\left(-\xi_0+\coth^{-1}\xi_0\left(1+\xi_0^2\right)\right)}{320\xi_0\left(1-2\xi_0^2\right)^2}, \tag{2.82}$$

$$G_1^p(\xi_0,\lambda) = \frac{\left(-1+\lambda^2\right)\left(2-5\xi_0^2+3\xi_0^4\right)\left(-\xi_0+\coth^{-1}\xi_0\left(1+\xi_0^2\right)\right)}{40\xi_0\left(1-2\xi_0^2\right)^2}, \tag{2.83}$$

$$G_2^p(\xi_0,\lambda) = -\frac{\left(-1+\lambda^2\right)\xi_0\left(-1+\xi_0^2\right)\left(-\xi_0+\coth^{-1}\xi_0\left(1+\xi_0^2\right)\right)}{40\left(1-2\xi_0^2\right)^2} \tag{2.84}$$

$$G_3^p(\xi_0,\lambda) = -G_4^p(\xi_0,\lambda) = \frac{(1+\lambda)^2\left(-1+\xi_0^2\right)\left(-\xi_0+\coth^{-1}\xi_0\left(1+\xi_0^2\right)\right)}{40\xi_0\left(1-2\xi_0^2\right)^2}. \tag{2.85}$$

The functions for an oblate spheroid can be obtained using the transformation $\xi_0 \leftrightarrow \mathrm{i}\bar{\xi}_0$ and $d \leftrightarrow -\mathrm{i}d$, on the dimensional angular velocity, having accounted for the aspect-ratio dependence that occurs in the relevant non-dimensional parameter - *St* here and *Re* in section 2.6). Einarsson *et al.* (2014) had derived the O(*St*) correction to the angular velocities for a spheroid in a planar linear flow in an invariant form and the expressions in (2.78)and (2.77) match with those. However they restrict their analysis to finding the orbit that is stabilized at long-times for the particular case of simple shear flow ($\lambda = 0$).

In the analysis that follows, we investigate the effect of the inertial angular velocity corrections given in (2.77) and (2.78) on the trajectory of the orientation vector for all (λ, κ) combinations below the λ_{crit} -curve in figure 2.3. There are two approaches for carrying out this investigation. The first, brute-force, approach is to numerically integrate the differential equations governing θ_j and ϕ_j, obtained by adding the angular velocities given in (2.78) and (2.77) and the corresponding leading order angular velocities given in equations (2.29) and

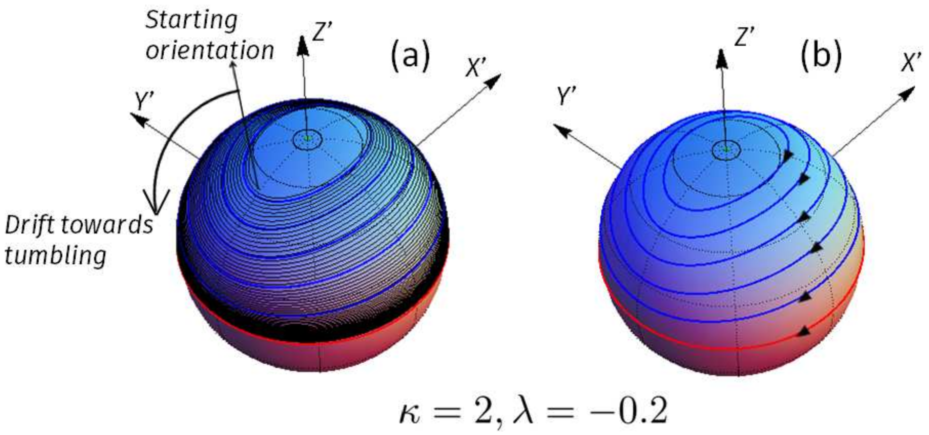

Fig. 2.5 (a) The O(St) inertial trajectory (black) is plotted on a unit sphere. For the purpose of illustation a Stokes number is chosen to be 1. The orientation drifts towards the tumbling orbit (red curve). The blue curves on the unit sphere in (a) and (b) are the Jeffery orbits.

(2.30), to obtain the trajectory on the unit sphere. The trajectory obtained in the manner described above, starting from a particular initial condition ($St = 1$, θ_{j0}=0.5, $\phi_{j0} = \pi$) is shown in figure 2.5(a) for a prolate spheroid of aspect ratio 2 in an elliptic flow with $\lambda = -0.2$. The Jeffery orbits, for the same set of parameters are plotted in figure 2.5(b) for purposes of comparison. As is evident, the orientation of the spheroid drifts towards the tumbling orbit (red curve on the unit sphere in figure 2.5(a)). To repeat this exercise for the whole (κ-λ) plane below the λ_{crit}- curve in figure 2.3, and for all possible initial orientation on the unit sphere, is cumbersome and is not pursued further.

In the second approach, the orbital drift across the closed trajectories in the Stokes limit is calculated using (2.77) and (2.78). The orbital drift ($\frac{dC}{dt}$) can be obtained by differentiating (2.70) and is given by:

$$\frac{dC}{dt} = \frac{C}{\sin\theta_j\cos\theta_j}\frac{d\theta_j}{dt} + \frac{C(\kappa_{eq}^2 - 1)\cos\phi_j\sin\phi_j}{\kappa_{eq}^2\sin^2\phi_j + \cos^2\phi_j}\frac{d\phi_j}{dt}. \tag{2.86}$$

The drift takes the form:

$$\frac{dC}{dt} = StC\left[\frac{1}{\sin\theta_j\cos\theta_j}\left(\frac{d\theta_j}{dt}\right)_{St} + \frac{(\kappa_{eq}^2 - 1)\cos\phi_j\sin\phi_j}{\kappa_{eq}^2\sin^2\phi_j + \cos^2\phi_j}\left(\frac{d\phi_j}{dt}\right)_{St}\right], \tag{2.87}$$

where $(\frac{d\theta_j}{dt})_{St}$ and $(\frac{d\phi_j}{dt})_{St}$ are given by (2.77) and (2.78). As expected, the drift is O(St), since $dC/dt = 0$ at leading order. The O(St) drift leads to an inertial trajectory where the spheroid orientation vector spirals towards the flow-gradient plane. For $St << 1$, this spiralling is tight, with each turn of the spiral closely approximating a Jeffery orbit (see figure 2.5 (a)). The orbital drift can then be conveniently characterized by the pitch of the spiral measured in units of C. This pitch, ΔC, defined at leading order as the change in C during a single Jeffery period (T_{jeff}=$2\pi(\kappa_{eq}^2+1)/\kappa_{eq}$), is given by:

$$\Delta C_p = \int_0^{T_{jeff}} \frac{dC}{dt} dt, \tag{2.88}$$

$$= (\frac{d\tau}{dt})^{-1} \int_0^{2\pi} \frac{dC}{dt} d\tau, \tag{2.89}$$

$$= St\frac{\kappa_{eq}^2+1}{(1-\lambda)\kappa_{eq}} \int_0^{2\pi} C \left(\frac{1}{\sin\theta_j \cos\theta_j} \left(\frac{d\theta_j}{dt}\right)_{St} + \frac{(\kappa_{eq}^2-1)\cos\phi_j \sin\phi_j}{\kappa_{eq}^2 \sin^2\phi_j + \cos^2\phi_j} \left(\frac{d\phi_j}{dt}\right)_{St} \right) d\tau. \tag{2.90}$$

where the subscript 'p' denotes particle inertia. The τ-integrals in (2.90) are to be evaluated for fixed C, implying closeness of the inertial spiralling trajectory at a given point to a Jeffrey orbit passing through the same point. Using (2.77) and (2.78):

$$\begin{aligned}\Delta C_p =& StC\frac{\kappa_{eq}^2+1}{(1-\lambda)\kappa_{eq}} \Bigg\{ \int_0^{2\pi} \Big[F_1^p(\xi_0,\lambda) + F_2^p(\xi_0,\lambda)\cos 2\phi_j + F_3^p(\xi_0,\lambda)\cos 2\theta_j + F_4^p(\xi_0,\lambda)\cos 4\phi_j \\ & + F_5^p(\xi_0,\lambda)\cos(2\theta_j - 4\phi_j) + F_6^p(\xi_0,\lambda)\cos(2\theta_j+4\phi_j) \Big] d\tau + \int_0^{2\pi} \frac{(\kappa_{eq}^2-1)\cos^2\phi_j \sin^2\phi_j}{\kappa_{eq}^2 \sin^2\phi_j + \cos^2\phi_j} \\ & \Big[G_1^p(\xi_0,\lambda) + G_2^p(\xi_0,\lambda)\cos 2\theta_j + G_3^p(\xi_0,\lambda)\cos 2\phi_j + G_4^p(\xi_0,\lambda)\cos 2\theta_j \cos 2\phi_j \Big] d\tau \Bigg\}.\end{aligned} \tag{2.91}$$

This may in turn be written as:

$$\Delta C_p = St\,C\,\frac{\kappa_{eq}^2+1}{(1-\lambda)\kappa_{eq}}\left\{\left[I_1F_1^p(\xi_0,\lambda)+I_2F_2^p(\xi_0,\lambda)+I_3F_3^p(\xi_0,\lambda)+I_4F_4^p(\xi_0,\lambda)+I_5F_5^p(\xi_0,\lambda)\right.\right.$$
$$\left.\left.+I_6F_6^p(\xi_0,\lambda)\right]+\left[J_1G_1^p(\xi_0,\lambda)+J_2G_2^p(\xi_0,\lambda)+J_3G_3^p(\xi_0,\lambda)+J_4G_4^p(\xi_0,\lambda)\right]\right\}, \tag{2.92}$$

where the I_i's and the J_i's result from integrating the corresponding trigonometric functions in (2.91) over τ. The trigonometric functions are related to C and τ through (2.70) and (2.71). The expressions for $I_1 - J_4$ as functions of C and κ_{eq} are given in Appendix A. The orbital drift approximation in (2.92) has reduced the need to consider all possible initial conditions in the brute force mentioned earlier, to a one dimensional examination of all possible C's. The average change, however, should be much less than C, therefore the above analysis implies $\frac{\Delta C}{C} << 1$. It can be seen from (2.92) that this condition breaks down for when $St \sim \kappa_{eq}\,(1/\kappa_{eq})$ (F_i's and G_i's are O(1) numbers in this limit) that is for extreme values of equivalent aspect ratios that is $\kappa_{eq} << 1(\kappa_{eq} >> 1)$ for oblate (prolate) spheroid. This would mean that close to $\lambda = \lambda_{crit}$ curve in figure 2.3, the average drift approximation is valid when $Re < \kappa_{eq}$, and this is one of the limitations of the orbital drift approximation and we discuss those, in the context of a formal multiple scales analysis, in section 2.8.

The orbital drift in (2.92) is a function of C, the flow parameter λ as well as the aspect ratio (through ξ_0 which is the inverse of the eccentricity of the spheroid). It is shown later in section 2.8 that the orbital drift interpretation, motivated here using physical arguments, emerges naturally as the leading order term in the framework of a multiple time scales analysis. The drift is positive for a prolate spheroid of any aspect ratio in a planar linear flow with a nonpositive λ (all elliptic linear flows including the limiting case of solid body rotation and simple shear flow). In particular for $\lambda = -1$, one expects the particle inertia to cause the prolate spheroid centrifuge out towards the tumbling orbit. The long-time orientation dynamics of a prolate spheroid in a flow with $\lambda \leq 0$ approach therefore that of the tumbling orbit. This is noted in the fourth quadrant of the $\lambda - \kappa$ plane in figure 2.6(a). In a hyperbolic flow ($0 < \lambda < \lambda_{crit}$), the tumbling orbit continues to be the long-time orientation limit for a prolate spheroid with κ approximately 30. However, if the aspect ratio of the spheroid is smaller than 30, the orbit that is stabilized at long-times is the tumbling orbit, only till a particular $\lambda_1(\kappa)$ ($0 < \lambda_1 < \lambda_{crit}$), indicated by the red curve in the first quadrant of figure 2.6(a). For these aspect ratios, if λ characterizing the flow is larger than λ_1, a repeller (a Jeffery orbit at the order of approximation considered) exists on the unit hemisphere dividing it into two distinct basins of attraction; with the attractor being the tumbling orbit for one basin and the spinning orbit for the other. The shaded region in figure 2.6(a) corresponds to all those λ values for which two distinct basins of attraction exist on the unit hemisphere. Eventually, with increasing λ, the spinning orbit becomes the sole attractor at a particular $\lambda_2(\kappa)(\lambda_1 < \lambda_2)$ indicated by the magenta curve in the zoomed plot in figure 2.6(b), and this remains so for the narrow range of λ's in the interval $\lambda_2(\kappa) < \lambda < \lambda_{crit}$.

In figure 2.6(c), the orbital drift ΔC_p is plotted against $C/(C+1)$ for a particular aspect ratio, $\kappa = 2$, for different λ's. The drift is positive for all λ's below $\lambda \approx 0.13(\lambda_1$ for $\kappa = 2)$, and the long-time orientation dynamics approaches the tumbling orbit. As λ becomes larger than 0.13, the sign of the drift changes across a critical C (Jeffery orbit with $C = C^*$, say). This Jeffery orbit acts as a repeller. It emerges from the spinning orbit at around $\lambda = 0.13$ (λ_1), and with increasing λ, moves towards the tumbling orbit, eventually coinciding with it at $\lambda \approx 0.20(\lambda_2)$. The repeller orbits for $\kappa = 2$ at various λ's are plotted on the unit sphere in figures 2.6(d) (e) and (f).

The long-time orientation dynamics of an oblate spheroid is simpler compared to that of the prolate spheroid discussed above. An oblate spheroid drifts towards the spinning orbit irrespective of its initial orientation and aspect ratio in any planar linear flow with λ $(< \lambda_{crit})$. In figure 2.7(b), the orbital drift is plotted against $C/(C+1)$ for various λ's for an oblate spheroid of aspect ratio 0.1 and is negative irrespective of C and λ.

It is important to understand the effect of particle inertia on a spheroid rotating in a simple shear flow to understand the rheological properties of a suspension, which is presented in detail in chapter 3. The drift for a prolate spheroid is plotted as a function of the normalized orbit constant, $C/(C+1)$ in figure 2.8 for various aspect ratios. The drift is evidently zero for $C = 0$ and $C = \infty\,[C/(C+1) = 1]$ on account of symmetry, but is positive for all other values of C and for all aspect ratios. Thus, a massive prolate spheroid always drifts towards the tumbling mode. In the near-sphere limit $(\xi_0 \to \infty)$, $\Delta C_p \approx St\,\frac{\pi C}{30}\,\xi_0^{-2}$, as is expected on account of the drift being proportional to the square of the eccentricity $(e = 1/\xi_0)$. In the limit of a slender fiber $(\xi_0 \to 1)$, one finds $\Delta C_p \approx -St\,\frac{\pi\sqrt{2}C}{5}(\xi_0 - 1)^{\frac{3}{2}}\ln(\xi_0 - 1)$. A leading-order estimate from the non-aligned phase of a rotating fiber comes out to be larger of $O[(\xi_0 - 1)\ln(\xi_0 - 1)]$. This estimate arises from transverse moments of inertia of $O(\xi_0 - 1)$ driving a drift against a resistive torque of $O[\ln(\xi_0 - 1)]^{-1}$ predicted by slender body theory; the next correction in the non-aligned phase is $O[(\xi_0 - 1)^2\ln(\xi_0 - 1)]$. The actual estimate of $O[(\xi_0 - 1)^{\frac{3}{2}}\ln(\xi_0 - 1)]$ above must therefore involve the dominant flow-aligned phase of the fiber. These near-sphere and slender fiber

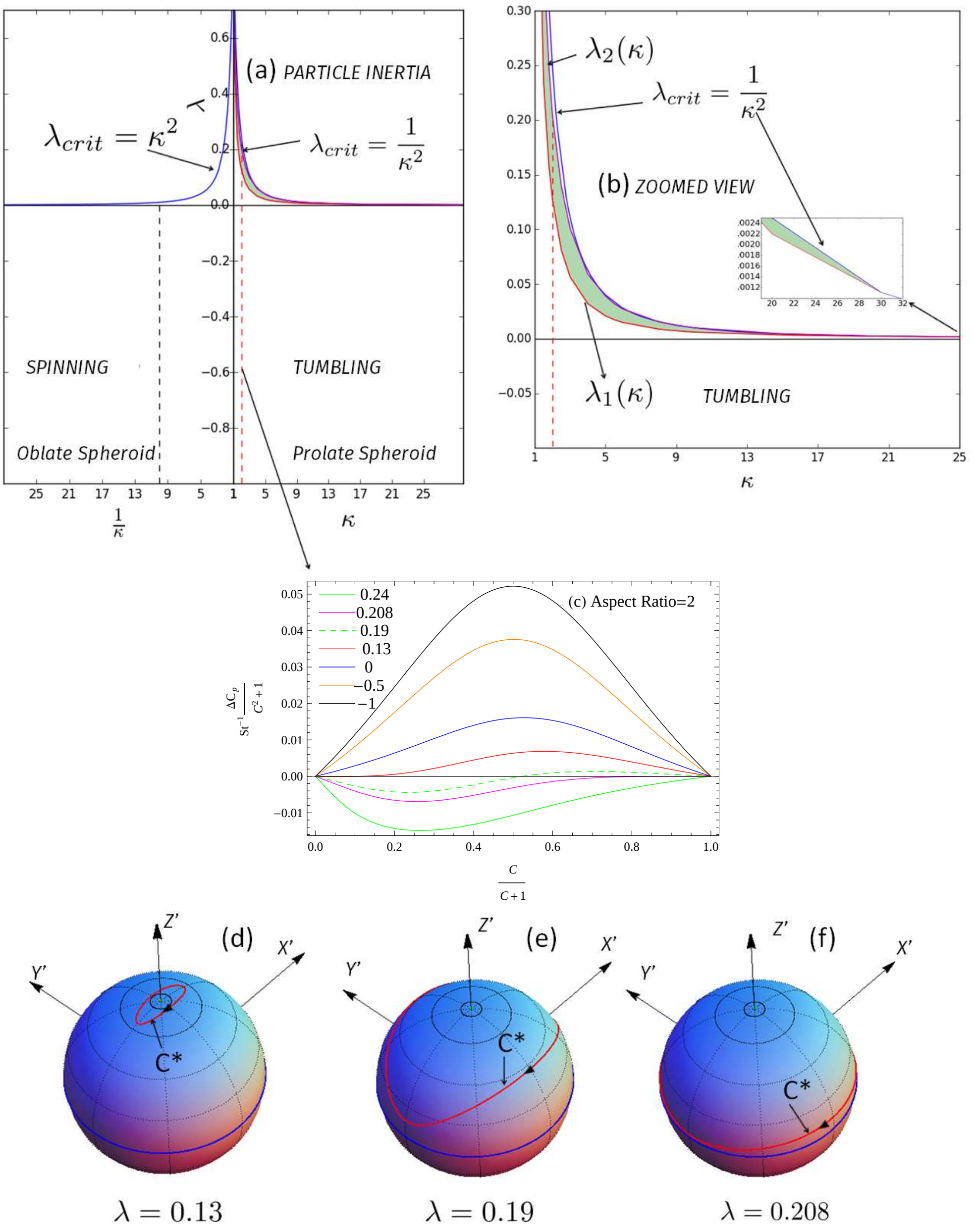

Fig. 2.6 (a) The orbit stabilized at long-times due to particle inertia are identified for all combinations of λ -κ below the λ_{crit} curve (blue curve). Red curve denotes the (λ, κ) value at which the repeller emerges from spinning. The shaded region denote the combinations of (λ, κ) for which there is a repeller on the unit hemisphere. (b) The zoomed view of the shaded region. (c) The orbital drift is plotted against $\frac{C}{C+1}$ for a prolate spheroid of aspect ratio 2. The C over which drift changes sign correspond to the repeller (C^*) location. The repeller orbit (red) is plotted for the prolate spheroid of aspect ratio 2 and for λ's (d) 0.13 (e) 0.19 and (f) 0.208. The blue orbit in (d),(e) and (f) corresponds to the tumbling orbit.

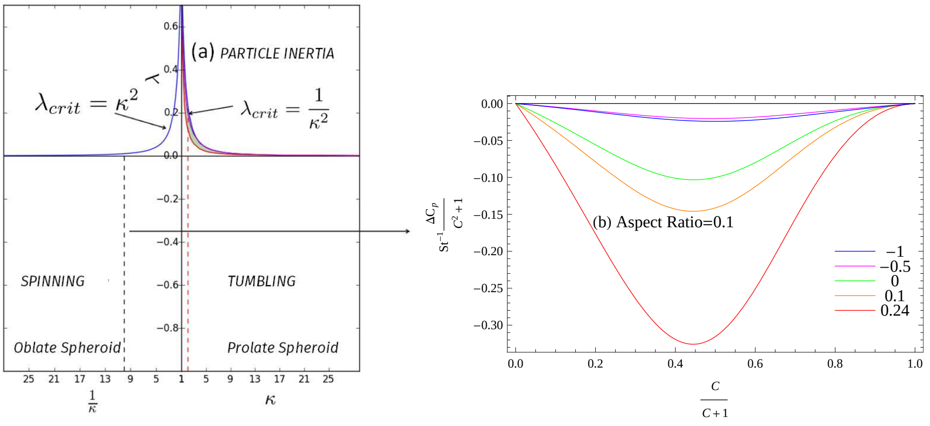

Fig. 2.7 (a) The orbit stabilized at long-times due to particle inertia are indicated. (b) The orbital drift is plotted against $\frac{C}{C+1}$ for an oblate spheroid of aspect ratio 0.1. The drift does not change sign for an oblate spheroid.

scalings, together with a normalizing factor of $(C^2+1)^{-1}$, are accounted for in figure 2.8 in order to render the ΔC_p curve, in the relevant asymptotic limit, a finite one for all C.

The normalized ΔC_p for a massive oblate spheroid in simple shear flow is plotted as a function of $C/(C+1)$ in figure 2.9, and is negative for all C's and aspect ratios, implying that the spheroid would asymptote to a steady spinning mode starting from any initial orientation. In the near-sphere limit, ΔC_p is just negative of that for a prolate spheroid. In contrast to a prolate spheroid, however, a normalization based on this near-sphere scaling of $O(\xi_0^{-2})$ alone suffices for plotting ΔC_p, since the inertial drift remains finite in the flat-disk limit - $\lim_{\xi_0 \to 1}$ $\Delta C_p \approx -\pi^2 \frac{(C^2+1)^{\frac{1}{2}}-1}{20C}$. The moments of inertia of a thin oblate spheroid are only $O(\xi_0-1)^{\frac{1}{2}}$, but their smallness appears to be compensated by the long, $O(\xi_0-1)^{-\frac{1}{2}}$, period available for inertia to act, leading to ΔC_p being $O(1)$ for $\xi_0 \to 1$. Note that the ΔC_p curve for any oblate spheroid crosses that of a near-sphere, with this cross-over point moving in from $C/(C+1) = 1$ to a limiting value of about 0.75 for a flat disk. Thus, for sufficiently thin spheroids, the inertial drift increases in magnitude below this cross-over C, while decreasing for greater C's.

2.6 The effect of fluid inertia (St=0 and $Re \ll 1$)

In this section we investigate the effect of fluid inertia on the orientation dynamics of a spheroid in a planar linear flow. The rates of change, of $\dot{\phi}_j$ and $\dot{\theta}_j$, at O(Re), is obtained

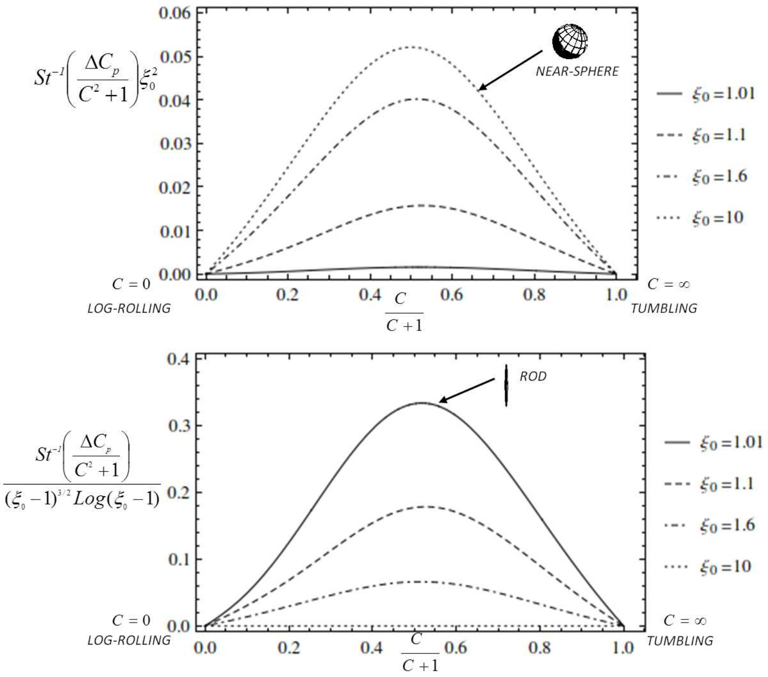

Fig. 2.8 The drift due to the particle inertia in simple shear flow, as characterized by the normalized change in the orbit constant in a single Jeffery period, $St^{-1}\frac{\Delta C_p}{(C^2+1)}$, plotted as a function of $\frac{C}{C+1}$, for a prolate spheroid; $\frac{C}{C+1} = 0$ and $\frac{C}{C+1} = 1$ correspond to the log-rolling and tumbling modes. The upper plot uses the additional normalization factor of ξ_0^2, so the drift remains finite in the near-sphere limit ($\xi_0 \to \infty$). The lower plot uses the normalisation factor $((\xi_0-1)^{3/2}\log(\xi_0-1))^{-1}$, to make the drift finite in the slender fiber limit ($\xi_0 \to 1$).

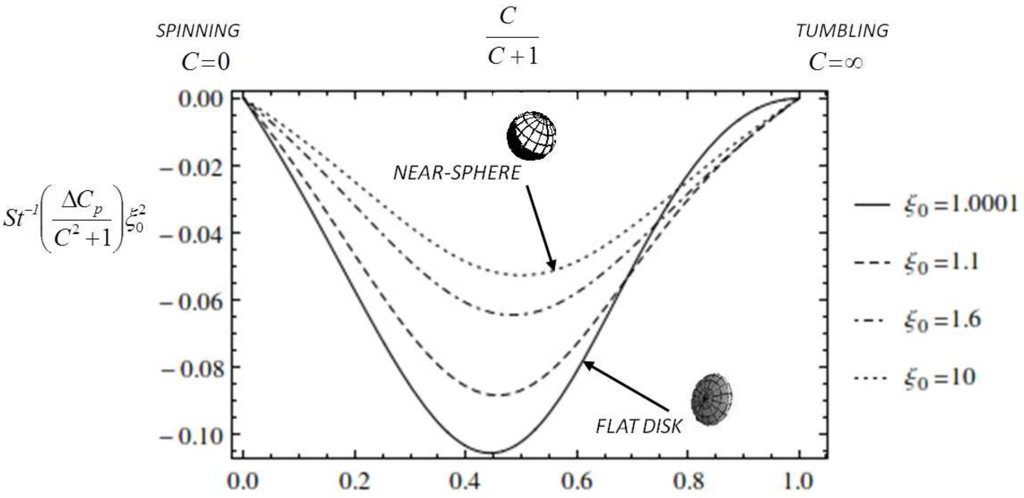

Fig. 2.9 The drift due to the particle inertia in simple shear flow, as characterized by the normalized change in the orbit constant in a single Jeffery period, $St^{-1}\frac{\Delta C_p}{(C^2+1)}$, plotted as a function of $\frac{C}{C+1}$, for an oblate spheroid; $\frac{C}{C+1}=0$ and $\frac{C}{C+1}=1$ correspond to the spinning and the tumbling modes.

by evaluating the integrals proportional to Re in the right hand side of (2.31), using the velocity fields given in section 2.3. The rates of change are given by :

$$\left(\frac{d\theta_j}{dt}\right)_{Re} = \sin\theta_j\cos\theta_j\Big[F_1^f(\xi_0,\lambda)+F_2^f(\xi_0,\lambda)\cos 2\phi_j+F_3^f(\xi_0,\lambda)\cos 2\theta_j+F_4^f(\xi_0,\lambda)\cos 4\phi_j$$
$$+F_5^f(\xi_0,\lambda)\cos(2\theta_j-4\phi_j)+F_6^f(\xi_0,\lambda)\cos(2\theta_j+4\phi_j)\Big], \qquad (2.93)$$

$$\left(\frac{d\phi_j}{dt}\right)_{Re} = \sin\phi_j\cos\phi_j\Big[G_1^f(\xi_0,\lambda)+G_2^f(\xi_0,\lambda)\cos 2\theta_j+G_3^f(\xi_0,\lambda)\cos 2\phi_j$$
$$+G_4^f(\xi_0,\lambda)\cos(2\theta_j)\cos(2\phi_j)\Big]. \qquad (2.94)$$

The aspect ratio and λ dependent functions for a prolate spheroid are given by:

$$F_1^f(\xi_0,\lambda) =(1+\lambda)^2 F_1^f(\xi_0,0)+\frac{\lambda\left(\xi_0-\xi_0^3+\left(-1+\xi_0^4\right) coth^{-1}\xi_0\right)}{20\xi_0\left(-1+2\xi_0^2\right)}, \tag{2.95}$$

$$F_2^f(\xi_0,\lambda) =(1-\lambda^2)F_2^f(\xi_0,0), \tag{2.96}$$

$$F_3^f(\xi_0,\lambda) =(\lambda+1)^2 F_3^f(\xi_0,0), \tag{2.97}$$

$$F_4^f(\xi_0,\lambda) =(\lambda+1)^2 F_4^f(\xi_0,0), \tag{2.98}$$

$$F_5^f(\xi_0,\lambda) =F_6^f(\xi_0,\lambda)=(\lambda+1)^2 F_5^f(\xi_0,0), \tag{2.99}$$

$$G_1^f(\xi_0,\lambda) =(1-\lambda^2)G_1^f(\xi_0,0), \tag{2.100}$$

$$G_2^f(\xi_0,\lambda) =(1-\lambda^2)G_2^f(\xi_0,0), \tag{2.101}$$

$$G_3^f(\xi_0,\lambda) =(\lambda+1)^2 G_3^f(\xi_0,0), \tag{2.102}$$

$$G_4^f(\xi_0,\lambda) =(\lambda+1)^2 G_4^f(\xi_0,0), \tag{2.103}$$

where $F_i^f(\xi_0,0)$ and $G_i^f(\xi_0,0)$ are those corresponding to simple shear flow given by:

$$\begin{aligned}F_1^f(\xi_0,0) =&(\xi_0^2(-648\xi_0^{12}+1350\xi_0^{10}-5571\xi_0^8+11841\xi_0^6-9269\xi_0^4+2263\xi_0^2+6)\\ &-27\xi_0^2(24\xi_0^8-14\xi_0^6-19\xi_0^4+16\xi_0^2-3)\overline{\xi_0}^{8}\coth^{-1}(\xi_0)^4\\ &+9\xi_0(288\xi_0^{12}-564\xi_0^{10}-20\xi_0^8+799\xi_0^6-743\xi_0^4+261\xi_0^2-29)\overline{\xi_0}^{4}\coth^{-1}(\xi_0)^3\\ &+\xi_0(2592\xi_0^{14}-7020\xi_0^{12}+13932\xi_0^{10}-21123\xi_0^8+14255\xi_0^6-577\xi_0^4-2711\xi_0^2\\ &+652)\coth^{-1}\xi_0-3(1296\xi_0^{16}-4320\xi_0^{14}+5346\xi_0^{12}-1477\xi_0^{10}-4260\xi_0^8\\ &+6116\xi_0^6-3492\xi_0^4+849\xi_0^2-58)\coth^{-1}(\xi_0)^2)\\ &(480\xi_0^2(-1+2\xi_0^2)^3(-3\xi_0^2+3\overline{\xi_0}^{2}\xi_0\coth^{-1}\xi_0+2)(-3\xi_0^3+5\xi_0+3\overline{\xi_0}^{4}\coth^{-1}\xi_0)\\ &((3\xi_0^2-1)\coth^{-1}\xi_0-3\xi_0))^{-1}\end{aligned} \tag{2.104}$$

$$\begin{aligned}F_2^f(\xi_0,0)=&-(\overline{\xi_0}^{2}(-9\xi_0^9+30\xi_0^7-115\xi_0^5+90\xi_0^3-12\xi_0+9\overline{\xi_0}^{8}(\xi_0^2+1)\xi_0^2\coth^{-1}(\xi_0)^3\\ &-3\overline{\xi_0}^{4}(9\xi_0^6-10\xi_0^4-17\xi_0^2+14)\xi_0\coth^{-1}(\xi_0)^2\\ &+(27\xi_0^{10}-87\xi_0^8+133\xi_0^6-33\xi_0^4-52\xi_0^2+12)\coth^{-1}\xi_0))\\ &(40(\xi_0-2\xi_0^3)^2(-3\xi_0^2+3\overline{\xi_0}^{2}\xi_0\coth^{-1}\xi_0+2)(-3\xi_0^3+5\xi_0+3\overline{\xi_0}^{4}\coth^{-1}\xi_0))^{-1}\end{aligned} \tag{2.105}$$

$$\begin{aligned}F_3^f(\xi_0,0) =&-(\xi_0^2(378\xi_0^{10}+801\xi_0^8-4731\xi_0^6+5551\xi_0^4-2369\xi_0^2+342)\\&-27\xi_0^2(6\xi_0^6+\xi_0^4-4\xi_0^2+1)\bar{\xi}_0^{8}\coth^{-1}(\xi_0)^4+9\xi_0(12\xi_0^{10}+28\xi_0^8-201\xi_0^6\\&+273\xi_0^4-147\xi_0^2+27)\bar{\xi}_0^{4}\coth^{-1}(\xi_0)^3+(-972\xi_0^{13}-324\xi_0^{11}+7365\xi_0^9\\&-10409\xi_0^7+5143\xi_0^5-847\xi_0^3+44\xi_0)\coth^{-1}\xi_0+3(216\xi_0^{14}-378\xi_0^{12}\\&+109\xi_0^{10}-412\xi_0^8+1204\xi_0^6-1028\xi_0^4+311\xi_0^2-22)\coth^{-1}(\xi_0)^2)\\&(480\xi_0^2(-1+2\xi_0^2)^3(-3\xi_0^2+3\bar{\xi}_0^{2}\xi_0\coth^{-1}\xi_0+2)(-3\xi_0^3+5\xi_0+3\bar{\xi}_0^{4}\coth^{-1}\xi_0)\\&((3\xi_0^2-1)\coth^{-1}\xi_0-3\xi_0))^{-1}\end{aligned}\tag{2.106}$$

$$F_4^f(\xi_0,0) = -2F_5^f(\xi_0,0) = -2F_6^f(\xi_0,0) = F_3^f(\xi_0,0)\tag{2.107}$$

$$\begin{aligned}G_1^f(\xi_0,0) =&(\xi_0^2(81\xi_0^{10}-414\xi_0^8+1074\xi_0^6-1162\xi_0^4+479\xi_0^2-54)+9\xi_0^2(9\xi_0^6-7\xi_0^2+2)\\&\bar{\xi}_0^{8}\coth^{-1}(\xi_0)^4-3\xi_0(108\xi_0^{10}-246\xi_0^8+69\xi_0^6+167\xi_0^4-129\xi_0^2+23)\bar{\xi}_0^{4}\coth^{-1}(\xi_0)^3\\&+(-324\xi_0^{13}+1566\xi_0^{11}-3309\xi_0^9+3133\xi_0^7-1023\xi_0^5-79\xi_0^3+36\xi_0)\coth^{-1}\xi_0\\&+(486\xi_0^{14}-2214\xi_0^{12}+3819\xi_0^{10}-2568\xi_0^8-222\xi_0^6+1036\xi_0^4-355\xi_0^2+18)\\&\coth^{-1}(\xi_0)^2)(40(\xi_0-2\xi_0^3)^2(-3\xi_0^2+3\bar{\xi}_0^{2}\xi_0\coth^{-1}\xi_0+2)(-3\xi_0^3+5\xi_0\\&+3\bar{\xi}_0^{4}\coth^{-1}\xi_0)((3\xi_0^2-1)\coth^{-1}\xi_0-3\xi_0))^{-1}\end{aligned}\tag{2.108}$$

$$\begin{aligned}G_2^f(\xi_0,0) =&(-\xi_0^2(27\xi_0^{10}-180\xi_0^8+204\xi_0^6+68\xi_0^4-133\xi_0^2+18)-9\xi_0^4(3\xi_0^4+2\xi_0^2-1)\bar{\xi}_0^{8}\\&\coth^{-1}(\xi_0)^4+3\xi_0(36\xi_0^{10}-78\xi_0^8+73\xi_0^6-69\xi_0^4+35\xi_0^2-5)\bar{\xi}_0^{4}\coth^{-1}(\xi_0)^3\\&+\xi_0(108\xi_0^{12}-630\xi_0^{10}+1041\xi_0^8-617\xi_0^6+115\xi_0^4-29\xi_0^2+12)\coth^{-1}\xi_0\\&+(-162\xi_0^{14}+810\xi_0^{12}-1551\xi_0^{10}+1600\xi_0^8-1054\xi_0^6+448\xi_0^4-97\xi_0^2+\\&6)\coth^{-1}(\xi_0)^2)(40(\xi_0-2\xi_0^3)^2(-3\xi_0^2+3\bar{\xi}_0^{2}\xi_0\coth^{-1}\xi_0+2)(-3\xi_0^3+5\xi_0\\&+3\bar{\xi}_0^{4}\coth^{-1}\xi_0)((3\xi_0^2-1)\coth^{-1}\xi_0-3\xi_0))^{-1}\end{aligned}\tag{2.109}$$

$$
\begin{aligned}
G3^{f}(\xi_0,0) =& (\xi_0^2(378\xi_0^{10}+801\xi_0^8-4731\xi_0^6+5551\xi_0^4-2369\xi_0^2+342)-27\xi_0^2(6\xi_0^6+\xi_0^4-4\xi_0^2 \\
&+1)\bar{\xi}_0^{8}\coth^{-1}(\xi_0)^4+9\xi_0(12\xi_0^{10}+28\xi_0^8-201\xi_0^6+273\xi_0^4-147\xi_0^2+27)\bar{\xi}_0^{4} \\
&\coth^{-1}(\xi_0)^3+(-972\xi_0^{13}-324\xi_0^{11}+7365\xi_0^9-10409\xi_0^7+5143\xi_0^5-847\xi_0^3 \\
&+44\xi_0)\coth^{-1}\xi_0+3(216\xi_0^{14}-378\xi_0^{12}+109\xi_0^{10}-412\xi_0^8+1204\xi_0^6-1028\xi_0^4 \\
&+311\xi_0^2-22)\coth^{-1}(\xi_0)^{2})(120\xi_0^2(2\xi_0^2-1)^3(-3\xi_0^2+3\bar{\xi}_0^{2}\xi_0\coth^{-1}\xi_0+2) \\
&(-3\xi_0^3+5\xi_0+3\bar{\xi}_0^{4}\coth^{-1}\xi_0)((3\xi_0^2-1)\coth^{-1}\xi_0-3\xi_0))^{-1} \qquad (2.110)
\end{aligned}
$$

$$
G_4^f(\xi_0,0) = -G_3^f(\xi_0,0) \qquad (2.111)
$$

The near sphere limits of the above functions ($\xi_0 \to \infty$,) are given by:

$$
F_1^f(\xi_0,0) \approx \frac{11}{280{\xi_0}^2},\ F_2^f(\xi_0,0) \approx -\frac{37}{840{\xi_0}^2},\ F_3^f(\xi_0,0) \approx -\frac{163}{31360{\xi_0}^4} \qquad (2.112)
$$

$$
\frac{1}{71}G_1^f(\xi_0,0) = \frac{1}{3}G_2^f(\xi_0,0) \approx \frac{1}{840\xi_0^2},\ G_3^f(\xi_0,0) \approx \frac{163}{7840\xi_0^4}, \qquad (2.113)
$$

and the slender fibre limits ($\xi_0 \to 1$) are given by:

$$
F_1^f(\xi_0,0) = -F_3^f(\xi_0,0) \approx -\frac{7}{240[\log(\xi_0-1)-\log 2+3]}, \qquad (2.114)
$$

$$
F_2^f(\xi_0,0) \approx -\frac{2}{5}(\xi_0-1), \qquad (2.115)
$$

$$
G_1^f(\xi_0,0) = -G_2^f(\xi_0,0) = -\frac{3}{7}G_3^f(\xi_0) \approx \frac{1}{20[\log(\xi_0-1)-\log 2+3]}. \qquad (2.116)
$$

The second term in (2.95) is the contribution due to the ambient pressure field, and vanishes for a simple shear flow. The functions for an oblate spheroid can be obtained using the prolate-oblate transformation mentioned in sections 2.3 and 2.5. The analytical approach introduced in section 2.5 is used to evaluate the orbital drift due to the fluid inertia and the drift is given by :

$$
\begin{aligned}
\Delta C_f =& ReC\frac{\kappa_{eq}^2+1}{(1-\lambda)\kappa_{eq}}\Bigg\{\Bigg[I_1F_1^f(\xi_0,\lambda)+I_2F_2^f(\xi_0,\lambda)+I_3F_3^f(\xi_0,\lambda)+I_4F_4^f(\xi_0,\lambda)+I_5F_5^f(\xi_0,\lambda) \\
&+I_6F_6^f(\xi_0,\lambda)\Bigg]+\Bigg[J_1G_1^f(\xi_0,\lambda)+J_2G_2^f(\xi_0,\lambda)+J_3G_3^f(\xi_0,\lambda)+J_4G_4^f(\xi_0,\lambda)\Bigg]\Bigg\}, \\
& \qquad (2.117)
\end{aligned}
$$

with I's and J's given in appendix A. Note that I's and J's are same as that seen in section 2.5.

The sign of the fluid inertial drift varies in a non-trivial manner with λ. The orbits stabilized by fluid inertia, for long times, for all λ's below the λ_{crit} curve in figure 2.3 are indicated in figure 2.10(a). For a prolate spheroid of any aspect ratio, in solid body rotation ($\lambda = -1$), the orbital drift is negative for all C's and the spheroid drifts towards the spinning orbit. This is expected, because in solid body rotation, the pressure gradient set up by inertial forces results in an inward centrifugal buoyancy, which stabilizes the spinning orbit. The spinning orbit continues to be the stable orbit for all λ's less than a particular λ that is a function of aspect ratio, and denoted by $\lambda_3(\kappa)(<0)$, indicated by the magenta curve in the fourth quadrant in figure 2.10(a)). At $\lambda = \lambda_3$, a repeller emerges from the tumbling orbit, splitting the orientation space on a unit hemisphere, for larger λ's into two distinct basins of attraction, with the attractors being the tumbling and the spinning orbits. The repeller moves towards the spinning orbit with increasing λ, and eventually merges with the spinning orbit at a second λ denoted by $\lambda_4(\kappa)(<0$ and indicated by the red curve in the fourth quadrant in figure 2.10(a)). The shaded region in figure 2.10(a) indicates the (λ, κ) combinations for which the fluid inertial drift changes sign, across a certain Jeffery orbit (the repeller), leading to two distinct basins of attraction. On the either side of this region, that is for λ's in the range $\lambda_4 < \lambda < \lambda_{crit}$ and $-1 < \lambda < \lambda_3$, the tumbling and spinning orbits, respectively, remain the sole attractors. In figure 2.10(b), the orbital drift is plotted against $C/(C+1)$ for a spheroid of aspect ratio 2 as an example to illustrate the above mentioned bifurcation. The shifting of the repeller location from tumbling to spinning as one traverses the shaded bifurcation region($\lambda_3 < \lambda < \lambda_4$) in figure 2.10(a), can be seen in the magnified view in figure 2.10(c).

An oblate spheroid drifts from any initial orientation towards the tumbling orbit for $\lambda = -1$, again driven by centrifugal buoyancy. However, there exists a range of λ's, for which there are two distinct basins of attraction separated by a repeller on a unit hemisphere. This range is indicated by the shaded region, bounded by the curves $\lambda_3(\kappa)$ and $\lambda_4(\kappa)$, in the third quadrant in figure 2.11(a)). However, unlike the prolate spheroid, the repeller in this case first emerges from the spinning orbit at λ=λ_3(red curve in the third quadrant of figure 2.11 (a)) and shifts towards the tumbling orbit with increasing λ, finally merging with it when λ=λ_4 (magenta curve in the third quadrant of 2.11(a). If the aspect ratio of the spheroid is less than approximately 0.32, there exists a second bifurcation region above $\lambda > \lambda_4$(indicated by the shaded region near $\lambda = 0$ in figure 2.11(a)). In this region, the repeller (say C^*) first emerges from the tumbling orbit at $\lambda = \lambda_5$ and flat out to increasingly thin ellipses centered around the gradient-vorticity plane as $\lambda \to \lambda_{crit}$. At $\lambda = \lambda_{crit}$, the repeller reduce to an arc on the

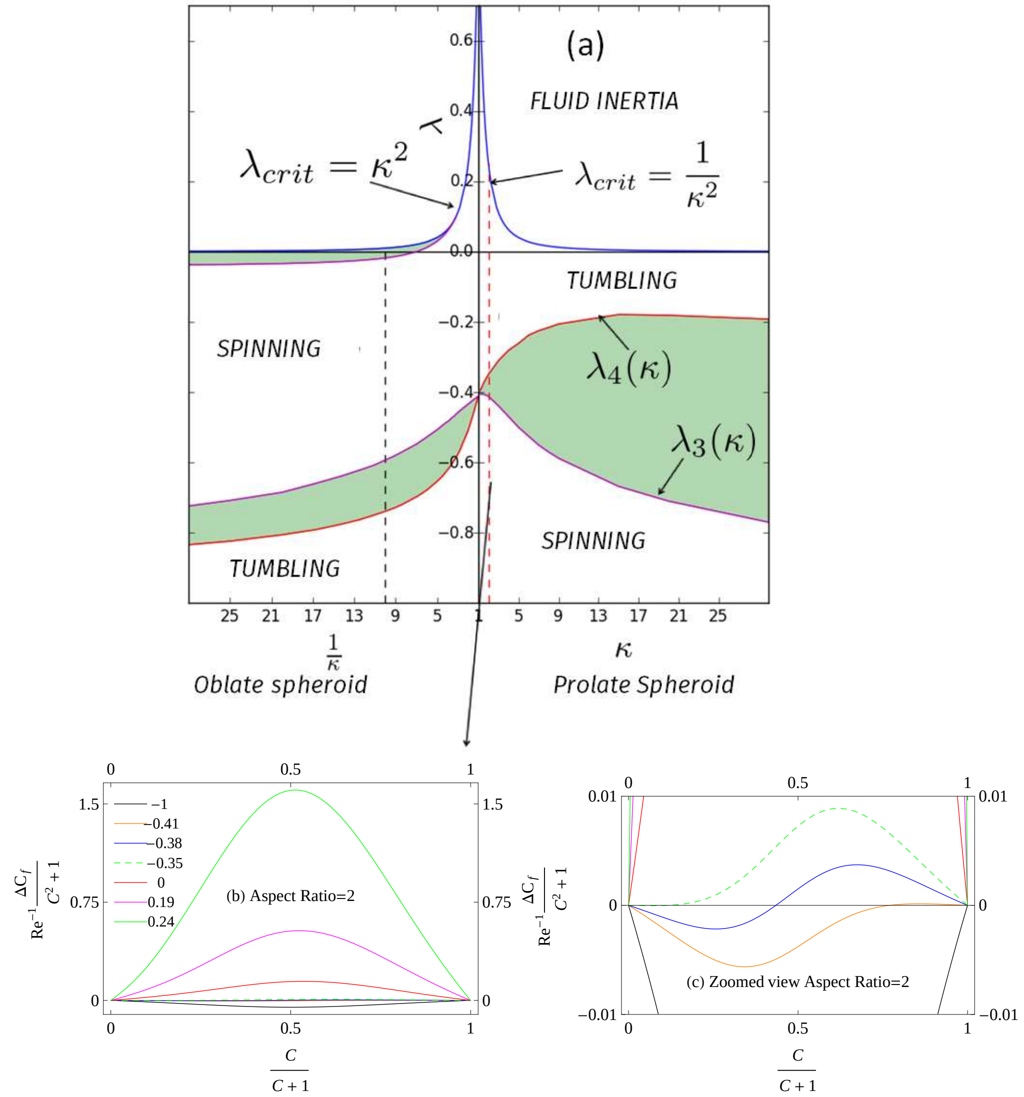

Fig. 2.10 (a) The orbits that are stabilized at long-times are identified for all combinations of λ -κ below the λ_{crit} curve(blue). The shaded region corresponds to the combinations of (λ, κ) for which there are two distinct basins of attraction separated by a repeller. The red and magenta curves corresponds to all combinations of (λ, κ) for which the repeller coincide with the spinning orbit and the tumbling orbit respectively. (b) The drift is plotted against $\frac{C}{C+1}$ for a prolate spheroid of aspect ratio 2.(c) Zoomed view of (b) .

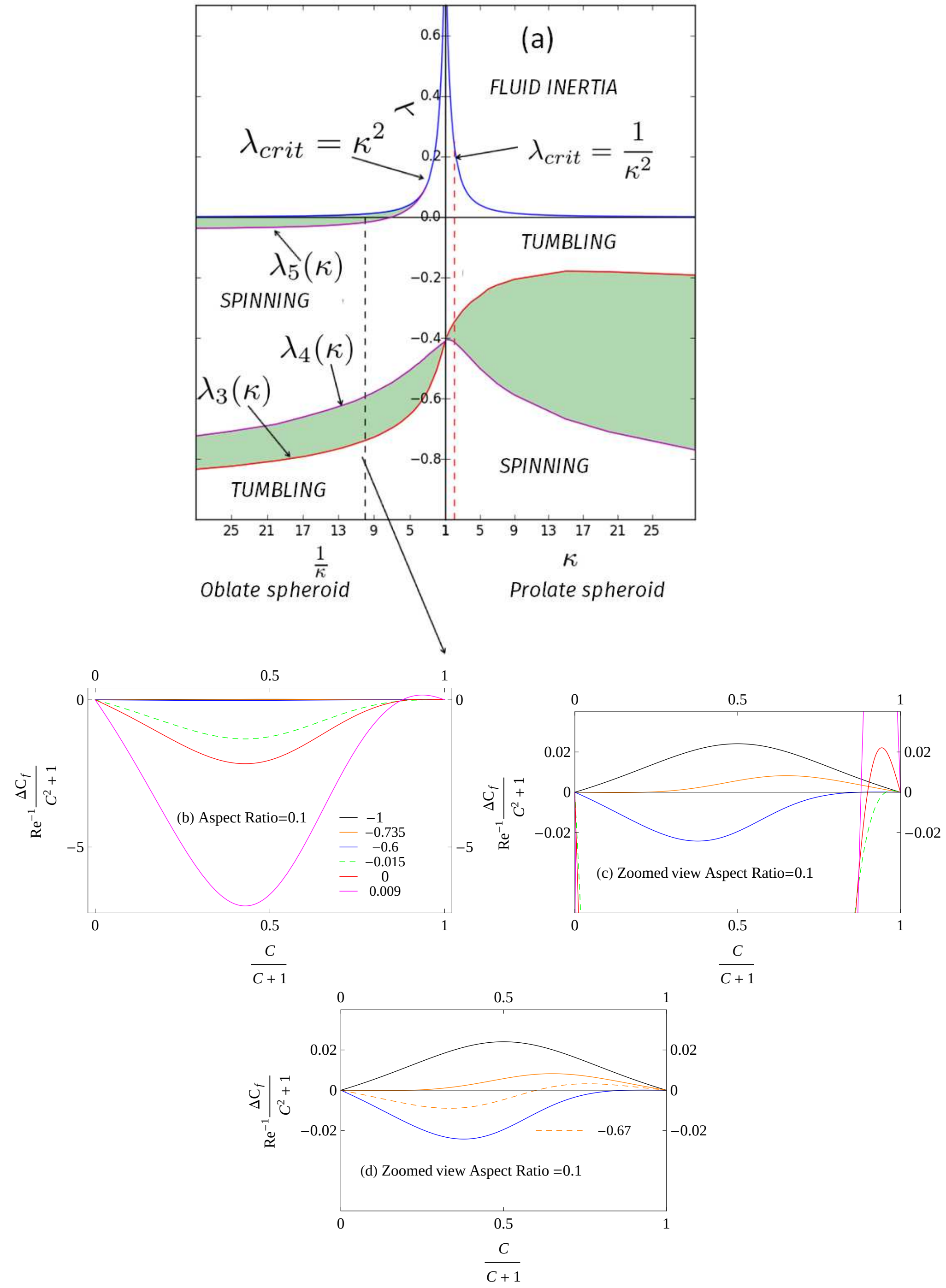

Fig. 2.11 (a) The orbits that are stabilized at long-times are identified for all combinations of λ -κ below the λ_{crit} curve(blue).(b) The drift is plotted against $\frac{C}{C+1}$ for an oblate spheroid of aspect ratio 0.1. (c) and (d) The zoomed view of (b) to show the shifting of the repeller in the two bifurcation regions identified in (a).

great circle in which the gradient-vorticity plane intersects the unit sphere. This is because C^* is finite in the limit of $\kappa_{eq} \to 0$ ($\lambda- > \lambda_{crit}$), and therefore the angular extent of the arc is $\theta_j = tan^{-1}C^*$ (see 2.70). In figure 2.11(b), the orbital drift is plotted for an aspect ratio of 0.1 to show the above mentioned bifurcations. The shifting of the repeller location in the shaded bifurcation region ($\lambda_3 < \lambda < \lambda_4$) in the third quadrant of figure 2.11(a) is plotted in figure 2.11(c) and the shifting in the shaded region corresponding to $\lambda > \lambda_5$ is plotted in figure 2.11(d) and the angle of extent of the arc as $\lambda \to \lambda_{crit}$ is 163^0.

In the particular case of simple shear flow, the normalized change in the drift constant (ΔC_f) is plotted for a prolate spheroid as a function of C in figure 2.12 for various aspect ratios. ΔC_f is positive for all aspect ratios and for all values of C. Fluid inertia in simple shear flow therefore causes a prolate spheroid to drift towards the tumbling mode starting from an arbitrary initial orientation. For a near-sphere, ΔC_f reduces to:

$$\lim_{\xi_0 \to \infty} \Delta C_f = \frac{11\pi C}{70\xi_0^2}, \tag{2.118}$$

at leading order and, for a slender fiber, one obtains:

$$\lim_{\xi_0 \to 1} \Delta C_f = -\frac{\sqrt{2}\pi C}{15(\xi_0 - 1)^{\frac{1}{2}} \ln(\xi_0 - 1)}. \tag{2.119}$$

These expressions motivate the normalizations used in figure 2.12. The factor ξ_0^2 in the near-sphere limit is identical to that for particle inertia, as would be expected since an inertial drift in either case would scale with the square of the eccentricity. In the limit of a slender fiber, the inertial terms may be linearized at leading order, being proportional to the leading order Stokes disturbance field of $O[\ln(\xi_0 - 1)]^{-1}$ associated with the axisymmetric extensional component of the simple shear (given by (2.39) in section 2.3). The resulting inertial angular velocity is $Re.O[\ln(\xi_0 - 1)]^{-1}$. Over the $O(\xi_0 - 1)^{-\frac{1}{2}}$ Jeffery period, this leads to an angular displacement and a ΔC_f of $O[(\xi_0 - 1)^{-\frac{1}{2}} / \ln(\xi_0 - 1)]$ as in (2.119). Recall from section 2.5 that $\Delta C_p \sim (\xi_0 - 1)^{3/2} \ln(\xi_0 - 1)$, so $\Delta C_f \gg \Delta C_p$, and fluid inertia is dominant for $\xi_0 \to 1$. In other words, one requires an asymptotically large density ratio of $St/Re \sim O[1/((\xi_0 - 1)\ln(\xi_0 - 1))]^2$ for particle inertia to influence the inertial drift of a slender fiber.

The functions, $F_i^f(\xi_0, 0)$ and $G_i^f(\xi_0, 0)$, for an oblate spheroid are obtained from those for a prolate spheroid in the usual manner. The flat disk limits of the resulting functions are given

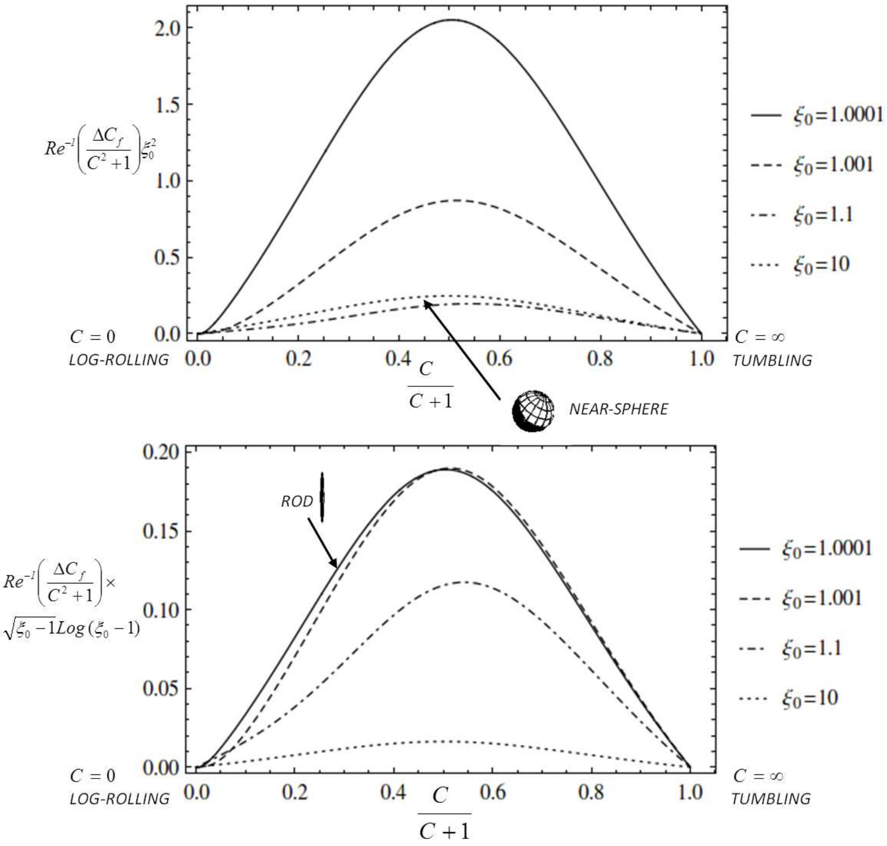

Fig. 2.12 The drift due to fluid inertia, as characterized by the normalized change in the orbit constant in a single Jeffery period, $Re^{-1}\frac{\Delta C_f}{(C^2+1)}$, plotted as a function of $\frac{C}{C+1}$, for a prolate spheroid in simple shear flow; $\frac{C}{C+1}=0$ and $\frac{C}{C+1}=1$ correspond to the log-rolling and tumbling modes. The upper plot uses the additional normalization factor of ξ_0^2, so the drift remains finite in the near-sphere limit ($\xi_0 \to \infty$). The lower plot uses the normalisation factor $(\xi_0 - 1)^{\frac{1}{2}}\ln(\xi_0-1)$, to render the drift finite in the slender fiber limit ($\xi_0 \to 1$).

by

$$F_1^f(\xi_0,0) \approx -\frac{29}{480}, F_2^f(\xi_0,0) \approx -\frac{1}{20}, F_3^f(\xi_0,0) \approx -\frac{11}{480}, \tag{2.120}$$

$$G_1^f(\xi_0,0) \approx \frac{3}{40}, G_2^f(\xi_0,0) \approx \frac{1}{40}, G_3^f(\xi_0,0) \approx \frac{11}{120}. \tag{2.121}$$

The ΔC_f for an oblate spheroid in simple shear flow is plotted against C in figure 2.13. In contrast to the particle inertia case (see figure 2.9), the near-sphere normalization alone is not sufficient for an oblate spheroid. The inertial angular velocity approaches a finite $O(Re)$ value independent of aspect ratio in the flat-disk limit, and this leads to $\Delta C_f \sim Re.O(\xi_0-1)^{-\frac{1}{2}}$ for $\xi_0 \to 1$ owing to the diverging Jeffery period . The differing scalings for particle and fluid inertia imply that the density ratio St/Re must become asymptotically large, of $O(\xi_0-1)^{-\frac{1}{2}}$ (although still far smaller than the corresponding prolate estimate), before particle inertia can begin to exert an influence on the orientation distribution of flat disks. Figure 2.13 includes separate plots of ΔC_f with the near-sphere and the flat-disk normalizations. From the plots in figure 2.13, it can be seen that ΔC_f is not single-signed as predicted in figure 2.11. Now, ΔC_f must certainly be negative, for all values of C, for a near-sphere, as is implied by the prolate-oblate transformation and a ΔC_f of $O(\xi_0^{-2})$. This remains true for aspect ratios greater than about 0.142 ($\xi_0 \approx 1.01$), and such oblate spheroids drift towards a steady spinning mode starting from any initial orientation. For aspect ratios smaller than this critical value, the ΔC_f curves cross the C-axis, so the drift becomes positive beyond a critical value of C (say, C^*). C^* is a function of ξ_0, and equals ∞ for an oblate spheroid with the critical aspect ratio (0.142), decreasing to $\sqrt{35}$ in the limit $\xi_0 \to 1$. For a flat disk, ΔC_f is given by:

$$\lim_{\xi_0\to 1} \Delta C_f = \frac{\pi(7+C^2-7(1+C^2)^{\frac{1}{2}})}{15\sqrt{2}C(\xi_0-1)^{\frac{1}{2}}}. = \frac{\pi(\sqrt{1+C^2}-1)(\sqrt{1+C^2}-\sqrt{1+C^{*2}})}{15\sqrt{2}C(\xi_0-1)^{\frac{1}{2}}} \tag{2.122}$$

The movement of C^* towards its limiting value in the range $1<\xi_0<1.01$ is highlighted by the magnified view in figure 2.13. As the aspect ratio decreases below 0.142, a repeller (which is a Jeffery orbit at this order of approximation) emerges from the tumbling orbit, separating the unit hemisphere into distinct basins of attraction. The region on the unit hemisphere between the repeller and the tumbling orbits, corresponds now to orientations that asymptote towards a tumbling mode, while the region around the vorticity axis enclosed by the repeller corresponds to orientations that asymptote towards a steady spinning mode. With decreasing aspect ratio, the repeller flatten out into increasingly thin ellipses centered about the gradient-vorticity plane. Eventually, in the flat disk limit, the repeller reduce to an arc (with an angular extent of about 161^o), on the great circle in which the gradient-vorticity plane intersects the unit sphere. As a result, a flat disk, like a prolate spheroid, approaches a tumbling mode from almost any initial orientation (except for a set of measure zero corresponding to the repeller). This happens despite the movement of C^* towards a finite limiting value (from ∞ to $\sqrt{35}$) for $\xi_0 \rightarrow 1$. This is because, for sufficiently thin oblate spheroids, the orbit constant is appropriately defined as $C = \tan\theta_j \cos\phi_j/\kappa = \tan\theta_j \cos\phi_j \xi_0/(\xi_0^2-1)^{1/2}$, so that for a given Jeffery orbit to remain bounded away from the gradient-vorticity plane as $\kappa \rightarrow 0$ ($\xi_0 \rightarrow 1$), C must diverge as $1/\kappa$ ($1/\sqrt{\xi_0^2-1}$); in other words, Jeffery orbits corresponding to any finite C in the flat disk limit (including the $C^* = \sqrt{35}$, the zero-crossing of the ΔC_f curve for a flat disk) must collapse onto the gradient-vorticity plane (the angular extent of the resulting arc is $C/\sqrt{1+C^2}$, and with $C = C^*$, this gives 161^o as mentioned above). To illustrate the approach of the ΔC_f zero-crossing towards $C = 0$ for a flat disk, the fluid inertial drift is plotted against the re-scaled orbital coordinate $\frac{C(\xi_0^2-1)^{1/2}}{1+C(\xi_0^2-1)^{1/2}}$ in figure 2.14. Figure 2.15 illustrates the repelling (Jeffery) orbits starting from the equator of the unit sphere ($C = \infty$), and moving towards smaller C's with decreasing aspect ratio. Figure 2.16 shows the nature of the finite-*Re* spiralling trajectories of the orientation vector on either side of the repeller. solutions, at the critical aspect ratio, renders the tumbling orbit unstable, and the system migrates to a distant equilibrium (the spinning mode). In the vicinity of the critical aspect ratio, the repeller locations are given by $1/C^* = \pm 1.48(\xi_0 - 0.142)^{\frac{1}{2}}$.

2.7 The effect of fluid inertia on neutrally buoyant spheroids (*Re*=*St*)

The inertial drifts presented in the earlier sections apply to certain limiting scenarios. Drift in section 2.5 is important for massive spheroids that occur in gas-solid systems, where as the drift in section 2.6 is important for hollow spheroids in an inertial ambient. From a rheological perspective, which we discuss in chapter 3, one would want to know the effect of weak inertia on a neutrally buoyant spheroid ($\rho_p = \rho_f$, $Re = St$). In this section we investigate the effect of the combined fluid and particle inertial drift, with $Re = St$, on the orientation of a neutrally buoyant spheroid in a planar linear flow.

The drifts given in (2.92) and (2.117) are summed up to obtain the drift for a neutrally buoyant spheroid. The orbits stabilized by the combined drift at long-times are indicated in figure 2.17. For a prolate spheroid irrespective of $\lambda(< \lambda_{crit})$ and κ, the orbit is the tumbling orbit. For an oblate spheroid, for a given aspect ratio there exist a critical λ ($\lambda_5(\kappa)$) below

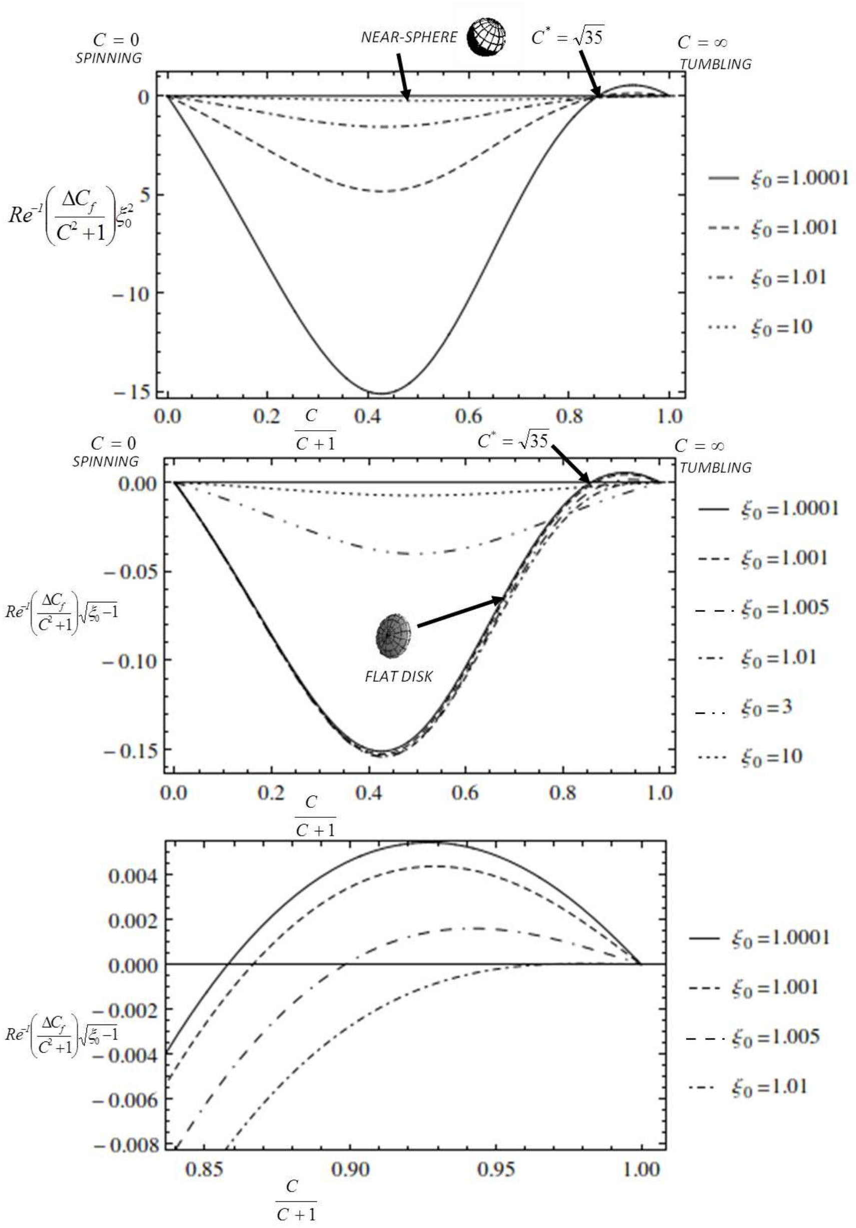

Fig. 2.13 The drift due to fluid inertia, as characterized by the normalized change in the orbit constant in a single Jeffery period, $Re^{-1}\frac{\Delta C_f}{(C^2+1)}$, plotted as a function of $\frac{C}{C+1}$, for an oblate spheroid in simple shear flow; $\frac{C}{C+1} = 0$ and $\frac{C}{C+1} = 1$ correspond to the spinning and the tumbling modes. The upper plot uses the additional normalization factor of ξ_0^2, so the drift remains finite in the near-sphere limit ($\xi_0 \to \infty$). The middle plot uses the normalisation factor $(\xi_0 - 1)^{\frac{1}{2}}$, to render the drift finite in the flat disk limit ($\xi_0 \to 1$). The lower plot is the magnified view highlighting the shift in the repeller location with changing ξ_0.

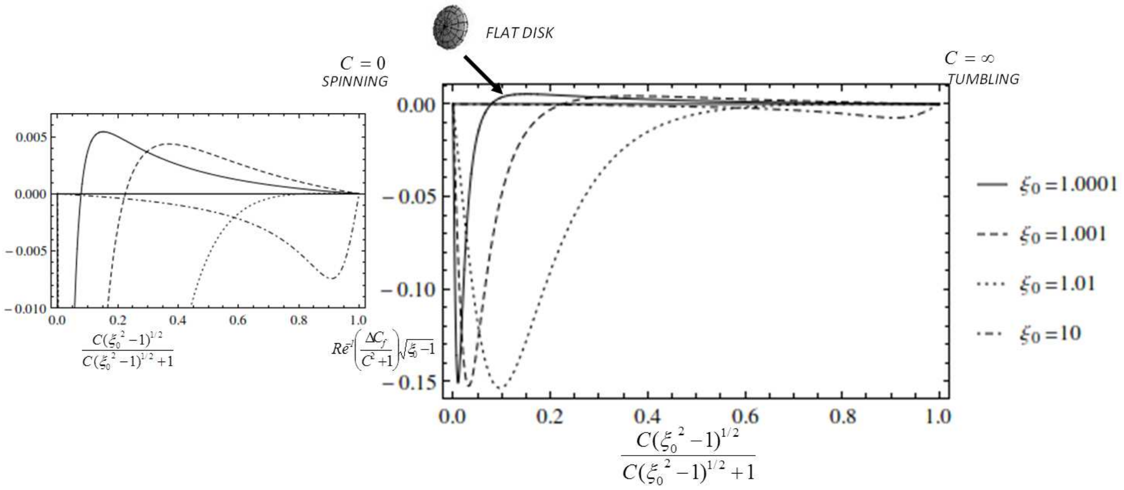

Fig. 2.14 The drift for the oblate spheroid in simple shear flow is plotted against a rescaled orbital coordinate in the right figure. The cross-over point shifts towards zero with decreasing aspect ratio. The magnified view is shown to the left.

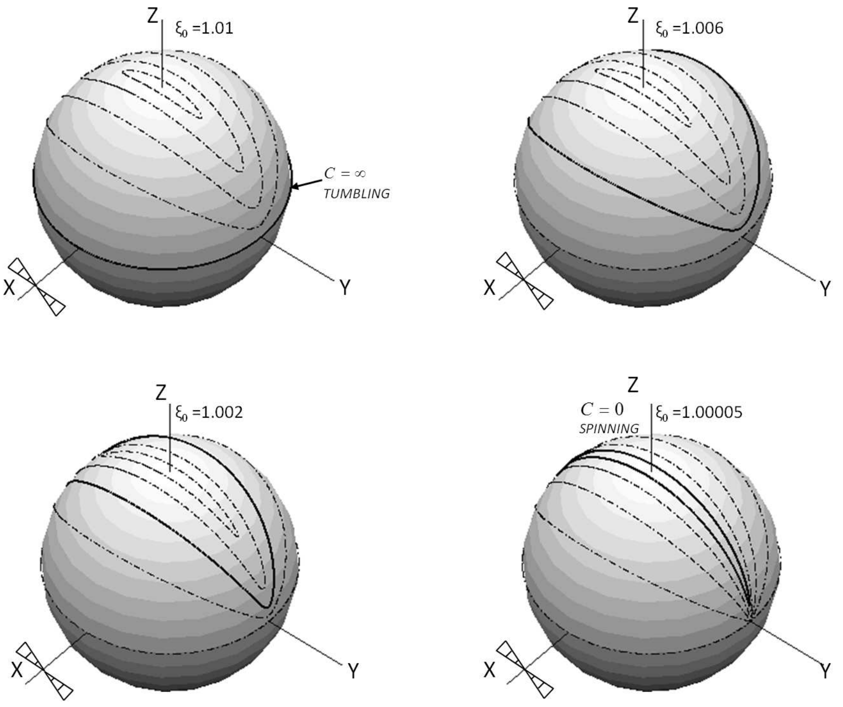

Fig. 2.15 The repeller orbit location for various aspect ratios. As the aspect ratios decreases below 0.142 ($\xi_0 = 1.01$) a repeller orbit(denoted by thick black lines) emerges from C/C+1 =1(the tumbling orbit). With further decrease in the aspect ratio, the repeller progressively shrinks, collapsing into the vicinity of the gradient-vorticity plane in the flat-disk limit.

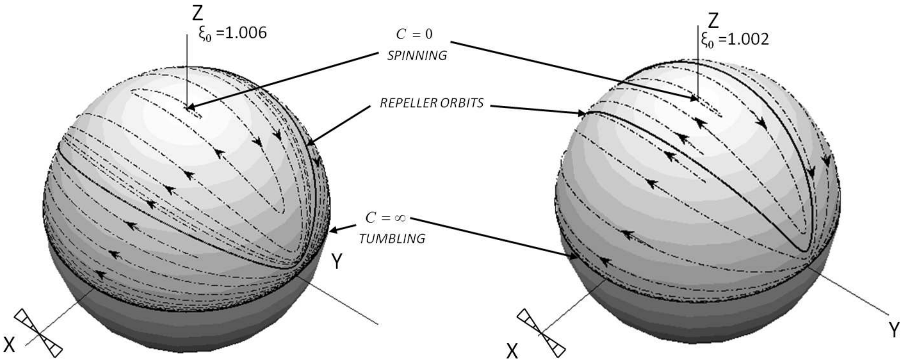

Fig. 2.16 The nature of the spiralling trajectories on either side of the repeller is shown for a pair of aspect ratios. For the purpose of illustration, a large Reynolds number ($Re = 0.8$) is chosen.

which the steady state is the spinning orbit, with $\lambda_5(\kappa)$ approaching λ_{crit} as the aspect ratio increases to about 0.32. For $\kappa < 0.32$ and $\lambda_5(\kappa) < \lambda < \lambda_{crit}$, there exists a repeller as seen in the earlier sections, and the (λ,κ) combinations in this range are indicated by the shaded region in figure 2.17. It is interesting to compare figures 2.17 , 2.11(a) and 2.7(a). In the range $\lambda_3(\kappa) < \lambda < \lambda_4(\kappa)$, the bifurcation regions which existed due to the fluid inertial drift alone, vanish for the neutrally buoyant spheroids, since the drift due to particle inertia tend to be stronger than fluid inertial drift when the ambient vortical component dominates the extensional component. However if the λ's are closer to simple shear than solid-body rotation, that is in the range $\lambda_5(\kappa) < \lambda < \lambda_{crit}$, the drift due to fluid inertia dominates that due to particle inertia, and therefore the bifurcation region in this range, in figure 2.11(a), is not altered much. In the case of solid body rotation, the drift on a neutrally buoyant spheroid is zero for both prolate and oblate spheroids, as must be the case, owing to the exact compensation between the centrifugal buoyancy and the centrifugal force on the particle.

For the particular case of simple shear flow, the drifts for prolate and oblate spheroids are plotted against the normalized orbit constant in figures 2.18 and 2.19, respectively. These curves closely resemble those in figures 2.12 and 2.13, showing that fluid inertia dominates the inertia of the particle for most aspect ratios. Accordingly, the critical aspect ratio at which $(\Delta C_f + \Delta C_p)$ first changes sign (for $C \to \infty$) is only slightly altered from the original value, 0.142, for hollow oblate spheroids (fluid inertia acting alone), to 0.137 for a neutrally buoyant oblate spheroid.

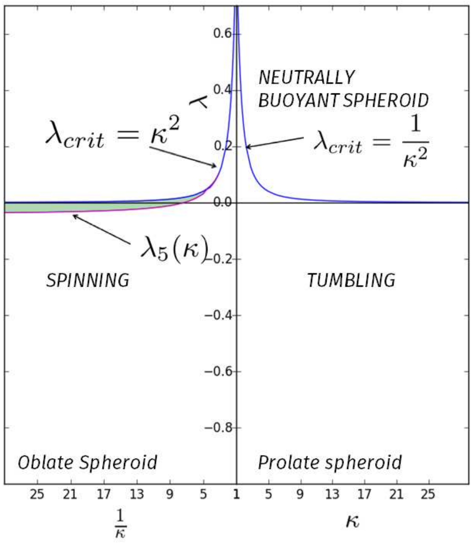

Fig. 2.17 The orbits stabilized for a neutrally buoyant spheroid by the combined particle and fluid inertial drifts.

2.8 Multiple time scale analysis

The orbital drifts in (2.92) and (2.117) were derived from (2.86) based on an assumption that C remains constant over each turn of the finite-Re trajectory that is an inertial spiral (an example of such a spiralling trajectory was shown in figure 2.5). As mentioned in section 2.5, for $Re,St << 1$, the advantage of such an approximation is that it reduces the need to numerically integrate the differential equations governing θ_j and ϕ_j over initial orientations spanning the entire unit sphere, to the determination of ΔC_f(or ΔC_p) as a function of C. In this section, we derive the expression for the orbital drift formally using a multiple time scale analysis, and substantiate the above physically motivated characterization of inertial effects. This allows us to discuss the limitations of the orbital drift approximation, particularly for extreme aspect ratios (slender fibres and flat disks).

The inertial drift occurs on a slow time scale ($t_2 \sim Re^{-1}\dot{\gamma}^{-1}$ or $St^{-1}\dot{\gamma}^{-1}$) compared to the leading order Stokesian convection time scale ($t_1 \sim \dot{\gamma}^{-1}$). The orbital coordinate of the spheroid can then be written as a two time scale series, $C = C_0(t_1,t_2) + Re(\text{or}St)C_1(t_1,t_2)$, where C_0 will turn out to be the average drift at leading order, and C_1 is the fluctuation about the average. The distinction between the fast and the slow time scales arises from the fact that there can be no secular growth on the t_1- scale. As is the case in this formalism, this is enforced

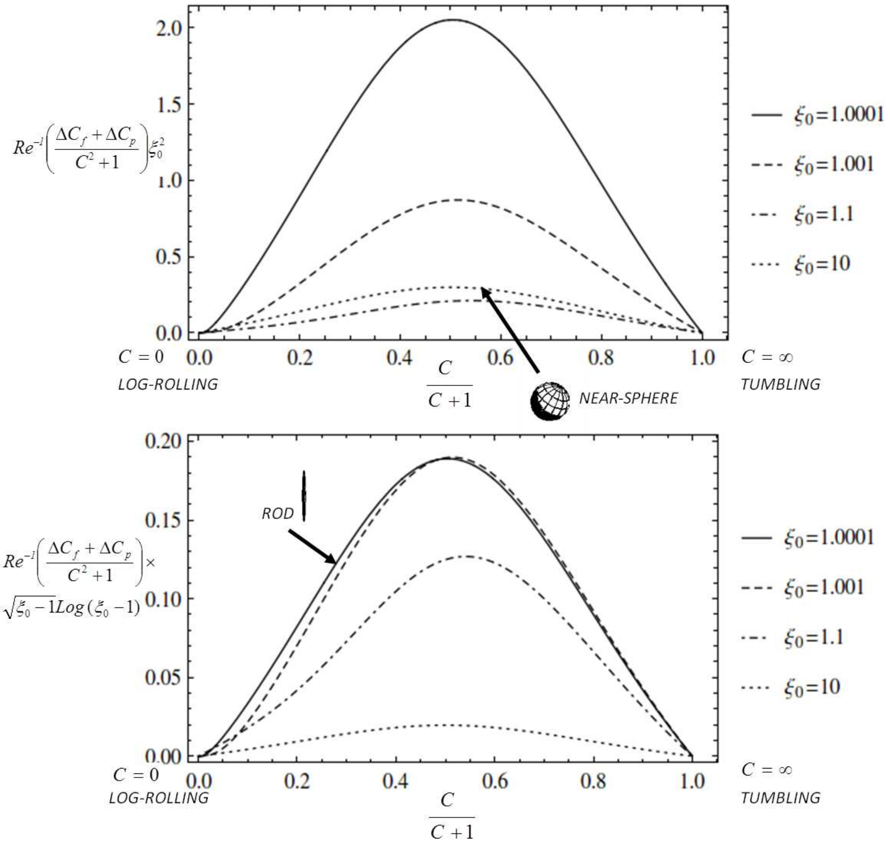

Fig. 2.18 The drift due to fluid and particle inertia for a prolate (neutrally buoyant) spheroid in simple shear flow, as characterized by the normalized change in the orbit constant in a single Jeffery period, $Re^{-1}\frac{\Delta C_f+\Delta C_p}{(C^2+1)}$, plotted as a function of $\frac{C}{C+1}$; $\frac{C}{C+1}=0$ and $\frac{C}{C+1}=1$ correspond to the log-rolling and tumbling modes. The upper plot uses the additional normalization factor of ξ_0^2, so that the drift remains finite in the near-sphere limit $(\xi_0\to\infty)$, while the second plot uses the normalization factor $(\xi_0-1)^{1/2}\log(\xi_0-1)$ such that the drift remains finite in the slender rod limit $(\xi_0\to 1)$. The contribution due to fluid inertia dominates particle inertia for all aspect ratios.

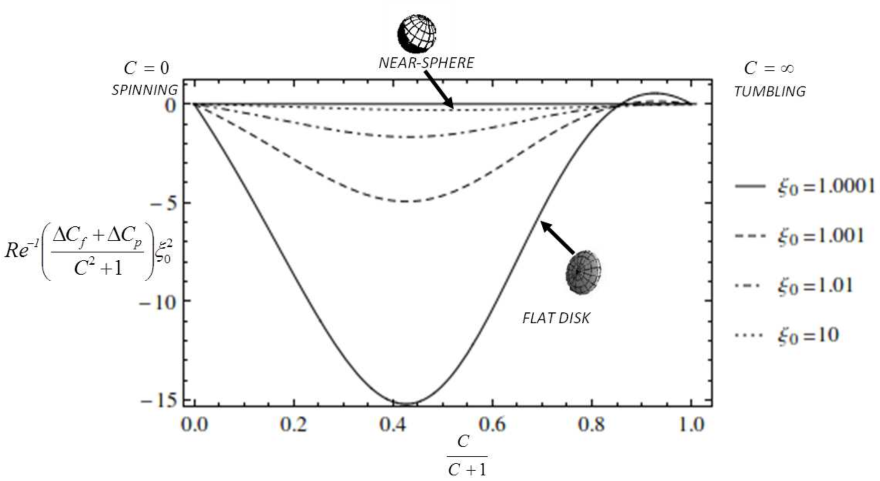

Fig. 2.19 The drift due to fluid and particle inertia for an oblate (neutrally buoyant) spheroid in simple shear flow, as characterized by the normalized change in the orbit constant in a single Jeffery period, $Re^{-1}\frac{\Delta C_p+\Delta C_f}{(C^2+1)}$, plotted as a function of $\frac{C}{C+1}$; $\frac{C}{C+1}=0$ and $\frac{C}{C+1}=1$ correspond to the spinning and tumbling modes. The plot uses the additional normalization factor of ξ_0^2, so the drift remains finite in the near-sphere limit ($\xi_0 \to \infty$).

by the condition that C be a periodic function of t_1, with period T_{jeff}(=$2\pi(\kappa_{eq}^2+1)/\kappa_{eq}$), for t_2 fixed. We will focus our analysis on the fluid inertial drift, although the analysis holds good for the particle inertial drift too. Denoting the right-hand side of (2.86) as $ReH(C,\tau,\xi_0)$, with $d\theta_j/dt$ and $d\phi_j/dt$ given in (2.93) and (2.94), and noting that $\tau=\kappa_{eq}t_1/(\kappa_{eq}^2+1)$, (2.86) can be rewritten as $dC/dt = ReH(C,\kappa_{eq}t_1/(\kappa_{eq}^2+1),\xi_0)$. Substituting the series for C above, and using the usual splitting of the time derivative into fast and slow components, $\frac{d}{dt}=\frac{d}{dt_1}+Re\frac{d}{dt_2}$, as part of the multiple scale formalism (Subramanian & Brady 2004; Bender & Orszag 1999), one gets:

$$\frac{dC_0}{dt_1}=0, \tag{2.123}$$

at leading order and

$$\frac{dC_1}{dt_1}+\frac{dC_0}{dt_2}=H(C,\kappa_{eq}t_1/(\kappa_{eq}^2+1),\xi_0), \tag{2.124}$$

at O(Re). The average orbital drift C_0, which is the solution to the leading order equation in (2.123) is therefore independent of t_1, $C_0(t_1,t_2)=C_0(t_2)$. To evaluate both the dependence of C_0 on t_2, and the fluctuation C_1, one can integrate (2.124) over the time period, and noting that the integral of the first term on the left-hand side of (2.124) evaluates to zero, one gets:

$$\frac{dC_0}{dt_2} = \frac{1}{T_{jeff}} \int_0^{T_{jeff}} H(C_0, \kappa_{eq} t_1/(\kappa_{eq}^2 + 1), \xi_0) dt_1 = \frac{1}{2\pi} \int_0^{2\pi} H(C_0, \tau, \xi_0) d\tau = \frac{\Delta C_f}{Re T_{jeff}}, \tag{2.125}$$

where ΔC_f is the average change in C over a Jeffery time period, which was already evaluated in (2.117). Using (2.125) in (2.124) one gets C_1 as:

$$C_1 = \frac{T_{jeff}}{2\pi} \left(\int_0^{\tau} H(C_0, \tau', \xi_0) d\tau' - \frac{\tau \Delta C_f}{Re T_{jeff}} \right), . \tag{2.126}$$

Thus, the multiple scale analysis allows one to fit ΔC_f into a differential equation for C, thereby allowing one to track the leading order evolution of C with time. In figure 2.20, we have plotted the C coordinate of spheroids with two aspect ratios, rotating in a simple shear flow ($\kappa = \kappa_{eq}$), as a function of time as well as ϕ, starting from ($C = 10$, $\tau = \pi/2$) using two methods; the first by numerically integrating (2.93) and (2.94), and then evaluating $C(t)$ using its definition (2.70) in terms of $\theta_j(t)$ and $\phi_j(t)$, and the second using the orbital drift obtained from the multiple scale analysis presented above. In figures 2.20 a and c, it can be seen that the results from two methods compare well (the blue and green curve match almost exactly). Figures 2.20(b) and (d) are plotted to identify the phases at which the drift is maximum. It can be seen that for the O(1) aspect ratio spheroid in figure 2.20(d), the drift in the aligned and nonaligned phases are of the same order. However, for the extreme aspect ratio spheroid in figure 2.20(b), the maximum drift occurs closer to the aligned phase. This is expected and can be seen from a simple scaling analysis. The dC/dt in (2.86) is order ReC in the extreme aspect ratio limit ($\kappa_{eq} \to 0$ or ∞). The rotation is however nonuniform, and therefore the spheroid spends O(1) time in the non-aligned phase and O(κ_{eq})(O($1/\kappa_{eq}$)) time in the aligned phase if it is oblate (prolate) spheroid. Thus, $\Delta C_{nonaligned}/\Delta C_{aligned}$ is O(κ_{eq}) (O($1/\kappa_{eq}$)) for oblate (prolate) spheroid, making the change in C much larger in the aligned phase compared to the non-aligned phase for extreme aspect ratios. As explained earlier in section 2.5, the prediction from the multiple scale analysis should eventually break down when Re or $St \sim \kappa_{eq}$ for an oblate spheroid. The cases plotted in figure 2.20 are for $Re = 0.01$, and they satisfy the restriction $Re < \kappa_{eq}$ mentioned above. The relaxation of this restriction however leads to a breakdown of the average drift analysis. To illustrate the breakdown, in figure 2.21 we have plotted the C coordinate of a spheroid rotating in a simple shear flow ($\kappa = \kappa_{eq}$) for different Re's as a function of ϕ_j, starting from ($C = 10$, $\tau = \pi/2$). It can be seen from the figure that the sum of the orbital drift approximation (C_0) and the fluctuation (C_1) fails to capture the actual variation in C with increasing ratio of $Re/\kappa_{eq} = \widetilde{Re}$. In what follows we discuss a way

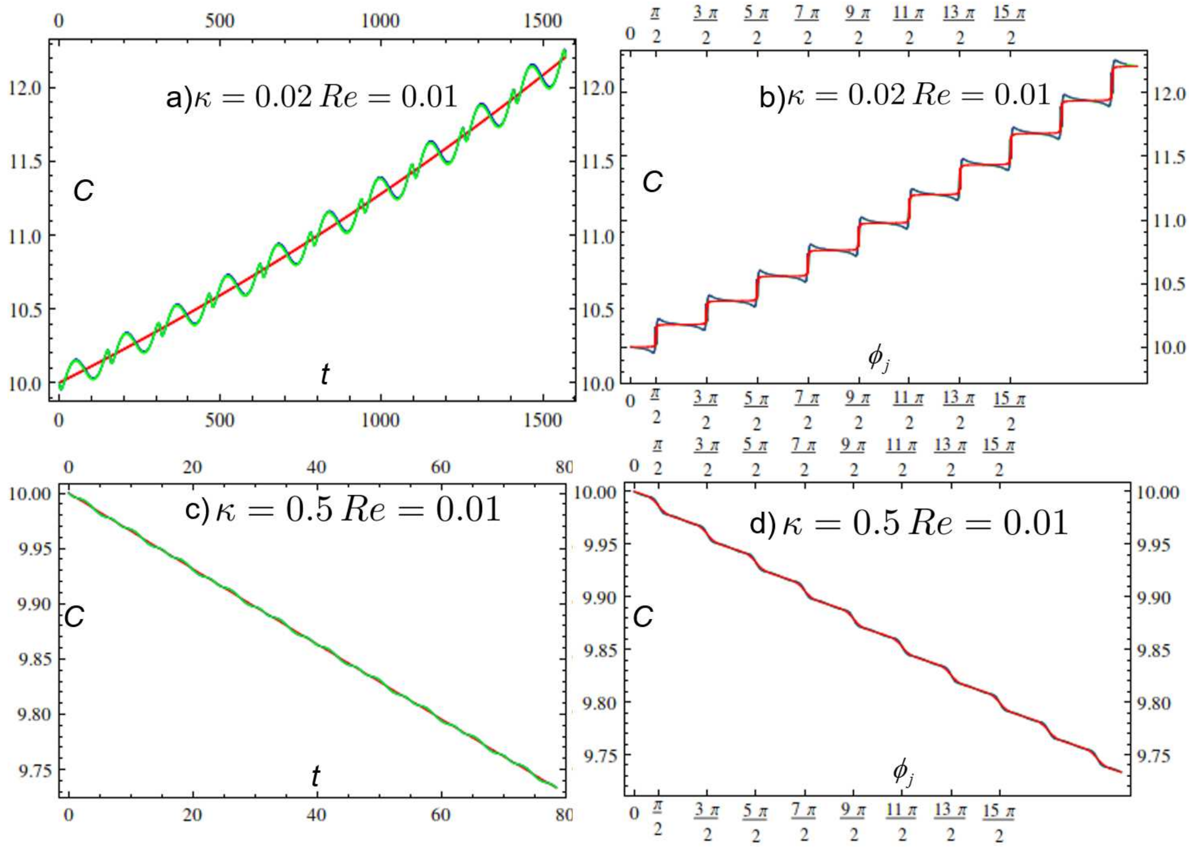

Fig. 2.20 The orbital coordinate C starting from $C = 10$ and $\tau = 0$, estimated from 1) the orbital drift alone (red), 2) the orbital drift together with the fluctuations (green) and 3) the C obtained from numerical integrating the governing equations of θ_j and ϕ_j (blue) are plotted against time for spheroids of aspect ratios 0.02 and 0.5 rotating in a simple shear flow in (a) and (c) respectively. The orbital coordinate is plotted against ϕ_j for the same aspect ratios in (b) and (d).

to capture this actual variation for an oblate spheroid, primarily because it has an interesting bifurcation in the orientation dynamics in the extreme aspect ratio limit, as already seen in section 2.17, although an analogous analysis can be performed for a prolate spheroid, the extreme aspect ratio analysis for an oblate spheroid will help in determining the location of the repeller well beyond the regime accessible to an orbital drift interpretation.

For an extreme aspect ratio spheroid, the maximum change in C occurs during the aligned phase, and therefore a boundary layer analysis allows one to capture the actual variation for O(1) values of $\widetilde{Re}$. One can write the net change in C as:

$$\int_0^{-2\pi} \frac{dC}{d\phi_j} d\phi_j = \int_0^{-2\pi} \frac{\frac{dC}{dt}}{\frac{d\phi_j}{dt} + Re \frac{d\phi_j}{dt}|_{Re}} d\phi_j, \tag{2.127}$$

where $\frac{d\phi_j}{dt}, \frac{dC}{dt}$ and $\frac{d\phi_j}{dt}|_{Re}$ are given in (2.29), (2.86), and (2.94) respectively. Now in the limit of $\kappa_{eq} \to 0$(equivalently $\lambda \to 1/\kappa^2$), (2.29) is proportional to $\cos^2 \phi_j$ and (2.86) is proportional to $\cos \phi_j$, making the integrand in (2.127) proportional to $1/cos^2 \phi_j$ and therefore divergent at $\phi_j = -\pi/2$ and $\phi_j = -3\pi/2$. These divergences suggest that the contribution to the integral comes from the aligned phase as expected from figure 2.21 (e), and one can therefore rewrite (2.127) as:

$$\begin{aligned} \int_0^{-\pi} \frac{dC}{d\phi_j} = \int_0^{-\pi} \left(\frac{dC}{d\phi_j} - \lim_{\phi_j \to -\frac{\pi}{2}} \frac{dC}{d\phi_j} \right) d\phi_j + \int_{-\pi}^{-2\pi} \left(\frac{dC}{d\phi_j} - \lim_{\phi_j \to -\frac{3\pi}{2}} \frac{dC}{d\phi_j} \right) d\phi_j \\ + \int_0^{-\pi} \lim_{\phi_j \to -\frac{\pi}{2}} \frac{dC}{d\phi_j} d\phi_j + \int_{-\pi}^{-2\pi} \lim_{\phi_j \to -\frac{3\pi}{2}} \frac{dC}{d\phi_j} d\phi_j \end{aligned} \tag{2.128}$$

where we have isolated the divergences at $-\pi/2$ and $-3\pi/2$. Using a rescaled coordinate defined as $\hat{\phi} = (\phi_j + \pi/2)/\kappa$, one can rewrite divergent integral at $-\pi/2$ as:

$$\int_0^{-\pi} \left(\left. \frac{\frac{dC}{dt}}{\frac{d\phi_j}{dt} + Re \left. \frac{d\phi_j}{dt} \right|_{Re}} \right|_{\lim_{\phi_j \to -\frac{\pi}{2}}} \right) d\phi_j = \int_{\infty}^{-\infty} \frac{C\widetilde{Re}\widetilde{F} - C\widetilde{Re}\widetilde{F}\frac{\hat{\phi}^2}{1+\hat{\phi}^2}}{-(1+\hat{\phi}^2) - \widetilde{Re}\widetilde{G}\hat{\phi}} d\hat{\phi} = \Delta C_{jump}, \tag{2.129}$$

where $\widetilde{F} = \lim_{\lambda \to \frac{1}{\kappa^2}} (F_1^f - F_2^f - F_3^f + F_4^f - 2F_5^f)$ and $\widetilde{G} = \lim_{\lambda \to \frac{1}{\kappa^2}} (G_1^f - G_2^f - G_3^f + G_4^f)$, where F^f's and G^f's are defined in section 2.5. One could write the divergence at $\phi_j \to -3\pi/2$ also in a similar manner. The jump in C close to the aligned phase obtained from (2.128) and (2.129), is plotted against the rescaled coordinate in figure 2.22 for a spheroid in a simple shear flow. This jump (green) predicts the total change in C (blue curve) near the aligned phase, obtained

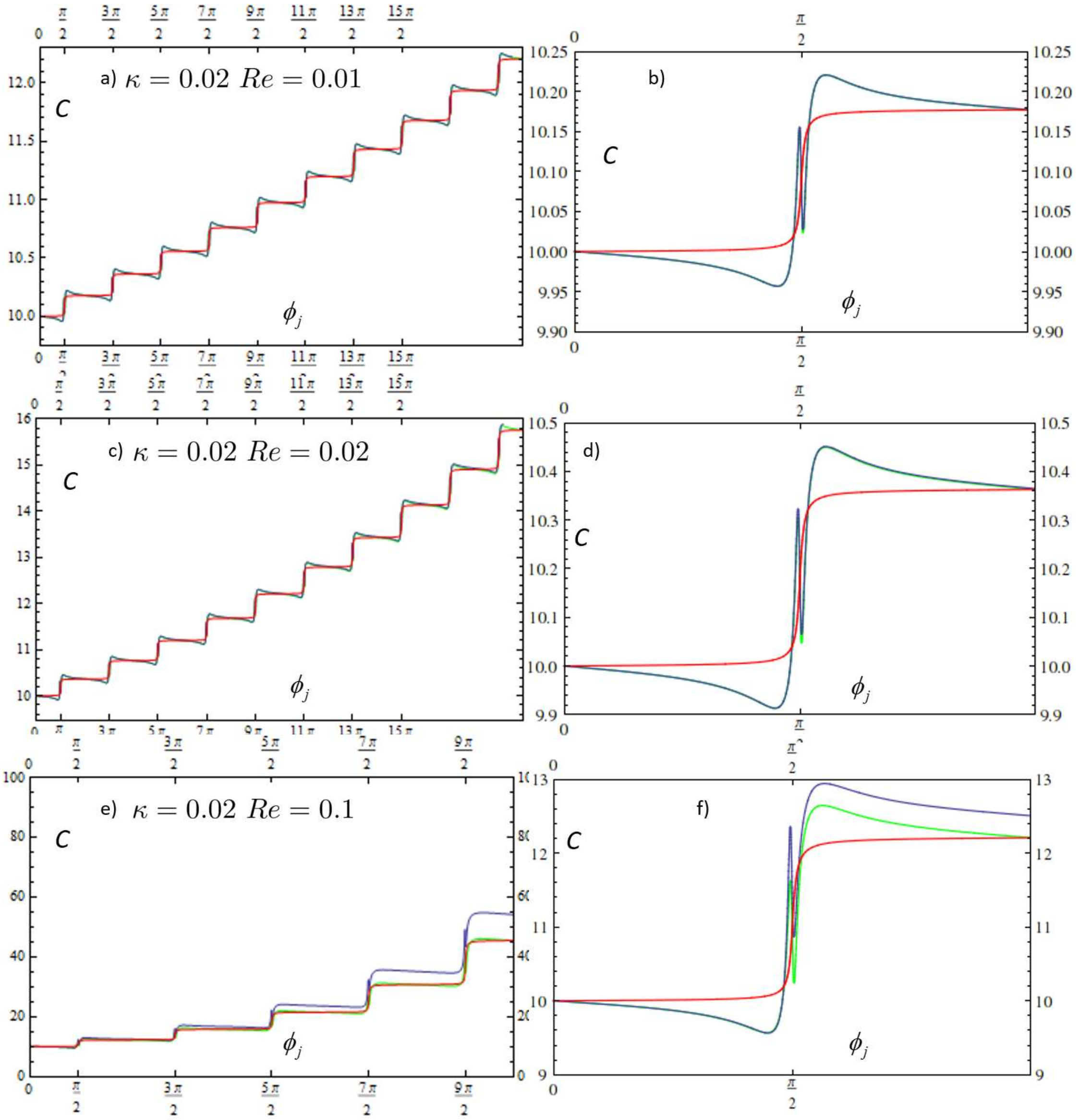

Fig. 2.21 The orbital coordinate C starting from $C = 10$ and $\tau = 0$, estimated from 1) the orbital drift alone (red), 2) the orbital drift together with the fluctuations (green) and 3) the C obtained from numerical integrating the governing equations of θ_j and ϕ_j (blue) are plotted for various *Re*'s in (a), (c) and (e). The plots on the right side (b),(d) and (f) are zoomed views of the plot to its left.

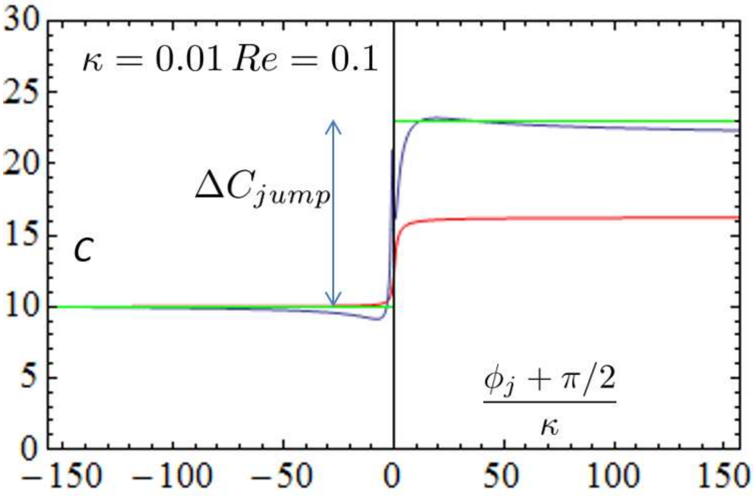

Fig. 2.22 The orbital coordinate is plotted against the rescaled boundary layer variable for a spheroid in simple shear flow. The average drift approximation, numerical integration result and the prediction from the boundary layer analysis are shown in red, blue and green color respectively.

from numerically solving the differential equations for the angular velocities; note that the orbital drift approximation breaks down for these parameters ($Re = 0.1$, $\kappa = .01$,$\tilde{Re} = 10$).

The bifurcation region shown in figure 2.17 was estimated on the basis of the orbital drift approximation. As we have seen above, the orbital drift need not be a good approximation to the numerical solution of the differential equations for $O(1)\ \widetilde{Re}$. In such cases, one would want to check the actual repeller location with that predicted by the orbital drift approximation. In figure 2.23, we have shown the shift in the repeller location for various values of *Re* in three planar linear flows. It is clear from the figure that despite being unable to predict the actual drift, the average drift approximation predicts the repeller location with reasonable accuracy down to an O(1) $\widetilde{Re}$. The plots show an eventual deviation for larger $\tilde{Re}$.

2.9 Conclusions and future work

In this chapter we have analyzed the effect of particle and fluid inertia on the orientation dynamics of a spheroid in a planar linear flow. The corrections to the leading order angular velocity at O(*St*) are given in (2.77) and (2.78) . The corrections at O(*Re*) are given in (2.93) and (2.94). We have used an average drift approximation to analyze the solution of the differential equations governing the rates of change of orientation. The average drift is interpreted

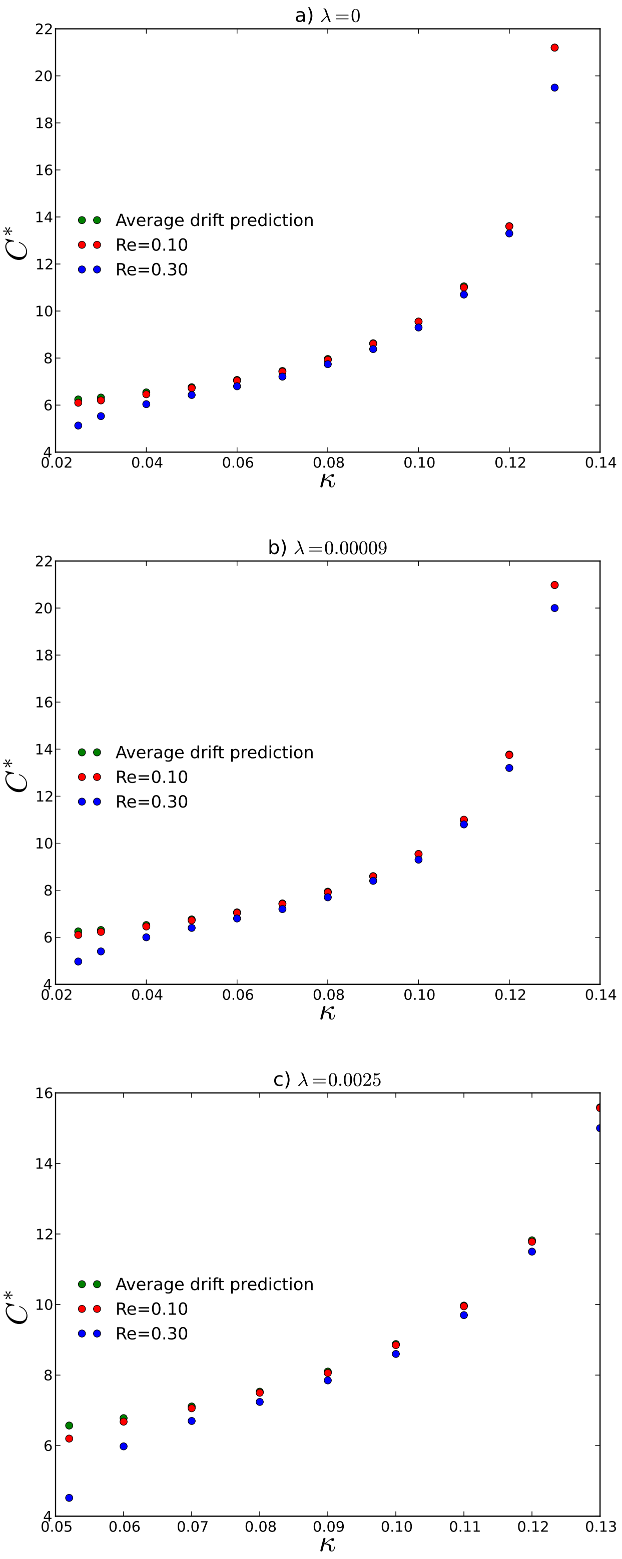

Fig. 2.23 The repeller location C^* is plotted against aspect ratio for various *Re*'s, for planar linear flows characterized by (a) $\lambda = 0$,(b) $\lambda = 0.00009$ and (c) $\lambda = 0.0025$. The minimum value of $\widetilde{Re}$ in each of the cases are (a)12 (b)13 and (c)21.

in terms of the orbital coordinate defined in (2.70). The average drift for the particle and fluid inertia are given in (2.92) and (2.117). The orbits stabilized by particle and fluid inertia are identified in the $\lambda - \kappa$ plane in figures 2.6, 2.7 and figures 2.10, 2.11 respectively. The shaded regions in these figures correspond to the $\lambda - \kappa$ combinations for which a bifurcation in the orientation dynamics leads to the existence of a repeller on the unit-hemisphere which divides the orientation space into two basins of attraction, with attractors being the tumbling and spinning orbits respectively. Typical examples of the repeller are shown in 2.6(d),(e) and (f). The orbits stabilized by inertia for a neutrally buoyant spheroid are identified in figure 2.17. In the neutrally buoyant case, the bifurcation region exist only for oblate spheroids. For the spheroids in this region inertia does not stabilize an unique orbit. Fot the particular case of simple shear flow the aforementioned repeller exists for neutrally buoyant oblate spheroids whose aspect ratios are smaller than 0.137.

Finally, we note that a very recent work (Einarsson *et al.* (2015*a*,*b*)) has also investigated the effect of weak fluid inertia on spheroidal particles of arbitrary aspect ratio in a simple shear flow. The reciprocal theorem volume integral for the rate of change of the orientation vector of the spheroid is written in a general tensorial form, and is evaluated after applying symmetry arguments to reduce it to a set of four scalar integrals. The functions of aspect ratio that multiply the trigonometric functions in the expressions for the inertial angular velocity contributions are not given in closed form; rather, they are plotted as a function of the aspect ratio. The authors investigate the stability of the spinning and the tumbling modes for both prolate and oblate spheroids and arrive at the same conclusions as the present work with respect to the stability of the tumbling and log-rolling/spinning modes in simple shear flow. Importantly, however the authors have not interpreted their results in terms of the physically significant orbital drift and the consequences for rheology given in chapter 3 are not explored.

Chapter 3

The effect of inertia on the rheology of a dilute suspension of spheroids

3.1 Introduction

This chapter is concerned with the theoretical determination of the viscosity of a dilute non-interacting suspension of non-Brownian anisotropic particles as a function of the particle volume fraction, a classical problem in microhydrodynamics (Batchelor (1977)). The relevant volume fraction here is the hydrodynamic one, nL^3, where n is the particle number density and L is the largest characteristic dimension of an individual particle; $nL^3 \ll 1$ implies hydrodynamic diluteness. We consider the simplest geometry for a non-spherical particle, that of a spheroid, wherein the deviation from sphericity is characterized by a single parameter, the particle aspect ratio, and in which case L would be the semi-major axis (see chapter 2). The analogous problem for spheres was first analysed by Einstein in 1906 (Leal (1992)) who showed that a suspension of rigid spheres, in the dilute non-interacting limit, behaves as a Newtonian fluid with an effective viscosity that is enhanced relative to that of the suspending fluid by a factor $\frac{5}{2}\phi$, ϕ ($\ll 1$) being the volume fraction, and the factor $\frac{5}{2}$ often referred to as the Einstein coefficient. The determination of the analog of the Einstein coefficient for a suspension of spheroids, a dimensionless function of the spheroid aspect ratio that multiplies nL^3, turns out to be considerably more involved. Stokesian hydrodynamics alone does not, in fact, provide for a unique answer in this regard.

In order to better understand the above difficulty, one may again examine a suspension of spheres where a similar difficulty occurs in determining the $O(\phi^2)$ correction to the effective viscosity. This calculation, which includes the first effects of hydrodynamic interactions, was accomplished much later (than Einstein) by Batchelor and Green in 1972 (Batchelor & Green (1972*b*);Batchelor & Green (1972*a*)). The difficulty in the pair-problem arises because a naive summation of the long-ranged pair interactions in the suspension viscosity problem, and in other related ones that include the determination of the hindered settling velocity (Batchelor (1972)) and the permeability of a dilute fixed bed (Hinch (1977)), leads to either divergent or conditionally convergent integrals, and only in the 1970's was it shown that appropriate renormalizations were needed to sensibly characterize the effects of hydrodynamic interactions on the bulk characteristics of Stokesian suspensions. For the suspension viscosity problem in particular, even after the renormalization, the notion of the particulate phase modifying the shear viscosity to O(ϕ^2), and thence, of a Newtonian rheology for a Stokesian suspension at this order, was found to be crucially dependent on the topology of the pair-sphere trajectories. This is due to the occurrence of closed pair-pathlines, and the resulting indeterminacy of the pair-distribution function on such trajectories in the purely hydrodynamic limit (Batchelor & Green (1972*a*)). The occurrence of closed particle (Kao *et al.* (1977*a*)) or fluid trajectories (Subramanian & Koch (2006*a*);Subramanian & Koch (2006*c*);Subramanian & Koch (2007)) in Stokes flows is not uncommon, the underlying reason being the principle of reversibility associated with the quasi-steady Stokes equations. The above indeterminacy associated with the pair probability on closed pair-particle pathlines prevents a straightforward determination of the stress tensor, at O(ϕ^2), for a range of linear flows that includes the rheologically important case of simple shear flow(Kao *et al.* (1977*a*)). Any calculation of the O(ϕ^2) contribution in such flows must therefore appeal to physics outside of Stokesian hydrodynamics in the dilute regime such as three-particle interactions, weak particle (Subramanian & Brady (2006)) or fluid inertia (Morris *et al.* (2007)) or weak Brownian motion (Morris & Brady (1997)).

For a suspension of spheroids, the aforementioned rheological indeterminacy is already present at O(nL^3), that is, even in the absence of hydrodynamic interactions. The aspect-ratio-dependent analog of the Einstein coefficient depends only on the single particle orientation distribution in the dilute limit (owing to the absence of positional correlations at this order), and the latter is indeterminate. As we have seen in chapter 2, an isolated spheroid in simple shear flow (and over a range of planar linear flows) rotates along any of a one-parameter family of closed orbits, now known as Jeffery orbits (Jeffery 1922). The existence of such closed orbits on the unit sphere of orientations leads to the indeterminacy above. In the convective limit, that is in the absence of any inter-particle interactions, the orientation probability density may be conveniently written in the form $g(C,\tau)f(C)$ (Leal & Hinch (1971)). The coordinates (C,τ) form a non-orthogonal system on the unit sphere that characterizes the particle motion along Jeffery orbits(see chapter 2), with C being an orbit constant that ranges from 0 to ∞ and

τ being the phase that changes at a constant aspect-ratio-dependent rate along a given orbit. The first factor in the orientation probability density, $g(C,\tau)$, determines the distribution of orientations along a Jeffery orbit, while the second factor, $f(C)$, determines the distribution of orientations across the various Jeffery orbits. Strictly speaking, neither of these two components is uniquely determined in the convective limit in the absence of inter-particle interactions. A tiny polydispersity in the particle aspect ratio, however, is sufficient for the orientation distribution along a single Jeffery orbit to converge to a unique steady distribution given by the inverse rate of change of the azimuthal angle as found by Jeffery, and is a function of the particle aspect ratio (Okagawa *et al.* (1973*a*);Okagawa *et al.* (1973*b*)). On the other hand, the function $f(C)$ is, by definition, unchanged by particle motion along Jeffery orbits, and therefore preserves its functional form in the absence of interactions. As a result, one predicts a sensitive dependence of the rheology of a dilute non-interacting suspension of non-Brownian spheroids on the initial orientation distribution! As for spherical particle suspensions, earlier authors have appealed to mechanisms like Brownian motion (Leal & Hinch (1971);Hinch & Leal (1972)),viscoelasticity (Leal (1975)), fluid and particle inertia (Subramanian & Koch (2005);Subramanian & Koch (2006*b*)), and pair-hydrodynamic interactions in the limit of large aspect ratios (Okagawa *et al.* (1973*a*);Rahnama *et al.* (1995)), to obtain a drift across Jeffery orbits in an effort to endow the suspension with a finite memory, and thereby, arrive at a unique steady state distribution across Jeffery orbits. The aforementioned efforts that consider inertia, viscoelasticity or hydrodynamic interactions are restricted to limiting particle geometries(large or near-unity aspect ratios)

In chapter 2, we have seen that weak inertial effects, at O(*Re*) ($Re << 1$), stabilize a unique orbit for a neutrally buoyant spheroid rotating in a simple shear flow, provided its aspect ratio is larger than 0.137. The unique orbit is the tumbling orbit for a prolate spheroid of any aspect ratio and it is the spinning orbit for an oblate spheroid whose aspect ratio is larger than 0.137 (see chapter 2). Hence, for the above mentioned range of aspect ratios, the distribution across Jeffery orbits are delta functions peaked either at $\theta_j = \pi/2$ or $\theta_j = 0$, where the polar angle θ_j is defined in figure 2.2. The viscosity of a suspension of spheroids mentioned above can be readily evaluated from the unique delta function orbit distribution. For neutrally buoyant oblate spheroids with aspect ratios smaller than 0.137, depending on the initial condition, inertia stabilizes either the tumbling or the spinning orbit. For these spheroids, as shown in chapter 2, a repeller exists on the unit hemisphere separating the orientation space into two distinct basins of attractions with the attractors being the tumbling and spinning orbits(see figure 2.15 for a typical example of such a repeller). For a suspension of such spheroids, this would mean that the distribution is given by a couple of delta functions peaked at $\theta_j = 0$ and $\theta_j = \pi/2$, and the relative amplitudes of these delta functions are determined by the initial distribution of orientations. The steady-state partitioning of orientations between these two orbits is uniquely determined only when physical effects other than inertia are included. In order to render the viscosity of the suspension unique, we consider stochastic orientation fluctuations in the form of rotary Brownian motion as an example of such a physical effect. The importance of rotary Brownian motion in relation to rotation by shear flow is characterized by the rotary Peclet number (Pe_r), defined as $\frac{\dot{\gamma}}{D_r}$, where D_r is the rotary diffusivity of the spheroid. Interestingly, the distribution that is set up across the Jeffery orbits due to rotary Brownian motion and inertia is of the Boltzmann form and is dependent on the nondimenstional parameter $RePe_r$. This allows for an equivalent thermodynamic interpretation of the unique steady state orientation distribution. The original pair of Jeffery orbits, smeared out by thermal fluctuations, may be regarded as tumbling and spinning phases, and comprise the small and large-C branches of a two-phase envelope ending in a critical point. The transition between the tumbling and spinning phases is interpreted as a phase transition and we call it a 'tumbling-spinning transition'. The three-dimensional parameter space, with the parameters being $RePe_r$, κ and C, characterizing this tumbling-spinning transition has a one-to-one correspondence with the familiar thermodynamic description of the one-component phase transition. Specifically, κ and C are analogous to the pressure and specific volume, respectively, while an appropriate nondimensional shear rate plays the role of an inverse non-equilibrium temperature. One can also draw an analogy between the famous coil-stretch transition (De Gennes 1974; Hinch 1974) and the tumbling-spinning transition, with the transitions in both cases endowing the system, suspension in here and polymer solution in case of coil-stretch transition, with a memory that exceeds the nominal microstructural relaxation time.

This chapter is divided into different sections as follows. In section 3.2, we express the viscosity as an integral which gives the average of the stresslet over the steady state orientation distribution. Note that this is the hydrodynamic stress; the direct Brownian stress is negligible in the limit examined ($Pe_r >> 1$). For prolate spheroids of any aspect ratio and oblate spheroids whose aspect ratios are larger than 0.137, inertial effects at O(Re) alone set up the unique steady state distribution and we present the viscosity of a suspension of such spheroids in section 3.3. For oblate spheroids whose aspect ratios are smaller than 0.137, we calculate the steady state distribution set up by rotary Brownian motion at O(Pe_r^{-1}) and inertia at O(Re) in section 3.4.1. The thermodynamic interpretation of the 'tumbling-spinning transition' based on the steady state distribution determined in section 3.4.2, and the associated three dimensional phase diagram including the two-phase 'tumbling-spinning' envelope is developed in this section, first for the simple shear flow. Next, we examine the phase diagrams for the class of planar linear flows investigated in chapter 2, and that have closed orbits in the Stokes limit. The two-phase envelope is the largest in extent for simple shear flow, and rapidly diminishes in extent on either side (that is with increase in extension or vorticity). In section 3.4.3, we return to the case of simple shear flow and analyze the time-dependent orientation distribution for different initial conditions, and show that the finite-time evolution in the two-phase envelope is characterized by a pronounced hysteresis, leading to the suspension viscosity being sensitively dependent on the precise shear history. We summarize our findings in section 3.5, where we also argue that the tumbling-spinning hysteresis characterized here should be observable in more general circumstances.

3.2 Formulation for the viscosity

In this section, we formulate the integral for estimating the shear viscosity of a dilute suspension of neutrally buoyant spheroidal particles. The contribution of the particulate phase to the averaged suspension stress may be written as $\langle \sigma^p_{ij} \rangle = n\langle S_{ij} \rangle$ where, in the dilute limit, the stresslet, S_{ij}, is that associated with an isolated torque-free spheroid immersed in an ambient simple shear flow. Note that the stress above is due to hydrodynamics alone. The Brownian stress is negligible in the nearly athermal limit of interest. This stresslet is a function of the instantaneous spheroid orientation $\boldsymbol{p}$, and the angled brackets therefore denote an average over the relevant orientation probability density. Thus, $\langle S_{ij} \rangle$ is given by:

$$\langle S_{ij} \rangle = \int \Omega(\boldsymbol{p}) d\boldsymbol{p} \int_{S_p} \frac{1}{2}[\sigma_{ik} x_j n_k + \sigma_{jk} x_i n_k - \frac{2}{3}\delta_{ij}(\sigma_{lk} x_l n_k)] dA, \tag{3.1}$$

where S_p denotes the surface of the spheroid, and $\Omega(\boldsymbol{p})$ is the orientation distribution of an isolated spheroid in an ambient simple shear flow. For finite $Re \, (= St)$, as originally shown by (Batchelor (1970*b*)), the suspension stress contains additional terms involving both the particle phase acceleration and the fluid phase velocity fluctuations, and these have been shown to lead to a non-Newtonian rheology, even for suspensions of spherical inclusions (Lin *et al.* (1970*a*),Subramanian *et al.* (2011)). However, these effects scale with Re, and become vanishingly small for $Re \to 0$. Thus, for small but finite Re, the dominant effect of inertia is an indirect one in terms of determining the steady state orientation probability density (and thereby, the shear viscosity). In the Stokes limit, as noted in chapter 2, a spheroid continues to rotate in a Jeffery orbit corresponding to its initial orientation. As a result, $\Omega(\boldsymbol{p})$ and therefore the particle contribution to the stress given in (3.1), depends on the initial orientation distribution of the spheroid. As seen in chapter 2, weak inertial effects lead to a drift which stabilizes a unique orbit for spheroids of aspect ratio larger than 0.137. The steady-state orientation distribution corresponding to this unique orbit is set up on an asymptotically long time scale which is given by $O(Re^{-1})$. For oblate spheroids with aspect ratio smaller than 0.137, the drift stabilizes either the spinning orbit or the tumbling orbit, depending on the initial orientation. As mentioned in section 3.1, we need an additional orientational decorrelation mechanism in this case to make the steady state distribution unique. We consider rotary Brownian motion as a canonical example of the decorrelation mechanism, and Brownian motion together with the inertial drift result in a unique steady state orientation distribution for the spheroid. This unique steady state distribution is set up on an exponentially long time scale ($\propto \exp[RePe_r]$).

The instantaneous stresslet in (3.1) is a function of $\boldsymbol{p}$ and may be written down from symmetry arguments as:

$$\begin{aligned} S_{ij}(\boldsymbol{p}) = \frac{3}{2} D_1^{(p/o)}(\xi_0)(E_{kl}p_k p_l)(p_i p_j - \frac{1}{3}\delta_{ij}) + D_2^{(p/o)}(\xi_0)[(\delta_{ik} - p_i p_k)E_{kl}p_l p_j + (\delta_{jk} - p_j p_k) \\ E_{kl}p_l p_i] + D_3^{(p/o)}(\xi_0)[(\delta_{ik} - p_i p_k)E_{kl}(\delta_{jl} - p_l p_j) + \frac{1}{2}(E_{kl}p_k p_l)(\delta_{ij} - p_i p_j)], \end{aligned} \tag{3.2}$$

where the coefficients $D_1^{(p/o)}$, $D_2^{(p/o)}$ and $D_3^{(p/o)}$, respectively, denote the aspect-ratio-dependent strength of the stresslet singularities (recall that ξ_0 is the inverse of eccentricity of the spheroid and $\boldsymbol{E}$ is the rate of strain tensor of the simple shear flow) corresponding to the component flows (axisymmetric, longitudinal and transverse planar extensions, see section 2.3) that make up the ambient simple shear in the body-fixed reference frame (XYZ in figure 2.2) for prolate (p) and oblate (o) spheroids. The number of coefficients (three) is fewer than the number of component flows (five), since the axisymmetry of the spheroid implies identical responses to the two longitudinal ($\boldsymbol{u}_{4s}$ and $\boldsymbol{u}_{5s}$) and transverse planar extensional flows ($\boldsymbol{u}_{2s}$ and $\boldsymbol{u}_{3s}$), which combine to give the terms proportional to D_2 and D_3, respectively, in (3.2). For the limiting case of a sphere, $D_1^{(p/o)} = D_2^{(p/o)} = D_3^{(p/o)} = \frac{20\pi}{3}$, and (3.2) takes the familiar form $S_{ij} = \frac{20\pi}{3}E_{ij}$ which yields the Einstein coefficient. From Kim & Karrila (1991), the expressions for the coefficients, translated to our notation, are given by:

$$D_1^{(p)}(\xi_0) = \frac{16\pi}{9\xi_0^3[(3\xi_0^2 - 1)\coth^{-1}\xi_0 - 3\xi_0]}, \tag{3.3}$$

$$D_2^{(p)}(\xi_0) = \frac{16\pi\bar{\xi}_0^2}{[3\xi_0^2(1 - 2\xi_0^2)(2 - 3\xi_0^2 + 3\xi_0\xi_0^2\coth^{-1}\xi_0)]}, \tag{3.4}$$

$$D_3^{(p)}(\xi_0) = \frac{32\pi\bar{\xi}_0^2}{3\xi_0^3(5\xi_0 - 3\xi_0^3 + 3\xi_0^4\coth^{-1}\xi_0)}, \tag{3.5}$$

$$\tag{3.6}$$

$$D_1^{(o)}(\xi_0) = \frac{16\pi}{9\xi_0^3[(3\xi_0^2-2)\cot^{-1}\xi_0 - 3\xi_0]}, \tag{3.7}$$

$$D_2^{(o)}(\xi_0) = \frac{16\pi\bar{\xi}_0}{[3\xi_0(1-2\xi_0^2)(1-3\xi_0^2+3\xi_0^2\xi_0\cot^{-1}\xi_0)]}, \tag{3.8}$$

$$D_3^{(o)}(\xi_0) = \frac{32\pi}{3\xi_0(-(2+3\xi_0^2)\xi_0+3\xi_0^4\cot^{-1}\xi_0)}. \tag{3.9}$$

The above expressions may also be obtained from the far-field limit (for $\xi \to \infty$) of each of the component velocity fields ($\boldsymbol{u}_{1s} - \boldsymbol{u}_{5s}$), of the form $\frac{(\boldsymbol{E}_i:\boldsymbol{xx})\boldsymbol{x}}{r^5}$, $\boldsymbol{E}_i$ ($i = 1-5$) being the component rate-of-strain tensor (see section 2.3), with the constant of proportionality, a function of ξ_0, giving the ξ_0-dependent stresslet coefficient.

The excess stress in a dilute suspension is therefore given by:

$$\boldsymbol{\sigma}^p = nE_{kl}\int\Bigg\{\frac{3D_1^{(p/o)}(\xi_0)}{2}p_kp_l(p_ip_j-\frac{1}{3}\delta_{ij})+D_2^{(p/o)}(\xi_0)[(\delta_{ik}-p_ip_k)p_lp_j+(\delta_{jk}-p_jp_k)p_lp_i]$$
$$+D_3^{(p/o)}(\xi_0)[(\delta_{ik}-p_ip_k)(\delta_{jl}-p_lp_j)+\frac{1}{2}p_kp_l(\delta_{ij}-p_ip_j)]\Bigg\}\Omega(\boldsymbol{p})d\boldsymbol{p}. \tag{3.10}$$

The orientation distribution $\Omega(\boldsymbol{p})$ needed in (3.10) is governed by the convection-diffusion equation given by:

$$\frac{\partial\Omega}{\partial t} + \boldsymbol{\nabla}_{\boldsymbol{p}}.[(\dot{\boldsymbol{p}}_{jeff} + Re\,\dot{\boldsymbol{p}}_i)\Omega] = \frac{1}{Pe_r}\nabla^2_{\boldsymbol{p}}\Omega, \tag{3.11}$$

where $\dot{\boldsymbol{p}}_{jeff}$ and $\dot{\boldsymbol{p}}_i$ are respectively, the rate of change of orientation vector due to the angular velocity at the leading order given in (2.29 and 2.30) and that due to the inertial correction to the angular velocity given in (2.77,2.78,2.93 & 2.94). The term on the right-hand side above is the diffusion in the orientation space due to rotary Brownian motion. In both the non-Brownian case (spheroids with $\kappa > 0.137$) this term is zero. In the Brownian(spheroids with $\kappa < 0.137$) and the non-Brownian cases, it will be seen in the next two sections that $\Omega(\boldsymbol{p})$ can be written in a separable form $\Omega(\boldsymbol{p})$=$f(C)g(C,\tau)$, where $f(C)$ and $g(C,\tau)$ are the distributions across and along the Jeffery orbits respectively. The distribution across the orbits in the non-Brownian case can be determined by weak inertial effects alone and is a delta function peaked either at $C = 0$ or $C = \infty$. The distribution across the orbit is set up by inertia together with rotary Brownian motion in the Brownian case. While solving (3.11), an assumption is made that there is an aspect ratio polydispersity in the suspension (as is always the case in experiments), and it will be shown that the distribution along the orbit $g(C,\tau)$ is set up by the polydispersity on shorter time scales. In sections 3.3 and 3.4, (3.11) is solved in the asymptotic regime where the time scales governing the orientation distribution along and across orbits is well separated. The solutions are used to evaluate (3.10) for the non-Brownian and the Brownian cases, respectively.

3.3 Rheology non-Brownian case

3.3.1 Derivation of orientation distribution

In this section, we derive the orientation distribution $\Omega(\boldsymbol{p})$ set up by the inertial drift required to evaluate the integral in (3.10) for the non-Brownian case. The orientation distribution set up by the inertial drift alone, is relevant for prolate spheroids of any aspect ratio and oblate spheroids, whose aspect ratio is larger than 0.137. In the absence of Brownian motion, (3.11) can be rewritten as:

$$\frac{\partial \Omega}{\partial t} + \boldsymbol{\nabla_p}.(\dot{\boldsymbol{p}}_{jeff}\Omega) = -Re\boldsymbol{\nabla_p}.(\dot{\boldsymbol{p}}_i\Omega). \tag{3.12}$$

There are two time scales in the problem; the first of $O(\dot{\gamma}^{-1})$ corresponds to the Stokesian convection due to the imposed shear and the second corresponds to the slower drift due to fluid inertia, and is of $O(\dot{\gamma}^{-1}Re^{-1})$. For $Re << 1$, the solution of (3.12) is obtained using a multiple scales analysis. Defining the non-dimensional fast and slow time scales as t_1 and t_2 respectively, with $t_1 = t$ and $t_2 = Ret$, and writing $\Omega = \Omega_0(C,\tau,t_1,t_2) + Re\Omega_1(C,\tau,t_1,t_2)$, (3.12) takes the form:

$$\frac{\partial \Omega_0}{\partial t_1} + \boldsymbol{\nabla_p}.[\dot{\boldsymbol{p}}_{jeff}\Omega_0] = 0, \tag{3.13}$$

at leading order, and

$$\frac{\partial \Omega_1}{\partial t_1} + \boldsymbol{\nabla_p}.[\dot{\boldsymbol{p}}_{jeff}\Omega_1] = -\boldsymbol{\nabla_p}.[\dot{\boldsymbol{p}}_i\Omega_0] - \frac{\partial \Omega_0}{\partial t_2}, \tag{3.14}$$

at $O(Re)$. The $O(Re)$ term in the expansion for Ω is the direct effect of inertia which is, of course, small. The $O(1)$ term is the indirect effect, via the alteration of the orbit constant distribution at leading order, for long times.

The rate of change of orientation $\dot{\boldsymbol{p}}_{jeff}$ in (3.13) takes the form $\frac{h_\tau}{\kappa+1/\kappa}\hat{\boldsymbol{\tau}}$ in the (C,τ) orbital coordinate system. Here, h_τ is the metric factor for the τ coordinate, and $\hat{\boldsymbol{\tau}}$ is the unit vector in the τ direction in the orbital coordinate system (see Appendix B). The divergence operator in the (C,τ) orbital coordinate system given in (B.6) is used to simplify (3.13) which gives:

$$\frac{\partial \Omega_0}{\partial t_1} + \frac{1}{h_C h_\tau \sin\alpha}\frac{\partial}{\partial \tau}\left(\frac{\Omega_0 h_c h_\tau \sin\alpha}{\kappa + 1/\kappa}\right) = 0, \tag{3.15}$$

The first-order hyperbolic equation above admits an infinite number of solutions, each corresponding to a particular initial orientation distribution, and with all of them, except one, being time dependent. However, as is shown below, if there is a tiny polydispersity in the particle aspect ratios (as is invariably the case in experiments) all the time dependent solutions approach the steady one at an exponential rate on a time scale inversely proportional to the polydispersity. To see this, we assume that the probability density for the spheroid aspect ratios is given by $h(\kappa;\bar{\kappa},\sigma)$, with mean $\bar{\kappa}$ and standard deviation σ. The assumption of a tiny polydispersity implies that the variance of $h(\kappa;\bar{\kappa},\sigma)$ given by $\sigma^2 = \int(\kappa-\bar{\kappa})^2 h(\kappa;\bar{\kappa},\sigma)d\kappa$ satisfies $\sigma^2 << \bar{\kappa}^2$. Defining $f_1 = \Omega_0 h_c h_\tau \sin\alpha$, (3.15) can be rewritten as:

$$\frac{\partial f_1}{\partial t} + \left(\frac{\kappa}{\kappa^2+1}\right)\frac{\partial f_1}{\partial \tau} = 0. \tag{3.16}$$

Note that κ in the above equation is a random variable and therefore f_1, which is the probability density for spheroids of a given aspect ratio κ, is also a random variable. Defining a new variable $\tau_0 = \tau - \frac{\bar{\kappa}}{\bar{\kappa}^2+1}t_1$, where τ_0 denotes the (fictitious) initial phase calculated from the current phase (of a spheroid of aspect ratio κ) using the Jeffery angular velocity of the spheroid of mean aspect ratio. Rewriting (3.16) in terms of τ_0 leads to:

$$\frac{\partial f_1}{\partial t_1} + \left(\frac{\kappa}{\kappa^2+1} - \frac{\bar{\kappa}}{\bar{\kappa}^2+1}\right)\frac{\partial f_1}{\partial \tau_0} = 0. \tag{3.17}$$

The solution to the equation above is given by $f_1 = g(C,\tau_0 - \left(\frac{\kappa}{\kappa^2+1} - \frac{\bar{\kappa}}{\bar{\kappa}^2+1}\right)t_1) = g(C,\tau_1 + \frac{\bar{\kappa}}{\bar{\kappa}^2+1}t_1)$, where $\tau_1 = \tau_0 - \left(\frac{\kappa}{\kappa^2+1}\right)t_1$ and the function g is specified by the initial condition. For $\kappa = \bar{\kappa}$, the equation reduces to $\frac{\partial f_1}{\partial t_1} = 0$, and the solution is therefore $f_1 = g(C,\tau_0)$; that is if the initial distribution $h(\kappa;\bar{\kappa},\sigma) = \delta(\bar{\kappa})$, then the solution for f_1 merely reflects the fact that the initial distribution of both orbit constants C and phase angles τ_0 is preserved for all times. However when $h(\kappa;\bar{\kappa},\sigma)$ is not a δ function, the initial distribution is not preserved and the measurable distribution would then be the average of f_1 which is defined as:

$$\bar{f_1} = \int f_1 h(\kappa;\bar{\kappa},\sigma)d\kappa. \tag{3.18}$$

The average of (3.17) gives the governing equation for $\bar{f_1}$:

$$\int \frac{\partial f_1}{\partial t_1} h(\kappa;\bar{\kappa},\sigma)dk + \int \left(\frac{\kappa}{\kappa^2+1} - \frac{\bar{\kappa}}{\bar{\kappa}^2+1}\right)\frac{\partial f_1}{\partial \tau_0} h(\kappa;\bar{\kappa},\sigma)dk = 0. \tag{3.19}$$

In the analysis that follows, we will show that $\bar{f_1}$, at long times, converges to a time-independent distribution. The first term on the left-hand side of (3.19) is $\frac{\partial \bar{f_1}}{\partial t_1}$. Expanding the bracketed term on the left-hand side of (3.19) about $\kappa = \bar{\kappa}$ and defining $A = \frac{(1-\bar{\kappa}^2)}{(1+\bar{\kappa}^2)^2}$ and $B = \frac{\bar{\kappa}^3-3\bar{\kappa}}{(1+\bar{\kappa}^2)^3}$ the second integral in (3.19) becomes:

$$\int_0^1 \left(\frac{\kappa}{\kappa^2+1} - \frac{\bar{\kappa}}{\bar{\kappa}^2+1}\right)\frac{\partial f_1}{\partial \tau_0} h(\kappa;\bar{\kappa},\sigma)dk = \int_0^1 \left(A(\kappa-\bar{\kappa}) + B(\kappa-\bar{\kappa})^2\right) \left(\left.\frac{\partial f_1}{\partial \tau_0}\right|_{\kappa=\bar{\kappa}} + (\kappa-\bar{\kappa})\frac{\partial}{\partial \kappa}\left(\frac{\partial f_1}{\partial \tau_0}\right)\Bigg|_{\kappa=\bar{\kappa}}\right) h(\kappa;\bar{\kappa},\sigma)dk. \tag{3.20}$$

The solution of (3.17) shows that f_1 is an explicit function of τ_1. Therefore $\frac{\partial f_1}{\partial \tau_0}$ is an explicit function of τ_1. $\frac{\partial}{\partial \kappa}$ can be transformed to $\frac{\partial}{\partial \tau_0}$ as:

$$\frac{\partial}{\partial \kappa} = \frac{\partial \tau_1}{\partial \kappa}\frac{\partial}{\partial \tau_1} = \frac{\kappa^2-1}{(1+\kappa^2)^2}t_1\frac{\partial}{\partial \tau_1} = \frac{\kappa^2-1}{(1+\kappa^2)^2}t_1\frac{\partial}{\partial \tau_0}. \tag{3.21}$$

Substituting (3.21) in the rhs of (3.20) one obtains:

$$\int_0^1 \left(\frac{\kappa}{\kappa^2+1} - \frac{\bar{\kappa}}{\bar{\kappa}^2+1}\right)\frac{\partial f_1}{\partial \tau_0} h(\kappa;\bar{\kappa},\sigma)dk = \int_0^1 \left(A(\kappa-\bar{\kappa}) + B(\kappa-\bar{\kappa})^2\right) \left(\left.\frac{\partial f_1}{\partial \tau_0}\right|_{\kappa=\bar{\kappa}} - At_1(\kappa-\bar{\kappa})\frac{\partial}{\partial \tau_0}\left(\frac{\partial f_1}{\partial \tau_0}\right)\Bigg|_{\kappa=\bar{\kappa}}\right) h(\kappa;\bar{\kappa},\sigma)dk, \tag{3.22}$$

where we have replaced κ by $\bar{\kappa}$ in the relevant terms to the required order of approximation. Using $\sigma^2 = \int_0^1 (\kappa-\bar{\kappa})^2 h(\kappa;\bar{\kappa},\sigma)dk$ and neglecting higher order corrections, (3.22) becomes:

$$\int_0^1 \left(\frac{\kappa}{\kappa^2+1} - \frac{\bar{\kappa}}{\bar{\kappa}^2+1}\right)\frac{\partial f_1}{\partial \tau_0} h(\kappa;\bar{\kappa},\sigma)dk = \left(-A^2 t_1 \sigma^2 \frac{\partial}{\partial \tau_0}\left(\frac{\partial f_1}{\partial \tau_0}\right)\Bigg|_{\kappa=\bar{\kappa}} + B\sigma^2 \left.\frac{\partial f_1}{\partial \tau_0}\right|_{\kappa=\bar{\kappa}}\right). \tag{3.23}$$

To O(σ^2), the derivatives in (3.23) may be replaced by the corresponding derivatives of $\bar{f_1}$, and one obtains the following equation for $\bar{f_1}$:

$$\frac{\partial \bar{f_1}}{\partial t_1} + B\sigma^2\frac{\partial \bar{f_1}}{\partial \tau_0} = A^2 t_1 \sigma^2 \frac{\partial}{\partial \tau_0}\left(\frac{\partial \bar{f_1}}{\partial \tau_0}\right). \tag{3.24}$$

Defining a new variable $\hat{\tau}_0$ = τ_0 - $B\sigma^2 t_1$, the equation above can be written as

$$\frac{\partial \bar{f_1}}{\partial t_1} = A^2 t_1 \sigma^2 \frac{\partial}{\partial \hat{\tau}_0}\left(\frac{\partial \bar{f_1}}{\partial \hat{\tau}_0}\right) \tag{3.25}$$

$$\Longrightarrow \frac{\partial \bar{f_1}}{\partial t_1^2} = D\frac{\partial}{\partial \hat{\tau}_0}\left(\frac{\partial \bar{f_1}}{\partial \hat{\tau}_0}\right). \tag{3.26}$$

The governing equation for $\bar{f_1}$ is a one-dimensional diffusion equation in a finite domain with the diffusion constant $D = A^2\sigma^2/2 = \frac{(1-\bar{\kappa}^2)^2}{(1+\bar{\kappa}^2)^4}\sigma^2/2$. The normalization condition on $\bar{\Omega}_0$, which is given by $\int \bar{\Omega}_0 \, h_C h_\tau \sin\alpha \, dC d\tau{=}1$, results in the following restriction on $\bar{f_1}$:

$$\int_0^\infty \int_0^{2\pi} \bar{f_1} dC d\tau = 1. \tag{3.27}$$

The no-flux condition leads to:

$$\frac{\partial \bar{f_1}}{\partial C} = 0 \;\; \text{at } C{=}0 \text{ and } \infty. \tag{3.28}$$

The solution for (3.26) can be found in terms of an eigenfunction expansion using separation of variables:

$$\bar{f_1} = \sum_{n=0}^{\infty} e^{-n^2 D t_1^2} (A_n \cos n\hat{\tau}_0 + B_n \sin n\hat{\tau}_0). \tag{3.29}$$

Applying the boundary and the normalisation condtion one gets

$$\int_0^\infty A_0 dC = \frac{1}{2\pi} \tag{3.30}$$

and

$$\frac{\partial A_0}{\partial C} = 0 \;\; \text{at } C{=}0 \text{ and } \infty. \tag{3.31}$$

The $n = 0$ term in the summation in (3.29), together with (3.30) and (3.31) gives the time-independent solution to (3.13) as:

$$\bar{\Omega}_0 = \frac{A_0}{h_C h_\tau \sin\alpha}. \tag{3.32}$$

In (3.32), A_0 is a function of C alone and therefore captures the orientation distribution across the Jeffery orbits. The term $h_C h_\tau \sin\alpha dC d\tau$ is the differential area element in the $C-\tau$ co-ordinate system, and ensures that $\bar{\Omega}_0$ satisfies the normalization condition above. The above expression for $\bar{\Omega}_0$ clearly shows that the polydispersity stabilizes a unique time independent distribution along the orbit, and the distribution is precisely the inverse of the Jeffery angular velocity.

It is clear from (3.32) that $\bar{\Omega}_0$ is of the form $f(C)g(C,\tau)$, where $f(C)$ is the distribution across orbits and $g(C,\tau)$ is the distribution along the orbit, with $f(C) = A_0$ and $g(C,\tau) = \frac{1}{h_C h_\tau \sin\alpha}$. If there were no inertia, $f(C)$ would be determined by the initial condition. The long-time orientation orbit stabilized by inertia, for a neutrally buoyant prolate spheroid is the tumbling orbit, and therefore $f(C)$ takes the form $\frac{\delta(1/C)}{2\pi}$ in the $C-\tau$ orbital coordinate system. For a neutrally buoyant oblate spheroid, whose aspect ratio is larger than 0.137, the long-time orientation orbit stabilized by inertia is the spinning orbit, and $f(C)$ takes the form $\frac{\delta(C)}{2\pi}$ in the orbital coordinate system. In terms of the polar and azimuthal angles, $\bar{\Omega}_0$ then takes form:

$$\bar{\Omega}_0(\boldsymbol{p}) = \frac{\kappa\delta(\theta_j - \frac{\pi}{2})}{2\pi\sin\theta_j\left(\kappa^2\sin^2\phi_j + \cos^2\phi_j\right)}, \tag{3.33}$$

for the tumbling spheroid, and

$$\bar{\Omega}_0(\boldsymbol{p}) = \frac{\delta(\theta_j)}{2\pi\sin\theta_j}, \tag{3.34}$$

for the spinning spheroid. Note that the above expressions are written in the spherical coordinate system using the relations given in appendix B.

For oblate spheroids of aspect ratio less than 0.137, inclusion of weak inertial effects does make the functional form of the steady-state orientation distribution determinate, which is given by a couple of delta functions peaked at $\theta_j = 0$ and $\theta_j = \pi/2$. However, in a suspension of such spheroids, the ratio of the amplitudes of these delta functions is determined by the initial distribution of spheroids in the suspension, and the orientation distribution of the spheroids in the suspension is given by:

$$\bar{\Omega}_0(\boldsymbol{p}) = \frac{\mathscr{A}_1(C^*)\delta(\theta_j)}{2\pi\sin\theta_j} + \frac{\kappa[\mathscr{A}_2(C^*)\delta(\theta_j - \frac{\pi}{2})]}{2\pi\sin\theta_j\left(\kappa^2\cos^2\phi_j + \sin^2\phi_j\right)}, \tag{3.35}$$

where the constants $\mathscr{A}_1$ and $\mathscr{A}_2$, in addition to depending on C^* (and thereby on the aspect ratio), are functions of the initial orientation distribution. This dependence arises because the relative proportions of oblate spheroids asymptoting to the tumbling and spinning modes depend on the number of particles located on the either side of the repeller (the Jeffery orbit with $C = C^*(\xi_0)$, see figure 2.15) on the unit sphere at the initial instant. Thus, for non-Brownian neutrally buoyant oblate spheroids in the range of aspect ratios $(0, 0.137)$, the inertial suspension rheology, at leading order, still depends on the initial state of the dilute suspension. Using the orientation distribution given in (3.33) (3.34) and (3.35), we calculate the viscosity of a dilute suspension of spheroids in the presence of inertia, in the next section.

3.3.2 Rheology of non-Brownian suspensions of inertial spheroids

In this section, the viscosity of a dilute suspension of spheroids in the presence of inertia alone is calculated by evaluating the integral in (3.10), using the distributions derived in (3.33) (3.34) and (3.35). For a dilute suspension of prolate spheroids, the distribution given in (3.33) is substituted in (3.10), with $\boldsymbol{p} = \cos\phi_j \mathbf{1}'_x + \sin\phi_j \mathbf{1}'_y$ (primed unit vectors are defined in the space-fixed coordinate system see figure 2.2), to obtain the particle contribution to the stress, which is given by:

$$\langle \sigma^p_{ij} \rangle = n \left[D_2^{(p)}(\xi_0) + \left(\frac{3}{2} D_1^{(p)}(\xi_0) - 2D_2^{(p)}(\xi_0) + \frac{D_3^{(p)}(\xi_0)}{2} \right) \frac{\xi_0 \bar{\xi}_0}{(\xi_0 + \bar{\xi}_0)^2} + \right] E_{ij}. \qquad (3.36)$$

The rheology is evidently Newtonian. In terms of an effective viscosity μ_{eff}, we have from (3.36) that $(\mu_{eff} - \mu)/[(nL^3)\mu] = \frac{1}{2}(D_2^{(p)}(\xi_0) + (\frac{3}{2}D_1^{(p)}(\xi_0) - 2D_2^{(p)}(\xi_0) + \frac{D_3^{(p)}(\xi_0)}{2})\frac{\xi_0 \bar{\xi}_0}{(\xi_0 + \bar{\xi}_0)^2})$ for a suspension of prolate spheroids at small but finite *Re*. The left-hand-side plot in figure 3.1 shows this intrinsic viscosity coefficient as a function of the spheroid eccentricity. It is seen to vary from a value corresponding to the Einstein coefficient (the value near 10 comes from the factor $4\pi/3$ involved in the spherical volume fraction) for a near-sphere to a vanishingly small contribution for a slender spheroid. This happens due to a change in the scaling of $(\mu_{eff} - \mu)/\mu$ from $O(nL^3)$ in the near-sphere limit to $O(nL^2 b)/\ln\kappa$ in the slender fiber limit; from (3.36), $\lim_{\xi_0 \to \infty}(\mu_{eff} - \mu)/\mu = \frac{10\pi}{3} nL^3$ and $\lim_{\xi_0 \to 1}(\mu_{eff} - \mu)/\mu = \frac{2\pi}{3\ln\kappa} nL^2 b$. For large aspect ratios ($\kappa \to \infty$), the dominant contribution to the averaged stresslet is from non-aligned fibers with the probability of such orientations only being $O(\kappa^{-1})$. From viscous slender body theory, the stresslet for a non-aligned fiber arises from a linear force density of $O[\mu\dot{\gamma}L/\ln\kappa]$ acting with a moment arm of $O(L)$ over the length of the spheroid, and is $O[\mu\dot{\gamma}L^3/\ln\kappa]$. The resulting (dimensional) stress is $O(n).O(\kappa^{-1}).O[\mu\dot{\gamma}L^3/\ln\kappa]$, leading to an effective viscosity $(\mu_{eff} - \mu)/\mu$ of $O[nL^2 b/\ln\kappa]$. The stresslet for flow-aligned fibers is smaller than the non-aligned contribution by $O(\kappa^{-2}\ln\kappa)$, and only contributes to a small correction of $O(nLb^2)$ to the above estimate. The right-hand side plot in figure 3.1 uses the slender fiber scaling above to obtain a finite viscosity coefficient in the slender fiber limit; note that the near-sphere asymptote is zero in these units owing to the additional logarithmic factor involved. The scaling of the intrinsic viscosity with aspect ratio, in the slender fiber limit, is controlled by the anisotropy of orientations within a given Jeffery orbit, and thus, Leal and Hinch's (Leal & Hinch (1971)) original calculation, involving the effect of weak Brownian diffusion in setting up a steady smooth distribution across Jeffery orbits, also leads to a viscosity coefficient of $O[nL^2 b/\ln\kappa]$ for large aspect ratios, albeit with a different $O(1)$ coefficient.

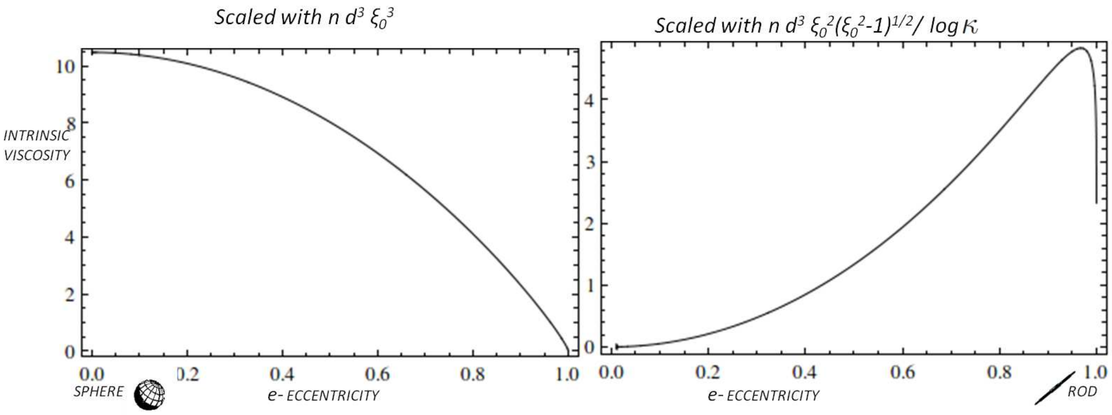

Fig. 3.1 The intrinsic viscosity coefficient as a function of eccentricity for a dilute suspension of neutrally buoyant prolate spheroids.

For oblate spheroids with aspect ratios greater than 0.137, $\boldsymbol{p} = \mathbf{1}'_z$, and only the two transverse planar extensions in (2.34) contribute to the rheology. Using (3.34), (3.10) reduces to:

$$\langle \sigma^p_{ij} \rangle = n D^{(o)}_3(\xi_0) E_{ij} \qquad 1.01 < \xi_0 < \infty, \tag{3.37}$$

For oblate spheroids with aspect ratios smaller than 0.137, (3.35) is substituted in (3.10) to obtain:

$$\langle \sigma^p_{ij} \rangle = n \Bigg[D^{(o)}_3(\xi_0)\,\mathscr{A}_1 + \left(D^{(o)}_2(\xi_0) + \left(\frac{3}{2} D^{(o)}_1(\xi_0) - 2D^{(o)}_2(\xi_0) + \frac{D^{(o)}_3(\xi_0)}{2} \right) \frac{\xi_0\, \bar{\xi}_0}{(\xi_0 + \bar{\xi}_0)^2} \right) \\ (1 - \mathscr{A}_1) \Bigg] E_{ij} \qquad 1 < \xi_0 < 1.01. \tag{3.38}$$

The area within a Jeffery orbit, with an orbit constant C, is given by $2\pi - 4\kappa(1+C^2)^{-\frac{1}{2}}\Pi[1-\kappa^2, -\frac{C^2(\kappa^2-1)}{1+C^2}]$, and normalizing by the area of the unit hemisphere, one obtains $\mathscr{A}_1 = 1 - \frac{2\kappa}{\pi}(1+C^2)^{-\frac{1}{2}}\Pi[1-\kappa^2, -\frac{C^2(\kappa^2-1)}{1+C^2}]$ and $\mathscr{A}_2 = 1 - \mathscr{A}_1$ for an initially isotropic orientation distribution, $\Pi(x,y)$ being the complete elliptic function of the third kind (Gradshteyn & Ryzhik (2007)). The intrinsic viscosity coefficient, $(\mu_{eff} - \mu)/[(nL^3)\mu]$ for a suspension of oblate spheroids, over the entire range of eccentricities, is plotted on the left in figure 3.2. There is a kink (a discontinuity in slope) in the curve at $e \approx 0.99$ due to the oblate spheroids transitioning from a pure spinning mode to a weighted combination of spinning and tumbling modes. The part of the viscosity curve for $e > 0.9905$ (aspect ratios smaller than 0.137) is plotted as a discrete sequence of points because the relative proportions of spinning and tumbling spheroids in this range of aspect ratios is a function of the repeller location C^*, and this is found numerically from the zero-crossing in a plot of ΔC against $C/(C+1)$ for a particular aspect ratio (similar to figure 2.13). The right-hand side plot shows a magnified view of the aforementioned kink. Here, the curve corresponding to the pure spinning mode is continued until $e=1$ to emphasize the transition from spinning oblate spheroids, of aspect ratio 0.137, at $e=0.9905$, to tumbling flat disks at $e=1$. Note that the spinning-mode curve would terminate in a finite coefficient at $e=1$, since the viscosity coefficient for spinning disks is $O(nL^3)$ as for spheres. The bifurcation at $e=0.9905$, however, implies that the viscosity coefficient at $e=1$, arises almost entirely from tumbling flat disks, and is asymptotically smaller than $O(nL^3)$. The appropriate scale in the flat-disk limit may be obtained by noting that the averaged stresslet arises from the combination of an $O(\mu\dot{\gamma}L^3)$ stresslet associated with an $O(\kappa)$ fraction of spinning disks, and a comparable $O(\mu\dot{\gamma}bL^2)$ stresslet associated with disks that tumble in the flow-gradient plane (unlike the prolate case, both aligned and non-aligned flat disks end up contributing, at the same order, to the tumbling stress component). This leads to an effective viscosity $\mu_{eff}-\mu \sim O(nbL^2)\mu$ in the flat-disk limit. Figure 3.3 plots $(\mu_{eff}-\mu)/[(nbL^2)\mu]$ as a function of the spheroid eccentricity which leads to a finite value in the flat-disk limit; the spinning-mode coefficient diverges as $O(\xi_0-1)^{-\frac{1}{2}}$ with this normalization. The viscosity coefficient for sufficiently thin oblate spheroids is again controlled by the anisotropy of orientations within a given Jeffery orbit, and the effects of weak Brownian motion, although resulting in a different distribution across Jeffery orbits, lead to a similar scale in the flat-disk limit (Leal & Hinch (1971)).

Apart from the kink at $e=0.9905$ discussed above, there are two points worth noting in figure 3.3. The first is that the intrinsic viscosity curve corresponds to a steady state orientation distribution. Within the framework of an orbital drift, the time required to attain such a steady state diverges in the flat-disk limit owing to the diverging Jeffery period; recall that the Jeffery period is $2\pi\frac{\kappa^2+1}{\kappa}$ and is $O(\kappa^{-1})$ for $\kappa \to 0$. Note, however, that the orbital drift interpretation, that assumes the inertial trajectory to be a tightly wound spiral, becomes increasingly restrictive for both large and small aspect ratios (see section 2.8). Notwithstanding this restriction, the viscosity coefficient, plotted for any finite time, will deviate from the steady-state plot for sufficiently thin oblate spheroids, asymptoting to a (frozen-in-time) isotropic orientation distribution at $e=1$. For longer times, this deviation from the steady-state curve will occur at progressively smaller aspect ratios. The second feature is the difference between the value of the intrinsic viscosity coefficient at $e=1$, and that corresponding to a suspension consisting only of tumbling flat disks (indicated by the horizontal dashed line in the right-hand side of the figure). This jump comes from the implicit assumption of an infinite suspension for which

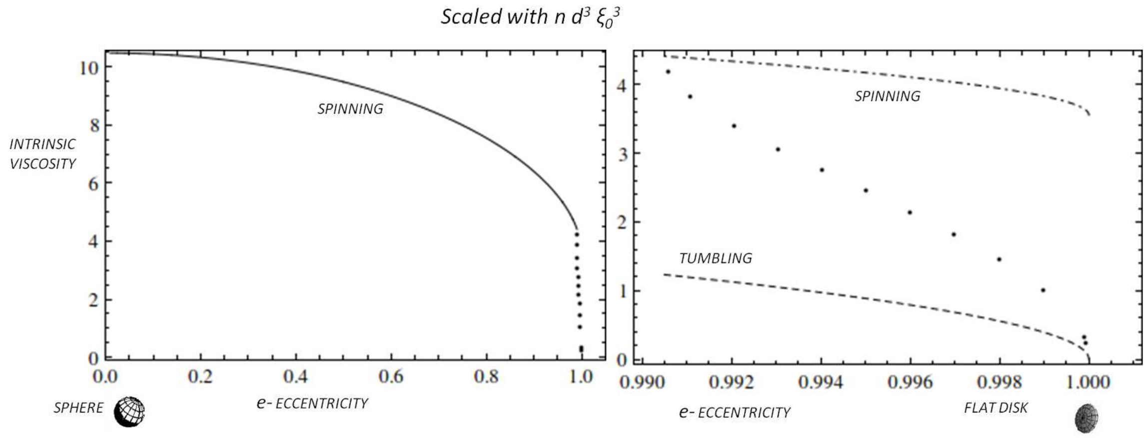

Fig. 3.2 The intrinsic viscosity coefficient as a function of eccentricity for a dilute suspension of neutrally buoyant oblate spheroids. An initial isotropic orientation distribution is assumed while calculating the viscosity for aspect ratios less than the critical aspect ratio (0.137). The dotted line denotes the viscosity coefficient for these viscosity ratios. The plot on the right is a magnified view of the viscosity coefficient transitioning from the spinning to the tumbling asymptote close to the flat-disk limit.

a statistical description, in terms of an orientation probability density, is appropriate. For any finite-sized system, there will be a small enough aspect ratio when the area within the Jeffery repeller, corresponding to $C^* = \sqrt{35}$, is small enough that the number of spheroid orientations in this tiny region of the unit sphere is of order unity, and a probabilistic description is no longer valid. Below such an aspect ratio, the viscosity coefficient will approach the lower value corresponding to the pure tumbling mode (again of $O(nbL^2)$). Said differently, the jump in the viscosity coefficient at $e = 1$ is an artifact of the thermodynamic (infinite system size) limit.

3.4 Rheology- Brownian case

3.4.1 Derivation of orientation distribution

In this section, we derive the orientation distribution $\Omega(\boldsymbol{p})$ which is set up by the combined effect of inertial drift and the rotary Brownian motion. The orientation distribution is relevant for thin oblate spheroids, whose aspect ratio is smaller than 0.137. As in the non-Brownian case, there are two time scales in the problem; the first one due to the Stokesian convection and is of O($\dot{\gamma}^{-1}$) and the second time scale being the inertial time scale and is of O($Re\dot{\gamma}^{-1}$) (the parameter $RePe_r$ is assumed arbitrary, so that Brownian motion, formally, occurs on a time

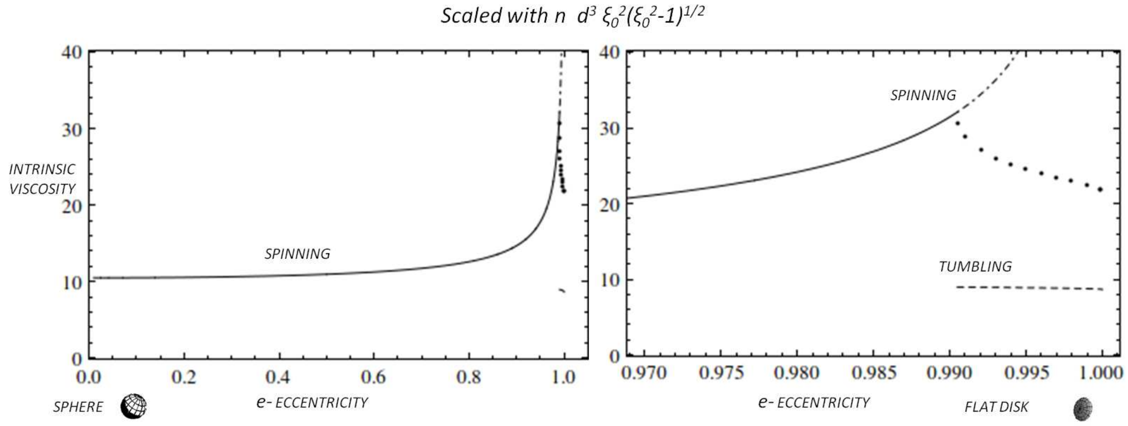

Fig. 3.3 The intrinsic viscosity coefficient as a function of eccentricity for a dilute suspension of neutrally buoyant oblate spheroids presented in figure 3.2, is now appropriately re-scaled in the flat-disk limit.

scale comparable to the inertial drift; as is shown later, the actual time scale might be much larger in the limit $RePe_r >> 1$). The multiple scale analysis proceeds in a similar manner to the non-Brownian case, with the leading order equation same as (3.13), and the equation at O(Re) takes the form:

$$\frac{\partial \Omega_1}{\partial t_1} + \boldsymbol{\nabla}_{\boldsymbol{p}}\cdot[\dot{\boldsymbol{p}}_{jeff}\Omega_1] = \frac{1}{RePe_r}\nabla^2_{\boldsymbol{p}}\Omega_0 - \boldsymbol{\nabla}_{\boldsymbol{p}}\cdot[\dot{\boldsymbol{p}}_i\Omega_0] - \frac{\partial \Omega_0}{\partial t_2}. \tag{3.39}$$

Compared to (3.14), the above equation has an additional term on the right-hand side due to the rotary Brownian motion. Since (3.39) is an inhomogeneous version of (3.13), one needs to find the Green's function of (3.13), to solve (3.39). Recall that after accounting for the effects of phase mixing due to polydispersity, the averaged version of (3.13) is shown to be (3.26), in section 3.3.1, and therefore, solving (3.39) requires the Greens function of (3.26). This Green's function is the solution of:

$$\frac{\partial \overline{f_1}}{\partial t_1^2} - D\frac{\partial}{\partial \hat{\tau}_0}\left(\frac{\partial \overline{f_1}}{\partial \hat{\tau}_0}\right) = \delta(t_1^2 - t_1'^2)\delta(\hat{\tau}_0 - \hat{\tau}_0'). \tag{3.40}$$

The Greens function is given by :

$$G(\hat{\tau}_0 - \hat{\tau}_0', t_1^2 - t_1'^2) = \sum_{n=0}^{\infty} \frac{e^{-n^2 D(t_1^2 - t_1'^2)}}{\pi}\left(\cos n\left(\tau_0 - \tau_0' - B\sigma^2(t_1 - t_1')\right)\right). \tag{3.41}$$

Using the Green's function given above, the solution for $\bar{\Omega}_1$ in (3.39) can be formally written as:

$$\bar{\Omega}_1 = \frac{1}{h_C h_\tau \sin\alpha} \int_0^{t_1^2} dt_1'^2 \int_0^{2\pi} G(\hat{\tau}_0 - \hat{\tau}_0', t_1^2 - t_1'^2) \left\{ \left(\frac{1}{RePe_r} \nabla_{\boldsymbol{p}}^2 \bar{\Omega}_0 - \boldsymbol{\nabla}_{\boldsymbol{p}} \boldsymbol{.} [\dot{\boldsymbol{p}}_i \bar{\Omega}_0] - \frac{\partial \bar{\Omega}_0}{\partial t_2} \right) \right.$$
$$\left. h_C h_\tau \sin\alpha \right\} d\hat{\tau}_0'. \tag{3.42}$$

For times much longer than $1/D^{1/2}$, neglecting exponentially small corrections, one may obtain the leading order estimate of (3.42) by using the time-independent form for $\bar{\Omega}_0$, given in (3.32), and further, retaining only the time-independent terms in the Green's function in (3.42). As result, $\bar{\Omega}_1$, for long times, is given by:

$$\bar{\Omega}_1 = \frac{1}{h_C h_\tau \sin\alpha} t_1^2 \int_0^{2\pi} \frac{1}{\pi} \left\{ \left(\frac{1}{RePe_r} \nabla_{\boldsymbol{p}}^2 \left(\frac{A_0}{h_C h_\tau \sin\alpha} \right) - \boldsymbol{\nabla}_{\boldsymbol{p}} \boldsymbol{.} \left[\dot{\boldsymbol{p}}_i \left(\frac{A_0}{h_C h_\tau \sin\alpha} \right) \right] \right. \right.$$
$$\left. \left. - \frac{\partial}{\partial t_2} \left(\frac{A_0}{h_C h_\tau \sin\alpha} \right) \right) h_C h_\tau \sin\alpha \right\} d\hat{\tau}_0'. \tag{3.43}$$

Clearly, $\bar{\Omega}_1$ grows as O(t_1^2) for long times. In order to avoid this aphysical secular growth, one must have:

$$\int_0^{2\pi} \frac{1}{\pi} \left\{ \left(\frac{1}{RePe_r} \nabla_{\boldsymbol{p}}^2 \left(\frac{A_0}{h_C h_\tau \sin\alpha} \right) - \boldsymbol{\nabla}_{\boldsymbol{p}} \boldsymbol{.} \left[\dot{\boldsymbol{p}}_i \left(\frac{A_0}{h_C h_\tau \sin\alpha} \right) \right] \right. \right.$$
$$\left. \left. - \frac{\partial}{\partial t_2} \left(\frac{A_0}{h_C h_\tau \sin\alpha} \right) \right) h_C h_\tau \sin\alpha \right\} d\hat{\tau}_0' = 0. \tag{3.44}$$

Denoting A_0 as f, the third term in (3.44) becomes:

$$\int_0^{2\pi} -\frac{\partial}{\partial t_2} \left(\frac{f}{h_C h_\tau \sin\alpha} \right) h_C h_\tau \sin\alpha \, d\tau = -2\pi \frac{\partial f}{\partial t_2}. \tag{3.45}$$

Note that in (3.45), we have changed the variable $\hat{\tau}_0'$ to τ using the relation $\hat{\tau}_0'$=τ-$B\sigma^2 t_1$-$\frac{\kappa^2}{\kappa^2+1} t_1$ (see above (3.25)). The fluid inertial correction to the angular velocity is given by $\dot{\boldsymbol{p}}_i = u_{CC} \hat{\boldsymbol{C}} + u_{C\tau} \hat{\boldsymbol{\tau}}$. The component along $\hat{\boldsymbol{C}}$, u_{CC} , is responsible for the drift across Jeffery orbits (proportional to $\frac{dC}{dt}$ given in (2.86)). The divergence operator in (B.6) is then used to simplify the second term in (3.44). Noting that the τ derivative integrates to zero over (0 to

2π), the second term simplifies as:

$$\begin{aligned}\int_0^{2\pi}\left(-\nabla_p\cdot\left(\dot{\boldsymbol{p}}_i\left(\frac{f}{h_C h_\tau \sin\alpha}\right)\right)\right)h_C h_\tau \sin\alpha\, d\tau &= \int_0^{2\pi}\left(-\frac{\partial}{\partial C}\left(h_\tau \sin\alpha\, u_{CC}\left(\frac{f}{h_C h_\tau \sin\alpha}\right)\right)\right)d\tau \\ = \int_0^{2\pi}-\frac{\partial}{\partial C}\left(\frac{u_{CC}}{h_C}f\right)d\tau &= -\frac{\partial}{\partial C}(2\pi\Delta C_i f),\end{aligned} \tag{3.46}$$

where $\Delta C_i = \int_0^{2\pi}\frac{u_{CC}}{2\pi h_C}d\tau$ is given in ($\Delta C_i = \frac{\kappa^2+1}{\kappa}\Delta C$, ΔC is given in (2.90) and (2.117) chapter 2).

The first term in (3.44) is simplified using the Laplacian, derivable from the gradient and divergence operators in section B, and the term reduces to:

$$\begin{aligned}\int_0^{2\pi}\left(\frac{1}{RePe_r}\nabla_p^2\left(\frac{f}{h_C h_\tau \sin\alpha}\right)\right)h_C h_\tau \sin\alpha\, d\tau = \int_0^{2\pi}\frac{1}{RePe_r}\frac{\partial}{\partial C}\left(\left(\frac{1}{h_C \sin^2\alpha}\frac{\partial\left(\frac{f}{h_C h_\tau \sin\alpha}\right)}{\partial C}\right.\right.\\ \left.\left.-\frac{\cot\alpha}{h_\tau \sin\alpha}\frac{\partial\left(\frac{f}{h_C h_\tau \sin\alpha}\right)}{\partial\tau}\right)h_\tau \sin\alpha\right)d\tau = \frac{\pi}{RePe_r}\frac{\partial}{\partial C}\left(\frac{df}{dC}\chi_1 + \frac{f}{C}\chi_2\right),\end{aligned} \tag{3.47}$$

where $\chi_1(C;\kappa) = \left(\frac{\kappa^2+1}{\kappa^2} + C^2\left(\frac{7}{2}+\frac{1}{4\kappa^2}+\frac{\kappa^2}{4}\right) + C^4(\kappa^2+1)\right)$ and $\chi_2 = \left(-\frac{\kappa^2+1}{\kappa^2} + C^2\left(6-\left(\frac{7}{2}+\frac{1}{4\kappa^2}+\frac{\kappa^2}{4}\right)\right) + 2C^4(\kappa^2+1)\right)$. The final equation for the evolution of f, the distribution across Jefferys orbits, can be obtained by substituting (3.45),(3.46) and (3.47) in (3.44) and is given by

$$\frac{\partial f}{\partial t_2} + \frac{\partial}{\partial C}(\Delta C_i f) = \frac{1}{2RePe_r}\frac{\partial}{\partial C}\left(\frac{df}{dC}\chi_1 + \frac{f}{C}\chi_2\right). \tag{3.48}$$

The orientation distribution in the presence of Brownian motion therefore takes the form:

$$\bar{\Omega}_0 = \frac{f(C)}{h_C h_\tau \sin\alpha}, \tag{3.49}$$

where $f(C)$ is governed by (3.48). The steady state solution for $f(C)$ is given by:

$$f_s(C) = N\exp\left[-RePe_r\int^C\left(\frac{\frac{\chi_2}{RePe_r C'} - 2\Delta C_i(C';\kappa)}{\chi_1}\right)dC'\right], \tag{3.50}$$

where N is a normalization constant. To calculate the steady state viscosity in the Brownian case, one would want to substitute (3.49) together with (3.50) in (3.10) and evaluate the integral. This calculation is done in section 3.4.3. It is of interest to note that $f_s(C)$ in (3.50) is a distribution of the Boltzmann form. Thus, $(RePe_r)^{-1}$ in (3.50) is the kT-equivalent, and the function of C multiplying it may be interpreted as an effective potential $U(C;\kappa, RePe_r)$. Inertia and Brownian motion cause any initial Jeffery-orbit distribution to slide down to the potential minima, this tendency being balanced by the $O(RePe_r)^{-1}$ diffusive fluctuations in C due to Brownian motion alone. Before presenting the viscosity estimation for the Brownian case, we will first focus on understanding the nature of the potential in the next section.

3.4.2 Thermodynamic Interpretation: The ‘tumbling-spinning transition’

In this section, we will try to develop an understanding of the potential $U(C;\kappa, RePe_r)$, that governs the steady state distribution given in (3.50), from a thermodynamic point of view. It is evident from the Boltzmann form in (3.50) that $1/RePe_r$ is like the temperature. One can develop a one-one to analogy between the parameters in the potential above; that is C, κ and $RePe_r$, respectively, with specific volume, pressure and temperature which are the parameters in the free energy for a single component system. The steady state distribution peaks at the minima of the potential and these peaks can be interpreted as phases. This is analogous to defining the liquid and gas phases as the minima of the Gibss free energy in the case of a one component system in thermodynamics. Depending on $RePe_r$, the nature of the potential changes with increasing aspect ratio, from a single welled potential peaked closed to tumbling, to a double welled potential, and eventually to a single welled potential peaked close to spinning, and therefore to identify the phases it is important to track the minima of the potential. The loci of the potential extrema in the κ–C plane, for various $RePe_r$, are plotted in figure 3.4a.

In the limit $RePe_r \ll 1$, $Pe_r \gg 1$, when Brownian motion alone controls the distribution across Jeffery orbits, $U(C;\kappa, RePe_r)$ always has a single minimum that moves to progressively larger C’s with decreasing κ. This corresponds to $RePe_r = 0$ curve in figure 3.4a. For the oblate spheroids of interest with $\kappa < 1$, the potential minimum lies in the vicinity of the tumbling mode, and the corresponding $f_s(C)$ was originally derived in Leal & Hinch (1971). The emergence of an inertial drift with increasing $RePe_r$ leads to a broadening of the minimum until, for sufficiently large $RePe_r$, $U(C;\kappa, RePe_r)$ transitions to a double-welled structure below a critical κ, with a pair of minima separated by an intermediate maximum. This transition is due to the bi-directional nature of the inertial drift. The critical κ is a function of $RePe_r$, approaching a maximum of 0.137 in the deterministic limit $(RePe_r \rightarrow \infty)$ with the pair of minima asymptoting to the spinning $(C = 0)$ and tumbling $(C = \infty)$ modes, and the intermediate maximum approaching the κ-dependent repeller in figure (see figure 2.15). Note that at a given $RePe_r$, if the potential at a particular aspect ratio has a double welled structure, then the constant κ line(horizontal) should cross the constant-$RePe_r$ curve at three points in (see figure 3.4a); in other words, the constant $RePe_r$ curve is a multivalued(κ) locus.

For a given multivalued locus in figure 3.4a, a horizontal dashed line is drawn at the κ for which the two potential minima have equal magnitudes, in analogy with thermodynamic tie-lines. The shifting of the deeper minimum of the potential across the tie-line for a particular $RePe_r$ of 70000 is shown in 3.4b. The small-C and large-C minima that the tie line connects may be identified, respectively, with 'spinning' and 'tumbling' phases that co-exist at the particular κ and $RePe_r$. This leads to a phase diagram with a two-phase (tumbling-spinning) envelope that ends in a critical point, $(\kappa, C, RePe_r) \equiv (0.0665, 3.1, 1150)$. The projections of the phase diagram in the $\kappa - C$ and $RePe_r - C$ planes are shown in figures 3.4c and 3.4d, respectively. The constant $RePe_r$ loci in figure 3.4c may be regarded as isotherms, the non-dimensional inverse shear rate squared, $(RePe_r)^{-1}$, being the non-equilibrium temperature equivalent. Tie-lines in both figures replace the intermediate non-monotonic (and, in the one-component case, thermodynamically inaccessible) portion of the isotherms in the range $1150 < RePe_r < \infty$. The phase diagrams in figures 3.4a,c and d arise from a one-dimensional description of the orientation dynamics along the C-coordinate, and for $\kappa \ll 1$, this requires $Pe_r \gg \kappa^{-3}$(Hinch & Leal 1972). Interestingly, the phase diagram in figure 3.4a includes, on one hand, the infinite-temperature isotherm calculated in Leal & Hinch (1971); on the other hand, the two-phase envelope in figure 3.4c is bounded below by the zero-temperature isotherm at $\kappa = 0.0126$. This piecewise linear isotherm is defined by $C = 0, \kappa > 0.0126$; $0 < C < \infty, \kappa = 0.0126$; $C = \infty, \kappa < 0.0126$, and implies a discontinuous transition from a suspension of spinning spheroids to tumbling ones across $\kappa = 0.0126$ in the limit $RePe_r \to \infty$. Thus in the limit of $RePe_r \to \infty$, the distribution across orbits $f_s(C)$, is a delta function peaked at spinning for $\kappa > 0.0126$ and at tumbling for $\kappa < 0.0126$.

The regions where the reduced description loses validity are shown in figures 3.4e and 3.4f (dashed red curves), and occupy only a small fraction of the parameter-plane for small Re. When Pe_r is $O(\kappa^{-3})$ or smaller, Brownian rotations affect the orientation distribution both across and along Jeffery orbits, close to the gradient-vorticity plane, and a reduced description requires first determining the full distribution on the unit sphere.

The tumbling-spinning transition identified above has a striking similarity to the coil-stretch transition of high molecular weight polymers in extension-dominated flows(De Gennes 1974;

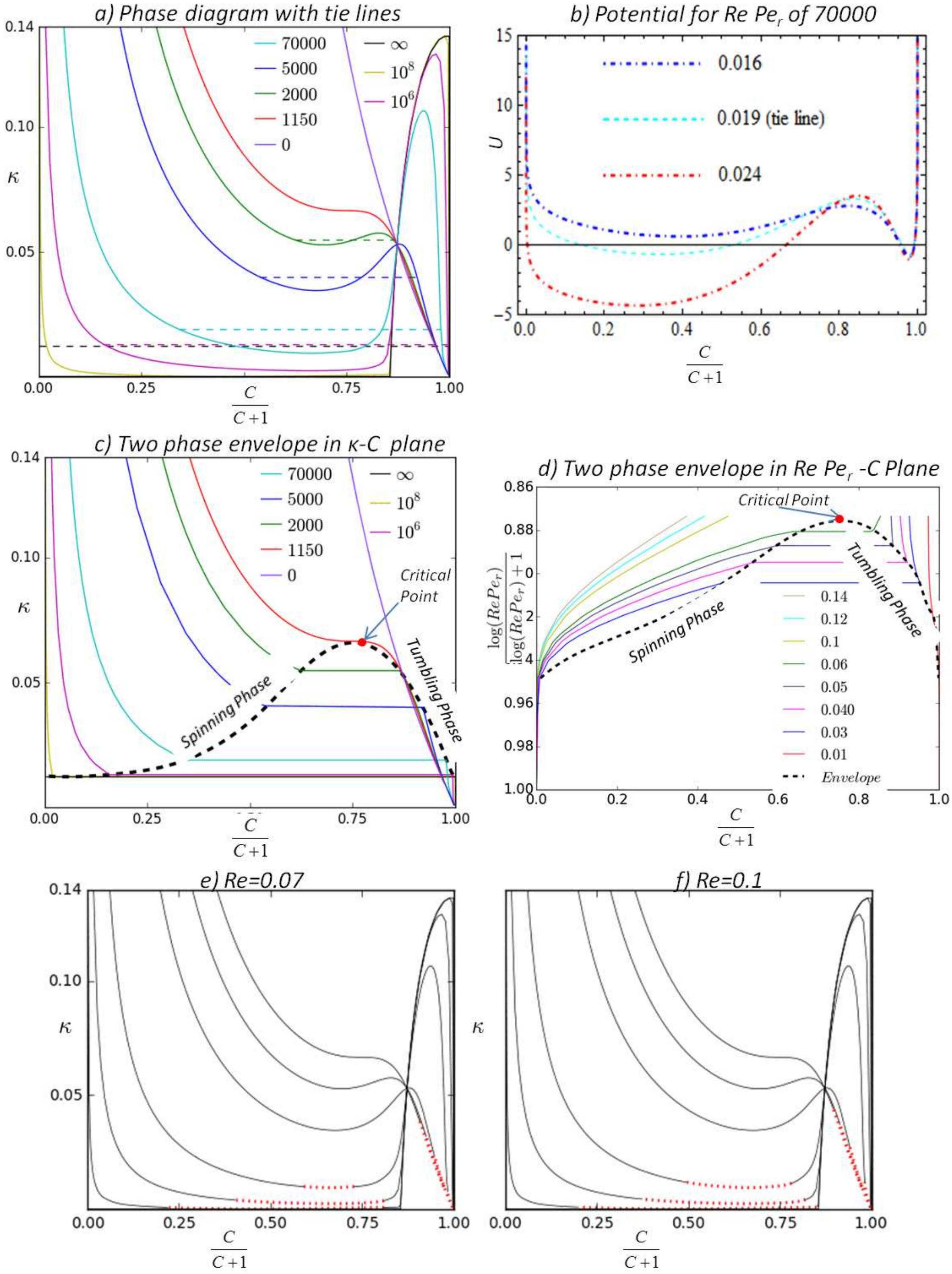

Fig. 3.4 (a) shows the extrema loci, together with dashed tie lines, for various $RePe_r$. (b) shows the nature of the potential(U) above and below the tie line for an $RePe_r$ of 70000. (c) and (d) show the envelope of the two phase region in the κ-C and $RePe_r$-C planes respectively. (e) and (f) delineate the regime of validity of the reduced one-dimensional description for two different Re's.

Hinch 1974). Intra-chain hydrodynamic interactions sharpen the transition from the coiled to the stretched configuration, with increasing flow strength (characterized by a Deborah number $De = \dot{\gamma}\tau_r$, τ_r being the longest relaxation time), so as to render it discontinuous. The discontinuous transition implies a hysteresis, and coiled and stretched states (produced by varying deformation histories) can co-exist at a given De for times much longer than τ_r(Schroeder *et al.* 2004). These states may be identified with the aforementioned tumbling and spinning phases, respectively, with the average polymer extension in a coarse-grained description playing the role of C, De being the analog of κ, and the polymer molecular weight being equivalent to $RePe_r$. The co-existence of multiple conformations has been verified in single-molecule experiments(Schroeder *et al.* 2003), and the approach in select scenarios, to a bi-modal equilibrium, has been verified in simulations(Beck & Shaqfeh 2006). A tentative phase diagram in the $extension-De$ plane, the analog of figure 3.4a, appears in Schroeder *et al.* (2003).

The hysteretic orientation dynamics of thin oblate spheroids is better understood in the three-dimensional $\kappa-C-RePe_r$ space in figure 3.5. The region of multiple extrema in figure 3.4a now defines a bi-nodal volume and the superposition of the shaded regions defines a smaller spinodal volume confined between the inflection-point loci of the double-welled potentials. Unlike the thermodynamic case, there is no equation of state that constrains κ to be a certain function of $RePe_r$ and C, and all points within the hysteretic bi-nodal volume remain accessible (this remains true for the polymeric case). The bi-nodal volume shrinks with decreasing $RePe_r$, and vanishes at $RePe_r$ of 1150.

In chapter 2, it was shown that for neutrally buoyant oblate spheroids, the bifurcation region exists in planar linear flows close to simple shear flow (λ's corresponding to the shaded region in figure 2.17). For various λ's in the shaded region of figure 2.17, the phase diagrams are plotted in figure 3.6. The phase diagrams for positive λ's are bounded below by $\kappa_{min} = \sqrt{\lambda}$, the smallest aspect ratio at which the orbits of the spheroid are closed in the Stokes limit. When λ is positive, for a given $RePe_r$, the upper limit of the range of aspect ratios for which the potential is bi-stable, increases, with increasing λ from $\kappa = 0.14$ for $\lambda = 0$ and reaches around $\kappa = 0.2$ for $\lambda = 0.03$. However, this rate of increase is slow compared to that of the lower bound κ_{min}. When λ is negative, the upper limit decreases with decreasing λ. There are no lower bounds for the phase diagram in the case of negative λ's. Thus, the hysteretic region encountered in the simple shear flow case in figure 3.4, quickly shrinks on either side with increasing $|\lambda|$.

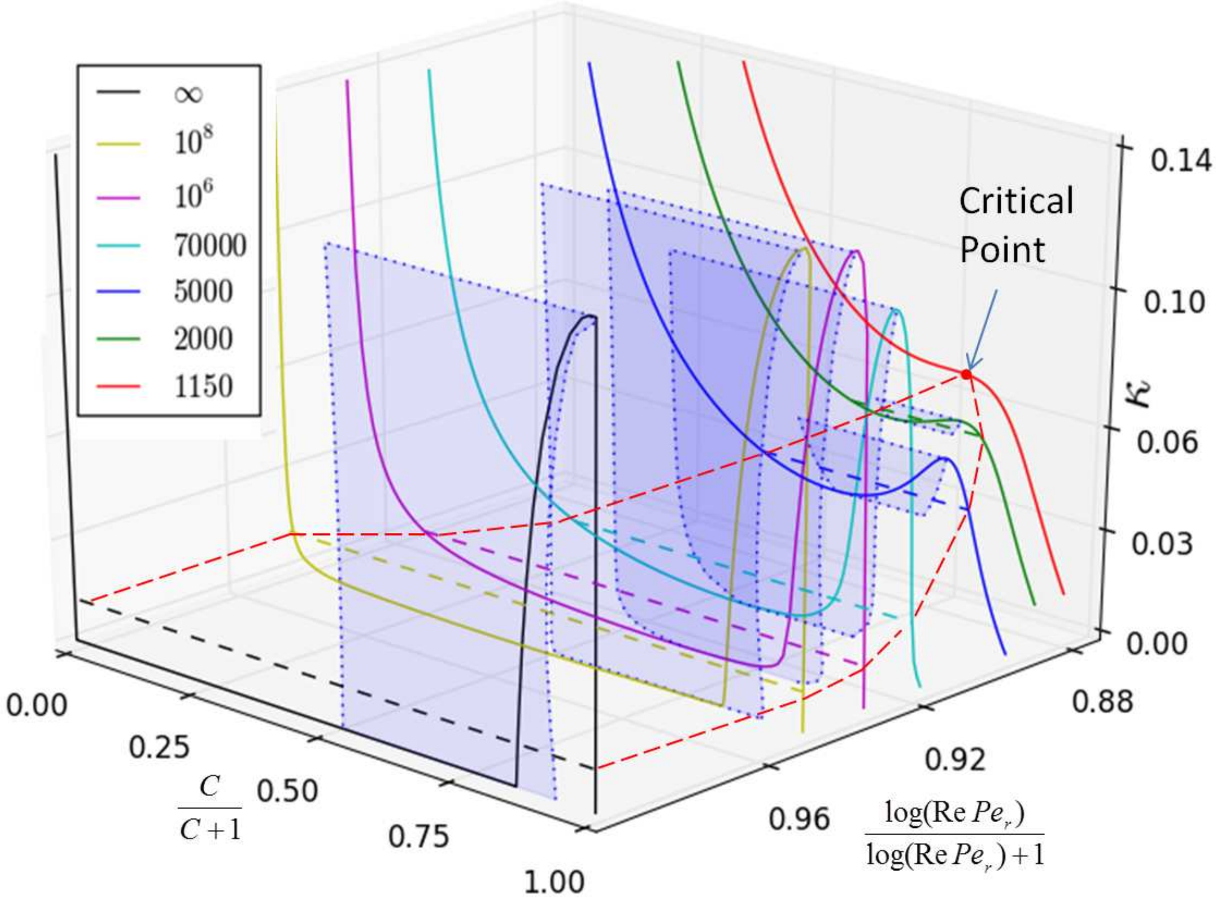

Fig. 3.5 The three-dimensional phase diagram in (κ-C-$RePe_r$) coordinates. The tumbling-spinning envelope ending in a critical point is shown as red-dashed lines.

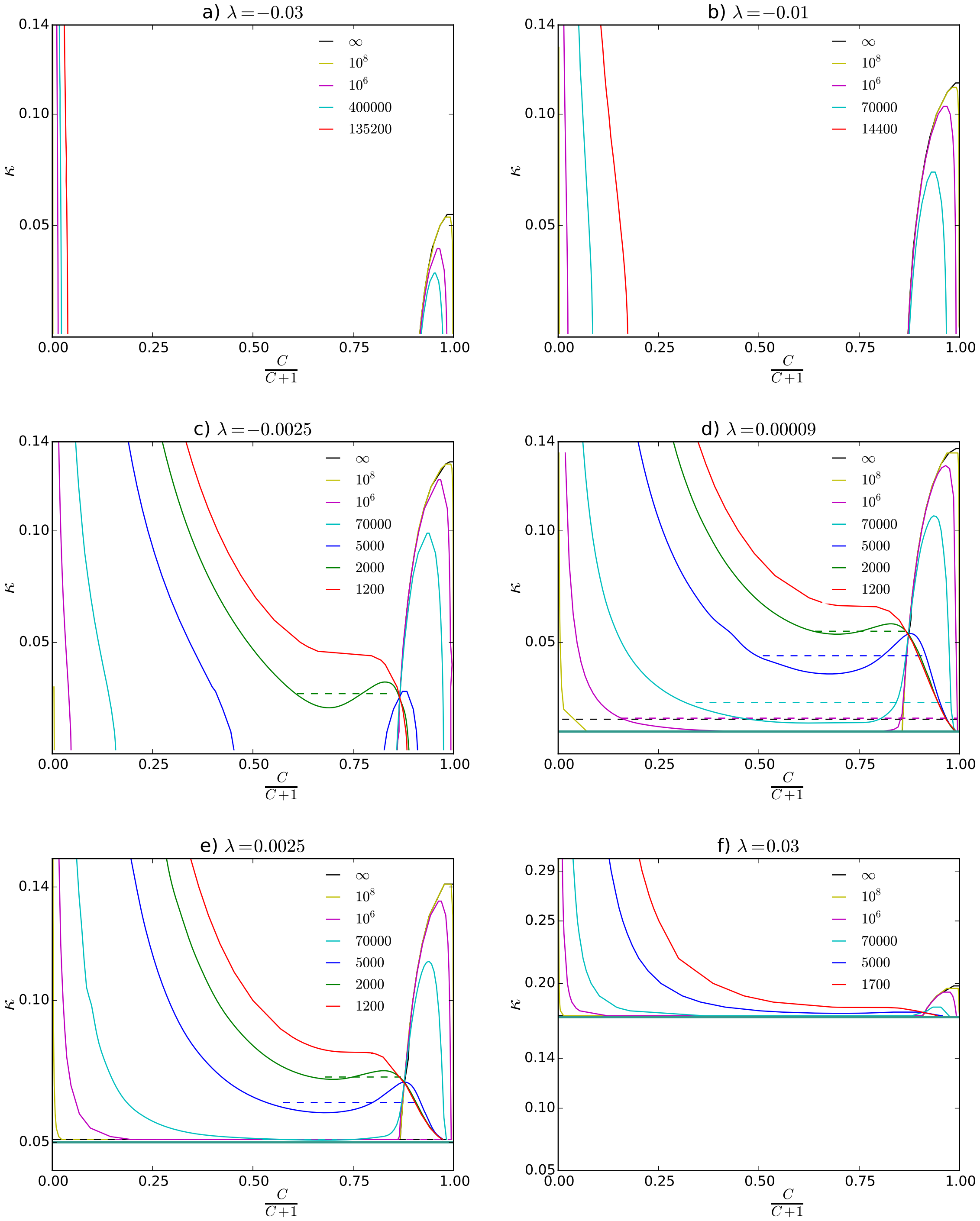

Fig. 3.6 The phase diagrams are plotted for various λ's.

3.4.3 The rheology of a suspension of oblate spheroids with aspect ratio less than 0.137: the role of weak Brownian motion

In this section we calculate the viscosity of a dilute suspension of oblate spheroids with $\kappa < 0.137$. We explore both the steady state rheology as a function of the (non-dimensional) shear rate, and the time-dependent evolution of the viscosity from its initial value (corresponding to a chosen orbit constant distribution) for points in the $\kappa - RePe_r - C$ parameter space that lie within the tumbling-spinning envelope.

At long times as shown in the previous sections the distribution takes the form $\bar{\Omega}_0 = \frac{f_s(C)}{h_C h_\tau \sin\alpha}$, with $f_s(C)$ defined in (3.4). The evolution to $f_s(C)$ however is governed by (3.48) and one has to solve this equation numerically to understand the transient dynamics. This evolution has a non-trivial character within the tumbling-spinning envelope owing to the bistable nature of the potential. As seen in figure 3.5, one can identify spinodal and binodal regions in the region of three dimensional parameter space corresponding to tumbling-spinning envelope. The evolution of the distribution can accordingly be classified into spinodal and binodal (nucleation-growth) routes. The analog of spinodal dynamics corresponds to the evolution of $f(C)$ from an initial condition $(f_0(C))$ peaked close to the potential maximum, while the analog of the nucleation-growth route ensues for an initial condition peaked outside the inflection-point interval. The narrow Gaussians are the only initial conditions that occurs in thermodynamical systems, in which case the fluctuations are O($N^{-1/2}$), and the spinodal-binodal classification is relevant to all initial conditions. This is not the case here. Figure 3.7a shows the rapid evolution for $RePe_r = 3 \times 10^5$, starting from a narrow Gaussian at the potential maximum, into a bimodal distribution peaked at the potential minima. In figure 3.7b, for an initial Gaussian adjacent to the small-C potential minimum, the distribution now remains unimodal, and a second peak is 'nucleated' at much later times via a barrier-hopping process. Kramer's theory gives the barrier hopping scale as $\frac{4\pi RePe_r}{\chi_1|_{C_{max}}(f''|_{C_{max}} f''|_{C_{min}})^{1/2}} e^{RePe_r \Delta U}$ Chandrasekhar (1943), where ΔU is the magnitude of the difference in the potential between the lowest minimum (C_{min}) and the central maximum (C_{max}) of the bi-stable potential. The time-dependent viscosities can be evaluated from 3.10, using the $f(C)$ at each instant and is plotted for aforementioned evolutions are shown in figure 3.7c (Dwivedi 2016). The viscosity for the spinodal case evolves quickly to begin with on account of peak splitting; this contrasts with the slow evolution of the bi-nodal viscosity via the barrier hopping process. As is evident at finite times, the viscosity of the suspension is therefore going to be strongly dependent on the initial orientation distribution, making the suspension hystertic.

Although a narrow Gaussian has been used to illustrate the spinodal and binodal routes to

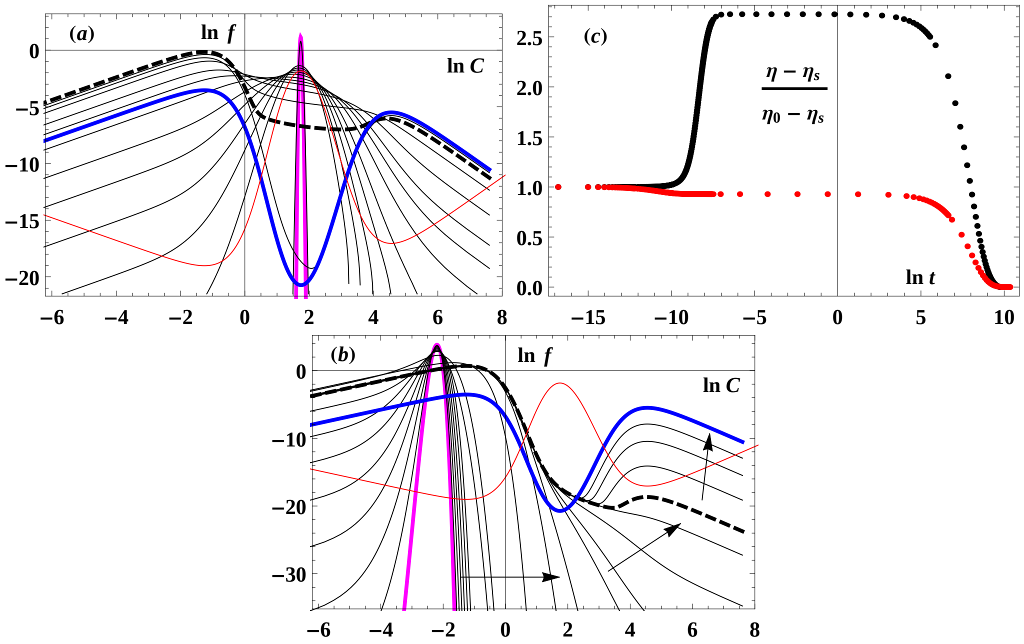

Fig. 3.7 The evolutions starting from localized Gaussians (magenta) peaked at the maximum (a) and adjacent to the small-C minimum (b) of the potential (red), respectively; $\kappa = 0.016$, $RePe_r = 3\times 10^5$. The $f_s(C)$ in each case is shown as a blue curve. The dashed line corresponds to the instant ((a) $6.5\times 10^{-4}\ D_r^{-1}$ and (b) $6.1\times 10^{-3}\ D_r^{-1}$) at which a tumbling peak first appears. (c) corresponding evolutions of the scaled viscosities, (a) black and (b)red (η_0 and η_s are the initial and steady state values).

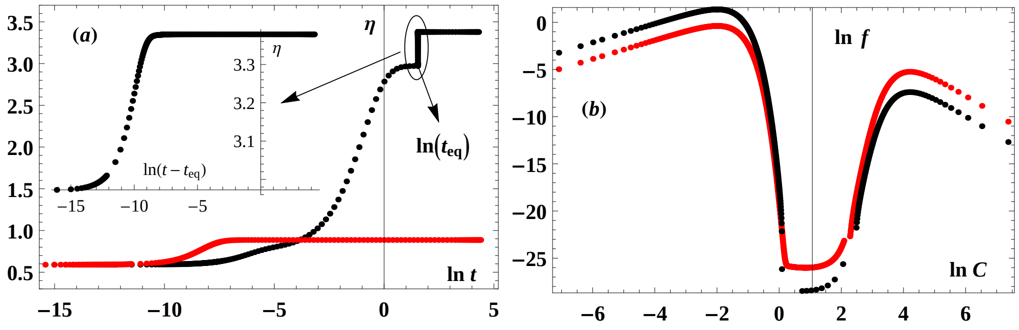

Fig. 3.8 (a) Intrinsic viscosity evolutions for the quenches identified in the text (inset shows the evolution for step 2 of the second quench) (b) The quasi-steady state orientation distributions at $RePe_r = 2\times 10^5$. The second quench leads to a greater fraction of spinning spheroids, and therefore, a higher viscosity.

equilibrium above, generating a localized orbit-constant distribution in an experiment requires the application of an external field (Okagawa & Mason 1974; Ennis *et al.* 1978). From an experimental point of view, an isotropic orientation distribution is readily generated by initial mixing. For an $f_0(C)$ corresponding to this well-mixed state (recall that $f_0(C)$ is the complete elliptic integral, see section 3.3.2), a signature of the hysteresis is the sensitive dependence of the viscosity in the bi-nodal volume to the precise shear rate history. To illustrate this dependence, we consider a pair of 'quenches' applied to an isotropic suspension of spheroids with $\kappa = 0.04$ [1]. In the first single-step quench, the suspension is sheared at an $RePe_r$ of 2×10^5. In the second quench, the suspension is first sheared at an $RePe_r$ of 25000 until a steady state (achieved at a time t_{eq}), and $RePe_r$ is then increased to the aforementioned value of 2×10^5. The evolution of the viscosities is plotted in figure 3.8a. In the first quench, the distribution, and thence, the viscosity settles down to a quasi-steady state arising from the partitioning of $f_0(C)$ across the potential maximum, followed by local equilibration in the spinning and tumbling wells. In the second quench, the viscosity evolves quickly to its steady state value in the first step owing to the lower $RePe_r$; in the second step, it evolves to a different quasi-steady state that corresponds to a partitioning of the steady state for $RePe_r = 25000$. The true steady states are inaccessible for both the first quench, and the second step of the second quench, owing to the exceedingly large barrier-hopping times. The pair of quasi-steady states, at $RePe_r = 2\times10^5$, are shown in figure 3.8b, and represent a viscosity contrast of approximately 3.8. Note that far higher viscosity contrasts are obtainable from 'spin-rich' initial conditions, but as indicated earlier, these require the imposition of external electric or magnetic fields .

At times larger than the barrier hopping time mentioned above, the viscosity asymptotes to a value independent of its shear history, and we now focus on this long-time rheology. In the limit of $RePe_r \rightarrow \infty$, the distribution across orbits $f_s(C)$ is a delta function peaked at the spinning for $\kappa > 0.0126$, and peaked at the tumbling for $\kappa < 0.0126$. In figure 3.9, the viscosity coefficient scaled with O(nL^2b) is plotted against eccentricity. It is obtained by averaging the stresslet using the orientation distribution given in (3.34) for $\kappa > .0126$, and (3.33) for $\kappa < .0126$. Note that the aforementioned critical aspect ratio differs from the critical value of 0.137 found in the absence of Brownian motion ($RePe_r = \infty$), implying the singular role of Brownian motion; the viscosity coefficient now varies smoothly across the earlier critical value. A relevant question one could ask is about the variation of the steady shear viscosity as a function of suitable non-dimensional shear rate for different aspect ratio spheroid and

---

[1] The quenches discussed may be achieved in an experiment in a time of approximately 3 hours, by shearing oblate spheroids of with $L \sim 10$ microns in an aqueous medium with the maximum shear rate needed to achieve $RePe_r = 2\times10^5$, being 900 s^{-1}.

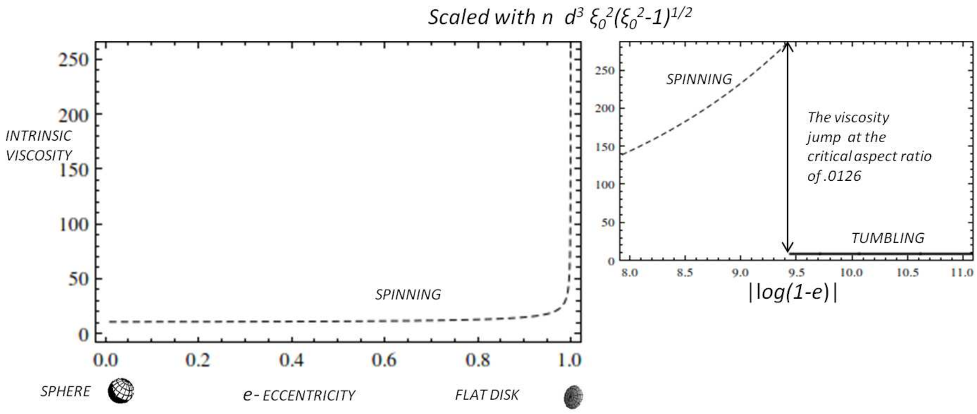

Fig. 3.9 The intrinsic viscosity for a suspension of Brownian oblate spheroids is plotted as a function of the aspect ratio. The right figure shows the jump from the spinning to the tumbling value at the critical aspect ratio of .0126.

not merely the viscosity values corresponding to the infinite shear rate limit reported above . The detailed review by Brenner (1974) describes the variation of the intrinsic viscosity coefficient for a non-interacting suspension of Brownian spheroids, as a function of Pe_r, in the inertialess limit (see figures 7 and 10 therein). As expected, for a general complex fluid with an isotropic microstructure at equilibrium, the imposition of shear and the resulting flow-alignment of the spheroidal particles leads to a shear-thinning rheology. More specifically, for a spheroid of a given aspect ratio, either prolate or oblate, $\frac{\mu_{eff}-\mu}{\mu}$ decreases from a zero-shear-rate plateau of $O(nL^3)$, arising from a combination of the hydrodynamic and Brownian stress contributions for a nearly isotropic orientation distribution, to a smaller $O(nL^2b)$ high-shear plateau, arising solely from the hydrodynamic stress contribution associated with a flow-aligned orientation distribution. The high-shear plateau values were first calculated by Hinch & Leal (1972), numerically for arbitrary aspect ratio spheroids (see Kim & Karrila (1991)), and analytically in the slender fiber and flat disk limits. These plateaus correspond to the limit $Pe_r \gg 1, RePe_r = 0$ for spheroids with aspect ratios of order unity. For extreme aspect ratios, a more stringent requirement arises from the neglect of Brownian motion even close to the flow-vorticity (gradient-vorticity) plane for slender fibers (flat disks) given by $Pe_r \gg \kappa^3(\kappa^{-3}), RePe_r = 0$ (Hinch & Leal (1972)). The analysis here helps extend the behavior of the intrinsic viscosity coefficient beyond the 'Leal-Hinch' plateaus, as a function of $RePe_r$, up until the point where $Re \sim O(1), RePe_r \to \infty$. Said differently, the shear-thinning rheology of a dilute inertialess suspension of spheroids is known up until a Pe_r where a limiting Newtonian plateau results from Brownian motion only determining the distribution of orientations across Jeffery orbits. The viscosity versus shear rate curves given below, both the schematic and the actual numerical calculations, start from this point and determine the non-Newtonian rheology at higher $RePe_r$ due to the distribution given by (3.50).

The behavior of the vicosity for oblate spheroids with shear rate depends on the whether the aspect ratio is above or below 0.0126. In the former case, a shear-thickening rheology results for sufficiently large $RePe_r$, while for the latter case, the suspension continues to shear thin even with the onset of inertia. Accordingly, figure 3.10 shows the viscosity v/s shear curves, corresponding to the two aspect-ratio groups, separating out in the limit $RePe_r \to \infty$, this being consistent with a jump in the shear viscosity in this limit as seen mentioned earlier. The actual plots of the intrinsic viscosity coefficient plotted against $RePe_r$ are shown attached to the schematics in figures 3.10 and 3.11. These reveal the scenario for oblate spheroids, with aspect ratios greater than 0.0126, to be a little more complicated than that shown in the schematic, owing to the suspension first shear thinning substantially with increasing $RePe_r$, for aspect ratios just above the critical value, before eventually shear thickening for sufficiently large $RePe_r$. This non-monotonicity arises because of an initial Brownian peak close to tumbling, and the transition from this to a spinning peak with increasing $RePe_r$; the transition involves a sharpening of the tumbling peak (leading to shear thinning) prior to the development of a spinning peak. A similar calculation for oblate spheroids with smaller aspect ratios shows a monotonic shear-thinning; the viscosity coefficient here is plotted against $RePe_r\kappa^2$, this being the actual ratio of drift to diffusion for $\kappa \ll 1$.

As shown in figure 3.11, accounting for a non-zero $RePe_r$ will always lead to a shear-thickening rheology(relative to the Leal-Hinch plateau) for prolate spheroids owing to the drift towards the maximum dissipation (tumbling) orbit. Note that the inertial high-shear plateaus for a prolate spheroid are asymptotically small in relation to the zero-shear plateaus for large aspect ratios, becoming comparable (and even exceeding) only for nearly spherical particles. In contrast, for the oblate case, the inertial plateaus significantly exceed the zero-shear values even for small aspect ratios, implying that inertia leads to an overall shear thickening behavior of the suspension for most aspect ratios. For higher shear rates, *Re* would be of order unity or larger, and the rheology will begin to be influenced by the finite-*Re* bifurcations that have been identified in numerical simulations. Depending on *Re* as well as the aspect ratio, the suspension can exhibit shear thickening as well as shear thinning behaviour (Rosen *et al.* (2015)). It is important to note that the presence of multiple attractors at finite Re would again point to the role of stochastic orientation fluctuations in establishing a steady state rheology.

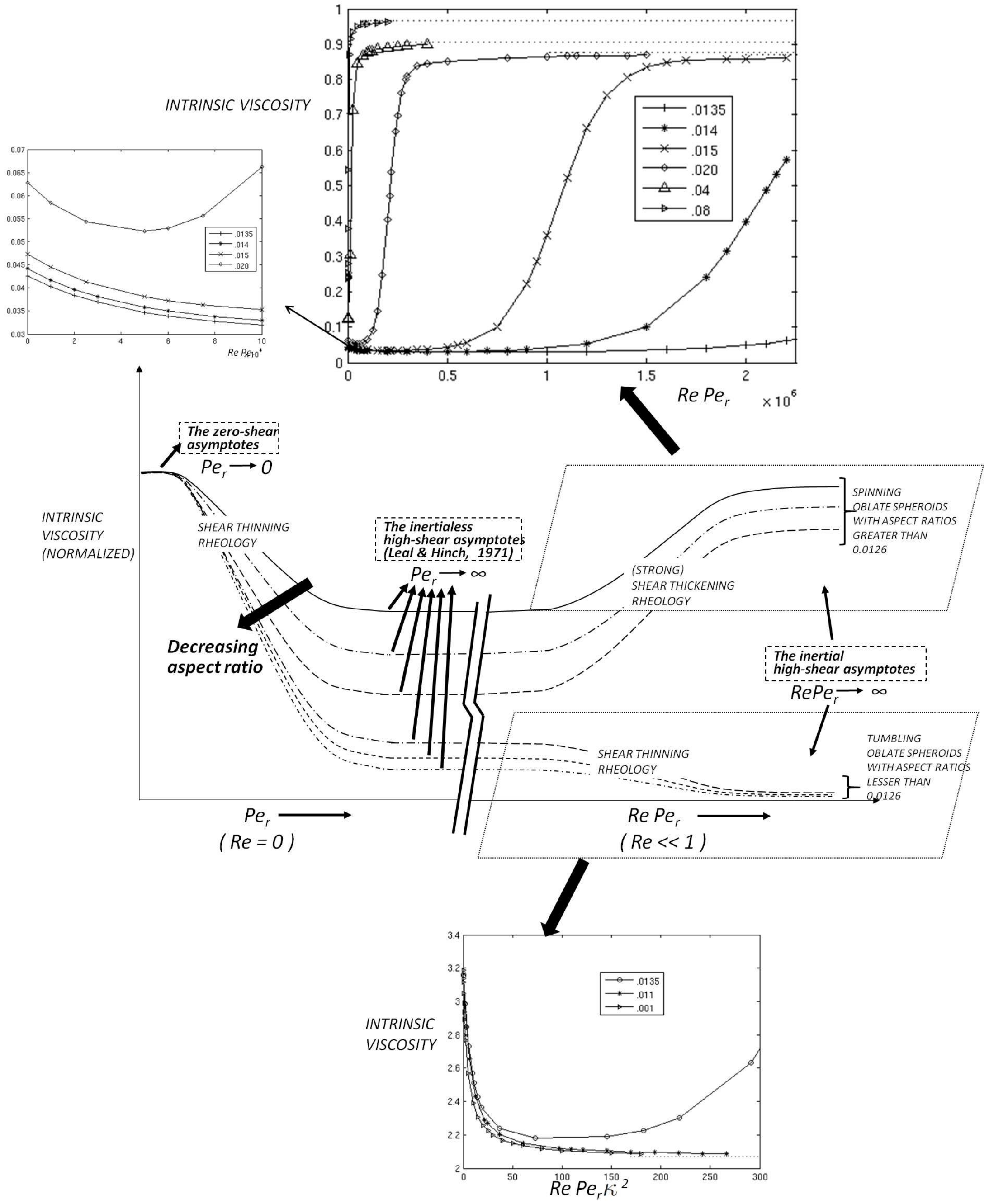

Fig. 3.10 The middle plot is a schematic of the expected variation of intrinsic viscosity for a suspension of Brownian oblate spheroids. The upper plot shows the variation of the viscosity, scaled with $nd^3\xi_0^3$, with $RePe_r$ for aspect ratios greater than the critical aspect ratio of 0.0126. The lower plot shows the variation of the viscosity, scaled with $nd^3\xi_0^2\bar{\xi}_0$, with $RePe_r$ for aspect ratios smaller than the critical aspect ratio of 0.0126. An aspect ratio greater than the critical aspect ratio is also included in the lower plot. The dotted lines in both the upper and the middle plots are the $RePe_r = \infty$ asymptotes.

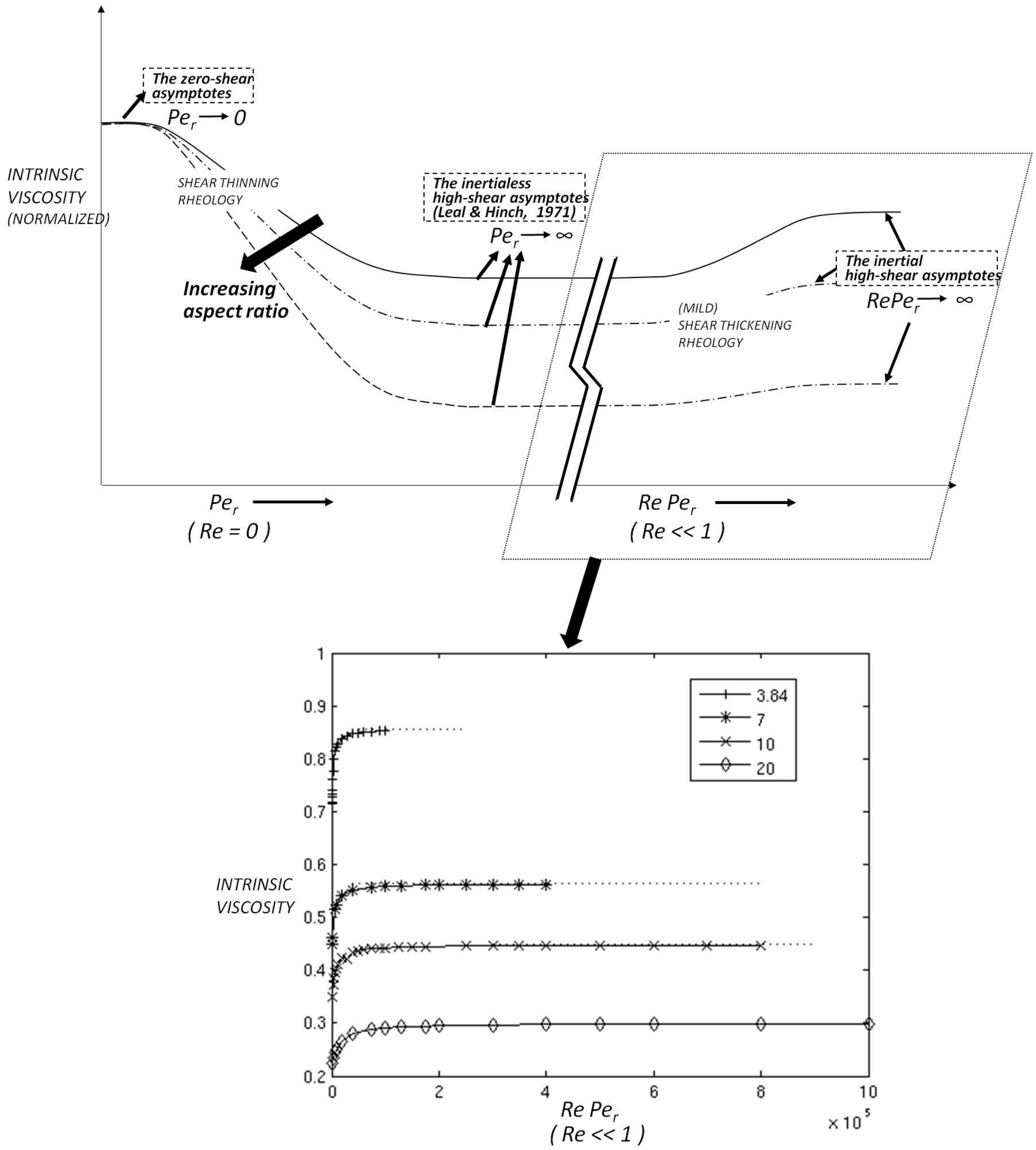

Fig. 3.11 The upper plot is a schematic of the expected variation of intrinsic viscosity for a suspension of Brownian prolate spheroids. The lower plot shows the variation of the viscosity, scaled with $nd^3\xi_0^2\bar{\xi}_0$, with $RePe_r$. The dotted lines in the lower plot are the $RePe_r = \infty$ asymptotes.

3.5 Conclusions

Inertia eliminates the rheological degeneracy, associated with the existence of Jeffery orbits in the Stokes limit, although the manner of elimination depends on the aspect ratio for oblate spheroids. For neutrally buoyant prolate spheroids, and for neutrally buoyant oblate spheroids with aspect ratios greater than 0.137, the inertial drift leads to a singular orientation distribution localized at either the tumbling or the spinning mode depending on whether ΔC is positive (prolate) or negative (oblate). In section 3.3, we calculate the associated intrinsic viscosity coefficients, in the absence of Brownian motion, as a function of the particle aspect ratio (see (3.36) and (3.37) for prolate and oblate spheroids, respectively) arising from the aforementioned singular distribution. Weak Brownian motion only leads to asymptotically small corrections to this estimate. In contrast, for oblate spheroids with aspect ratios less than 0.137, the inertial drift acting alone leads to an initial-condition-dependent rheology, and it is only with the inclusion of weak Brownian motion that a unique steady state rheology results. In section 3.3, we calculate the initial condition-dependent intrinsic viscosity for the non-Brownian case for an initial isotropic orientation distribution (see (3.38)). In section 3.4, we analyze in some detail the steady state distribution across Jeffery orbits in the presence of weak Brownian motion, the inclusion of which implies a dependence of the steady-state rheology on the parameter $RePe_r$. Interestingly, the steady state Jeffery-orbit distribution may be interpreted in terms of a one-dimensional drift-diffusion equilibrium along the orbit constant coordinate with $RePe_r$ governing the relative magnitudes of the convective and diffusive fluxes in orientation space. This distribution has a bi-modal character, with peaks corresponding to the tumbling and spinning modes, for sufficiently large $RePe_r$. For any finite $RePe_r$, the shear viscosity varies smoothly with changing aspect ratio of the oblate spheroid, but in the limit $RePe_r \rightarrow \infty$, the shear viscosity must exhibit a jump across a much smaller (in relation to the non-Brownian value of 0.14) critical aspect ratio of 0.0126 owing to a transition in the (limiting) orientation distribution from a delta function localized at $C = 0$ (the spinning mode) to one localized at the tumbling mode ($C = \infty$). As mentioned in section 3.2, we calculate here only the leading-order (indirect) effect of inertia on the suspension rheology. For prolate spheroids, and oblate spheroids with aspect ratios greater than 0.137, the direct effects of inertia enter at $O(Re)$. Interestingly for oblate spheroids with aspect ratios less than 0.137, the next correction to the drift occurs at $O(Re^{\frac{3}{2}})$ and this implies a larger $O(Re^{\frac{1}{2}})$ correction to the leading order rheology.

Inertia and Brownian motion are somewhat incompatible in terms of the relevant particle size ranges. Thus, the convergence to a unique long-time equilibrium, consistent with the thermodynamic picture in figure 3.4, may require unrealistically long times, especially for spheroids large enough for the inertial drift to be significant. The rheological signature of the hysteresis - a multi-valued shear viscosity at a given shear rate ($RePe_r$), as in figure 3.8, should, however, be measurable. The phase transition and the associated hysteresis discussed in section 3.4 arises due to the combined effect of a bi-stable potential induced by non-linearity and stochasticity; the bi-directionality of the inertial drift, in fact, persists at finite Re (Meibohm *et al.* 2016). Other sources of non-linearity and stochasticity should lead to similar behavior. Athermal orientation fluctuations arising from hydrodynamic interactions should control the tumbling-spinning transition at higher volume fractions (nL^3). Each such interaction changes C by a finite amount, and the resulting relaxation is non-local in orientation space, being governed by a Boltzmann equation:

$$\frac{\partial f}{\partial t}+Re\frac{\partial}{\partial C}(\Delta C_i f)=nL^3\int dC'\int d\boldsymbol{r}_{\perp}y\int d\hat{C}d\hat{C}'[f(\hat{C})f(\hat{C}')\mathscr{K}(\hat{C},\hat{C}'|C,C';\boldsymbol{r}_{\perp})-f(C)f(C')], \tag{3.51}$$

for small nL^3 when pair-interactions drive the fluctuations. The scattering kernel $\mathscr{K}$ in (3.51) relates the pre- ($[\hat{C},\hat{C}']$) and post- ($[C,C']$) interaction orbit-constant-pairs, and $d\boldsymbol{r}_{\perp}$ denotes the differential interaction cross-section. Note that $Re(nL^3)^{-1}$ in (3.51) is the analog of $RePe_r$ in (3.48). Although an analysis based on (3.51) is difficult due to $\mathscr{K}$ not being known, this might nevertheless be the most convenient experimental route with the hysteretic time scale capable of being tuned to modest values by varying the volume fraction, rendering both short-time dynamics and long-time orientational equilibria observable. Fluid viscoelasticity either in steady (Leal 1975) or large-amplitude oscillatory shear (Harlen & Koch 1997; Leahy *et al.* 2013) is an alternate (experimentally) more accessible source of non-linearity, and the ratio of normal stress differences (besides De) (Dabade *et al.* 2015) may allow one to additionally tune the nature of the non-linear drift.

The tumbling-spinning transition highlights an interesting connection between suspension rheology and polymer physics. Much like the coil-stretch transition for polymer solutions (Shaqfeh 2005; Larson 2005), the tumbling-spinning transition endows an inertial suspension of thin oblate spheroids with a memory that far exceeds the nominal microstructural relaxation times. This memory is likely to significantly influence the suspension stress response in inhomogeneous shearing flows, since the viscosities corresponding to different (Lagrangian) shear rate histories can differ by a large amount owing to the large difference in the dissipation associated with spinning and tumbling spheroids. Non-hydrodynamic forces, including Brownian motion, have been known to play a subtle role in determining the strong-shear rheology of spherical particle suspensions at high volume fractions (Brady & Morris 1997; Cheng *et al.* 2011). In contrast, the tumbling-spinning transition points to the subtle role played by Brownian motion in determining the rheology of anisotropic particle suspensions at much lower volume fractions. Furthermore, in being a simpler system with far fewer degrees of freedom when compared to high molecular weight polymers, a sheared suspension of anisotropic particles may serve as a model system for the study of hysteretic dynamics in complex fluid systems.

Chapter 4

The orientation dynamics of a spheroid sedimenting in a simple shear flow

4.1 Introduction

In this chapter we discuss the effect of inertia on a spheroid of arbitrary aspect ratio sedimenting in a simple shear flow. It is well known that in the Stokes limit, a translating spheroid does not rotate in a Newtonian fluid (Leal 1992). In a recent effort (Dabade *et al.* 2015), the effects of weak inertia as well as viscoelasticity on the orientation of a spheroid sedimenting in a quiescent fluid was investigated. The authors have estimated the torque acting on a translating spheroid at $O(Re_{sed})$, as well as at $O(De)$, using a generalized reciprocal theorem formulation. Here, Re_{sed} is the Reynolds number in the sedimentation defined as $\rho U_{sed} L/\mu$, where U_{sed} is the translational velocity of spheroid, L is the semi-major axis of the spheroid, μ and ρ are the viscosity and the density of the fluid. The non-dimensional number De, characterizes the time scale of the dominant relaxation process of the fluid microstructure, and is given by $U_{sed}\tau_r/L$, where τ_r is the microstructural relaxation time of the fluid. The limit of $De << 1$ considered allows for modelling of viscoelastic effects in terms of a second-order fluid constitutive equation. The torque was obtained as an integral using the generalized reciprocal theorem, and the integral was evaluated using the spheroidal harmonics formalism, which was used earlier in chapter 2. They find that the effect of inertia at $O(Re_{sed})$ results in a torque which makes the spheroid sediment with a broadside-on configuration. In the broadside-on configuration, the orientation of a prolate spheroid will be perpendicular to its translational velocity, whereas that of an oblate spheroid will be aligned to its velocity. Depending on the ratio of normal stress differences in the second-order fluid, the effect of viscoelasticity results in a torque, which makes the spheroid sediment either in a broadside-on configuration or in a longside-on configuration. In the latter configuration, the orientation is aligned with the translational velocity for a prolate spheroid, and is perpendicular to the velocity for an oblate spheroid. The effect of simple shear flow on the orientation dynamics of the spheroid is already discussed in chapter 2.

Understanding the orientation dynamics of a spheroid (or, more generally, anisotropic particles) sedimenting in a shear flow is important in many physical applications. For instance, the orientation of the suspended ice-crystals determine the scattering properties of a cirrus cloud and, thereby affecting the cloud radiation forcing (Liou 1986), which in turn plays a crucial role in the earth-atmosphere radiation budget. Typical ice crystals are small in size (Auer Jr & Veal 1970) and are subjected to both forces and torques due to gravity and shear flow due to the turbulence in the cloud, the turbulence being a random linear flow at the length scales of the sub-kolmogorov ice crystals. As a first step towards analyzing the scenario, in this chapter, we determine the inertial torque under the combined effects of sedimentation and a simple shear flow.

This chapter is organized as follows. In section 4.2 we determine the angular velocity of a spheroid sedimenting in a shear flow using a generalized reciprocal theorem. The derivation follows that seen in chapter 1, except for an additional term due to sedimentation. This term is related to the inertial torque acting on a translating spheroid that has already been derived in Dabade *et al.* (2015). A non-dimensional parameter, Re_{sed}/Re, characterizes the strength of this term relative to the torque due to fluid inertial effects in the shear flow. Here, Re is the Reynolds number in the shear flow, defined as $Re = \rho\dot{\gamma}L^2/\mu$, where $\dot{\gamma}$ is the shear rate. The angular velocity is also a function of another non-dimensional parameter, St/Re, which characterizes the strength of the torque due to particle inertial effects relative to that due to fluid inertial effects. Here, St is the Stokes number, $St = \rho_p\dot{\gamma}L^2/\mu$, where ρ_p is the particle density. Recall that in chapter 2, it was shown that for a neutrally buoyant spheroid in simple shear flow, the fluid inertial drift dominates the particle inertial drift. So for the particle inertial torque to be important, St/Re should be large. The reciprocal theorem formulation gives the angular velocity of a spheroid sedimenting due to a constant force, aligned arbitrarily with respect to the ambient simple shear flow, and the angular velocity is presented in section 4.3. To order Re, the results for sedimentation and shear flow may be superposed. It is simpler to analyze the orientation dynamics of the spheroid in three canonical cases, these being defined by the direction of the sedimenting force. The three canonical directions are the vorticity, the flow and the gradient directions of the simple shear flow, and the orientation dynamics in these three cases is analyzed in sections 4.4, 4.5 and 4.6. It turns out that for O(1) values of St/Re, when the force is along the flow or the gradient direction, the inertial drift due to sedimentation and that due to the shear flow stabilize different orbits; they stabilize the same orbit when the force is along the vorticity. Depending on the non-dimensional parameters mentioned above, the competing effects of sedimentation and inertial effects in shear flow may result in the emergence of a repeller, that divides the orientation space into two basins of attraction, for spheroids, with no repeller at $Re_{sed}/Re = 0$ and St/Re of O(1). The limitations of the analysis are discussed in section 4.7. The results are summarized in section 4.8.

4.2 Formulation for inertial drift: The generalized reciprocal theorem

The expression for the angular velocity of a spheroid sedimenting in a simple shear flow is derived using the reciprocal theorem discussed in chapter 2. The problem of interest here is a spheroid sedimenting in a simple shear flow due to a force $\mathbf{1}_g$ aligned arbitrary with respect to the simple shear flow. The simple shear flow is defined as $\boldsymbol{u} = \boldsymbol{\Gamma} \cdot \boldsymbol{x}$, with $\boldsymbol{\Gamma} = \mathbf{1}'_x \mathbf{1}'_y$ being the transpose of the non-dimensional velocity gradient tensor. The test problem is again a spheroid rotating in a quiescent fluid, similar to the test problem defined in chapter 2. The velocity and stress fields in the problem of interest are denoted by $\boldsymbol{u}^{(1)}$ and $\boldsymbol{\sigma}^{(1)}$ and that in the test problem are denoted by $\boldsymbol{u}^{(2)}$ and $\boldsymbol{\sigma}^{(2)}$. The velocity and stress are scaled with $\dot{\gamma}L$ and $\mu\dot{\gamma}L$, where L is the semi-major axis of the spheroid, μ is the viscosity of the fluid and $\dot{\gamma}$ is the shear rate. Note that the scaling has been done using the shear rate in the simple shear flow and not the translational velocity in the sedimentation. Due to sedimentation, a spheroid may move across the streamlines of the simple shear flow, and therefore, the velocity corresponding to the streamline passing through its centroid ($\boldsymbol{X}_{cen}$), changes with time. The velocity and stress fields defined above for the problem of interest are defined in a coordinate system that is translating with the centroid streamline velocity, given by $\boldsymbol{\Gamma} \cdot \boldsymbol{X}_{cen}$. In the same coordinate system, the disturbance velocity and stress fields in the problem of interest are denoted by $\boldsymbol{u}'^{(1)}$ and $\boldsymbol{\sigma}'^{(1)}$, and are related to the full velocity field as $\boldsymbol{u}'^{(1)} = \boldsymbol{u}^{(1)} - \boldsymbol{\Gamma} \cdot x$ and $\boldsymbol{\sigma}'^{(1)} = \boldsymbol{\sigma}^{(1)} - \boldsymbol{\sigma}^{\infty}$, where $\boldsymbol{\sigma}^{\infty}$ is the viscous stress due to the ambient simple shear flow. The boundary condition on the surface of the spheroid in the test problem is given by $\boldsymbol{u}^{(2)} = \boldsymbol{\Omega}_2 \times \boldsymbol{x}$, where $\boldsymbol{\Omega}_2$ is the angular velocity of the spheroid in this problem. The boundary condition on the surface of the spheroid in the problem of interest is given by $\boldsymbol{u}'^{(1)} = \boldsymbol{U}_{sed} + \boldsymbol{\Omega}_1 \times \boldsymbol{x} - \boldsymbol{\Gamma} \cdot \boldsymbol{x}$, where $\boldsymbol{\Omega}_1$ and $\boldsymbol{U}_{sed}$ are the angular and translational velocities of the spheroid in the translating coordinate system. Noting that the spheroid in the test problem is force free, the reciprocal theorem gives the angular velocity as:

$$\boldsymbol{\Omega}_1.\mathscr{L}_2 = \int_{S_p} \boldsymbol{\sigma}^{(2)} : (\boldsymbol{\Gamma}.\boldsymbol{x}) \cdot \boldsymbol{n} dS + \boldsymbol{\Omega}_2 \cdot \left(St \frac{d}{dt} \boldsymbol{I}.\boldsymbol{\Omega_1} \right) + \int_V \boldsymbol{u}^{(2)} \cdot \nabla \cdot \boldsymbol{\sigma}'^{(1)} dV. \tag{4.1}$$

The surface integral above is done over the surface of the spheroid (S_p) and the volume integral is done over the infinite fluid volume outside the spheroid (V). The torque acting on the spheroid in the test problem is denoted by $\mathscr{L}_2$, and given by $\mathscr{L}_2 = -8\pi(X_C\boldsymbol{pp} + Y_C(\boldsymbol{I} - \boldsymbol{pp})) \cdot \boldsymbol{\Omega}_2$, where $X_C = 4\left(\xi_0^2 - 1\right) / \left(3\xi_0^3 \left(2\xi_0 - 2\left(\xi_0^2 - 1\right) \coth^{-1}\xi_0\right)\right)$ and $Y_C = 4(2\xi_0^2 - 1)/(3\xi_0^3(2(\xi_0^2 + 1)\coth^{-1}\xi_0 - 2\xi_0))$ for a prolate spheroid (Kim & Karrila (1991)). Here, $\boldsymbol{p}$ is the orientation vector of the spheroid. The reciprocal theorem in (4.1) contains the angular velocity in the test problem ($\boldsymbol{\Omega}_2$), and as in chapter 2, one defines new tensors such as $\mathscr{L}_2 = \boldsymbol{L}_2 \cdot \boldsymbol{\Omega}_2$, $\boldsymbol{u}^{(2)} = \boldsymbol{U}^{(2)} \cdot \boldsymbol{\Omega}_2$ and $\boldsymbol{\sigma}^{(2)} = \boldsymbol{\Sigma}^{(2)} \cdot \boldsymbol{\Omega}_2$ to render the reciprocal theorem statement in (4.1) independent of $\boldsymbol{\Omega}_2$. The reciprocal theorem in terms of these tensors take the form:

$$\boldsymbol{\Omega}_1.\boldsymbol{L}_2 = \boldsymbol{\Gamma} : \int_{S_p} \boldsymbol{x}(\boldsymbol{\Sigma}^{(2)} \cdot \boldsymbol{n}) dS + St \frac{d}{dt} \boldsymbol{I}.\boldsymbol{\Omega_1} + \int_V \boldsymbol{U}^{(2)} \cdot \nabla \cdot \boldsymbol{\sigma}'^{(1)} dV. \tag{4.2}$$

The divergence of stress in the third term may be obtained from the equation governing the disturbance velocity field $\boldsymbol{u}'^{(1)}$, which is derived by subtracting the equation governing the ambient simple shear from that governing the full velocity field $\boldsymbol{u}^{(1)}$, and is given by:

$$\begin{aligned} \nabla^2 \boldsymbol{u}'^{(1)} - \nabla p' = \nabla \cdot \boldsymbol{\sigma}'^{(1)} &= Re \left(\frac{\partial \boldsymbol{u}'^{(1)}}{\partial t} + \boldsymbol{u}'^{(1)} \cdot \nabla \boldsymbol{u}'^{(1)} + (\boldsymbol{\Gamma}.\boldsymbol{x}) \cdot \nabla \boldsymbol{u}'^{(1)} + \boldsymbol{\Gamma} \cdot \boldsymbol{u}'^{(1)} \right) \\ &\quad - Re \frac{d}{dt} (\boldsymbol{\Gamma} \cdot \boldsymbol{X}_{cen}) \\ &= Re \left(\frac{\partial \boldsymbol{u}'^{(1)}}{\partial t} + \boldsymbol{u}'^{(1)} \cdot \nabla \boldsymbol{u}'^{(1)} + (\boldsymbol{\Gamma}.\boldsymbol{x}) \cdot \nabla \boldsymbol{u}'^{(1)} + \boldsymbol{\Gamma} \cdot \boldsymbol{u}'^{(1)} \right) - Re(\boldsymbol{1}'_y \cdot \boldsymbol{U}_{sed}) \boldsymbol{1}'_x \end{aligned} \tag{4.3}$$

The last term in the equation above, is the fictious force due to the acceleration of the translating coordinate system. The acceleration is determined by the component of the translation velocity along the gradient axis. The inertial drift under the combined effects of sedimentation and shear occurs at O(Re), and at this order, $\boldsymbol{u}'^{(1)}$ can be replaced by the Stokes velocity field, $\boldsymbol{u}'^{(1)}_s$. The Stokes velocity field, $\boldsymbol{u}'^{(1)}_s$, can be written as a sum of the disturbance velocity field in sedimentation ($\boldsymbol{u}'^{(sed\dot{\gamma})}$) and that in shear ($\boldsymbol{u}'^{(shear)}$) as follows:

$$\boldsymbol{u}'^{(1)}_S = \boldsymbol{u}'^{(shear)} + \boldsymbol{u}'^{(sed\dot{\gamma})}. \tag{4.4}$$

In the equation above, $\dot{\gamma}$ in the superscript of the sedimentation velocity field indicates that it is scaled with $\dot{\gamma}L$ instead of U_{sed}. Substituting (4.4) in (4.3), one can rewrite the volume integral in (4.2) as:

$$\begin{aligned}\int_V \boldsymbol{U}^{(2)}\cdot\nabla\cdot\boldsymbol{\sigma}'^{(1)}dV = Re\int_V \boldsymbol{U}^{(2)}\cdot\Bigg(&\frac{\partial \boldsymbol{u}'^{(shear)}}{\partial t}+\boldsymbol{u}'^{(shear)}\cdot\nabla\boldsymbol{u}'^{(shear)}+(\boldsymbol{\Gamma}.\boldsymbol{x})\cdot\nabla\boldsymbol{u}'^{(shear)}\\ &+\boldsymbol{\Gamma}\cdot\boldsymbol{u}'^{(shear)}\Bigg)dV+Re\int_V \boldsymbol{U}^{(2)}\cdot\Bigg(\frac{\partial \boldsymbol{u}'^{(sed\dot{\gamma})}}{\partial t}+\boldsymbol{u}'^{(sed\dot{\gamma})}\cdot\nabla\boldsymbol{u}'^{(sed\dot{\gamma})}+(\boldsymbol{\Gamma}.\boldsymbol{x})\cdot\nabla\boldsymbol{u}'^{(sed\dot{\gamma})}\\ &+\boldsymbol{\Gamma}\cdot\boldsymbol{u}'^{(sed\dot{\gamma})}\Bigg)dV+Re\int_V \boldsymbol{U}^{(2)}\cdot\left(\boldsymbol{u}'^{(shear)}\cdot\nabla\boldsymbol{u}'^{(sed\dot{\gamma})}+\boldsymbol{u}'^{(sed\dot{\gamma})}\cdot\nabla\boldsymbol{u}'^{(shear)}\right)dV\\ -Re\int_V \boldsymbol{U}^{(2)}\cdot\boldsymbol{1}'_x(\boldsymbol{1}'_y\cdot\boldsymbol{U}_{sed})dV. \qquad (4.5)\end{aligned}$$

The velocity $\boldsymbol{U}_{sed}$ is related to the sedimenting force $\boldsymbol{1}_g$ as $\boldsymbol{U}_{sed}= U_{sed}\,(\frac{1}{6\pi}\,\boldsymbol{1}_g\cdot(\frac{1}{X_A}\boldsymbol{pp}+\frac{1}{Y_A}(\boldsymbol{I}-\boldsymbol{pp})))$, where X_A and Y_A are the axisymmetric and transverse translation coefficients given by $X_A=8/(3\xi_0(-2\xi_0+(1+\xi_0^2)\log((\xi_0+1)/(\xi_0-1)))$ and $Y_A=-16/(3\xi_0(-2\xi_0+(-3+\xi_0^2)\log((\xi_0+1)/(\xi_0-1))))$ for a prolate spheroid (Kim & Karrila 1991). The coefficients for an oblate spheroid can be obtained from those of a prolate spheroid by using the transformation defined in chapter 2, or alternatively, from Kim & Karrila (1991). Noting that $\boldsymbol{1}'_x(\boldsymbol{1}'_y\cdot\boldsymbol{U}_{sed})$ is independent of $\boldsymbol{x}$, and $\boldsymbol{U}^{(2)}$ is an odd function of $\boldsymbol{x}$, it can be seen that the integral in the last term of (4.5) will vanish. Further noting that $\boldsymbol{u}'^{(shear)}$ and $\boldsymbol{u}'^{(sed\dot{\gamma})}$ are respectively odd and even functions of $\boldsymbol{x}$, it can be seen that the integral involving the cross terms in (4.5) also vanishes, and the above equation reduces to:

$$\begin{aligned}\int_V \boldsymbol{U}^{(2)}\cdot\nabla\cdot\boldsymbol{\sigma}'^{(1)}dV = Re\int_V \boldsymbol{U}^{(2)}\cdot\Bigg(&\frac{\partial \boldsymbol{u}'^{(shear)}}{\partial t}+\boldsymbol{u}'^{(shear)}\cdot\nabla\boldsymbol{u}'^{(shear)}+(\boldsymbol{\Gamma}.\boldsymbol{x})\cdot\nabla\boldsymbol{u}'^{(shear)}\\ &+\boldsymbol{\Gamma}\cdot\boldsymbol{u}'^{(shear)}\Bigg)dV+Re\int_V \boldsymbol{U}^{(2)}\cdot\left(\frac{\partial \boldsymbol{u}'^{(sed\dot{\gamma})}}{\partial t}+\boldsymbol{u}'^{(sed\dot{\gamma})}\cdot\nabla\boldsymbol{u}'^{(sed\dot{\gamma})}\right)dV. \qquad (4.6)\end{aligned}$$

The disturbance velocity field in sedimentation, scaled with U_{sed}, is related to the one scaled with $\dot{\gamma}$, in the equation above, through $\boldsymbol{u}'^{(sed\dot{\gamma})}=(Re_{sed}/Re)\boldsymbol{u}'^{(sed)}$. The disturbance velocity field as well as time in the second integral above can be rescaled with the dimensional quantities U_{sed} and L/U_{sed} (t =$(Re/Re_{sed})t_{sed}$) to give:

$$\begin{aligned}\int_V \boldsymbol{U}^{(2)}\cdot\nabla\cdot\boldsymbol{\sigma}'^{(1)}dV = Re\int_V \boldsymbol{U}^{(2)}\cdot\Bigg(&\frac{\partial \boldsymbol{u}'^{(shear)}}{\partial t}+\boldsymbol{u}'^{(shear)}\cdot\nabla\boldsymbol{u}'^{(shear)}+(\boldsymbol{\Gamma}.\boldsymbol{x})\cdot\nabla\boldsymbol{u}'^{(shear)}\\ &+\boldsymbol{\Gamma}\cdot\boldsymbol{u}'^{(shear)}\Bigg)dV+\frac{Re_{sed}}{Re}\int_V Re_{sed}\boldsymbol{U}^{(2)}\cdot\left(\frac{\partial \boldsymbol{u}'^{(sed)}}{\partial t_{sed}}+\boldsymbol{u}'^{(sed)}\cdot\nabla\boldsymbol{u}'^{(sed)}\right)dV. \qquad (4.7)\end{aligned}$$

In Dabade *et al.* (2015), the second integral on the right-hand side above is shown to be equal to the negative of the torque acting on a sedimenting spheroid ($\boldsymbol{L}_{sed}$) contracted with the second order tensor $\boldsymbol{U}^{(2)}$. The torque is given by $\boldsymbol{L}_{sed} = -Re_{sed}F(\xi_0)(\boldsymbol{U}_{sed}\times\boldsymbol{p})(\boldsymbol{U}_{sed}\cdot\boldsymbol{p}) = -Re_{sed}F(\xi_0)(\mathbf{1}_g\times\boldsymbol{p})(\mathbf{1}_g\cdot\boldsymbol{p})/(36\pi^2X_AY_A)$. The function $F(\xi_0)$ is negative for a prolate spheroid and is positive for an oblate spheroid, so the torque acts in a way to make $\boldsymbol{p}$ perpendicular to $\mathbf{1}_g$ for a prolate spheroid and make $\boldsymbol{p}$ align with $\mathbf{1}_g$ for an oblate spheroid. After substituting the sedimentation torque in the second integral in (4.7) one can rewrite (4.2) as:

$$\begin{aligned}\boldsymbol{\Omega}_1.\mathscr{L}_2 =\boldsymbol{\Gamma}:\int_{S_p}\boldsymbol{x}(\boldsymbol{\Sigma}^{(2)}\cdot\boldsymbol{n})dS+\boldsymbol{U}^{(2)}\cdot\left(St\frac{d}{dt}\boldsymbol{I}.\boldsymbol{\Omega_1}\right)+Re\int_V\boldsymbol{U}^{(2)}\cdot\Bigg(&\frac{\partial\boldsymbol{u}'^{(shear)}}{\partial t}\\ +\boldsymbol{u}'^{(shear)}\cdot\nabla\boldsymbol{u}'^{(shear)}+(\boldsymbol{\Gamma}.\boldsymbol{x})\cdot\nabla\boldsymbol{u}'^{(shear)}+\boldsymbol{\Gamma}\cdot\boldsymbol{u}'^{(shear)}\Bigg)dV&\\ +\frac{Re_{sed}^2}{36Re\pi^2X_AY_A}\boldsymbol{U}^{(2)}.(F(\xi_0)(\mathbf{1}_g\times\boldsymbol{p})(\mathbf{1}_g.\boldsymbol{p}))& \qquad (4.8)\end{aligned}$$

Note that the first three terms in the above reciprocal theorem are the same as those seen in chapter 2 for simple shear flow alone. The last term on the right-hand side of (4.8) is the contribution due to the sedimentation. The reciprocal theorem above is simplified for a force aligned in an arbitrary direction with respect to the simple shear flow in the next section.

4.3 Sedimentation along an arbitrary direction with respect to flow

As in chapter 2, we evaluate the reciprocal theorem in a body aligned coordinate system defined by the unit vectors $\mathbf{1}_x = \cos\theta_j\cos\phi_j\mathbf{1}'_x+\cos\theta_j\sin\phi_j\mathbf{1}'_y-\sin\theta_j\mathbf{1}'_z$, $\mathbf{1}_y = -\sin\phi_j\mathbf{1}'_x+\cos\phi_j\mathbf{1}'_y$ and $\mathbf{1}_z = \sin\theta_j\cos\phi_j\mathbf{1}'_x+\sin\theta_j\sin\phi_j\mathbf{1}'_y+\cos\theta_j\mathbf{1}'_z$ (see figure 2.2). The angular velocity $\boldsymbol{\Omega}_1$ can be expanded as $\boldsymbol{\Omega}_1$= $\boldsymbol{\Omega}_{jeff}$+ $Re\boldsymbol{\Omega}_{Re}$. Defining $\mathbf{1}_g = 1_g^x\mathbf{1}_x+1_g^y\mathbf{1}_y+1_g^z\mathbf{1}_z$ and

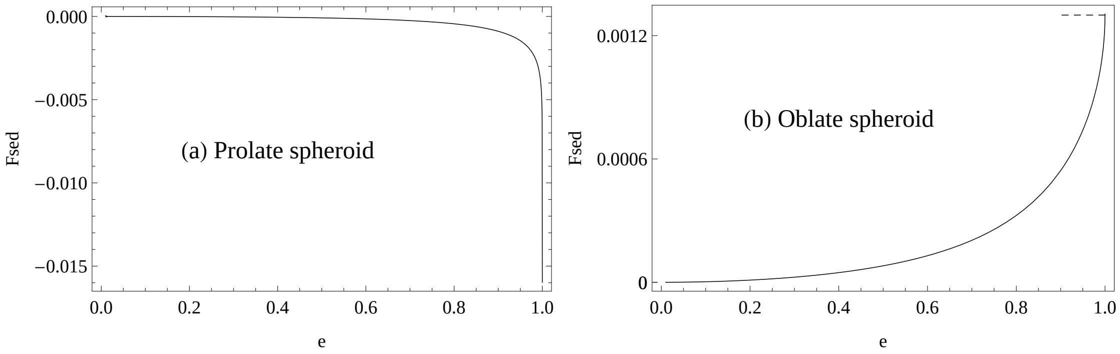

Fig. 4.1 F_{sed} plotted against eccentricity for (a) prolate spheroid (b) oblate spheroid. It diverges as $\log\kappa$ for prolate spheroid as eccentricity goes to 1 and is a constant for oblate spheroid, in this limit.

$\mathbf{\Omega}_{Re} = -\dot{\phi}_j \sin\theta_j \mathbf{1}_x + \dot{\theta}_j \mathbf{1}_y + \dot{\phi}_j \cos\theta_j \mathbf{1}_z$, and substituting in (4.8) one gets at O(Re):

$$\dot{\phi}_j = \frac{St}{Re}\dot{\phi}_j^{\,part} + \dot{\phi}_j^{\,fluid} + \left(\frac{Re_{sed}}{Re}\right)^2 \frac{F_{sed}(\xi_0)}{\sin\theta_j} 1_g^y 1_g^z, \tag{4.9}$$

$$\dot{\theta}_j = \frac{St}{Re}\dot{\theta}_j^{\,part} + \dot{\theta}_j^{\,fluid} + \left(\frac{Re_{sed}}{Re}\right)^2 F_{sed}(\xi_0)\, 1_g^x 1_g^z, \tag{4.10}$$

where

$$F_{sed}(\xi_0) = \frac{F(\xi_0)}{288\pi^3 X_A Y_A Y_c}. \tag{4.11}$$

The angular velocities $\dot{\theta}_j^{\,part}$, $\dot{\phi}_j^{\,part}$, $\dot{\theta}_j^{\,fluid}$ and $\dot{\phi}_j^{\,fluid}$ in (4.9-4.10) are defined in equations (2.77) (2.78), (2.93) and (2.94) respectively. The angular dependence of these terms are therefore known. The third term on the right-hand side of each of (4.9) and (4.10) is due to sedimentation. The angular dependence of these terms would depend on the orientation of the sedimenting force, while the amplitude would depend on $F_{sed}(\xi_0)$, which is plotted for prolate and oblate spheroids in figures 4.1 a and b. The function asymptotes to a constant for flat disk ($\kappa \to 0$) and that for a slender fibre ($\kappa \to \infty$) diverges as $\log\kappa$.

As seen in chapter 2, there are two approaches to understand the orientation dynamics of the spheroid. The first brute-force approach is to numerically integrate the set of differential equations governing θ_j and ϕ_j, obtained by adding the angular velocities given in (4.9) and (4.10) and the corresponding leading order angular velocities given in equations (2.29) and

(2.30), to obtain the trajectories on the unit sphere. However, doing the numerical integration for various combinations of nondimensional parameters (St/Re, Re_{shear}/Re and κ), and for all possible initial orientation on the unit sphere, is cumbersome, and is not pursued further here. Since the correction to the angular velocities are small, one would expect the orbit of a spheroid to be approximately equal to a Jeffery orbit during a period of rotation. Therefore we approximate C, the orbital coordinate of the spheroid defined in chapter 2, as a constant over a period of rotation. The change in C during a single Jeffery period in the presence of sedimentation and inertia, defined as ΔC_{ss}, can be derived in a manner similar to that in chapter 2 and is given by:

$$\Delta C_{ss} = \int_0^{T_{jeff}} \frac{dC}{dt} dt, \tag{4.12}$$

$$= (\frac{d\tau}{dt})^{-1} \int_0^{2\pi} \frac{dC}{dt} d\tau, \tag{4.13}$$

$$= Re\frac{\kappa^2+1}{\kappa} \int_0^{2\pi} C \left(\frac{1}{\sin\theta_j \cos\theta_j} \left(\frac{d\theta_j}{dt}\right) + \frac{(\kappa^2-1)\cos\phi_j \sin\phi_j}{\kappa^2 \sin^2\phi_j + \cos^2\phi_j} \left(\frac{d\phi_j}{dt}\right) \right) d\tau, \tag{4.14}$$

with $\frac{d\phi_j}{dt}$ and $\frac{d\theta_j}{dt}$ defined in (4.9) and (4.10). Characterizing the trajectories corresponding to all possible initial orientations is equivalent to examining ΔC_{ss} over the entire range of C's.

To evaluate the drift above, one needs to know the orientation of the sedimenting force. To begin with, we consider the force to be aligned with any of the the vorticity, the gradient and the flow axes of the simple shear flow. The response of a spheroid to an arbitrarly aligned force can be easily obtained from the three cases mentioned above. The drifts are presented for these three cases in the next three sections. It turns out that the drift is of the same form as we have encountered in chapter 2 and is given by:

$$\Delta C_{ss} = ReC\frac{\kappa^2+1}{\kappa}\left\{\left[I_1F_1^s(\xi_0,\frac{Re_{sed}}{Re},\frac{St}{Re}) + I_2F_2^s(\xi_0,\frac{Re_{sed}}{Re},\frac{St}{Re}) + I_3F_3^s(\xi_0,\frac{Re_{sed}}{Re},\frac{St}{Re}) + I_4F_4^s(\xi_0,\frac{Re_{sed}}{Re},\frac{St}{Re}) + I_5F_5^s(\xi_0,\frac{Re_{sed}}{Re},\frac{St}{Re}) + I_6F_6^s(\xi_0,\frac{Re_{sed}}{Re},\frac{St}{Re})\right] + \left[J_1G_1^s(\xi_0,\frac{Re_{sed}}{Re},\frac{St}{Re}) + J_2G_2^s(\xi_0,\frac{Re_{sed}}{Re},\frac{St}{Re}) + J_3G_3^s(\xi_0,\frac{Re_{sed}}{Re},\frac{St}{Re}) + J_4G_4^s(\xi_0,\frac{Re_{sed}}{Re},\frac{St}{Re})\right]\right\}, \tag{4.15}$$

with functions F_i^s and G_i^s are defined for the three cases mentioned above, in sections that follow, and I's and J's defined in Appendix A. When $Re_{sed}/Re = 0$, these functions take the form $F_i^s = \frac{St}{Re}F_i^p + F_i^f$ and $G_i^s = \frac{St}{Re}G_i^p + G_i^f$, and these are defined in chapter 2. We analyze the drift for the simplest case in which the sedimentation force is aligned with the vorticity axis in section 4.4, followed by the case in which it is aligned with the flow axis in section 4.5, and finally the case in which it is aligned with the gradient axis, in section 4.6.

4.4 Sedimentation along vorticity axis

In this section we analyze the orientation dynamics of a spheroid rotating in a simple shear flow but subjected to a force aligned with the vorticity axis. In this alignment, the sedimentation force will try to push the orientation vector of a prolate spheroid towards the flow-gradient plane, and that of an oblate spheroid towards the vorticity axis. Thus, the drift due to sedimentation should be positive for a prolate spheroid and negative for an oblate spheroid. The force, when expressed in the body aligned coordinate system, takes the form:

$$\boldsymbol{F} = -sin\theta_j \mathbf{1}_x + \cos\theta_j \mathbf{1}_z \tag{4.16}$$

For a spheroid, the angular velocities given in (4.9)-(4.10) take the form:

$$\dot{\phi}_j = \frac{St}{Re}\dot{\phi}_j^{\,part} + \dot{\phi}_j^{\,fluid}, \tag{4.17}$$

$$\dot{\theta}_j = \frac{St}{Re}\dot{\theta}_j^{\,part} + \dot{\theta}_j^{\,fluid} - \left(\frac{Re_{sed}}{Re}\right)^2 F_{sed}\sin\theta_j\cos\theta_j\,. \tag{4.18}$$

Thus, the contribution due to sedimentation only affects $\dot{\theta}_j$. From figure 4.1 it can be noted that F_{sed} is negative for a prolate spheroid and positive for an oblate spheroid and therefore sedimentation pushes a prolate spheroid towards the tumbling and an oblate one towards the spinning orbit. The drift takes the form in (4.15) with functions therein given by:

$$F_i^s = \frac{St}{Re}F_i^p + F_i^f, (i = 2, ..6), \tag{4.19}$$

$$G_i^s = \frac{St}{Re}G_i^p + G_i^f (i = 1, ..4), \tag{4.20}$$

$$F_1^s = \frac{St}{Re}F_1^p + F_1^f - \left(\frac{Re_{sed}}{Re}\right)^2 F_{sed}. \tag{4.21}$$

For O(1) values of St/Re, the drift due to particle inertia is small compared to that due to fluid inertia, as seen in chapter 2. We analyze the drift due to (4.17-4.18) for $St/Re = 2$. For this St/Re, and in the absence of sedimentation ($Re_{sed}/Re = 0$), a repeller exists only for oblate spheroids whose aspect ratios are less than 0.131. For various values of the nondimensional parameter Re_{sed}/Re, the drift is plotted for prolate spheroids of aspect ratios 70.7($\xi_0 = 1.001$)

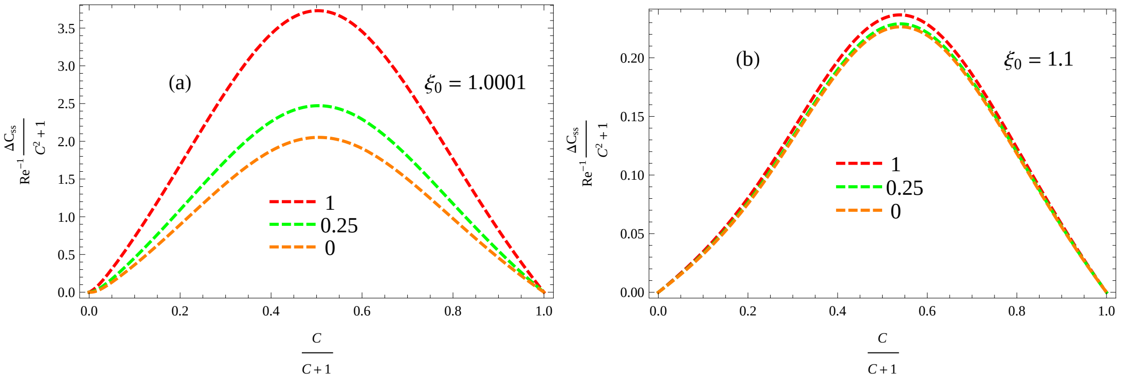

Fig. 4.2 The drift is plotted for prolate spheroids of aspect ratio (a) 70.7 and (b) 2.4 sedimenting due to a force along the vorticity axis. The drift is positive for $Re_{sed}/Re = 0$ and remains positive for all values of Re_{sed}/Re.

and 2.4($\xi_0 = 1.1$) in figure 4.2, and for oblate spheroids of aspect ratios 0.014($\xi_0 = 1.0001$), 0.044($\xi_0 = 1.001$) and 0.3($\xi_0 = 1.051$) in figure 4.3. When the nondimensional parameter Re_{sed}/Re is zero, the inertial effects stabilize the tumbling orbit for a prolate spheroid. As explained above, sedimentation also results in a drift towards the tumbling orbit. Thus, the drift due to the combined effect of sedimentation and shear, increases with Re_{sed}/Re as shown in figure 4.2. For oblate spheroids with aspect ratios larger than 0.131(see figure 4.3 e) the sole attractor is the spinning orbit at $Re_{sed}/Re = 0$. Similar to prolate, sedimentation only results in an increase in the drift rate, with increasing value of the non-dimensional parameter . For oblate spheroids of aspect ratio less than 0.131, a repeller exists dividing the orientation space into two distinct basins of attraction at $Re_{sed}/Re = 0$ (see 4.3 a and c,). In these figures, the repeller locations correspond to the C location at which the drift changes its sign. As Re_{sed}/Re increases, the repeller shift towards the tumbling orbit, and at a critical Re_{sed}/Re (marked in red color), merges with the tumbling orbit making the spinning orbit the sole attractor for the whole orientation space.

4.5 Sedimentation along flow axis

In this section we analyze the orientation dynamics of a spheroid rotating in a simple shear flow but subjected to a force aligned with the flow axis. In this alignment, the sedimentation force will try to push the orientation vector of a prolate spheroid towards the gradient-vorticity plane and that of an oblate spheroid towards the flow axis. One would then expect sedimentation to affect both $\dot{\theta}_j$ and $\dot{\phi}_j$. The force when expressed in the body aligned coordinate system takes

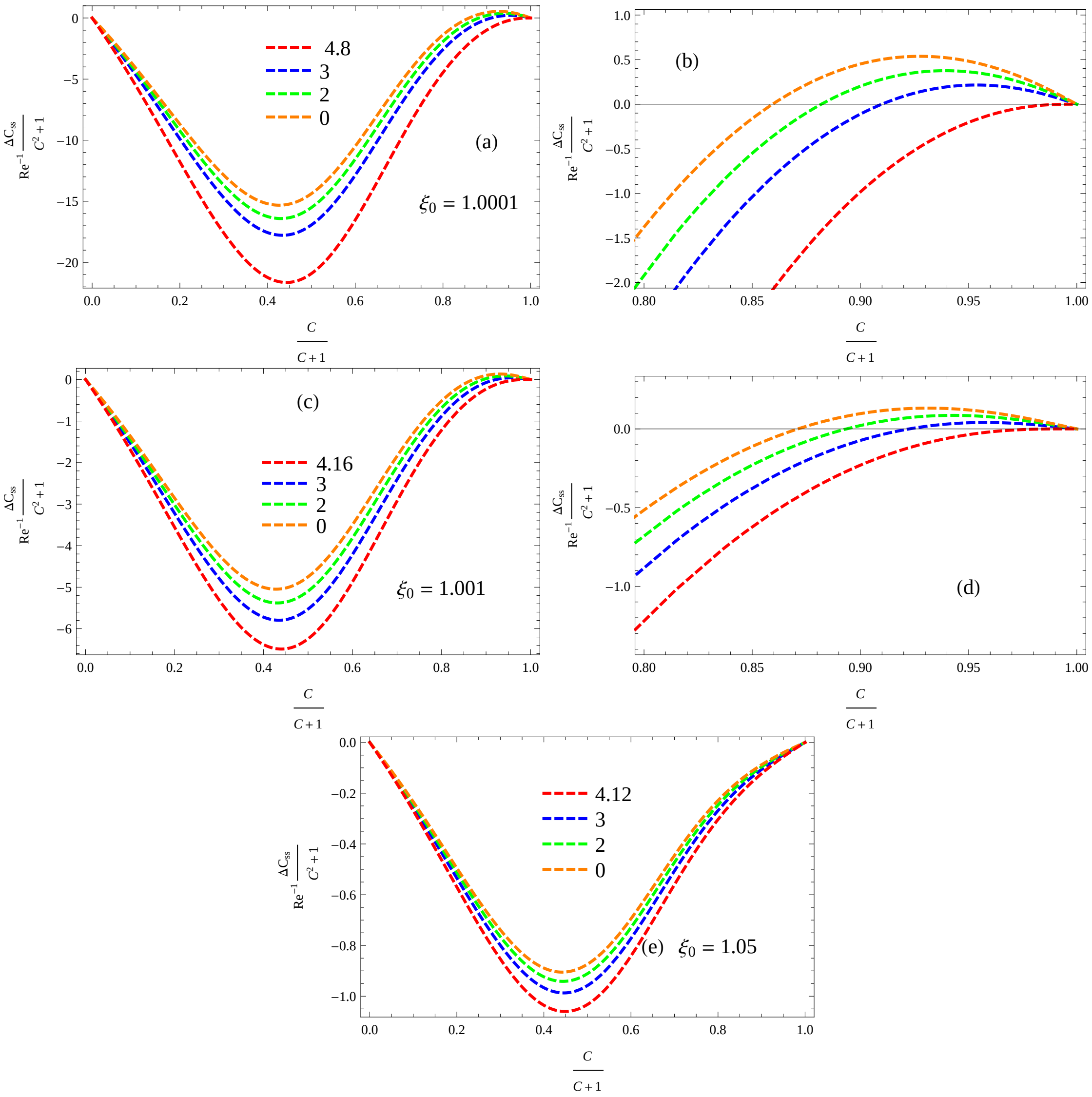

Fig. 4.3 The drift is plotted for oblate spheroids of aspect ratio (a) 0.014 (c).044 and (e) 0.3 sedimenting due to a force along the vorticity axis. The zoomed view of (a) and (c) are shown in (b) and (d). The repeller moves towards the tumbling orbit with increasing Re_{sed}/Re for both aspect ratios.

the form:

$$\boldsymbol{F} = \cos\theta_j \cos\phi_j \mathbf{1}_x - \sin\phi_j \mathbf{1}_y + \sin\theta_j \cos\phi_j \mathbf{1}_z. \tag{4.22}$$

The angular velocities of the spheroid take the form:

$$\dot{\phi}_j = \frac{St}{Re}\dot{\phi}_j^{\,part} + \dot{\phi}_j^{\,fluid} - \left(\frac{Re_{sed}}{Re}\right)^2 F_{sed} \sin\phi_j \cos\phi_j \tag{4.23}$$

$$\dot{\theta}_j = \frac{St}{Re}\dot{\theta}_j^{\,part} + \dot{\theta}_j^{\,fluid} + \left(\frac{Re_{sed}}{Re}\right)^2 F_{sed} \sin\theta_j \cos\theta_j \cos^2\phi_j. \tag{4.24}$$

The drift takes the form in (4.15) with the functions therein defined as:

$$F_i^s = \frac{St}{Re}F_i^p + F_i^f \, (i = 3, ..6), \tag{4.25}$$

$$G_i^s = \frac{St}{Re}G_i^p + G_i^f \, (i = 2, ..4), \tag{4.26}$$

$$F_1^s = \frac{St}{Re}F_1^p + F_1^f + (1/2)F_{sed}, \tag{4.27}$$

$$F_2^s = \frac{St}{Re}F_2^p + F_2^f + (1/2)F_{sed}, \tag{4.28}$$

$$G_1^s = \frac{St}{Re}G_i^p + G_i^f - \left(\frac{Re_{sed}}{Re}\right)^2 F_{sed}. \tag{4.29}$$

The contribution due to sedimentation pushes a prolate spheroid towards the spinning and an oblate one towards the tumbling orbit. We fix $St/Re = 2$, similar to the vorticity case analyzed in the previous section.The drift is plotted for various values of the nondimensional parameter, Re_{sed}/Re, for prolate spheroids of aspect ratios 70.7($\xi_0 = 1.001$) and 2.4($\xi_0 = 1.1$) in figure 4.4, and for oblate spheroids of aspect ratios 0.014($\xi_0 = 1.0001$) and 0.3($\xi_0 = 1.051$) in figure 4.5. The prolate spheroid has only a single attractor at $Re_{sed}/Re = 0$ which is the tumbling orbit. With increasing Re_{sed}/Re, at first a repeller emerges from the spinning orbit (green curves) and then moves towards the tumbling orbit, eventually coinciding with it (red curves). The spinning orbit remains the sole attractor for Re_{sed}/Re values larger than that corresponding to the red curve. For an oblate spheroid of aspect ratio less than 0.131 (see figure 4.5 a), the repeller present at $Re_{sed}/Re = 0$ shifts towards the spinning orbit with increasing Re_{sed}/Re, and eventually coincides with the spinning orbit(red curve). For Re_{sed}/Re larger than the one corresponding to that of the red curve, the tumbling orbit remains the sole attractor. For oblate spheroids of aspect ratio larger than 0.131 (see figure 4.5 c), the spinning orbit is the sole attractor at $Re_{sed}/Re = 0$. However with increasing Re_{sed}/Re, a repeller emerges from the

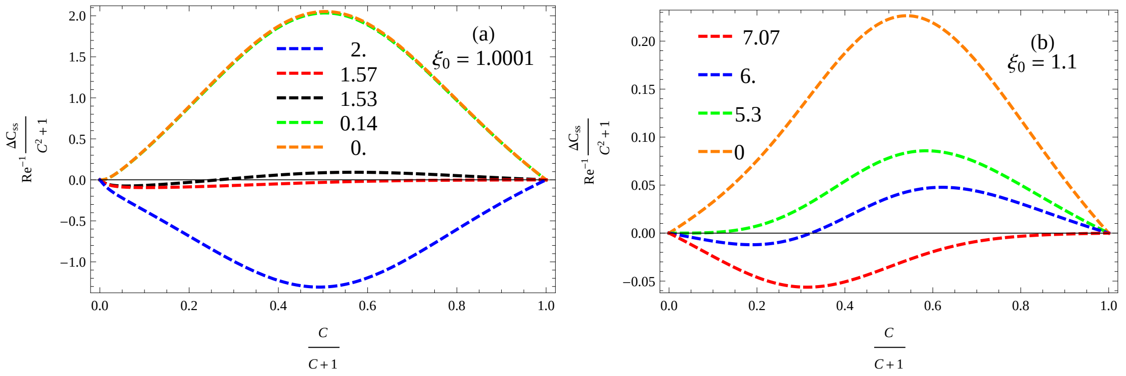

Fig. 4.4 The drift is plotted for prolate spheroids of aspect ratio (a)70.7 and (b)2.4 sedimenting due to a force along the flow axis.

tumbling orbit (green curve), and then moves towards the spinning orbit eventually coinciding with it (red), making the tumbling orbit the sole attractor for larger Re_{sed}/Re values.

4.6 Sedimentation along gradient axis

In this section we analyze the orientation dynamics of a spheroid rotating in a simple shear flow but subjected to a force aligned with the gradient axis. In this alignment, the sedimentation force will try to push the orientation vector of a prolate spheroid towards the flow-vorticity plane and that of an oblate spheroid towards the gradient axis. The force when expressed in the body aligned coordinate system takes the form:

$$\boldsymbol{F} = \cos\theta_j \sin\phi_j \mathbf{1}_x + \cos\phi_j \mathbf{1}_y + \sin\theta_j \sin\phi_j \mathbf{1}_z. \tag{4.30}$$

The angular velocities of the spheroid take the form:

$$\dot{\phi}_j = \frac{St}{Re}\dot{\phi}_j^{\,part} + \dot{\phi}_j^{\,fluid} + \left(\frac{Re_{sed}}{Re}\right)^2 F_{sed} \sin\phi_j \cos\phi_j \tag{4.31}$$

$$\dot{\theta}_j = \frac{St}{Re}\dot{\theta}_j^{\,part} + \dot{\theta}_j^{\,fluid} + \left(\frac{Re_{sed}}{Re}\right)^2 F_{sed} \sin\theta_j \cos\theta_j \sin^2\phi_j. \tag{4.32}$$

The drift takes the form in (4.15) with functions given by :

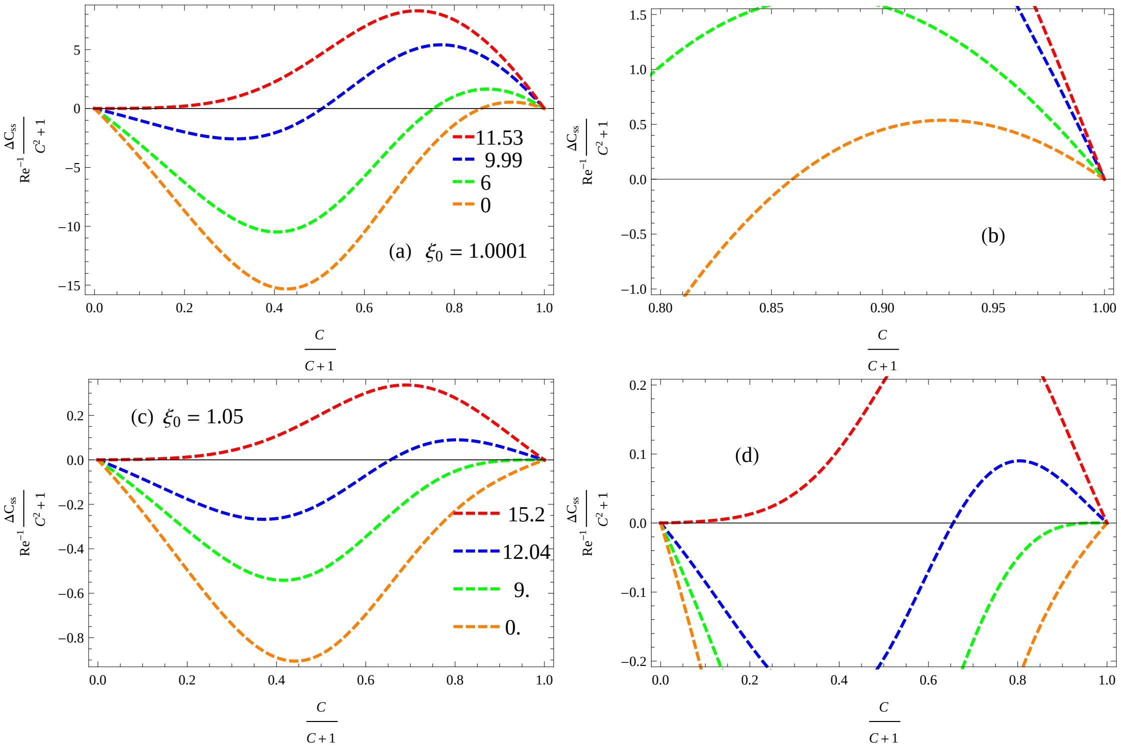

Fig. 4.5 The drift is plotted for oblate spheroids of aspect ratio (a)0.014 and (c)0.3 sedimenting due to a force along the flow axis. The zoomed views of (a) and (c) are shown in (b) and (d). The repeller moves towards the spinning orbit with increasing Re_{sed}/Re for both aspect ratios.

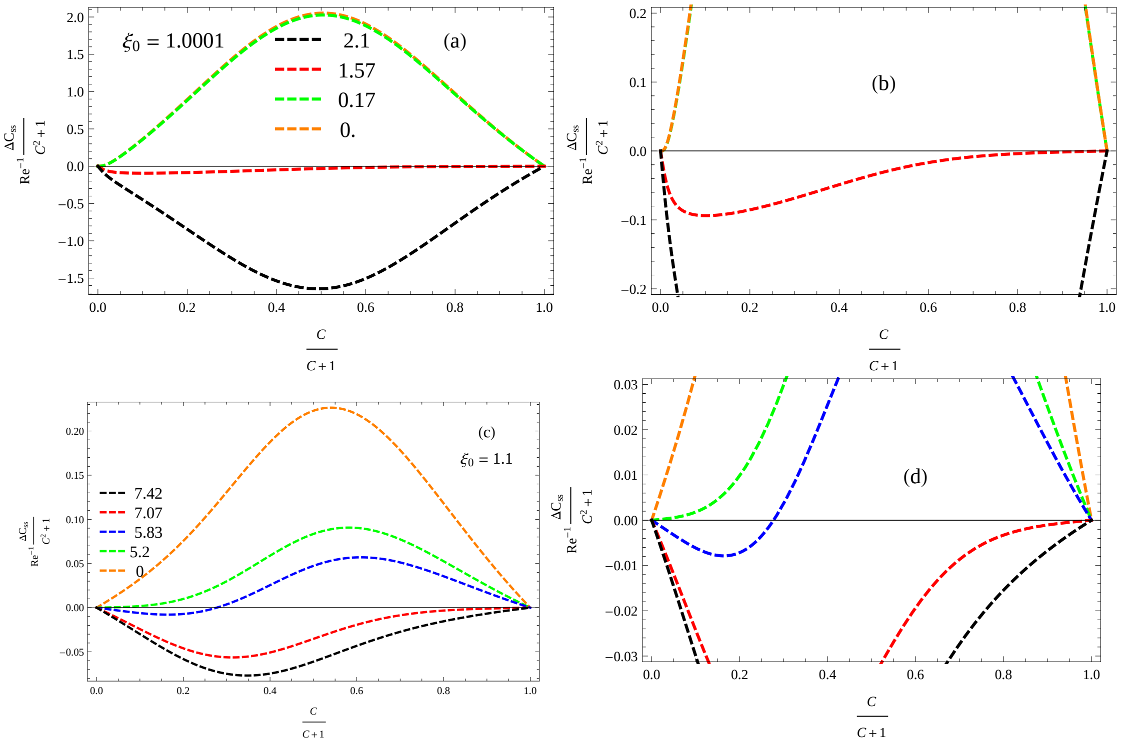

Fig. 4.6 The drift is plotted for prolate spheroids of aspect ratio (a)70.7 and (b)2.4 sedimenting due to a force along the gradient axis. The zoomed views of (a) and (c) are shown in (b) and (d).

$$F_i^s = \frac{St}{Re} F_i^p + F_i^f (i = 3, ..6), \tag{4.33}$$

$$G_i^s = \frac{St}{Re} G_i^p + G_i^f (i = 2, ..4), \tag{4.34}$$

$$F_1^s = \frac{St}{Re} F_1^p + F_1^f + (1/2) F_{sed}, \tag{4.35}$$

$$F_2^s = \frac{St}{Re} F_2^p + F_2^f - (1/2) F_{sed}, \tag{4.36}$$

$$G_1^s = \frac{St}{Re} G_i^p + G_i^f + \left(\frac{Re_{sed}}{Re}\right)^2 F_{sed}. \tag{4.37}$$

The contribution due to sedimentation pushes a prolate spheroid towards the spinning orbit, and an oblate one towards the tumbling orbit. Again we fix $St/Re = 2$. The drift is plotted for various values of the nondimensional parameter, Re_{sed}/Re, for prolate spheroids of aspect ratios 70.7($\xi_0 = 1.001$) and 2.4($\xi_0 = 1.1$) in figure 4.6, and for oblate spheroids of aspect ratios 0.014($\xi_0 = 1.0001$) and 0.3($\xi_0 = 1.051$) in figure 4.7. The prolate spheroid has only a single attractor at $Re_{sed}/Re = 0$ which is the tumbling orbit. Like the flow aligned case seen in the previous section, with increasing Re_{sed}/Re, at first a repeller emerges from the spinning orbit (green curves), and then moves towards the tumbling orbit, eventually coinciding with it (red curves), and the spinning orbit remains the sole attractor thereafter. For an oblate spheroid with aspect ratio less than 0.131 (figure 4.7 a), the repeller present at $Re_{sed}/Re = 0$ shifts towards the spinning orbit with increasing Re_{sed}/Re and eventually coincides with the spinning orbit(red curves). For oblate spheroids of aspect ratio larger than 0.131 (figure 4.7 c), the spinning orbit is the sole attractor at $Re_{sed}/Re = 0$. However with increasing Re_{sed}/Re, a repeller emerges from the tumbling orbit (green curve) and then eventually move towards the spinning orbit and eventually coinciding with it (red), making the tumbling orbit the sole attractor for larger Re_{sed}/Re values.

4.7 Limitations of drift analysis

In this section we look at the limitation of the average drift analysis presented in previous sections. The drift analysis is based on the approximation that the initial orbital coordinate C of a spheroid is constant over a time period of rotation. As already seen in chapter 2, this approximation can be formally derived from a multiple scale analysis. The average drift analysis eliminates the need to numerically integrate the angular velocities for initial conditions ranging over the entire unit sphere for understanding the orientation dynamics of the spheroid. However, this analysis has certain limitations and we discuss them below. We will rewrite

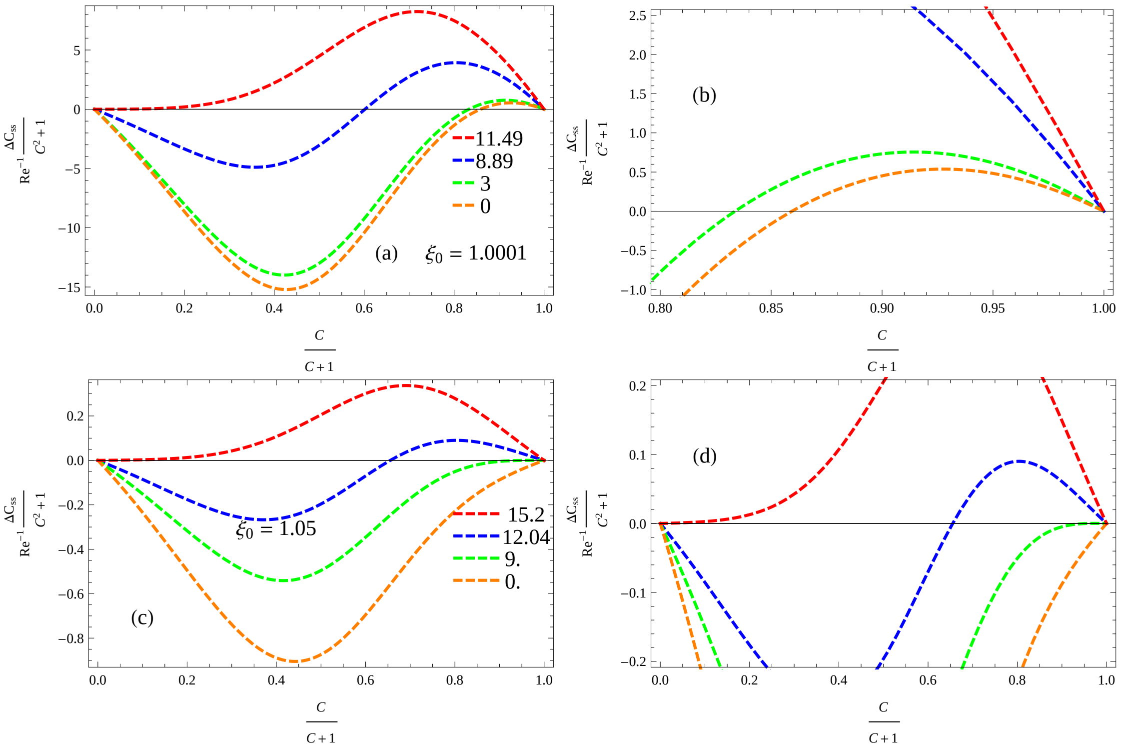

Fig. 4.7 The drift is plotted for oblate spheroids of aspect ratio (a)0.014 and (c)0.3 sedimenting due to a force along the gradient axis. The zoomed views of (a) and (c) are shown in (b) and (d). The repeller moves towards the spinning orbit with increasing Re_{sed}/Re for both aspect ratios.

(4.15) as follows:

$$\Delta C_{ss} = \Delta C_p + \Delta C_f + Re\, C\, \frac{\kappa^2+1}{\kappa} \left(\frac{Re_{sed}}{Re}\right)^2 \left(I_1 F_1^s + I_2 F_2^s + J_1 G_1^s\right), \tag{4.38}$$

where F_1^s, F_2^s and G_1^s are defined in previous sections for the three canonical cases. In (4.38), ΔC_p and ΔC_f are the contributions to drift due to particle and fluid inertia presented in chapter 2, and the third term is the contribution due to sedimentation. The contribution due to particle and fluid inertia comes at O(St) and O(Re) whereas that due to sedimentation comes at O(Re_{sed}^2/Re), and the latter contribution is proportional to C. The analytical approximation would be valid when the constraint $\Delta C_{ss}/C << 1$ is satisfied. For neutrally buoyant spheroids of O(1) aspect ratios this would impose the condition $Re_{sed}^2 < Re$ and $Re < 1$. Provided Re is sufficiently small, this restriction on Re_{sed} is satisfied for the spheroids of O(1) aspect ratios analyzed in earlier sections.

To illustrate that the average drift analysis and the drift obtained from numerical integration of the angular velocities compare well, we have plotted the drift predicted using both methods in figure 4.8 for an oblate spheroid subjected to a sedimentation force along the gradient direction. The oblate spheroid is of an aspect ratio 0.3 ($\xi_0 = 1.05$), and the average drift analysis predicts that, for an $\frac{Re_{sed}}{Re}$ of 12.04, a repeller exists at $C = 1.85$, and therefore, the drift is negative for $C < 1.85$ and positive $C > 1.85$ (see figure 4.7 c). In figure 4.8, the drifts are plotted against $|\phi_j|$, with the red curve corresponding to the change in C predicted by the average drift analysis, and the blue curve corresponding to that obtained from the numerical integration of angular velocities. The initial C value is above $C = 1.85$ in figure 4.8 a, and below $C = 1.85$ in figure 4.8 b. As is evident, the average drift analysis is a good approximation for the average of the drift from numerical integration, and the repeller location predicted by the average drift analysis is also consistent with that observed from the numerical integration.

In the case of oblate spheroids of extreme aspect ratios ($\kappa \to 0$), the sedimentation contribution in (4.38) is proportional to $CRe_{sed}^2/(Re\kappa)$ and the inertial contributions are proportional to ReC/κ. Note that F_{sed} for an oblate spheroid is a constant in the limit of $\kappa \to 0$ as seen in figure 4.1 b and therefore F_1^s, F_2^s and G_1^s in (4.38) are also constants. The drift analysis is valid when $Re < \kappa$ and $Re_{sed}^2 < Re$. Recall that in chapter 2, we had already seen that the constraint $Re < \kappa$ is necessary for the validity of the average inertial drift. Provided this constraint is met, the range of Re_{sed} for which the drift analysis is valid would be given by Re_{sed} less than approximately $20\sqrt{Re}$, which is satisfied in the cases considered in previous section (the maximum value of Re_{sed}/Re where a significant change in the repeller behaviour occurs is 11.49).

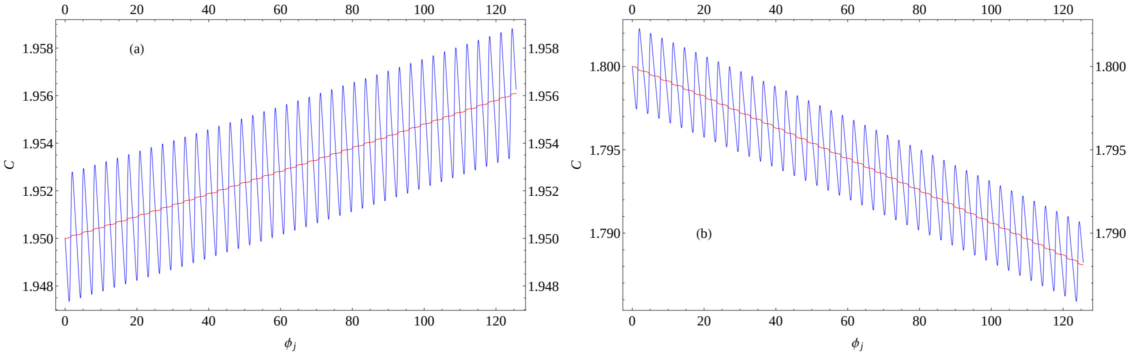

Fig. 4.8 The drift is plotted against angular coordinate ϕ_j for an oblate spheroid of aspect ratio 0.3. The prediction from the average drift analysis (red) and the numerical integration (blue) are plotted starting from Cs on the either side of the repeller.

In the case of prolate spheroid of extreme aspect ratios ($\kappa \to \infty$), the sedimentation contribution in ΔC_{ss} is proportional to $C\kappa \log \kappa Re_{sed}^2/Re$ and the inertial contribution is proportional to $ReC\kappa$. Note that F_{sed} diverges as O($\log \kappa$) in the limit of $\kappa \to \infty$ as seen in figure 4.1 and therefore F_1^s, F_2^s and G_1^s in (4.38) also diverge as $\log \kappa$. So for the drift analysis to be valid, one gets $Re < \kappa$ and Re_{sed} less than approximately $22.45\sqrt{Re/(\kappa \log \kappa)}$ which is satisfied in the cases considered in previous section (the maximum value of Re_{sed}/Re where a significant change in the repeller behaviour occurs is 1.57).

4.8 Conclusions

In this chapter we have investigated the effects of sedimentation on a spheroid rotating in a simple shear flow. The inertial effects on the orientation dynamics of a spheroid in the absence of sedimentation is already analyzed in chapter 2. A reciprocal theorem formulation was used to obtain the angular velocity of the spheroid in the presence of sedimentation. The angular velocities of the spheroid, while sedimenting due to a force aligned arbitrarily with respect to the simple shear flow, are given in equations (4.9) and (4.10). The angular velocities for the canonical cases of the force being aligned with vorticity, flow and gradient axes are analyzed in sections 4.4-4.6. For O(1) values St/Re, it is found that the drift due to sedimentation opposes that due to inertial effects in the simple shear flow, when the force is aligned with the gradient or the flow axes, and it complements each other when the force is aligned with the vorticity. The limitations of the drift analysis are discussed in section 4.7. It is shown that the average drift analysis is reasonably good in predicting the repeller locations as well as the final stabilized orbits in the cases considered here.

Chapter 5

The time period of rotation of a spheroid in simple shear flow

5.1 Introduction

In the Stokes limit, it is well known that in simple shear flow a spheroid rotates in any of a one parameter family of orbits (Jeffery 1922), eponymously called the Jeffery orbits. The generic Jeffery orbit is a spherical ellipse corresponding to a time-dependent three-dimensional precessional motion of the orientation vector about the vorticity axis. The limiting members of the aforementioned family are the tumbling orbit, a great circle in the flow-gradient plane, and the spinning orbit, where the angular velocity vector is time independent and aligned with ambient vorticity(see figures 5.1 (a) and (b)). In the Stokes limit a spheroid will continue to rotate in a Jeffery orbit determined by its initial orientation for all time. It was shown in chapter 2 that weak inertia in the suspending fluid and that of the particle, at O(*Re*) and O(*St*), respectively, stabilize either the spinning or the tumbling orbit. Here, *Re* and *St* are the Reynolds and the Stokes numbers with $Re = \dot{\gamma}L^2\rho/\mu$ and $St = \dot{\gamma}L^2\rho_p/\mu$, where $\dot{\gamma}$ is the shear rate corresponding to the ambient flow, L is the length of the semi-major axis of the spheroid, μ is the viscosity of the fluid, and ρ and ρ_p are the densities of the fluid and particle respectively. The time period of rotation at leading order is given by $T_{jeff} = 2\pi\dot{\gamma}^{-1}(\kappa + 1/\kappa)$ in the tumbling orbit and 4π in the spinning orbit. Here, $\kappa = L/b(b/L)$ is the aspect ratio of the prolate(oblate) spheroid, with b being the semi-minor axis of the spheroid. A recent simulation (Mao & Alexeev 2014) has shown that, fluid inertia increases the time period of rotation in the stable orbits from its leading order Jeffrey value, although the simulation had largely explored *Re*'s of order unity; the small *Re* regime, characterizing the first effects of inertia has not been systematically investigated. This simulation has also shown that the time period of rotation in the stable orbits decreases from its Jeffery value in the presence of particle inertia. In this chapter, we will investigate the effect of inertia on the time period of rotation in the stable orbits. To begin with, the effects of inertia at O(Re) and O(St) on the time period are investigated based on the angular velocities derived in chapter 2, and it is shown that the inertia at these orders do not alter the time period from its leading order value. It turns out that the time period gets altered due to corrections at O($Re^{3/2}$) and O(St^2).

The estimation of the O(St^2) correction to the angular velocity of a spheroid in a simple shear flow is straightforward due to the regular nature of the problem. In a simple shear flow, the O($Re^{3/2}$) correction arises due to the fluid inertial effects in the regions of order and beyond the inertial screening length defined as $LRe^{-1/2}$ ($Re << 1$). In this so-called outer region, the Stokes approximation breaks down and the inertial forces balance the viscous forces. The aforementioned inertial screening length can be obtained from this precise balance as follows: the Stokes disturbance field due to a spheroid in simple shear flow decays as $1/r^2$. Here, r is the distance from the center of the spheroid. The inertial term would scale as Re/r^2 and the viscous term would scale as $1/r^4$ and the balancing of these terms would give $r \sim Re^{-1/2}$. To calculate the effects of fluid inertia based on an analysis of the outer region is non-trivial. Saffman (1965) had estimated the lift force on a translating sphere 'slipping' past an ambient simple shear flow using an analysis based on the outer region. The Fourier space analysis in Saffman (1965) was originally used in Childress (1964) in the context of estimating the correction to the well known Stokes' drag formula for a sphere. In the rheological context, Lin *et al.* (1970*b*) (also see Stone *et al.* (2000)) analyzed the effects of fluid inertia at O($Re^{3/2}$) in order to characterize the O(ϕ) rheology of a dilute suspension of rigid neutrally buoyant spheroids; Here, ϕ is the volume fraction of the suspended spheres. Specifically in Lin *et al.* (1970*b*), a matched asymptotics expansion was used to estimate the O($\phi Re^{3/2}$) correction to the viscosity of a suspension of rigid spheres, which contributes to a shear thickening rheology. Stone *et al.* (2000) redid the calculation using a concise Fourier-space formulation based on the reciprocal theorem by treating the sphere as a force-dipole singularity. The concise formulation was used by Subramanian *et al.* (2011) to characterize the complete non-Newtonian rheology of an emulsion to O($\phi Re^{3/2}$), for arbitrary ratios of the viscosity of the disperse (drop) phase to the continuous phase. Note that in all the above mentioned cases, the leading order disturbance velocity field due to the particle is steady on account of its spherical shape. The steady disturbance velocity field around the spherical particle also allows one to calculate the correction to the angular velocity at O($Re^{3/2}$) (Stone *et al.* 2000; Subramanian *et al.* 2011) and is shown to be $-0.054Re^{3/2}$, so that inertia slows down the rotation of the sphere. In the case of a sphere one can easily see that the angular velocity correction at O(Re) in a simple shear flow is zero. This is because the correction is quadratic in the shear rate, and it being a pseudo vector, should be proportional to $\boldsymbol{\omega} \cdot \boldsymbol{E}$, where $\boldsymbol{E}$ and $\boldsymbol{\omega}$ are the rate-of-strain tensor and the vorticity vector in the simple shear flow, respectively. Vorticity is perpendicular to the flow-gradient plane of the simple shear flow and therefore, $\boldsymbol{\omega} \cdot \boldsymbol{E} = 0$.

The disturbance velocity field for a spheroid in a spinning orbit is steady, and therefore the scaling of the inertial correction to the angular velocity would again be similar to that of a sphere. The detailed calculation can be easily seen from the $O(Re^{3/2})$ Fourier space formulation as shown in a later section; although, in a recent work (Meibohm *et al.* 2016), the $O(Re^{3/2})$ correction for a spheroid in a spinning orbit, has been estimated using the traditional matched asymptotic expansions approach. In the tumbling orbit, however, the disturbance velocity field due to the spheroid is unsteady, and the torque-free spheroid acts as a time-dependent force dipole singularity in the outer region. This dependence, when represented in frequency space, is an infinite Fourier series and this makes the evaluation of $O(Re^{3/2})$ correction to the angular velocity difficult. However, as shown in a later section, if one has to only evaluate correction to time period at $O(Re^{3/2})$, one only needs the Jeffrey averaged angular velocity correction, and the relevant infinite series truncates to three terms, allowing one to determine the correction. The correctness of the $O(Re^{3/2})$ correction to the angular velocity for a sphere mentioned above, and the associated increase in time period was also confirmed in a numerical investigation by Mikulencak & Morris (2004). They have extended the results for the inertial correction to $O(1)$ Re. More recently, Mao & Alexeev (2014) have investigated the effect of inertia on the time period of rotation of spheroids of different aspect ratios using the lattice Boltzmann method. This work concluded that the time period of rotation increases with Reynolds number, but they find the scaling for the inertial correction to be $O(Re)$ for small Reynolds numbers. However based on the $O(Re)$ correction of the angular velocity derived in chapter 2, it can be easily seen that the correction to the time period at this order is zero. The accurate estimation of the $O(Re^{3/2})$ inertial correction, in a numerical effort, is not easy, since the correction originates in the outer region, and demands that the outer boundary for the computational domain be much farther than the (large) inertial screening length.

This paper is organized as follows. In section 5.2 we derive the expression for the inertial correction to angular velocity using a reciprocal theorem formulation. We express the reciprocal theorem in Fourier space similar to Stone *et al.* (2000) and Subramanian *et al.* (2011). In section 5.3, we summarize the Stokesian scenario and investigate the effects of $O(Re)$ and $O(St)$ correction to the angular velocities, derived in chapter 2, on the time period . It is shown that that the time period correction vanishes at $O(Re)$ and $O(St)$ in the stabilized (spinning or tumbling) orbits. The calculation of the $O(St^2)$ correction to the time period is presented in section 5.4. We investigate the effect of fluid inertia on the time period for the simpler case of the spinning spheroid in section 5.5, and show that the Fourier space integral for the $O(Re^{3/2})$ angular velocity correction reduces to that of the sphere as given in Stone *et al.* (2000). A numerical evaluation of this integral yields the spinning correction over the relevant range of aspect ratios. As mentioned above, this is expected since a spinning spheroid acts as a time-independent force-dipole singularity. In section 5.6, we evaluate the reciprocal theorem integral for the difficult case of the tumbling orbit, the difficulty arising from the time-dependent nature of the force-dipole singularity. However, as shown therein, for the time period correction one can reduce the reciprocal theorem integral to the sum of a three-dimensional integral and a four-dimensional integral. These integrals are evaluated numerically and the results are presented in section 5.7. We summarize our findings in section 5.8.

5.2 Formulation for the time period: The reciprocal theorem

In this section, we derive the formal expression for the correction to the time period of rotation of a spheroid, in a simple shear flow, for small *Re*. The time period is related to the angular velocity of the spheroid, and the latter can be evaluated using a generalized reciprocal theorem formulation. The reciprocal theorem relates the velocity and stress fields of two problems, the first one being the problem of interest and the second one being a simpler test problem with a known solution. The flow physics in the two problems can be different, however the configuration, size and shape of the particle, a spheroid here in an unbounded fluid domain, are the same (Leal (1979);Subramanian & Koch (2005);Subramanian & Koch (2006*b*) and chapter 2). The problem of interest here is a torque-free spheroid rotating in a simple shear flow, accounting for the inertial acceleration of the fluid in an unbounded domain; the objective is to relate its angular velocity, $\boldsymbol{\Omega}_1$, to the time period of rotation, to $O(Re^{3/2})$ and $O(St^2)$, and determine the latter. The test problem corresponds to the Stokesian rotation of a spheroid in a quiescent ambient with an angular velocity $\boldsymbol{\Omega}_2$, and with the same instantaneous orientation as that of the spheroid in the problem of interest. The velocity and stress fields in the problem of interest are denoted by $\boldsymbol{u}^{(1)}$ and $\boldsymbol{\sigma}^{(1)}$, and those in the test problem are $\boldsymbol{u}^{(2)}$ and $\boldsymbol{\sigma}^{(2)}$. The reciprocal theorem is formulated in terms of the scaled disturbance fields (both stress and velocity) in the problem of interest which are given by $\boldsymbol{\sigma}'^{(1)} = \boldsymbol{\sigma}^{(1)} - 2\boldsymbol{E}$ and $\boldsymbol{u}'^{(1)} = \boldsymbol{u}^{(1)} - \boldsymbol{\Gamma}\cdot\boldsymbol{x}$, where $\boldsymbol{\Gamma}\cdot\boldsymbol{x}$ is the ambient simple shear defined in a coordinate system, whose origin is at the center of the spheroid. The space-fixed coordinate system has its X, Y and Z along the flow, gradient and vorticity directions, respectively, of the ambient simple shear (see figure 5.1(a)),

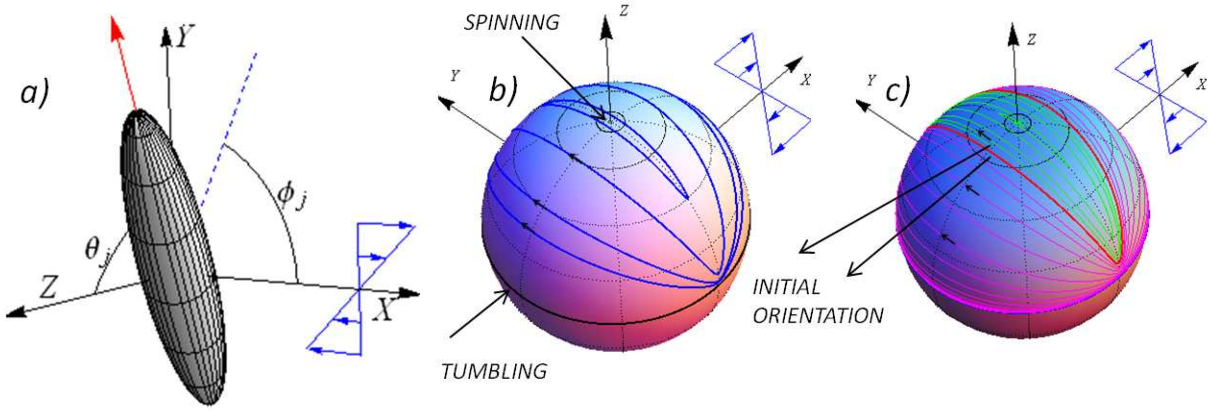

Fig. 5.1 (a) The orientation vector (red) defined by the angles θ_j and ϕ_j in the space-fixed coordinate system XYZ. The X,Y and Z axes correspond to the flow, the gradient and the vorticity directions of the simple shear flow.(b) Jeffery orbits (blue) for an oblate spheroid of aspect ratio 0.05 for different initial conditions. The limiting Jeffery orbits that is the tumbling and spinning orbits are indicated. (c) The repeller orbit (red) for an oblate spheroid of aspect ratio 0.05 which divides the unit hemisphere into two distinct basins of attractions. The trajectories of the spheroid due to fluid inertial drift at O(Re), starting from either side of the repeller, and ending at the attractors of the corresponding basins, are shown as purple and green curves. Note that the notation of the unit vectors and the definition of body-fixed coordinate system are different from chapter 2

with the unit vectors in the X, Y and Z directions being $\mathbf{1}_1$, $\mathbf{1}_2$ and $\mathbf{1}_3$ respectively. Note that the notation of the unit vectors and the definition of body-fixed coordinate system are different from chapter 2. The disturbance velocity and stress fields are scaled with $\dot{\gamma}L$ and $\mu\dot{\gamma}L$. Thus, $\boldsymbol{\Gamma} = \mathbf{1}_1\mathbf{1}_2$ and $\boldsymbol{E} = \frac{1}{2}(\mathbf{1}_1\mathbf{1}_2 + \mathbf{1}_2\mathbf{1}_1)$ are the transpose of the non-dimensional velocity gradient and the rate-of-strain tensors, respectively. The expression for the inertial angular velocity, has already been derived in (2.20), using a reciprocal theorem formulation and takes the following form in non-dimensional terms for $\lambda = 0$:

$$\begin{aligned}\boldsymbol{\Omega}_1 \cdot \boldsymbol{\mathscr{L}}_2 = {} & \boldsymbol{\Gamma} : \int_{S_p} \boldsymbol{x}(\boldsymbol{\sigma}^{(2)} \cdot \boldsymbol{n}) dS + St\left[\frac{d}{dt}(\boldsymbol{I}_p \cdot \boldsymbol{\Omega}_1)\right] \cdot \boldsymbol{\Omega}_2 \\ & + Re \int_V \left[\frac{\partial \boldsymbol{u}'^{(1)}}{\partial t} + (\boldsymbol{\Gamma} \cdot \boldsymbol{x}) \cdot \nabla \boldsymbol{u}'^{(1)} + \boldsymbol{\Gamma} \cdot \boldsymbol{u}'^{(1)} + \boldsymbol{u}'^{(1)} \cdot \nabla \boldsymbol{u}'^{(1)}\right] \cdot \boldsymbol{u}^{(2)} dV, \end{aligned} \tag{5.1}$$

where, $\boldsymbol{\Omega}_1$ and $\boldsymbol{\mathscr{L}}_2$ are, respectively, the angular velocity of the spheroid in the problem of interest and the torque acting on the spheroid in the test problem. The latter is given by $\boldsymbol{\mathscr{L}}_2 = -8\pi(X_C\boldsymbol{pp} + Y_C(\boldsymbol{I} - \boldsymbol{pp})) \cdot \boldsymbol{\Omega}_2$, $\boldsymbol{p}$ here being the orientation vector of the spheroid, and the torque coefficients being given by $X_C = 4\left(\xi_0^2 - 1\right) / \left(3\xi_0^3\left(2\xi_0 - 2\left(\xi_0^2 - 1\right)\coth^{-1}\xi_0\right)\right)$

and $Y_C = 4\left(2\xi_0^2-1\right)/(3\xi_0^3\left(2\left(\xi_0^2+1\right)\coth^{-1}\xi_0-2\xi_0\right))$ for a prolate spheroid (Kim & Karrila (1991)), where ξ_0 is the inverse of the eccentricity of the spheroid ($\xi_0 = 1/\sqrt{1-1/\kappa^2}$ for a prolate spheroid). The expressions for X_C and Y_C, for an oblate spheroid, can be obtained by using the transformation $\xi_0 = i\sqrt{\xi_0^2-1}$ and $d = -id$ (d is the interfocal distance of the spheroid) in the dimensional forms of the prolate torque coefficients ($\xi_0 = 1/\sqrt{1-\kappa^2}$, for an oblate spheroid). The volume integral on the right-hand side of (5.1) gives the contribution to the angular velocity due to fluid inertia, the domain of integration being the unbounded fluid volume outside the spheroid. The leading order contribution due to fluid inertia, at O(Re), can be obtained by replacing $\boldsymbol{u}'^{(1)}$ with the disturbance velocity field in the Stokes limit($\boldsymbol{u}'^{(s)}$) in the integral. The resulting integral is convergent, implying the regular nature of the O(Re) correction. This correction has been evaluated in section 2.6, and it stabilizes certain Stokesian orbits of the spheroid. Specifically, while at $Re = 0$ and $St = 0$, the spheroid may rotate in any of a one-parameter family of precessional orbits known as Jeffery orbits (Jeffery 1922), for finite Re (or St), only the limiting members of this family (the tumbling and the spinning modes; see figure 5.1(b)) are rendered stable by the O(Re) (O(St)) orbit drift induced by inertia. As shown later in section 5.3, the O(Re) and O(St) corrections to the angular velocity of a spheroid rotating in either of the asymptotic states above, does not change the time period of rotation from its leading order value given, in non-dimensional terms by $T_{jeff} = 2\pi(\kappa^2+1)/\kappa$ ($=4\pi$) for the tumbling (spinning) orbit. However, as mentioned in section 5.1, numerical simulations have observed a change in the time period in presence of fluid inertia(Mao & Alexeev 2014), although the scaling for this change has not been rigorously characterized in the limit $Re, St << 1$. Thus there is the need to calculate the next correction to the angular velocity. As shown later in this section, this comes at O($Re^{3/2}$) for fluid inertia, and at O(St^2) for particle inertia (see section 5.4).

To calculate the next correction due to fluid inertia, we will first examine the assumptions made while replacing $\boldsymbol{u}'^{(1)}$ with $\boldsymbol{u}'^{(s)}$ to obtain the O(Re) correction. The equation governing $\boldsymbol{u}'^{(1)}$ is given by:

$$\nabla^2\boldsymbol{u}'^{(1)} - \nabla p = Re\left(\frac{\partial \boldsymbol{u}'^{(1)}}{\partial t} + \boldsymbol{u}'^{(1)}.\nabla\boldsymbol{u}'^{(1)} + (\boldsymbol{\Gamma}.\boldsymbol{x})\cdot\nabla\boldsymbol{u}'^{(1)} + \boldsymbol{\Gamma}.\boldsymbol{u}'^{(1)}\right) \tag{5.2}$$

The equation above, is obtained by taking the difference of the governing equations for the full velocity field $\boldsymbol{u}^{(1)}$ and the ambient $\boldsymbol{\Gamma}\cdot\boldsymbol{x}$. Neglecting the inertial terms proportional to Re in (5.2), one gets the Stokes equation, whose solution is denoted by $\boldsymbol{u}'^{(s)}$. It is well known that $\boldsymbol{u}'^{(s)}$ is not a uniformly valid approximation for the velocity field throughout the unbounded domain outside the spheroid. To see this, we compare the magnitudes of the viscous and the inertial terms in (5.2). The Stokes solution $\boldsymbol{u}'^{(s)}$ decays as $1/r^2$, where r is the distance away from the spheroid, and therefore the viscous terms on the left-hand side of (5.2) decay as $1/r^4$ as $r \to \infty$. The inertial terms on the right-hand side decays as $1/r^2$, and cannot be neglected when $r \approx Re^{-1/2}$, the inertial screening length, and the Stokes solution ceases to be a good approximation to the disturbance velocity field at distances of order and beyond this length. The region around the sphere can therefore be divided into two, depending on whether the inertial terms can be neglected compared to the viscous terms; the inner region ($r \sim 1$) and the outer region ($r \sim O(Re^{-1/2})$). The Stokes velocity field is a good approximation to the actual disturbance velocity field only in the inner region. The leading order velocity field in the outer region should, however, be obtained by solving (5.2). The velocity fields in the inner and outer regions, however, reduce to the same functional form in a matching region ($1 << r << Re^{-1/2}$). To calculate the $O(Re^{3/2})$ correction to the angular velocity, the velocity field in the integrand on the right-hand-side of (5.1) is written, formally, as the following uniformly valid expansion(Hinch (1991)):

$$\boldsymbol{u}'^{(1)} = \boldsymbol{u}^{inner} + \boldsymbol{u}^{outer} - \boldsymbol{u}^{match}. \tag{5.3}$$

In (5.3), $\boldsymbol{u}^{inner}$ is the velocity field in the inner region, and is $\boldsymbol{u}'^{(s)}$ at leading order, $\boldsymbol{u}^{outer}$ is the velocity field in the outer region being governed by linearized version of (5.2). In the matching region, both $\boldsymbol{u}^{inner}$ and $\boldsymbol{u}^{outer}$ reduce to $\boldsymbol{u}^{match}$. Next, defining $\boldsymbol{u}^f = \boldsymbol{u}^{outer} - \boldsymbol{u}^{match}$, the reciprocal theorem in (5.1) becomes

$$\begin{aligned}
\boldsymbol{\Omega}_1 \cdot \mathscr{L}_2 = \boldsymbol{\Gamma} : \int_{S_p} \boldsymbol{x}(\boldsymbol{\sigma}^{(2)} \cdot \boldsymbol{n}) dS + St \left[\frac{d}{dt}(\boldsymbol{I}_p \cdot \boldsymbol{\Omega}_1) \right] \cdot \boldsymbol{\Omega}_2 \\
+ Re \int_V \left[\frac{\partial \boldsymbol{u}^{inner}}{\partial t} + (\boldsymbol{\Gamma} \cdot \boldsymbol{x}) \cdot \boldsymbol{\nabla} \boldsymbol{u}^{inner} + \boldsymbol{\Gamma} \cdot \boldsymbol{u}^{inner} + \boldsymbol{u}^{inner} \cdot \boldsymbol{\nabla} \boldsymbol{u}^{inner} \right] \cdot \boldsymbol{u}^{(2)} dV \\
+ Re \int_V \left[\frac{\partial \boldsymbol{u}^f}{\partial t} + (\boldsymbol{\Gamma} \cdot \boldsymbol{x}) \cdot \boldsymbol{\nabla} \boldsymbol{u}^f + \boldsymbol{\Gamma} \cdot \boldsymbol{u}^f + \boldsymbol{u}^f \cdot \boldsymbol{\nabla} \boldsymbol{u}^f \right] \cdot \boldsymbol{u}^{(2)} dV \\
+ Re \int_V \left[\boldsymbol{u}^f \cdot \boldsymbol{\nabla} \boldsymbol{u}^{inner} + \boldsymbol{u}^{inner} \cdot \boldsymbol{\nabla} \boldsymbol{u}^f \right] \cdot \boldsymbol{u}^{(2)} dV
\end{aligned} \tag{5.4}$$

In the inner region, $\boldsymbol{u}^f$ is zero at leading order and in the outer region the nonlinear cross terms, $\boldsymbol{u}^f \cdot \boldsymbol{\nabla} \boldsymbol{u}^{inner}$ and $\boldsymbol{u}^{inner} \cdot \boldsymbol{\nabla} \boldsymbol{u}^f$, decay faster than the linear terms, and therefore the integrals involving the cross terms in (5.4) contribute at a higher order. The second term on the right-hand side in (5.4) gives the O(Re) correction to the angular velocity ($\boldsymbol{\Omega}_1$), arising from the inner region, and is evaluated in chapter 2. The third term on the right-hand side is the contribution to the angular velocity from the outer region. To explicitly see the scaling with respect to Re for this contribution, the velocity fields in the third term are written in terms of a rescaled coordinate defined as $\rho = Re^{1/2}r$. The rescaled coordinate is of O(1) when r is of order the inertial screening length, and is therefore the coordinate appropriate for the outer region. The radial vector and the differential volume can be expressed in the outer coordinate as $\boldsymbol{\rho} = Re^{1/2}\boldsymbol{x}$, $dV_\rho = Re^{3/2}dV$. Since the spheroid acts as a force-dipole singularity for $r >> L$, the disturbance velocity fields in the problem of interest as well as the test problem decay as $1/r^2$ when $L << r << Re^{-1/2}$, and can be written as $\boldsymbol{u}^{f_\rho} = Re^{-1}\boldsymbol{u}^f$ and $\boldsymbol{u}^{(2_\rho)} = Re^{-1}\boldsymbol{u}^{(2)}$. Note that $\boldsymbol{u}^{f_\rho} = (\boldsymbol{u}^{outer\rho} - \boldsymbol{u}^{match\rho})$, the superscript ρ in the outer and matching velocity fields indicate that they are now expressed in the outer coordinate ρ. The reciprocal theorem in (5.4), with the third term expressed in terms of the rescaled outer coordinate, is given by:

$$\begin{aligned}
\boldsymbol{\Omega}_1 \cdot \mathscr{L}_2 = & \boldsymbol{\Gamma} : \int_{S_p} \boldsymbol{x}(\boldsymbol{\sigma}^{(2)} \cdot \boldsymbol{n}) dS + St \left[\frac{d}{dt}(\boldsymbol{I}_p \cdot \boldsymbol{\Omega}_1) \right] \cdot \boldsymbol{\Omega}_2 \\
& + Re \int_V \left[\frac{\partial \boldsymbol{u}^{inner}}{\partial t} + (\boldsymbol{\Gamma} \cdot \boldsymbol{x}) \cdot \boldsymbol{\nabla} \boldsymbol{u}^{inner} + \boldsymbol{\Gamma} \cdot \boldsymbol{u}^{inner} + \boldsymbol{u}^{inner} \cdot \boldsymbol{\nabla} \boldsymbol{u}^{inner} \right] \cdot \boldsymbol{u}^{(2)} dV. \\
& + Re^{\frac{3}{2}} \int_{V_\rho} \left[\frac{\partial \boldsymbol{u}^{f_\rho}}{\partial t} + (\boldsymbol{\Gamma} \cdot \boldsymbol{\rho}) \cdot \boldsymbol{\nabla} \boldsymbol{u}^{f_\rho} + \boldsymbol{\Gamma} \cdot \boldsymbol{u}^{f_\rho} \right] \cdot \boldsymbol{u}^{(2_\rho)} dV_\rho .
\end{aligned} \tag{5.5}$$

Note that the nonlinear term $\boldsymbol{u}^f \cdot \boldsymbol{\nabla} \boldsymbol{u}^f$ in (5.4), when expressed in terms of the outer coordinate, contributes at a higher order, and is neglected in the second integral in (5.5). It is evident from (5.5) that the correction from the outer region comes at O($Re^{3/2}$). The volume of the spheroid expressed in outer variables is O($Re^{3/2}$), and its omission only leads to an error of O(Re^3). This is equivalent to treating the spheroid as an equivalent point force-dipole singularity. Thus, the outer integral in (5.5) may be extended right until the origin, and the resulting calculation is then more conveniently done in Fourier space. The convolution theorem (Arfken *et al.* (2011)) is applied to the O($Re^{3/2}$) integral in (5.5) to obtain:

$$\begin{aligned}
\int_{V_\rho} \left[\frac{\partial \boldsymbol{u}^{f_\rho}}{\partial t} + (\boldsymbol{\Gamma} \cdot \boldsymbol{\rho}) \cdot \boldsymbol{\nabla} \boldsymbol{u}^{f_\rho} + \boldsymbol{\Gamma} \cdot \boldsymbol{u}^{f_\rho} \right] \cdot \boldsymbol{u}^{(2_\rho)} dV_\rho = & \int \left[\frac{\partial \hat{\boldsymbol{u}}^f}{\partial t} - (\boldsymbol{\Gamma}^\dagger \cdot \boldsymbol{k}) \cdot \boldsymbol{\nabla}_{\boldsymbol{k}} \hat{\boldsymbol{u}}^f + \boldsymbol{\Gamma} \cdot \hat{\boldsymbol{u}}^f \right] \\
& \cdot \hat{\boldsymbol{u}}^{(2)}(-\boldsymbol{k}) d\boldsymbol{k}.
\end{aligned} \tag{5.6}$$

where the hatted variables above, denote the Fourier transform which is defined as $\hat{f}(\boldsymbol{k}) = \int f(\boldsymbol{r}) e^{-i2\pi \boldsymbol{k}\cdot\boldsymbol{r}} d\boldsymbol{r}$. In (5.6), $\hat{\boldsymbol{u}}^{(2)}(-\boldsymbol{k})$ and $\hat{\boldsymbol{u}}^f(\boldsymbol{k})$ are the Fourier transforms of the test velocity field $\boldsymbol{u}^{(2_\rho)}$ and the velocity field in the problem of interest $\boldsymbol{u}^{f_\rho}$. Note that the ambient simple shear flow takes the form $\hat{\boldsymbol{u}}_2 = -k_1 \mathbf{1}_2$ in Fourier space. Here, k_1 is the component of the wave vector $\boldsymbol{k}$ in the X direction(see figure 5.1 (a)).

To evaluate (5.6), we need to find the Fourier transforms of $\boldsymbol{u}^{(2\rho)}$ and $\boldsymbol{u}^{f\rho}$. The governing equation for $\boldsymbol{u}^{(2\rho)}$ is:

$$\nabla^2 \boldsymbol{u}^{(2\rho)} - \nabla p^{(2\rho)} = \boldsymbol{S}^{(2)} \cdot \frac{\partial \delta(\boldsymbol{\rho})}{\partial \boldsymbol{\rho}}, \tag{5.7}$$

where $\boldsymbol{S}^{(2)}$ is the time-dependent force-dipole singularity corresponding to a spheroid rotating in a quiescent fluid. The singularity, $\boldsymbol{S}^{(2)}$, is given by:

$$\boldsymbol{S}^{(2)} = B_1 \left((\boldsymbol{\Omega}^{(2)} \wedge \boldsymbol{p})\boldsymbol{p} + \boldsymbol{p}(\boldsymbol{\Omega}^{(2)} \wedge \boldsymbol{p}) \right) + B_2 \left((\boldsymbol{\Omega}^{(2)} \cdot \boldsymbol{p})\boldsymbol{\varepsilon} \cdot \boldsymbol{p} \right) + B_3 (\boldsymbol{\varepsilon} \cdot \boldsymbol{\Omega}^{(2)}), \tag{5.8}$$

where $\boldsymbol{p}$ is the spheroid orientation vector and the constants B_1, B_2 and B_3 for a prolate spheroid are given by:

$$B_1 = \frac{8\pi}{\xi_0^3 \left(-3\xi_0 + 3\, coth^{-1}\xi_0 \left(1+\xi_0^2\right)\right)}, \tag{5.9}$$

$$B_2 = \frac{8\pi \left(2 + 3\xi_0 \left(-coth^{-1}\xi_0 + \xi_0 \left(-1 + \xi_0 coth^{-1}\xi_0\right)\right)\right)}{3\xi_0^2 \left(-coth^{-1}[\xi_0]^2 + \xi_0^2 \left(-1 + \xi_0 coth^{-1}\xi_0\right)^2\right)}, \tag{5.10}$$

$$B_3 = \frac{8\pi \left(1 - 2\xi_0^2\right)}{\xi_0^3 \left(-3\xi_0 + 3 coth^{-1}\xi_0 \left(1+\xi_0^2\right)\right)}. \tag{5.11}$$

The terms proportional to constants B_2 and B_3 correspond to rotlet singularities and the one multiplying B_1 corresponds to the stresslet singularity induced by the rotating spheroid. In the limit $\xi_0 \to \infty$, that is for a sphere, $B_3 = -4\pi$ and B_1 and B_2 are O$(1/\xi_0^2)$, consistent with a rotating sphere acting as a pure rotlet singularity. As before, the constants for an oblate spheroid can either be obtained using the transformation, $\xi_0 = i\sqrt{\xi_0^2 - 1}$ and $d = -id$, mentioned below (5.1) (alternatively, see Kim & Karrila (1991)). The Fourier transform of (5.7) gives:

$$\hat{\boldsymbol{u}}^{(2)}(-\boldsymbol{k}) = \frac{i\boldsymbol{S}^{(2)} \cdot \boldsymbol{k}}{2\pi k^2} \cdot \left(\boldsymbol{I} - \frac{\boldsymbol{kk}}{k^2} \right). \tag{5.12}$$

To evaluate $\hat{\boldsymbol{u}}^f$, we need to find the equation governing $\boldsymbol{u}^{f\rho}$, which can be derived from the equations governing $\boldsymbol{u}^{outer\rho}$ and $\boldsymbol{u}^{match\rho}$ given by:

$$\nabla^2 \boldsymbol{u}^{outer\rho} - \nabla p^{outer\rho} = \boldsymbol{S} \cdot \frac{\partial \delta(\boldsymbol{\rho})}{\partial \boldsymbol{\rho}} + \left(\frac{\partial \boldsymbol{u}^{outer\rho}}{\partial t} + (\boldsymbol{\Gamma}.\boldsymbol{x}) \cdot \nabla \boldsymbol{u}^{outer\rho} + \boldsymbol{\Gamma}.\boldsymbol{u}^{outer\rho} \right), \tag{5.13}$$

and

$$\nabla^2 \boldsymbol{u}^{match\rho} - \nabla p^{match\rho} = \boldsymbol{S} \cdot \frac{\partial \delta(\boldsymbol{\rho})}{\partial \boldsymbol{\rho}} \tag{5.14}$$

respectively. Here, to the order of approximation desired, $\boldsymbol{S}$ is the time-dependent force-dipole singularity corresponding to a torque-free spheroid in a simple shear flow. At $Re = 0$, $\boldsymbol{S}$ is given by

$$\begin{aligned}\boldsymbol{S} = {} & A_1 \frac{3}{2} (\boldsymbol{E} : \boldsymbol{pp}) \left(\boldsymbol{pp} - \frac{\boldsymbol{I}}{3} \right) + A_2 ((\boldsymbol{I} - \boldsymbol{pp}) \cdot \boldsymbol{E} \cdot \boldsymbol{pp} + \boldsymbol{pp} \cdot \boldsymbol{E} \cdot (\boldsymbol{I} - \boldsymbol{pp})) \\ & + A_3 \left((\boldsymbol{I} - \boldsymbol{pp}) \cdot \boldsymbol{E} \cdot (\boldsymbol{I} - \boldsymbol{pp}) + (\boldsymbol{I} - \boldsymbol{pp}) \frac{(\boldsymbol{E} : \boldsymbol{pp})}{2} \right).\end{aligned} \tag{5.15}$$

To understand $\boldsymbol{S}$ in more detail, we note that the Stokesian disturbance field induced in an ambient linear flow can be split into 5 component flows corresponding to the five degrees of freedom of the rate of strain tensor (see section 2.3). These may conveniently regarded as an axisymmetric flow, two planar extensional flows in both the longitudinal plane (containing $\boldsymbol{p}$) and transverse plane (orthogonal to $\boldsymbol{p}$), respectively, with the component amplitude dependent on the spheroid orientation. Due to its axisymmetry, a spheroid responds identically to the two extensions in the longitudinal and the transverse planes. Therefore, the force-dipole singularity can be written as a sum of only three stresslets as given in (5.15), with the terms proportional to A_1, A_2 and A_3 being the stresslets induced by the axisymmetric extension, the longitudinal and the transverse planar extensional flows, respectively. The constants for a prolate spheroid (Kim & Karrila (1991)) are :

$$A_1 = -\frac{16\pi}{9\xi_0^3 \left(-3\xi_0 + coth^{-1}\xi_0 \left(-1 + 3\xi_0^2\right)\right)}, \tag{5.16}$$

$$A_2 = \frac{16\pi \left(-1 + \xi_0^2\right)}{3\xi_0^2 \left(-1 + 2\xi_0^2\right) \left(2 - 3\xi_0^2 + 3\, coth^{-1}\xi_0 \xi_0 \left(-1 + \xi_0^2\right)\right)}, \tag{5.17}$$

$$A_3 = -\frac{32\pi \left(-1 + \xi_0^2\right)}{3\xi_0^3 \left(5\xi_0 - 3\xi_0^3 + 3\, coth^{-1}\xi_0 \left(-1 + \xi_0^2\right)^2\right)}. \tag{5.18}$$

In the limit $\xi_0 \to \infty$, that is for a sphere, all three constants equal $-20\pi/3$, making $\boldsymbol{S}_\infty = -(20\pi/3)\boldsymbol{E}$ corresponding to the well-known stresslet singularity of a freely rotating sphere ($n\boldsymbol{S}_\infty$ yields the well known Einstein coefficient). The equation governing $\boldsymbol{u}^{f\rho}$ is derived using

(5.13) and (5.14) and is given by:

$$\boldsymbol{\nabla}^2 \boldsymbol{u}^{f\rho} - \boldsymbol{\nabla} p^{f\rho} = \frac{\partial \boldsymbol{u}^{f\rho}}{\partial t} + (\boldsymbol{\Gamma}.\boldsymbol{x})\cdot\nabla\boldsymbol{u}^{f\rho} + \boldsymbol{\Gamma}.\boldsymbol{u}^{f\rho} + \frac{\partial \boldsymbol{u}^{match\rho}}{\partial t} + (\boldsymbol{\Gamma}.\boldsymbol{x})\cdot\nabla\boldsymbol{u}^{match\rho} + \boldsymbol{\Gamma}.\boldsymbol{u}^{match\rho}. \tag{5.19}$$

The bracketed term on the right-hand side of (5.6) is obtained by taking the Fourier transform of (5.19) and is given by

$$\frac{\partial \hat{\boldsymbol{u}}^f}{\partial t} - (\boldsymbol{\Gamma}^\dagger\cdot\boldsymbol{k})\cdot\boldsymbol{\nabla}_{\boldsymbol{k}}\hat{\boldsymbol{u}}^f + \boldsymbol{\Gamma}\cdot\hat{\boldsymbol{u}}^f = -4\pi^2k^2\hat{\boldsymbol{u}}^f - i2\pi\boldsymbol{k}\hat{p}^f - \left(\frac{\partial \hat{\boldsymbol{u}}^{match}}{\partial t} - (\boldsymbol{\Gamma}^\dagger\cdot\boldsymbol{k})\cdot\boldsymbol{\nabla}_{\boldsymbol{k}}\hat{\boldsymbol{u}}^{match} + \boldsymbol{\Gamma}\cdot\hat{\boldsymbol{u}}^{match}\right). \tag{5.20}$$

Substituting (5.12) and (5.20) in (5.6), the reciprocal theorem relation in (5.5) becomes

$$\begin{aligned}\boldsymbol{\Omega}_1\cdot\mathscr{L}_2 = \boldsymbol{\Gamma}\colon &\int_{S_p}\boldsymbol{x}(\boldsymbol{\sigma}^{(2)}\cdot\boldsymbol{n})dS + St\left[\frac{d}{dt}(\boldsymbol{I}_p\cdot\boldsymbol{\Omega}_1)\right]\cdot\boldsymbol{\Omega}_2\\ &+ Re\int_V\left[\frac{\partial\boldsymbol{u}^{inner}}{\partial t} + (\boldsymbol{\Gamma}\cdot\boldsymbol{x})\cdot\boldsymbol{\nabla}\boldsymbol{u}^{inner} + \boldsymbol{\Gamma}\cdot\boldsymbol{u}^{inner} + \boldsymbol{u}^{inner}\cdot\boldsymbol{\nabla}\boldsymbol{u}^{inner}\right]\cdot\boldsymbol{u}^{(2)}dV\\ &- Re^{\frac{3}{2}}\int\left[4\pi^2k^2\hat{\boldsymbol{u}}^f + \frac{\partial\hat{\boldsymbol{u}}^{match}}{\partial t} - (\boldsymbol{\Gamma}^\dagger\cdot\boldsymbol{k})\cdot\boldsymbol{\nabla}_{\boldsymbol{k}}\hat{\boldsymbol{u}}^{match} + \boldsymbol{\Gamma}\cdot\hat{\boldsymbol{u}}^{match}\right]\\ &\cdot\left(\frac{i\boldsymbol{S}^{(2)}\cdot\boldsymbol{k}}{2\pi k^2}\cdot\left(\boldsymbol{I} - \frac{\boldsymbol{k}\boldsymbol{k}}{k^2}\right)\right)d\boldsymbol{k}.\end{aligned} \tag{5.21}$$

Note that the term containing the Fourier transform of the pressure in (5.20), which is proportional to $\boldsymbol{k}$, vanishes when contracted with the Fourier transformed test velocity field, and has therefore been omitted in (5.21). For the test problem, we define two second order tensors $\boldsymbol{L}_2$ and $\boldsymbol{U}_2$, and two third order tensors $\boldsymbol{\Sigma}^{(2)}$ and $\boldsymbol{S}^{2t}$ such that $\mathscr{L}_2$=$\boldsymbol{L}_2\cdot\boldsymbol{\Omega}_2$, $\boldsymbol{u}^{(2)}$= $\boldsymbol{U}_2\cdot\boldsymbol{\Omega}_2$, $\boldsymbol{\sigma}^{(2)}$ = $\boldsymbol{\Sigma}^{(2)}\cdot\boldsymbol{\Omega}_2$ and $\boldsymbol{S}^{(2)}$ = $\boldsymbol{S}^{2t}\cdot\boldsymbol{\Omega}_2$. In terms of these newly defined tensors the relation (5.21) becomes independent of the angular velocity of the test spheroid ($\boldsymbol{\Omega}_2$). The correction to the angular velocity in the problem of interest ($\boldsymbol{\Omega}_1$), due to particle inertia to any order in St can be obtained by equating the left-hand side of (5.21) with the second term on its right-hand side. The O(St) correction is already evaluated in section 2.5. The next correction comes at O(St^2) and is evaluated in section 5.4. To evaluate the fluid inertial correction to $\boldsymbol{\Omega}_1$, it is expanded as $\boldsymbol{\Omega}_{jeff} + Re\,\boldsymbol{\Omega}_{c1} + Re^{3/2}\,\boldsymbol{\Omega}_{c2}$ and substituting the expansion as well as the newly defined tensors in (5.21) leads to

$$\boldsymbol{\Omega}_{jeff}\cdot\boldsymbol{L}_2 = \boldsymbol{\Gamma} : \int_{S_p} \boldsymbol{x}(\boldsymbol{\Sigma}^{(2)}\cdot\boldsymbol{n})dS, \tag{5.22}$$

$$\boldsymbol{\Omega}_{c1}\cdot\boldsymbol{L}_2 = \int_V \left[\frac{\partial \boldsymbol{u}^{inner}}{\partial t} + (\boldsymbol{\Gamma}\cdot\boldsymbol{x})\cdot\nabla\boldsymbol{u}^{inner} + \boldsymbol{\Gamma}\cdot\boldsymbol{u}^{inner} + \boldsymbol{u}^{inner}\cdot\nabla\boldsymbol{u}^{inner}\right]\cdot\boldsymbol{U}_2 dV, \tag{5.23}$$

and

$$\begin{aligned}\boldsymbol{\Omega}_{c2}\cdot\boldsymbol{L}_2 = -\int \Bigg[4\pi^2k^2\hat{\boldsymbol{u}}^f + \frac{\partial \hat{\boldsymbol{u}}^{match}}{\partial t} - (\boldsymbol{\Gamma}^{\dagger}\cdot\boldsymbol{k})\cdot\nabla_{\boldsymbol{k}}\hat{\boldsymbol{u}}^{match} + \boldsymbol{\Gamma}\cdot\hat{\boldsymbol{u}}^{match}\Bigg] \\ \cdot\left(\frac{i\boldsymbol{S}^{(2t)}\cdot\boldsymbol{k}}{2\pi k^2}\cdot\left(\boldsymbol{I}-\frac{\boldsymbol{k}\boldsymbol{k}}{k^2}\right)\right) d\boldsymbol{k}\end{aligned} \tag{5.24}$$

at successive orders. The detailed expression for $\boldsymbol{u}^{inner}$, obtained using a spheroidal harmonics formalism, was used to evaluate $\boldsymbol{\Omega}_{c1}$ in chapter 2. The Fourier transformed matching velocity field ($\hat{\boldsymbol{u}}^{match}$) in (5.24) is obtained by taking the Fourier transform of (5.14), and given by:

$$\hat{\boldsymbol{u}}^{match}(\boldsymbol{k}) = -\frac{i\boldsymbol{S}\cdot\boldsymbol{k}}{2\pi k^2}\cdot\left(\boldsymbol{I}-\frac{\boldsymbol{k}\boldsymbol{k}}{k^2}\right), \tag{5.25}$$

with $\boldsymbol{S}$ given by (5.15). To evaluate the integral in (5.24), one also needs $\hat{\boldsymbol{u}}^f$, which can be obtained by solving (5.20). This is a rather elaborate calculation, and is presented in sections 5.5 and 5.6.

5.3 Summary: Time period at leading order and at O(*Re*)

The leading order angular velocity $\boldsymbol{\Omega}_{jeff}$ in (5.22) may be expressed in terms of the rates of change of the polar and azimuthal angles θ_j and ϕ_j (Jeffery (1922)), defined in figure 5.1(a), and these are given by:

$$\dot{\phi}_{jeff} = -\frac{1}{2} + \frac{\kappa^2-1}{2(\kappa^2+1)}\cos 2\phi_j, \tag{5.26}$$

$$\dot{\theta}_{jeff} = \frac{\kappa^2-1}{4(\kappa^2+1)}\sin 2\theta_j \sin 2\phi_j. \tag{5.27}$$

The angular velocity also has an additional spin component along the orientation vector defined as $\dot{\psi} = -\cos\theta_j/2 - \dot{\phi}_{jeff}\cos\theta_j$. As is well known, the solution of (5.26) and (5.27) shows that the spheroid rotates in any of a one-parameter family of closed orbits (figure 5.1(b)), the particular orbit being determined by its initial orientation. The parameter is the orbit constant C, that takes values from 0 to ∞. The orbital or the natural coordinates (C,τ) were originally introduced by Leal & Hinch (1971), with the constant-C lines being Jeffery orbits, and the constant-τ lines (τ being the phase change along an orbit) being the constant-ϕ planes projected onto the unit sphere (see chapter 2). In these coordinates, the aforementioned rates of change take on a much simpler form: $dC/dt = 0$ and $d\tau/dt = \kappa/(\kappa^2+1)$. If the spheroid is initially aligned with the vorticity axis, it will continue to spin in that orientation. This particular orbit with $C = 0$ is called a log-rolling (spinning) orbit for a prolate (oblate) spheroid. At leading order, the angular velocity of the spinning spheroid is a constant and is equal to $-(1/2)\mathbf{1}_3$. The disturbance velocity field is steady in this orbit, just like a sphere, and the time period of rotation is 4π. If the initial orientation of the spheroid is in the flow-gradient plane, the orbit would be a unit circle in this plane and is called a tumbling orbit. The rotation in a Jeffery orbit is not uniform for any orbits other than the log-rolling (spinning) orbit. The disturbance velocity field due to a spheroid in these orbits, including the tumbling one in particular, is unsteady. The time period characterizing this changing orientation can be defined based on $\dot{\phi}_{jeff}$, and is given by $T_{jeff} = 2\pi\frac{\kappa^2+1}{\kappa}$. Note that the period is the same for all orbits because $\dot{\phi}_{jeff}$ is independent of θ_j.

As mentioned in section 5.2, the correction to the angular velocity at O(Re), $\mathbf{\Omega}_{c1}$, given in (5.23) is evaluated in section 2.6. The angular velocity components expressed in terms of the angles defined above are of the form:

$$\begin{aligned}\dot{\theta_{c1}} = \sin\theta_j\cos\theta_j \Big[&F_1^f(\xi_0) + F_2^f(\xi_0)\cos 2\phi_j + F_3^f(\xi_0)\cos 2\theta_j + F_4^f(\xi_0)\cos 4\phi_j \\ &+ F_5^f(\xi_0)\cos(2\theta_j - 4\phi_j) + F_6^f(\xi_0)\cos(2\theta_j + 4\phi_j)\Big], \qquad (5.28)\\ \dot{\phi}_{c1} = \sin\phi_j\cos\phi_j \Big[&G_1^f(\xi_0) + G_2^f(\xi_0)\cos 2\theta_j + G_3^f(\xi_0)\cos 2\phi_j + G_4^f(\xi_0)\cos(2\theta_j)\cos(2\phi_j)\Big]. \qquad (5.29)\end{aligned}$$

The functions F_i^f's and G_i^f's are defined for a prolate spheroid in (2.95-2.103) with $\lambda = 0$, the corresponding functions for an oblate spheroid being obtained using the transformation defined in section 5.2. The angular velocity components at O(St) is also of the same form as given in (5.28-5.29), but with the functions F_i^f's and G_i^f's replaced with F_i^p's and G_i^p's, respectively, and these functions are defined in (2.79-2.85) with $\lambda = 0$. The rates of change defined in (5.28) and (5.29), lead to a drift across Jeffery orbits. The orbital drift, defined as the average change in C over one complete rotation of the spheroid, can be obtained from a multiple time scale analysis and has been used to analyze the effect of inertia at O(Re) (Subramanian & Koch (2005, 2006*b*) and chapter 2). It has been found that on time scales of O(Re^{-1}), a prolate spheroid of any aspect ratio settles into the tumbling orbit, and an oblate spheroid with aspect ratio κ in the range $0.142 < \kappa < 1$ asymptotes to the spinning orbit. For oblate spheroids with $\kappa < 0.142$, a repeller exists on the unit sphere (see red curve in figure 5.1 (c)), dividing the orientation hemisphere into two basins of attraction with the attractors being the spinning and the tumbling orbits, and, in the absence of stochastic fluctuations, the spheroid can settle into either of these depending on its initial orientation. The angular velocity corrections at O(St) result in a drift which stabilizes the tumbling(spinning) orbit for prolate(oblate) spheroids. In the analysis below, we focus on the effect of inertia on the time periods of rotation, of both prolate and oblate spheroids, in the orbits into which they settle at long times due to the O(Re) and O(St) drifts.

The correction to the spinning time period at O(Re) is zero. The regular nature of the O(Re) correction implies that the alteration of the time period at this order is related to the symmetry of the inertial acceleration of the Stokes velocity field. The latter is symmetric about two planes; these being formed by the ambient vorticity with the extensional and compressional axes of the simple shear. The resulting acceleration field is antisymmetric. This antisymmetry together with the regular nature of O(Re) correction, makes the correction to angular velocity at this order zero and therefore the time period is unaltered. This can also be seen by noting that due to the regular nature of the inertial correction, the angular velocity must be quadratic in the velocity gradient tensor. Being a pseudo-vector it should therefore be proportional to $\boldsymbol{\omega} \cdot \boldsymbol{E}$ (note that $\boldsymbol{p}$ is coincident with $\boldsymbol{\omega}$), which is zero for a simple shear flow, since vorticity $\boldsymbol{\omega}$ is perpendicular to the components of the rate of strain tensor $\boldsymbol{E}$. The O(St) correction to the spinning time period is also zero. This is because, the leading order angular acceleration is 0 for a spinning spheroid, and therefore, the particle inertia cannot affect the rate of rotation of the spheroid.

In the tumbling orbit, $\dot{\phi}_j$ is not a constant, and depends on $\boldsymbol{p}$, further, the latter is not coincident with $\boldsymbol{\omega}$. The time period for a spheroid rotating in the tumbling orbit is given by:

$$\Delta T^{tumb} = \int_{\pi}^{-\pi} \frac{d\phi_j}{\dot{\phi}_{jeff} + Re\,\dot{\phi}_{c1} + Re^{3/2}\,\dot{\phi}_{c2}} = \int_{\pi}^{-\pi} \frac{d\phi_j}{\dot{\phi}_{jeff}} - Re \int_{\pi}^{-\pi} \frac{\dot{\phi}_{c1} d\phi_j}{\dot{\phi}^2_{jeff}} + O(Re^{3/2}), \tag{5.30}$$

where the expansion is valid for $\kappa \sim O(1)$, when $\dot{\phi}_{c1} Re << \dot{\phi}_{jeff}$. The leading order integral on the right-hand side above, evaluates to $2\pi(\kappa^2+1)/k$, which is of course, the Jeffery period.

The O(Re) integral in the above equation, evaluates to zero after substituting for $\dot{\phi}_{jeff}$ and $\dot{\phi}_{c1}$ from (5.26) and (5.29), respectively. The O(St) correction to time period in the tumbling orbit can be shown to be zero in a manner similar to that for the fluid inertial correction above. This follows from the identical angular dependence of the rates of change of orientation at O(St) and O(Re).

The correction to the time period due to fluid inertia therefore arises at O($Re^{3/2}$) for both the tumbling and the spinning orbits. As mentioned in the introduction, the O($Re^{3/2}$) correction for a rigid sphere is evaluated in (Stone *et al.* 2000; Subramanian *et al.* 2011). The evaluation of the correction for a spheroid in the spinning orbit is simpler in that it closely resembles the calculation for a sphere, and this simpler calculation is presented in section 5.5. The correction for a spheroid in the tumbling orbit, which is more involved, in having to account for the unsteadiness of the disturbance velocity field, is presented in section 5.6. The correction due to particle inertia at O(St^2) is presented in section 5.4.

5.4 Evaluation: Time period - particle inertia

The correction to the time period for an inertial spheroid at $O(St^2)$ is evaluated in this section. In the spinning orbit, the $O(St^2)$ correction to the angular velocity is zero due to the absence of angular acceleration at O(St). Recall that angular velocity correction at O(St) is 0. In what follows, we determine the correction to the Jeffery period for a tumbling prolate spheroid. Using $\dot{\phi}_j = \dot{\phi}_{jeff} + St\left(\frac{d\phi_j}{dt}\right)_{St} + St^2\left(\frac{d\phi_j}{dt}\right)_{St^2}$, the $O(St^2)$ correction to the period of rotation comes out to be:

$$\Delta T_{St^2} = St^2 \int_{\pi}^{-\pi}\left[\frac{1}{\dot{\phi}^3_{jeff}}\left(\frac{d\phi_j}{dt}\right)^2_{St} - \frac{1}{\dot{\phi}^2_{jeff}}\left(\frac{d\phi_j}{dt}\right)_{St^2}\right]. \tag{5.31}$$

where $\left(\frac{d\phi_j}{dt}\right)_{St}$ is given by (2.78). The correction to the angular velocity can be easily obtained by expanding $\boldsymbol{\Omega}_1$ in (5.21), with $Re = 0$, to O(St^2). The correction for the angular velocity at O(St^2), $\boldsymbol{\Omega}^{(1)}_{St^2}$, takes the form:

$$\boldsymbol{\Omega}^{(1)}_{St^2}\cdot\boldsymbol{L}^{(2)} = \boldsymbol{I}_p\cdot\left(\frac{d\boldsymbol{\Omega}_{jeff}}{dt_1} + \frac{d\boldsymbol{\Omega}^{(1)}_{1St}}{dt_{jeff}}\right) + \boldsymbol{\Omega}^t_{jeff}\wedge(\boldsymbol{I}_p\cdot\boldsymbol{\Omega}^{(1)}_{1St}) + \boldsymbol{\Omega}^t_{St}\wedge(\boldsymbol{I}_p\cdot\boldsymbol{\Omega}_{jeff}), \tag{5.32}$$

where d/dt_1 denotes the correction to the leading order rate of change, d/dt_{jeff} (defined in section 2.5), due to the O(St) deviation from a Jeffery orbit. In (5.32), $\boldsymbol{\Omega}^t_{St}$, is the O($St$) correction to the angular velocity of the body aligned coordinate system. For the tumbling orbit, simplifying (5.32) gives:

$$\left(\frac{d\phi_j}{dt}\right)_{St^2} = H_1^p(\xi_0)\cos 2\phi_j + H_2^p(\xi_0)\cos 4\phi_j + H_3^p(\xi_0)\cos 6\phi_j, \tag{5.33}$$

where

$$H_1^p(\xi_0) = -\frac{(16\xi_0^4 - 16\xi_0^2 + 5)(\bar{\xi}_0^{\,2}\xi_0 + (1-\xi_0^4)\coth^{-1}\xi_0)^2}{3200\xi_0^2\,(2\xi_0^2-1)^{\,3}}, \tag{5.34}$$

$$H_2^p(\xi_0) = \frac{(\bar{\xi}_0^{\,2}\xi_0 + (1-\xi_0^4)\coth^{-1}\xi_0)^2}{400\,(\xi_0 - 2\xi_0^3)^{\,2}}, \tag{5.35}$$

$$H_3^p(\xi_0) = -\frac{3(\bar{\xi}_0^{\,2}\xi_0 + (1-\xi_0^4)\coth^{-1}\xi_0)^2}{3200\xi_0^2\,(2\xi_0^2-1)^{\,3}}. \tag{5.36}$$

Using (5.33)-(5.36) in (5.31), the change induced by particle inertia in the period of rotation of a tumbling prolate spheroid is given by:

$$\Delta T_{St^2} = St^2\frac{\pi[2\xi_0(\bar{\xi}_0 - \xi_0) + 1][(1-\xi_0^4)\coth^{-1}\xi_0 + \xi_0^3 - \xi_0]^2}{100\xi_0^2(2\xi_0^2-1)}. \tag{5.37}$$

At $O(St)$, the inertial persistence leads to a shift in the locations of the angular velocity extrema relative to those for the original Jeffery orbit. The angular displacements are of $O(\Omega(\phi_m)\tau_p)$, $\tau_p = I/L^{(2)}$ being the inertial relaxation time that governs the persistence of the angular velocity. Here, $\Omega(\phi_m)$ is the angular speed at the extremum, I is the (non-dimensional) equatorial moment of inertia relevant to the tumbling mode while $L^{(2)}$ is the aspect-ratio scale for the test-torque coefficient. In the near-sphere limit, the angular displacements are $O(St)$ for both the maxima and minima, while for the slender fiber limit, the test-torque coefficient is $O[\ln(\xi_0-1)]^{-1}$, and these displacements are $O[St(\xi_0-1).\ln(\xi_0-1)]$ and $O[St(\xi_0-1)^2.\ln(\xi_0-1)]$ for the maxima ($\phi_m = \frac{\pi}{2}, \frac{3\pi}{2}$) and minima ($\phi_m = 0, \pi$), respectively. This $O(St)$ alteration in the angular velocity profile does not, however, change the period due to the anti-symmetry of the angular acceleration profiles in the compressional and extensional quadrants of the Jeffery orbit. At $O(St^2)$, this antisymmetry is broken with the result that the decrease in the traversal time of the extensional quadrants is greater than the corresponding increase in the compressional ones, leading to a net decrease in the period of rotation. For a near-sphere, this reduction in period is smaller than expected owing to a cancellation at $O(St^2\xi_0^{-2})$; (5.37) gives - $St^2\frac{\pi}{450\xi_0^4}$. For a slender fiber, the changes in angular velocity over the meridional portion of the trajectory (the non-aligned phase) govern the reduction in period. The $O(St)$ angular acceleration of a non-aligned slender fiber combines with a moment of

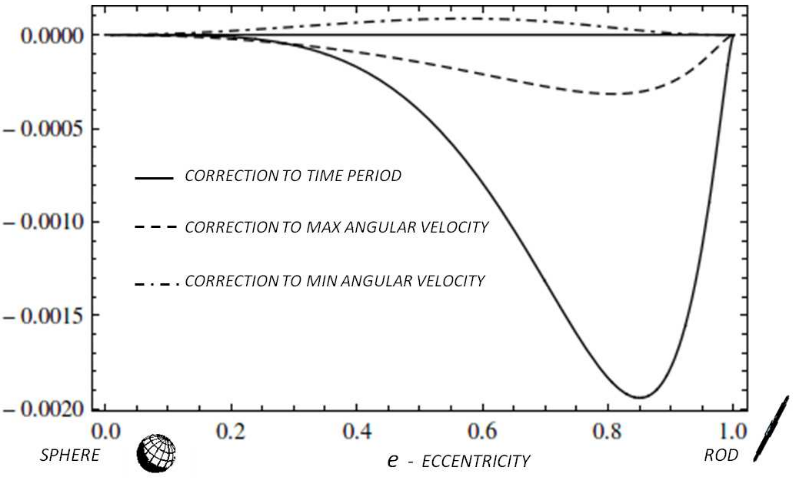

Fig. 5.2 The $O(St^2)$ corrections to the time period and the angular velocity extrema, as a function of ξ_0, for a prolate spheroid in the tumbling mode

inertia of $O(\xi_0 - 1)$, leading to a change in angular velocity of $St\,(\xi_0 - 1)\ln(\xi_0 - 1)$. An analogous argument implies that the change in angular velocity at $O(St^2)$ is $St^2(\xi_0-1)^2[\ln(\xi_0-1)]^2$, which then gives the aspect-ratio-scaling for the reduction in the period; the limiting form of (5.37) gives $-St^2\frac{\pi}{25}(\xi_0-1)^2[\ln(\xi_0-1)]^2$.

It turns out that the minimum and maximum angular velocities in the tumbling mode are unaltered at $O(St)$. Starting from (5.33), one obtains the following expressions, to $O(St^2)$, for the angular velocity extrema:

$$\Omega_{max} = -\frac{\xi_0^2}{2\xi_0^2-1} + St^2\frac{\xi_0^2[-\xi_0^3+\xi_0+(\xi_0^4-1)\coth^{-1}\xi_0]^2}{400(2\xi_0^2-1)^3}, \tag{5.38}$$

$$\Omega_{min} = -\frac{\overline{\xi}_0^{\,2}}{2\xi_0^2-1} - St^2\frac{\overline{\xi}_0^{8}[\xi_0-(\xi_0^2+1)\coth^{-1}\xi_0]^2}{400\xi_0^2(2\xi_0^2-1)^3}. \tag{5.39}$$

The corrections to the time period, maximum and minimum angular velocities are plotted as a function of the prolate spheroid eccentricity $(e = \frac{1}{\xi_0})$ in figure 5.2. The effect of particle inertia is to make the angular velocity extrema approach each other, consistent with the general notion of an inertial resistance to angular acceleration (for large St, the particle begins to rotate with a constant angular velocity of $4\,\pi$ in the flow-gradient plane (Lundell (2011))). Although the changes in the maxima and minima are of opposite signs, the correction to time period is negative for all ξ_0, implying that the time period decreases at $O(St^2)$. This decrease is consistent with consistent with recent simulations (Mao & Alexeev (2014)), although a quantitative comparison is not possible due to the simulations being carried out for much larger St.

5.5 Evaluation: Time period - spinning orbit

In this section we focus on the effect of fluid inertia on spinning spheroids. The spinning mode is the only steady state orbit for oblate spheroids with aspect ratios larger than 0.142, and one of two steady state orbits for oblate spheroids with aspect ratio less than 0.142. As explained in section 5.3, there is no correction to angular velocity at $O(Re)$. Noting that the leading order angular velocity in spinning is $-(1/2)\mathbf{1}_3$, and defining the correction to the angular velocity at $O(Re^{3/2})$ as $\dot{\psi}_{c2}\mathbf{1}_3$, $\dot{\psi}_{c2}$ being independent of the spin angle ψ due to symmetry, the $O(Re^{3/2})$ correction can be written as:

$$\Delta T_{c2}^{spin} = 8\pi Re^{3/2}\,\dot{\psi}_{c2}, \tag{5.40}$$

$\dot{\psi}_{c2}$ can be obtained by contracting (5.24) with $\mathbf{1}_3$ and is given by:

$$\dot{\psi}_{c2} = \frac{1}{8\pi X_C}\int\left[4\pi^2k^2\hat{\boldsymbol{u}}^f - (\boldsymbol{\Gamma}^{\dagger}\cdot\boldsymbol{k})\cdot\nabla_{\boldsymbol{k}}\hat{\boldsymbol{u}}^{match} + \boldsymbol{\Gamma}\cdot\hat{\boldsymbol{u}}^{match}\right] \cdot\left\{\frac{i\,(\boldsymbol{S}^{(2t)}\cdot\boldsymbol{k})\cdot\mathbf{1}_3}{2\pi k^2}\cdot\left(\boldsymbol{I}-\frac{\boldsymbol{kk}}{k^2}\right)\right\}d\boldsymbol{k}, \tag{5.41}$$

where all the terms in the integrand are evaluated at $\theta_j = 0$, corresponding to the spinning orbit, and X_C is the axisymmetric torque coefficient defined in section 5.2. The Fourier transforms of the velocity fields $\hat{\boldsymbol{u}}^{match}$ and $\hat{\boldsymbol{u}}^f$ are now independent of time. The integral for the time period in (5.40) then becomes:

$$\Delta T_{c2}^{spin} = -\frac{Re^{3/2}}{X_C}\int\left[-4\pi^2k^2\hat{\boldsymbol{u}}^f + (\boldsymbol{\Gamma}^{\dagger}\cdot\boldsymbol{k})\cdot\nabla_{\boldsymbol{k}}\hat{\boldsymbol{u}}^{match} - \boldsymbol{\Gamma}\cdot\hat{\boldsymbol{u}}^{match}\right] \cdot\left\{\frac{i\,(\boldsymbol{S}^{(2t)}\cdot\boldsymbol{k})\cdot\mathbf{1}_3}{2\pi k^2}\cdot\left(\boldsymbol{I}-\frac{\boldsymbol{kk}}{k^2}\right)\right\}d\boldsymbol{k}. \tag{5.42}$$

The term within braces above, is independent of time and can be written as:

$$\frac{i\,(\boldsymbol{S}^{(2t)}\cdot\boldsymbol{k})\cdot\mathbf{1}_3}{2\pi k^2}\cdot\left(\boldsymbol{I}-\frac{\boldsymbol{kk}}{k^2}\right) = \boldsymbol{T}_{\mathbf{1}}^{spin} = \frac{i(B_2+B_3)}{2k^2\pi}(k_2\,\mathbf{1}_1 - k_1\,\mathbf{1}_2) \tag{5.43}$$

using (5.8). For a sphere $B_2 + B_3$ above reduces to -4π, which is equal to half the torque exerted by a sphere rotating with a unit non-dimensional angular velocity.

The singularity $\boldsymbol{S}$ in the actual problem takes the form $\boldsymbol{S} = A_3\boldsymbol{E}$, and therefore $\hat{\boldsymbol{u}}^{match}$ is $-\frac{iA_3\boldsymbol{E}\cdot\boldsymbol{k}}{2\pi k^2}\cdot\left(\boldsymbol{I} - \frac{\boldsymbol{kk}}{k^2}\right)$ from (5.25), which is same as the Fourier transformed stresslet velocity field for a sphere($A_3 = -20\pi/3$), except for a ξ_0 dependent coefficient. The inertial terms in (5.42) involving $\hat{\boldsymbol{u}}^{match}$ take the form:

$$(\boldsymbol{\Gamma}^{\dagger}\cdot\boldsymbol{k})\cdot\nabla_{\boldsymbol{k}}\hat{\boldsymbol{u}}^{match} - \boldsymbol{\Gamma}\cdot\hat{\boldsymbol{u}}^{match} = \boldsymbol{R}_1^{spin}, \tag{5.44}$$

where $\boldsymbol{R}_1^{spin}$ is given by:

$$\boldsymbol{R}_1^{spin} = \frac{A_3}{2k^6\pi}\left(ik_1^3\left(k^2 - 4k_2^2\right)\boldsymbol{1}_1 + ik_1^2k_2\left(3k^2 - 4k_2^2\right)\boldsymbol{1}_2 + ik_1^2\left(k^2 - 4k_2^2\right)k_3\boldsymbol{1}_3\right). \tag{5.45}$$

The Fourier transform of the velocity field $\boldsymbol{u}^f$ in (5.42) is governed by (5.20). After eliminating the pressure term, (5.20) reduces, for the spinning case, to:

$$\begin{aligned} &-(\boldsymbol{\Gamma}^{\dagger}\cdot\boldsymbol{k})\cdot\nabla_{\boldsymbol{k}}\hat{\boldsymbol{u}}^f + \boldsymbol{\Gamma}\cdot\hat{\boldsymbol{u}}^f\cdot\left(\boldsymbol{I} - 2\frac{\boldsymbol{kk}}{k^2}\right) + 4\pi^2k^2\hat{\boldsymbol{u}}^f = \boldsymbol{R}_1^{spin}\cdot\left(\boldsymbol{I} - \frac{\boldsymbol{kk}}{k^2}\right) = \boldsymbol{Q}^{spin} \\ &= \frac{A_3}{k^6\pi}\left(-ik_1^3k_2^2A_3\boldsymbol{1}_1 + ik_1^2k_2\left(k_1^2 + k_3^2\right)\boldsymbol{1}_2 - ik_1^2k_2^2k_3\boldsymbol{1}_3\right). \end{aligned} \tag{5.46}$$

The equation governing $\hat{\boldsymbol{u}}^f$ above can be written in terms of its components in the space-fixed coordinate system as:

$$\frac{\partial\hat{u}_1^f}{\partial k_2} - 4\pi^2k^2\frac{\hat{u}_1^f}{k_1} - \left(1 - \frac{2k_1^2}{k^2}\right)\frac{\hat{u}_2^f}{k_1} = -\frac{Q_1^{spin}}{k_1}, \tag{5.47}$$

$$\frac{\partial\hat{u}_2^f}{\partial k_2} - 4\pi^2k^2\frac{\hat{u}_2^f}{k_1} + \left(\frac{2k_1k_2}{k^2}\right)\frac{\hat{u}_2^f}{k_1} = -\frac{Q_2^{spin}}{k_1}, \tag{5.48}$$

$$\frac{\partial\hat{u}_3^f}{\partial k_2} - 4\pi^2k^2\frac{\hat{u}_3^f}{k_1} + \left(\frac{2k_1k_3}{k^2}\right)\frac{\hat{u}_2^f}{k_1} = -\frac{Q_3^{spin}}{k_1}, \tag{5.49}$$

where subscripts 1, 2 and 3 denote the components along X, Y and Z axes of the space-fixed coordinate system. While the components along the flow ($\hat{u}_1^f$) and the vorticity ($\hat{u}_3^f$) axes are coupled to the component along the gradient axis ($\hat{u}_2^f$), the equation governing the latter is independent of the other two, and is therefore solved first. In (5.47)-(5.49), one can identify a simple shear flow in Fourier space, given by $\hat{\boldsymbol{u}}^{*\infty}(\boldsymbol{k}) = -k_1\boldsymbol{1}_2$. This simple shear flow is orthogonal to the one in physical space ($\boldsymbol{u}^{\infty}(\boldsymbol{x}) = x_2\boldsymbol{1}_1$). The orthogonality arises because the

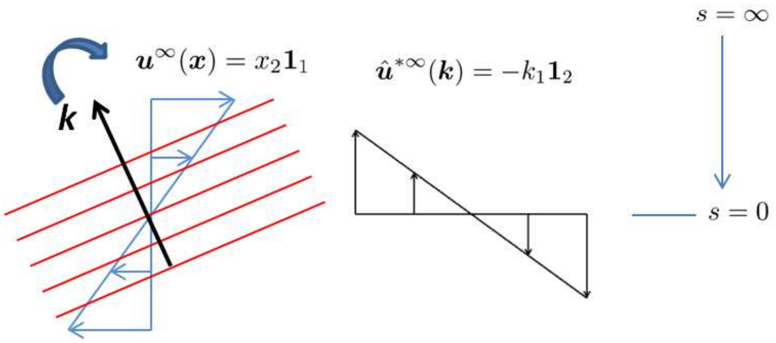

Fig. 5.3 The red lines denote the wave fronts. $\boldsymbol{k}$ is the wave vector which gets turned due to a simple shear flow of the form $\boldsymbol{u}^{\infty}(\boldsymbol{x}) = x_2 \mathbf{1}_1$. This is equivalent to a convection by a simple shear flow of the form $\hat{\boldsymbol{u}}^{*\infty}(\boldsymbol{k}) = -k_1 \mathbf{1}_2$ in the Fourier space.

wavevector is oriented normal to the wave fronts, the latter being turned by the simple shear flow in physical space (see figure 5.3). The components of the Fourier transformed velocity field are convected by the Fourier space simple shear flow with the streamlines of this flow being defined by $k_2' = k_2 + k_1 s$, where s is a time-like variable. This convection has the effect that $\hat{\boldsymbol{u}}^f(\boldsymbol{k})$, of a given $\boldsymbol{k}$, has contributions from all wavevectors turned onto $\boldsymbol{k}$ from orientations further upstream. The viscous term, proportional to $4\pi^2 k^2$ in (5.47-5.49) causes an exponential decay in amplitude which is proportional to the square of the changing wavevector during this 'turning' period. Thus, the solutions for the individual components $\hat{u}_2^{f\beta}$, $\hat{u}_1^f$ and $\hat{u}_3^f$ are written in terms of integrals over s as follows:

$$\hat{u}_2^f(\boldsymbol{k}) = \int_0^{\infty} e^{-4\pi^2\left(k^2 s + k_1 k_2 s^2 + \frac{k_1^2 s^3}{3}\right)} \left(\frac{1}{k^2}\right) \frac{i k_1^2 (k_2 + k_1 s)\left(k_1^2 + k_3^2\right) A_3}{k'^4 \pi}\, ds, \tag{5.50}$$

$$\hat{u}_1^f(\boldsymbol{k}) = \int_0^{\infty} e^{-4\pi^2\left(k^2 s + k_1 k_2 s^2 + \frac{k_1^2 s^3}{3}\right)} \left(-\frac{i k_1^3 (k_2 + k_1 s)^2 A_3}{k'^6 \pi} - \left(1 - \frac{2k_1^2}{k'^2}\right) \hat{u}_2^f(\boldsymbol{k}')\right) ds, \tag{5.51}$$

and

$$\hat{u}_3^f(\boldsymbol{k}) = \int_0^{\infty} e^{-4\pi^2\left(k^2 s + k_1 k_2 s^2 + \frac{k_1^2 s^3}{3}\right)} \left(-\frac{i k_1^2 (k_2 + k_1 s)^2 k_3 A_3}{k'^6 \pi} + \frac{2 k_1 k_3}{k'^2} \hat{u}_2^f(\boldsymbol{k}')\right) ds, \tag{5.52}$$

where the components in the flow and vorticity directions are coupled to the component in the gradient direction through the term $\hat{u}_2^f(\boldsymbol{k}')$. Here, $\boldsymbol{k}' = (k_1 \mathbf{1}_1 + (k_2 + k_1 s)\mathbf{1}_2 + k_3 \mathbf{1}_3)$ and

$k' = |\boldsymbol{k'}|$,and $\hat{u}_2^f(\boldsymbol{k'})$ in (5.51) and (5.52) is given by:

$$\hat{u}_2^f(\boldsymbol{k'}) = \int_0^\infty e^{-4\pi^2\left(k'^2 s' + k_1(k_2+k_1 s)s'^2 + \frac{k_1^2 s'^3}{3}\right)} \left(\frac{1}{k'^2}\right) \frac{ik_1^2 k_2'' \left(k_1^2+k_3^2\right) A_3}{k''^4 \pi}\, ds', \tag{5.53}$$

where $\boldsymbol{k''} = (k_1 \mathbf{1}_1 + (k_2 + k_1(s+s'))\mathbf{1}_2 + k_3 \mathbf{1}_3)$, $k'' = |\boldsymbol{k''}|$ and $k_2'' = (k_2 + k_1(s+s'))$. Thus, the expressions for components in the flow and vorticity direction given in (5.50) and (5.52) include a one-dimensional and a two-dimensional integral whereas that for the component in the gradient direction given in (5.51) consists of only a one-dimensional integral. The Fourier transform of the test velocity field given in (5.43) and the inertial terms given in (5.44)-(5.45) and (5.50)-(5.52) are now substituted in (5.42) to obtain:

$$\Delta T_{c2}^{spin} = -\frac{Re^{3/2}}{X_c} \int \left[-4\pi^2 k^2 (\hat{u}_1^f \mathbf{1}_1 + \hat{u}_2^f \mathbf{1}_2 + \hat{u}_3^f \mathbf{1}_3) + \boldsymbol{R}_1^{spin}\right] \cdot \boldsymbol{T}_1^{spin}\, d\boldsymbol{k}. \tag{5.54}$$

The different terms in the integral above can be expressed in a spherical coordinate system with $k_1 = k \sin\theta \cos\phi$, $k_2 = k \sin\theta \sin\phi$, $k_3 = k\cos\theta$ and $d\boldsymbol{k} = k^2 \sin\theta dk d\theta d\phi$ as :

$$\begin{aligned}\int (-4\pi^2 k^2\, \hat{u}_1^f(\boldsymbol{k})\, \mathbf{1}_1 \cdot \boldsymbol{T}_1^{spin}) d\boldsymbol{k} = \int_0^{2\pi}\int_0^{\pi}\int_0^{\infty} 4\pi^2 \Bigg\{ k^2 \frac{ik_1^3 k_2'^2 A_3}{k'^6 \pi} \\ \left[\frac{i(B_2+B_3)k_2}{2k^2\pi}\right]\Bigg\} \int_0^\infty k^2 e^{-4\pi^2\left(k^2 s + k_1 k_2 s^2 + \frac{k_1^2 s^3}{3}\right)} dk\, ds \sin\theta\, d\theta\, d\phi \\ + \int_0^{2\pi}\int_0^{\pi}\int_0^{\infty}\int_0^{\infty} \left\{ 4\pi^2 k^2 \left[\frac{i(B_2+B_3)k_2}{2k^2\pi}\right] \left(1 - \frac{2k_1^2}{k'^2}\right) \frac{ik_1^2 k_2''(k_1^2+k_3^2) A_3}{k''^4 k'^2 \pi} \right\} \\ \int_0^\infty e^{-4\pi^2\left(k^2 s + k_1 k_2 s^2 + \frac{k_1^2 s^3}{3}\right)} e^{-4\pi^2\left(k'^2 s' + k_1 k_2' s'^2 + \frac{k_1^2 s'^3}{3}\right)} k^2 dk\, ds'\, ds \sin\theta\, d\theta\, d\phi,\end{aligned} \tag{5.55}$$

$$\begin{aligned}\int (-4\pi^2 k^2\, \hat{u}_2^f(\boldsymbol{k})\, \mathbf{1}_2 \cdot \boldsymbol{T}_1^{spin}) d\boldsymbol{k} = -\int 4\pi^2 \Bigg\{ \left[\frac{-i(B_2+B_3)k_1}{2k^2\pi}\right] \\ \frac{ik_1^2 (k_2 + k_1 s)\left(k_1^2+k_3^2\right) A_3}{k^2 k'^4 \pi}\Bigg\} \int_0^\infty e^{-4\pi^2\left(k^2 s + k_1 k_2 s^2 + \frac{k_1^2 s^3}{3}\right)} k^2 dk\, ds \sin\theta\, d\theta\, d\phi,\end{aligned} \tag{5.56}$$

$$\int (-4\pi^2 k^2\, \hat{u}_3^f(\boldsymbol{k})\, \mathbf{1}_3 \cdot \boldsymbol{T}_1^{spin}) d\boldsymbol{k} = 0, \tag{5.57}$$

and

$$\int \boldsymbol{R}_1^{spin} \cdot \boldsymbol{T}_1^{spin} d\boldsymbol{k} = \int_0^{2\pi}\int_0^{\pi}\int_0^{\infty} \left\{ -\frac{A_3 k_1^3 (k^2 - 4k_2^2)}{\pi k^6} \frac{(B_2 + B_3) k_2}{4\pi} + \frac{A_3 k_1^2 k_2 (3k^2 - 4k_2^2)}{k^6 \pi} \frac{(B_2 + B_3) k_1}{4\pi} \right\} dk \sin\theta d\theta d\phi, \tag{5.58}$$

where we have retained the notation k_1, k_2 and k_3 for brevity and the terms grouped within the braces are such that they are independent of k. The test velocity field has no component along the vorticity axis and therefore the contribution to (5.54) due to the term proportional to $\hat{u}_3^f$ is zero.

The right-hand side of (5.55) is sum of a 4-dimensional and a 5-dimensional integral whereas that of (5.56) is a single 4-dimensional integral. In the 4 dimensional integrals, the integration over k gives a term proportional to $1/s^{3/2}$, which is a divergent term in the integration over 's', as $s \to 0$. Thus the integral over k is divergent as $k \to \infty$ when $s = 0$. The three dimensional integral in the rhs of (5.58) also diverges in the limit $k \to \infty$. Although, individually, the above mentioned integrals are divergent in the said limit, the sum is nevertheless convergent. This divergence arises because while deriving the expression for the angular velocity in (5.21), we had rewritten the three terms proportional to $\hat{u}^f$ in (5.6), as a sum of a term proportional to $\hat{u}^f$ and three terms proportional to $\hat{u}^{match}$, and each of these four terms are divergent in the limit of $k \to \infty$. Noting that $\int_0^\infty 4\pi^2 k^2 exp(-4\pi^2 k^2 s) ds = 1$ for $s \neq 0$ and is divergent as $s \to 0$, we isolate the divergence in (5.58) by introducing an additional integral over the dummy variable 's' as shown below:

$$\int \boldsymbol{R}_1^{spin} \cdot \boldsymbol{T}_1^{spin} d\boldsymbol{k} = \int_0^{2\pi}\int_0^{\pi}\int_0^{\infty} \left\{ \frac{-A_3 k_1^3 (k^2 - 4k_2^2)}{\pi k^6} \frac{(B_2 + B_3) k_2}{4\pi} + \frac{A_3 k_1^2 k_2 (3k^2 - 4k_2^2)}{k^6 \pi} \frac{(B_2 + B_3) k_1}{4\pi} \right\} \int_0^\infty 4\pi^2 k^2 e^{-4\pi^2 k^2 s} ds dk \sin\theta d\theta d\phi. \tag{5.59}$$

The k integrals in the above equation can be readily evaluated and is given by $\int_0^\infty k^2 e^{-4\pi^2 k^2 s} dk = 1/(32\pi^{5/2} s^{3/2})$ and (5.59) takes the form:

$$\int \boldsymbol{R}_1^{spin} \cdot \boldsymbol{T}_1^{spin} d\boldsymbol{k} = \int_0^{2\pi}\int_0^{\pi}\int_0^{\infty} \left\{ \frac{-A_3 k_1^3 (k^2 - 4k_2^2)}{\pi k^6} \frac{(B_2 + B_3) k_2}{4\pi} + \frac{A_3 k_1^2 k_2 (3k^2 - 4k_2^2)}{k^6 \pi} \frac{(B_2 + B_3) k_1}{4\pi} \right\} \frac{1}{\sqrt{\pi} s^{3/2}} ds \sin\theta d\theta d\phi. \tag{5.60}$$

The integration over k in the 4-dimensional integrals in (5.55) and (5.56) gives:

$$\int_0^\infty k^2 e^{-4\pi^2\left(k^2 s+k_1 k_2 s^2+\frac{k_1^2 s^3}{3}\right)} dk = \int_0^\infty k^2 e^{-4\pi^2 k^2 (s+\sin^2\theta\cos\phi\sin\phi s^2+\sin^2\theta\cos^2\phi s^3/3)} dk \\ = \frac{1}{32\pi^{5/2}(s+\sin^2\theta\cos\phi\sin\phi s^2+\sin^2\theta\cos^2\phi s^3/3)^{3/2}}. \tag{5.61}$$

The integration over k in the 5-dimensional integral in (5.55) gives:

$$\int_0^\infty k^2 e^{-4\pi^2\left(k^2 s+k_1 k_2 s^2+\frac{k_1^2 s^3}{3}\right)} e^{-4\pi^2\left(k'^2 s'+k_1 k_2' s'^2+\frac{k_1^2 s'^3}{3}\right)} dk = \int k^2 \\ e^{-4\pi^2 k^2 \frac{s'}{12}\left(3\left(4+s^2-s^2 cos2\theta+2s\sin^2\theta(s\cos 2\phi+2\sin 2\phi)\right)+4\cos\phi\sin^2\theta s'(3\sin\phi+\cos\phi(3s+s'))\right)} \\ e^{-4\pi^2 k^2 (s+\sin^2\theta\cos\phi\sin\phi s^2+\sin^2\theta\cos^2\phi s^3/3)} dk = \frac{1}{32\pi^{5/2}(f^{exp}(s,s',\theta,\phi))^{3/2}}, \tag{5.62}$$

where f^{exp} is the function that multiplies '$-4\pi^2 k^2$' in the exponent of the integrand. Note that there is no divergence for the five dimensional integral in the limit of $s \to 0$ or $s' \to 0$. The integration over k for the four-dimensional integrals given in (5.55) and (5.56) are substituted from (5.61), and the sum of the resulting three-dimensional integral together with the matching term contribution given in (5.60) is convergent in the limit of $s \to 0$. This sum, which is a three-dimensional integral (over s, θ, ϕ), and the four-dimensional (over s, s', θ, ϕ) integral obtained from the five-dimensional ones in (5.55) and (5.56), after substituting from (5.62), are evaluated numerically using Gaussian quadrature to give the time period correction as:

$$\Delta T_{c2}^{spin} = Re^{3/2}\frac{A_3(B_2+B_3)}{X_C}0.00516. \tag{5.63}$$

The angular velocity correction at O($Re^{3/2}$) can be obtained by using (5.40) and is given by $\frac{1}{8\pi}\Delta T_{c2}^{spin}$. For an oblate spheroid, $A_3(B_2+B_3)/X_c$=$128\pi^2/(9\ ArcCsc\xi_0\ \xi_0^5-6\xi_0\sqrt{-1+\xi_0^2}-9\xi_0^3\sqrt{-1+\xi_0^2})$. For a sphere, the angular velocity reduces to that obtained by (Stone *et al.* 2000; Subramanian *et al.* 2011).

5.6 Evaluation: Time period - tumbling orbit

In this section we focus on the tumbling orbit which is the long-time orbit for prolate spheroids of any aspect ratio and for oblate spheroids with aspect ratios less than 0.142. The integral for the O($Re^{3/2}$) correction to the tumbling time period can be obtained in a similar manner to that derived in (5.30) and is given by:

$$\Delta T_{c2}^{tumb} = -Re^{3/2}\int_{\pi}^{-\pi}\frac{\dot{\phi}_{c2}\,d\phi_j}{\dot{\phi}_{jeff}^2} = -Re^{3/2}\int_0^{T_{jeff}}\frac{\dot{\phi}_{c2}\,dt}{\dot{\phi}_{jeff}}. \tag{5.64}$$

In (5.64) above, we have changed the variable of integration back to time based on $d\phi_j/dt = \dot{\phi}_{jeff}$ since the error associated with this change of variable affects the time period only at O($Re^{3/2}$). The angular velocity of a spheroid in a tumbling orbit can be expressed in terms of $\dot{\phi}_j$ alone due to symmetry, and therefore, $\dot{\phi}_{c2}$ may be obtained by contracting (5.24) with $\mathbf{1}_3$ which gives:

$$\begin{aligned}\dot{\phi}_{c2} = \frac{1}{8\pi Y_C}\int\left[4\pi^2k^2\hat{\boldsymbol{u}}^f + \frac{\partial\hat{\boldsymbol{u}}^{match}}{\partial t} - (\boldsymbol{\Gamma}^\dagger\cdot\boldsymbol{k})\cdot\nabla_{\boldsymbol{k}}\hat{\boldsymbol{u}}^{match} + \boldsymbol{\Gamma}\cdot\hat{\boldsymbol{u}}^{match}\right]&\\ \cdot\left\{\frac{i\,(\boldsymbol{S}^{(2t)}\cdot\boldsymbol{k})\cdot\mathbf{1}_3}{2\pi k^2}\cdot\left(\boldsymbol{I}-\frac{\boldsymbol{kk}}{k^2}\right)\right\}d\boldsymbol{k},&\end{aligned} \tag{5.65}$$

where all the terms in the integrand are evaluated at $\theta_j = \pi/2$, corresponding to the tumbling orbit, and Y_c is the transverse torque coefficient defined in section 5.2. The angular velocity given in (5.65) is substituted in (5.64) to obtain the O($Re^{3/2}$) correction to the time period in the form:

$$\begin{aligned}\Delta T_{c2}^{tumb} = \frac{Re^{3/2}}{8\pi Y_c}\int\int_0^{T_{jeff}}\left[-4\pi^2k^2\hat{\boldsymbol{u}}^f - \frac{\partial\hat{\boldsymbol{u}}^{match}}{\partial t} + (\boldsymbol{\Gamma}^\dagger\cdot\boldsymbol{k})\cdot\nabla_{\boldsymbol{k}}\hat{\boldsymbol{u}}^{match} - \boldsymbol{\Gamma}\cdot\hat{\boldsymbol{u}}^{match}\right]&\\ \cdot\left\{\frac{i\,(\boldsymbol{S}^{(2t)}\cdot\boldsymbol{k})\cdot\mathbf{1}_3}{2\pi k^2\,\dot{\phi}_{jeff}}\cdot\left(\boldsymbol{I}-\frac{\boldsymbol{kk}}{k^2}\right)\right\}dt\,d\boldsymbol{k}.&\end{aligned} \tag{5.66}$$

The integral above is evaluated in the space-fixed coordinate system [XYZ in figure 5.1 (a)] and the details are presented in sections 5.6.1 - 5.6.4 below. The assumptions used when deriving the reciprocal theorem restricts the orientation of the spheroid in the test problem to be the same as that of the spheroid in the problem of interest. Therefore, in the tumbling orbit, the velocity field is unsteady in the test problem too. The singularities corresponding to both the problems are time-dependent point-force-dipole singularities, the time dependence arising from the motion of $\boldsymbol{p}$ along the tumbling orbit. The time dependent $\boldsymbol{p}$ determines $\boldsymbol{S}^{(2t)}$, $\boldsymbol{S}$, and thence $\hat{\boldsymbol{u}}^{match}$ and $\hat{\boldsymbol{u}}^f$. Thus, the term involving the test velocity field given within braces in (5.66), and the inertial terms in the problem of interest given in square brackets, are functions of time. The unsteadiness makes the evaluation of time period nontrivial when compared to the analysis done for the spinning in section 5.5.

To evaluate the integral in (5.66), in section 5.6.1, the term within braces is expressed in the aforementioned coordinate system as a Fourier time series which involves a combination of three Fourier modes, the mode independent of time that is already present for a sphere and modes proportional to $\cos(4\pi t/T_{jeff})$ and $\sin(4\pi t/T_{jeff})$, T_{jeff} being the Jeffrey period. Note that the combination $\boldsymbol{S}^{(2t)}/\dot{\phi}_{jeff}$ is crucial to a finite Fourier time series, and therefore correction to time period can be evaluated. If this combination was not there, for instance, while evaluating the correction to angular velocity in (5.65), the time dependence of $\boldsymbol{S}^{(2t)}$ would have led to an infinite Fourier series in time, in turn preventing an exact calculation of the $O(Re^{3/2})$ correction to the angular velocity. Note that the two time dependent modes have a frequency which is twice the Jeffrey frequency defined as $\omega_g = 2\pi/T_{jeff}$. Physically, this is due to the fore-aft symmetry of the particle which leads to the same disturbance field in the test problem, if $\boldsymbol{p}$ is replaced with $-\boldsymbol{p}$. In (5.66) since one is only interested in the integration over a time period, only the terms corresponding to these three Fourier modes, in the Fourier expansion of the inertial acceleration terms, will lead to non-zero contributions. The expansions for the inertial terms involving $\hat{\boldsymbol{u}}^{match}$ are done in section 5.6.2, and those for the inertial term proportional to $\hat{\boldsymbol{u}}^{f}$ is done in section 5.6.3. The details of the evaluation of the integral are presented in section 5.6.4.

5.6.1 Expression for the term proportional to the singularity in the test problem

In the tumbling orbit, the orientation vector $\boldsymbol{p}$ is of the form $\cos\phi_j \boldsymbol{1}_1 + \sin\phi_j \boldsymbol{1}_2$, where ϕ_j is now a function of time given by $\tan\phi_j = 1/(\kappa \tan(\omega_g t))$, which is obtained from the solution of the Jefferys equations in (5.26) and (5.27). This relation is used for both the orientation in the test problem, and that in the problem of interest. The term corresponding to the test velocity field in braces, in (5.66), simplifies to :

$$\begin{aligned}\frac{i\,(\boldsymbol{S}^{(2t)}\cdot\boldsymbol{k})\cdot\boldsymbol{1}_3}{2\pi k^2 \dot{\phi}_{jeff}}\cdot\left(\boldsymbol{I}-\frac{\boldsymbol{kk}}{k^2}\right) = -\boldsymbol{T_1}\frac{(\kappa^2+1)^2}{2\kappa^2}+\boldsymbol{T_2}\frac{(1-\kappa^4)}{2\kappa^2}+\left(\boldsymbol{T_1}\frac{(\kappa^4-1)}{2\kappa^2}+\boldsymbol{T_2}\frac{(\kappa^2+1)^2}{2\kappa^2}\right) \\ \cos(2\omega_g t)-\boldsymbol{T_3}\frac{\kappa^2+1}{\kappa}\sin(2\omega_g t), \\ = \boldsymbol{T}_{\boldsymbol{1}}^{tumb}+\boldsymbol{T}_{\boldsymbol{2}}^{tumb}\cos(2\omega_g t)+\boldsymbol{T}_{\boldsymbol{3}}^{tumb}\sin(2\omega_g t), \qquad (5.67)\end{aligned}$$

with $\omega_g = 2\pi/T_{jeff}$. In 5.67, $\boldsymbol{T}_{\mathbf{1}}$, $\boldsymbol{T}_{\mathbf{2}}$, $\boldsymbol{T}_{\mathbf{3}}$, $\boldsymbol{T}_{\mathbf{1}}^{tumb}$, $\boldsymbol{T}_{\mathbf{2}}^{tumb}$ and $\boldsymbol{T}_{\mathbf{3}}^{tumb}$ above, are given by:

$$\boldsymbol{T}_{\mathbf{1}} = \left(\frac{ik_2}{2k^2\pi}\mathbf{1}_1 - \frac{ik_1}{2k^2\pi}\mathbf{1}_2\right) B_3, \tag{5.68}$$

$$\boldsymbol{T}_{\mathbf{2}} = \left(\frac{i(k^2-2k_1^2)k_2}{2k^4\pi}\mathbf{1}_1 + \frac{ik_1(k^2-2k_2^2)}{2k^4\pi}\mathbf{1}_2 - \frac{ik_1k_2k_3}{k^4\pi}\mathbf{1}_3\right) B_1, \tag{5.69}$$

$$\boldsymbol{T}_{\mathbf{3}} = \left(-\frac{i(k^2-k_1^2+k_2^2)k_1}{2k^4\pi}\mathbf{1}_1 + \frac{ik_2(k^2+k_1^2-k_2^2)}{2k^4\pi}\mathbf{1}_2 + \frac{i(k_1^2-k_2^2)k_3}{2k^4\pi}\mathbf{1}_3\right) B_1, \tag{5.70}$$

$$\boldsymbol{T}_{\mathbf{1}}^{tumb} = -\boldsymbol{T}_{\mathbf{1}}\frac{(\kappa^2+1)^2}{2\kappa^2} + \boldsymbol{T}_{\mathbf{2}}\frac{(1-\kappa^4)}{2\kappa^2}, \tag{5.71}$$

$$\boldsymbol{T}_{\mathbf{2}}^{tumb} = \boldsymbol{T}_{\mathbf{1}}\frac{(\kappa^4-1)}{2\kappa^2} + \boldsymbol{T}_{\mathbf{2}}\frac{(\kappa^2+1)^2}{2\kappa^2}, \tag{5.72}$$

$$\boldsymbol{T}_{\mathbf{3}}^{tumb} = -\boldsymbol{T}_{\mathbf{3}}\frac{\kappa^2+1}{\kappa}. \tag{5.73}$$

The constants B_1 and B_3 above are defined in (5.9) and (5.11) for a prolate spheroid. In the tumbling mode, one need not consider the axial spin singularity corresponding to B_2, since the orientation vector is perpendicular to the angular velocity, and thus, (5.67) is independent of B_2. As is evident in (5.67), there are only three Fourier modes for an arbitrary aspect ratio spheroid. In the limiting case of a sphere ($\kappa \to 1$), $B_1 \to 0$, and therefore $\boldsymbol{T}_{\mathbf{2}}^{tumb}$, $\boldsymbol{T}_{\mathbf{3}}^{tumb}$ $\to 0$, and only the time-independent mode survives. In the limit of a flat disk ($\kappa \to 0$), $B_1 = B_3 = -16/3$, and $\boldsymbol{T}_{\mathbf{3}}^{tumb}$ is $O(\kappa)$ smaller than both $\boldsymbol{T}_{\mathbf{1}}^{tumb}$ and $\boldsymbol{T}_{\mathbf{2}}^{tumb}$, and can therefore be neglected. So, for a flat disk, (5.67) scales as $O(1/\kappa^2)$. In the limit of a slender fiber ($\kappa \to \infty$), $B_1 = -B_3 = 4\pi/(3\log\kappa)$, consistent with viscous slender body theory, and $\boldsymbol{T}_{\mathbf{3}}^{tumb}$ is $O(1/\kappa)$ smaller than both $\boldsymbol{T}_{\mathbf{1}}^{tumb}$ and $\boldsymbol{T}_{\mathbf{2}}^{tumb}$ and can again be neglected. So for a slender fiber (5.67) scales as $O(\kappa^2/\log\kappa)$. The scaling for ΔT_{c2}^{tumb} , for these extreme aspect ratio particles is further analyzed in section 5.6.5.

5.6.2 Expression for the inertial terms with $\hat{\boldsymbol{u}}^{match}$

In this section we expand the three terms involving $\hat{\boldsymbol{u}}^{match}$, in the integrand in (5.66), as a Fourier Series. The general Fourier expansion of the terms involving $\hat{\boldsymbol{u}}^{match}$ contains an infinite number of terms, but one needs to retain only terms corresponding to the three modes in (5.67). As for the test velocity field, the expression for $\hat{\boldsymbol{u}}^{match}$ given in (5.25) now depends on time through the singularity $\boldsymbol{S}$. Hence, we expand $\boldsymbol{S}$ as a Fourier series in time and retain only the aforementioned terms. This truncated expansion takes the form:

$$\begin{aligned}\boldsymbol{S} = &-2A_{112}\sin(2\omega_g t)\mathbf{1}_1\mathbf{1}_1 + (A_{120} + 2A_{122}\cos(2\omega_g t))(\mathbf{1}_1\mathbf{1}_2 + \mathbf{1}_2\mathbf{1}_1) \\ &- 2A_{222}\sin(2\omega_g t)\mathbf{1}_2\mathbf{1}_2 - 2A_{332}\sin(2\omega_g t)\mathbf{1}_3\mathbf{1}_3,\end{aligned} \tag{5.74}$$

where

$$A_{112} = -\left(\frac{3A_1}{2} - 2A_2 + \frac{A_3}{2}\right)\frac{\kappa^2}{(1+\kappa)^3} - \left(A_2 - \frac{A_3 + A_1}{2}\right)\frac{\kappa}{(1+\kappa)^2}, \tag{5.75}$$

$$A_{120} = \left(\frac{A_2}{2} + \left(\frac{3A_1}{2} - 2A_2 + \frac{A_3}{2}\right)\frac{\kappa}{2(1+\kappa)^2}\right), \tag{5.76}$$

$$A_{122} = -\left(\frac{3A_1}{2} - 2A_2 + \frac{A_3}{2}\right)\frac{\kappa(1-\kappa)}{2(1+\kappa)^3}, \tag{5.77}$$

$$A_{222} = -\left(\frac{3A_1}{2} - 2A_2 + \frac{A_3}{2}\right)\frac{\kappa}{(1+\kappa)^3} - \left(A_2 - \frac{A_3 + A_1}{2}\right)\frac{\kappa}{(1+\kappa)^2}, \tag{5.78}$$

$$A_{332} = \left(\frac{A_1 - A_3}{2}\right)\frac{\kappa}{(1+\kappa)^2}, \tag{5.79}$$

where the A_i's are defined in (5.16)-(5.18). In deriving (5.74), we have again used the relation between ϕ_j and t obtained from the Jefferys solution (see section 5.6.1). For a sphere ($\kappa \to 1$), $A_1 = A_2 = A_3 = -20\pi/3$ and therefore $\boldsymbol{S}$ in (5.74) reduces to $-10\pi/3(\mathbf{1}_1\mathbf{1}_2 + \mathbf{1}_2\mathbf{1}_1) = -(20\pi/3)\boldsymbol{E}$. For a flat disk ($\kappa \to 0$), $2A_1 = A_3 = -64/9$ and A_2 is $-8\pi\kappa/3$, therefore (5.74) is $O(\kappa)$. For a slender fiber ($\kappa \to \infty$), $A_1 = -8\pi/(9\log\kappa)$, A_2 and A_3 are $O(1/\kappa^2)$ and (5.74) is therefore $O(1/(\kappa\log\kappa))$.

Using (5.25) and (5.74), the truncated Fourier expansion of the terms involving $\hat{\boldsymbol{u}}^{match}$, to be used in (5.66), is obtained as:

$$(\boldsymbol{\Gamma}^\dagger \cdot \boldsymbol{k}) \cdot \nabla_{\boldsymbol{k}} \hat{\boldsymbol{u}}^{match} - \frac{\partial \hat{\boldsymbol{u}}^{match}}{\partial t} - \boldsymbol{\Gamma} \cdot \hat{\boldsymbol{u}}^{match} = \boldsymbol{R}_1^{tumb} + \boldsymbol{R}_2^{tumb}\cos(2\omega_g t) + \boldsymbol{R}_3^{tumb}\sin(2\omega_g t), \tag{5.80}$$

where $\boldsymbol{R}_1^{tumb}$, $\boldsymbol{R}_2^{tumb}$ and $\boldsymbol{R}_3^{tumb}$ are functions of k_1,k_2,k_3, ω_g and A_{ijk}'s are defined in (5.75)-(5.79), and are given by:

$$\boldsymbol{R}_1^{tumb} = \frac{iA_{120}k_1^3\left(k^2 - 4k_2^2\right)}{k^6\pi}\mathbf{1}_1 + \frac{iA_{120}k_1^2 k_2\left(3k^2 - 4k_2^2\right)}{k^6\pi}\mathbf{1}_2 + \frac{iA_{120}k_1^2\left(k^2 - 4k_2^2\right)k_3}{k^6\pi}\mathbf{1}_3, \tag{5.81}$$

$$\begin{aligned}\boldsymbol{R}_2^{tumb} = {} & \frac{2ik_1\left(A_{122}k_1^2\left(k^2-4k_2^2\right)+\omega_g k^2\left(A_{112}\left(-k^2+k_1^2\right)+A_{222}k_2^2+A_{332}k_3^2\right)\right)}{k^6\pi}\mathbf{1}_1 \\ & + \frac{2ik_2\left(A_{122}k_1^2\left(3k^2-4k_2^2\right)+\omega_g k^2\left(A_{112}k_1^2+A_{222}\left(-k^2+k_2^2\right)+A_{332}k_3^2\right)\right)}{k^6\pi}\mathbf{1}_2 \\ & + \frac{2ik_3\left(A_{122}k_1^2\left(k^2-4k_2^2\right)+\omega_g k^2\left(A_{112}k_1^2+A_{222}k_2^2+A_{332}\left(-k^2+k_3^2\right)\right)\right)}{k^6\pi}\mathbf{1}_3 \end{aligned} \tag{5.82}$$

$$\begin{aligned}\boldsymbol{R}_3^{tumb} = {} & \Bigg(-\frac{2i\omega_g A_{122}\left(k^2-2k_1^2\right)k_2}{k^4\pi}+\frac{iA_{112}k_1^2\left(-k^2+4k_1^2\right)k_2}{k^6\pi}+\frac{iA_{222}k_2\left(-k^2\left(k^2+2k_1^2\right)+\left(k^2+4k_1^2\right)k_2^2\right)}{k^6\pi} \\ & +\frac{iA_{332}\left(k^2+4k_1^2\right)k_2k_3^2}{k^6\pi}\Bigg)\mathbf{1}_1+\Bigg(-\frac{2i\omega_g A_{122}k_1\left(k^2-2k_2^2\right)}{k^4\pi}+\frac{iA_{112}k_1^3\left(-k^2+4k_2^2\right)}{k^6\pi} \\ & -\frac{iA_{222}k_1\left(k-k_2\right)\left(k+k_2\right)\left(-k^2+4k_2^2\right)}{k^6\pi}-\frac{iA_{332}k_1\left(k^2-4k_2^2\right)k_3^2}{k^6\pi}\Bigg)\mathbf{1}_2 \\ & +\Bigg(\frac{4i\omega_g A_{122}k_1k_2k_3}{k^4\pi}+\frac{4iA_{112}k_1^3k_2k_3}{k^6\pi}+\frac{2iA_{222}k_1k_2\left(-k^2+2k_2^2\right)k_3}{k^6\pi} \\ & +\frac{2iA_{332}k_1k_2k_3\left(-k^2+2k_3^2\right)}{k^6\pi}\Bigg)\mathbf{1}_3. \end{aligned} \tag{5.83}$$

For a sphere only the time independent mode survives in (5.80). In the limit of extreme aspect ratios , that is, a fiber or a flat disk one needs to consider only the first two terms in (5.80), since the test singularity has only those two modes, as seen in the last subsection.

5.6.3 Expression for the inertial term with $\hat{\boldsymbol{u}}^f$

In this section we expand the lone term proportional to $\hat{\boldsymbol{u}}^f$ in the integrand in (5.66) as a Fourier Series. As in the previous section, we need to only find the coefficients of the three modes present in (5.67). To begin with, (5.20) is contracted with $(\boldsymbol{I}-\boldsymbol{kk}/k^2)$ to eliminate the pressure, leading to the following governing equation for $\hat{\boldsymbol{u}}^f$:

$$\begin{aligned}\frac{\partial\hat{\boldsymbol{u}}^f}{\partial t}-(\boldsymbol{\Gamma}^\dagger\cdot\boldsymbol{k})\cdot\boldsymbol{\nabla}_{\boldsymbol{k}}\hat{\boldsymbol{u}}^f+\boldsymbol{\Gamma}\cdot\hat{\boldsymbol{u}}^f\cdot\left(\boldsymbol{I}-2\frac{\boldsymbol{kk}}{k^2}\right)+4\pi^2k^2\hat{\boldsymbol{u}}^f = -\Bigg(\frac{\partial\hat{\boldsymbol{u}}^{match}}{\partial t} \\ -(\boldsymbol{\Gamma}^\dagger\cdot\boldsymbol{k})\cdot\boldsymbol{\nabla}\hat{\boldsymbol{u}}^{match}+\boldsymbol{\Gamma}\cdot\hat{\boldsymbol{u}}^{match}\Bigg)\cdot\left(\boldsymbol{I}-\frac{\boldsymbol{kk}}{k^2}\right)\end{aligned} \tag{5.84}$$

The expression on the right-hand side above is evaluated using (5.80) to give:

$$\begin{aligned}
&\frac{\partial \hat{\boldsymbol{u}}^f}{\partial t} - (\boldsymbol{\Gamma}^\dagger \cdot \boldsymbol{k}) \cdot \nabla \hat{\boldsymbol{u}}^f + \boldsymbol{\Gamma} \cdot \hat{\boldsymbol{u}}^f \cdot \left(\boldsymbol{I} - 2\frac{\boldsymbol{kk}}{k^2} \right) + 4\pi^2 k^2 \hat{\boldsymbol{u}}^f \\
&\quad = (\boldsymbol{R}_1^{tumb} + \boldsymbol{R}_2^{tumb} \cos(2\omega_g t) + \boldsymbol{R}_3^{tumb} \sin(2\omega_g t)) \cdot \left(\boldsymbol{I} - \frac{\boldsymbol{kk}}{k^2} \right) \\
&\quad = \sum_{\beta \in \{0,2,-2\}} \boldsymbol{Q}^\beta e^{i\beta\omega_g t},
\end{aligned} \tag{5.85}$$

where $\boldsymbol{Q}^0 = \boldsymbol{R}_1^{tumb} - (\boldsymbol{R}_1 \cdot \boldsymbol{k})\boldsymbol{k}/k^2$, $\boldsymbol{Q}^2 = (\boldsymbol{R}_2^{tumb} - i\boldsymbol{R}_3^{tumb})/2$ and $\boldsymbol{Q}^{-2} = (\boldsymbol{R}_2^{tumb} + i\boldsymbol{R}_3^{tumb})/2$. The $\boldsymbol{Q}^\beta$ for $\beta = 0, 2\, and\, -2$ are given below.

$$\boldsymbol{Q}^{\mathbf{0}} = -\frac{2iA_{120}k_1^3k_2^2}{k^6\pi}\mathbf{1}_1 + \frac{2iA_{120}k_1^2k_2\left(k^2 - k_2^2\right)}{k^6\pi}\mathbf{1}_2 - \frac{2iA_{120}k_1^2k_2^2k_3}{k^6\pi}\mathbf{1}_3, \tag{5.86}$$

$$\boldsymbol{Q}^{\mathbf{2}} = \boldsymbol{Q}^{2Re} + i\boldsymbol{Q}^{2i}, \tag{5.87}$$

$$\boldsymbol{Q}^{-2} = -\boldsymbol{Q}^{2Re} + i\boldsymbol{Q}^{2i}, \tag{5.88}$$

$$\begin{aligned}
\boldsymbol{Q}^{2Re} = &\left(\frac{k_2\left(-k^4A_{222} - 2\omega_g k^2 A_{122}\left(k^2 - 2k_1^2\right) + A_{112}k_1^2\left(-k^2 + 2k_1^2\right)\right)}{2k^6\pi} \right. \\
&\left. + \frac{k_2\left(A_{222}\left(k^2 + 2k_1^2\right)k_2^2 + A_{332}\left(k^2 + 2k_1^2\right)k_3^2\right)}{2k^6\pi} \right)\mathbf{1}_1 + \left(-\frac{k_1\left(k^2 - 2k_2^2\right)A_{112}k_1^2}{2k^6\pi} \right. \\
&\left. - \frac{k_1\left(k^2 - 2k_2^2\right)\left(+A_{222}k_2^2 + A_{332}k_3^2 + k^2\left(-A_{222} + 2A_{122}\omega_g\right)\right)}{2k^6\pi} \right)\mathbf{1}_2 \\
&+ \frac{k_1k_2k_3\left(2\omega_g k^2 A_{122} + A_{112}k_1^2 + A_{222}k_2^2 + A_{332}\left(-k^2 + k_3^2\right)\right)}{k^6\pi}\mathbf{1}_3,
\end{aligned} \tag{5.89}$$

$$\begin{aligned}
\boldsymbol{Q}^{2i} = &\frac{k_1\left(-2A_{122}k_1^2k_2^2 + k^2\left(A_{112}\left(-k^2 + k_1^2\right) + A_{222}k_2^2 + A_{332}k_3^2\right)\omega_g\right)}{k^6\pi}\mathbf{1}_1 \\
&+ \frac{k_2\left(2A_{122}k_1^2\left(k^2 - k_2^2\right) + k^2\left(A_{112}k_1^2 + A_{222}\left(-k^2 + k_2^2\right) + A_{332}k_3^2\right)\omega_g\right)}{k^6\pi}\mathbf{1}_2 \\
&+ \frac{k_3\left(-2A_{122}k_1^2k_2^2 + k^2\left(A_{112}k_1^2 + A_{222}k_2^2 + A_{332}\left(-k^2 + k_3^2\right)\right)\omega_g\right)}{k^6\pi}\mathbf{1}_3.
\end{aligned} \tag{5.90}$$

We have written the Fourier modes in complex exponential form in (5.85) to simplify the analysis that follows. To reiterate, the general solution for $\hat{\boldsymbol{u}}^f$ would contain a forcing on the right-hand side of (5.85) that involves an infinite Fourier series. Only the three terms corresponding to the values of β above contribute to the increase in the time period of rotation, however.

To obtain the solution of (5.85), $\hat{\boldsymbol{u}}^f$ is expanded as a complex exponential Fourier series given by:

$$\hat{\boldsymbol{u}}^f = \sum_{\beta \in \{0,2,-2\}} \hat{\boldsymbol{u}}^{f\beta} e^{i\beta\omega_g t} \tag{5.91}$$

Substituting the expansion above in (5.85), the governing equations for each of the components of Fourier transformed velocity field may be written as:

$$\frac{\partial \hat{u}_1^{f\beta}}{\partial k_2} - (4\pi^2k^2 + i\omega_g\beta)\frac{\hat{u}_1^{f\beta}}{k_1} - \left(1 - \frac{2k_1^2}{k^2}\right)\frac{\hat{u}_2^{f\beta}}{k_1} = -\frac{Q_1^\beta}{k_1} \tag{5.92}$$

$$\frac{\partial \hat{u}_2^{f\beta}}{\partial k_2} - (4\pi^2k^2 + i\omega_g\beta)\frac{\hat{u}_2^{f\beta}}{k_1} + \left(\frac{2k_1k_2}{k^2}\right)\frac{\hat{u}_2^{f\beta}}{k_1} = -\frac{Q_2^\beta}{k_1} \tag{5.93}$$

$$\frac{\partial \hat{u}_3^{f\beta}}{\partial k_2} - (4\pi^2k^2 + i\omega_g\beta)\frac{\hat{u}_3^{f\beta}}{k_1} + \left(\frac{2k_1k_3}{k^2}\right)\frac{\hat{u}_2^{f\beta}}{k_1} = -\frac{Q_3^\beta}{k_1} \tag{5.94}$$

The equations above are similar to the ones seen for the spinning case in (5.47-5.49) except for an additional frequency dependent term(involving ω_g) on the left-hand side and a frequency-dependent forcing amplitude on the right-hand side. The solution to (5.92-5.94) therefore proceeds in a manner similar to that of the spinning case. The components of $\hat{\boldsymbol{u}}^{f\beta} (\beta = 0, 2, -2)$ along the flow ($\hat{u}_1^{f\beta}$) and the vorticity ($\hat{u}_3^{f\beta}$) axes are coupled to the component along the gradient axis ($\hat{u}_2^{f\beta}$). Thus, as for the spinning case, the gradient component is independent of the other components and is therefore solved first. The solution of (5.92)-(5.94) arising from the substitution of (5.91) corresponds to the neglect of an exponentially decaying transient, that governs the relaxation from a particular initial velocity field, and consideration of long time dynamics corresponding to the frequencies present in the applied forcing. The steady linear flow ensures that there is a one-to-one correspondence between the Fourier amplitudes of the forcing and the velocity field, with inertia determining the frequency dependent phase lag between the two via the terms proportional to $i\omega_g$ in (5.92-5.94). Note again that $\sum_{\beta \in \{0,2,-2\}} \boldsymbol{Q}^\beta e^{i\beta\omega_g t}$ is not the complete outer velocity field, but the part that is relevant for the determination of ΔT_{c2}^{tumb}.

Again, defining $k_2' = k_2 + k_1 s$, where 's' is a time-like variable, the solutions for the individual components $\hat{u}_2^{f\beta}$, $\hat{u}_1^{f\beta}$ and $\hat{u}_3^{f\beta}$ are written in terms of 's' as follows:

$$\hat{u}_2^{f\beta}(\boldsymbol{k}) = \int_0^\infty e^{-4\pi^2\left(k^2 s + k_1 k_2 s^2 + \frac{k_1^2 s^3}{3}\right)} \left(\frac{k^2 + k_1^2 s^2 + 2k_1 k_2 s}{k^2}\right) e^{-i\omega_g \beta s} Q_2^\beta(k_1, k_2 + k_1 s, k_3)\, ds, \tag{5.95}$$

$$\begin{aligned}\hat{u}_1^{f\beta}(\boldsymbol{k}) = &\int_0^\infty e^{-4\pi^2\left(k^2 s + k_1 k_2 s^2 + \frac{k_1^2 s^3}{3}\right)} e^{-i\omega_g \beta s} Q_1^\beta(k_1, k_2 + k_1 s, k_3)\, ds - \int_0^\infty e^{-i\omega_g \beta s} \\ &e^{-4\pi^2\left(k^2 s + k_1 k_2 s^2 + \frac{k_1^2 s^3}{3}\right)} \left(1 - \frac{2k_1^2}{(k^2 + k_1^2 s^2 + 2k_1 k_2 s)}\right) \hat{u}_2^{f\beta}(k_1, k_2 + k_1 s, k_3)\, ds,\end{aligned} \tag{5.96}$$

$$\begin{aligned}\hat{u}_3^{f\beta}(\boldsymbol{k}) = &\int_0^\infty e^{-4\pi^2\left(k^2 s + k_1 k_2 s^2 + \frac{k_1^2 s^3}{3}\right)} e^{-i\omega_g \beta s} Q_3^\beta(k_1, k_2 + k_1 s, k_3)\, ds + \int_0^\infty e^{-i\omega_g \beta s} \\ &e^{-4\pi^2\left(k^2 s + k_1 k_2 s^2 + \frac{k_1^2 s^3}{3}\right)} \left(\frac{2k_1 k_3}{k^2 + k_1^2 s^2 + 2k_1 k_2 s}\right) \hat{u}_2^{f\beta}(k_1, k_2 + k_1 s, k_3)\, ds.\end{aligned} \tag{5.97}$$

The solutions for $\hat{u}_1^{f\beta}$ and $\hat{u}_3^{f\beta}$ are coupled with $\hat{u}_2^{f\beta}$ as expected, and are given as a sum of a one-dimensional and a two-dimensional integral, with the latter integral arising from the coupling with $\hat{u}_2^{f\beta}$. The contributions in (5.95)-(5.97), for the different β's are substituted in (5.91) to obtain the components of $\hat{\boldsymbol{u}}^f$ in the space-fixed coordinate system, and are given by:

$$\hat{u}_2^f(\boldsymbol{k}) = \hat{u}_2^{f0}(k_1, k_2, k_3) + \hat{u}_2^{ft}(k_1, k_2, k_3, t), \tag{5.98}$$

$$\hat{u}_1^f(\boldsymbol{k}) = \hat{u}_1^{f0}(k_1, k_2, k_3) + \hat{u}_1^{ft}(k_1, k_2, k_3, t), \tag{5.99}$$

$$\hat{u}_3^f(\boldsymbol{k}) = \hat{u}_3^{f0}(k_1, k_2, k_3) + \hat{u}_3^{ft}(k_1, k_2, k_3, t), \tag{5.100}$$

where we have written the components as a sum of a time-independent term(superscript '$f0$') and time-dependent term(superscript 'ft'). Denoting the convected wave vector, $k_1\mathbf{1}_1 + (k_2 + k_1 s)\mathbf{1}_2 + k_3\mathbf{1}_3$, as $\boldsymbol{k'}$ and $k' = |\boldsymbol{k'}|$, the time-dependent and time-independent contributions in (5.98-5.100) which may be conveniently expressed in the form:

$$\hat{u}_2^{f0}(\boldsymbol{k}) = \int_0^\infty e^{-4\pi^2\left(k^2 s + k_1 k_2 s^2 + \frac{k_1^2 s^3}{3}\right)} \left(\frac{k^2 + k_1^2 s^2 + 2k_1 k_2 s}{k^2}\right) Q_2^0(\boldsymbol{k}')\, ds, \tag{5.101}$$

$$\begin{aligned}\hat{u}_2^{ft}(\boldsymbol{k},t) = \int_0^\infty & i2e^{-4\pi^2\left(k^2 s + k_1 k_2 s^2 + \frac{k_1^2 s^3}{3}\right)} \left(\frac{k^2 + k_1^2 s^2 + 2k_1 k_2 s}{k^2}\right) \big(\big(Q_2^{2i}(\boldsymbol{k}')\cos(2\omega_g s) \\ & -Q_2^{2Re}(\boldsymbol{k}')\sin(2\omega_g s)\big)\cos(2\omega_g t) + \big(Q_2^{2Re}(\boldsymbol{k}')\cos(2\omega_g s) + Q_2^{2i}(\boldsymbol{k}')\sin(2\omega_g s)\big)\sin(2\omega_g t)\big)\, ds\end{aligned} \tag{5.102}$$

$$= \hat{u}_2^{ftcos}(\boldsymbol{k},t)\cos(2\omega_g t) + \hat{u}_2^{ftsin}(\boldsymbol{k},t)\sin(2\omega_g t), \tag{5.103}$$

$$\hat{u}_1^{f0}(\boldsymbol{k}) = \int_0^\infty e^{-4\pi^2\left(k^2 s + k_1 k_2 s^2 + \frac{k_1^2 s^3}{3}\right)} \left(Q_1^0(\boldsymbol{k}') - \left(1 - \frac{2k_1^2}{k'^2}\right)\hat{u}_2^{f0}(\boldsymbol{k}')\right), ds \tag{5.104}$$

$$\begin{aligned}\hat{u}_1^{ft}(\boldsymbol{k}) = \int_0^\infty & i2e^{-4\pi^2\left(k^2 s + k_1 k_2 s^2 + \frac{k_1^2 s^3}{3}\right)} \big(\big(Q_1^{2i}(\boldsymbol{k}')\cos(2\omega_g s) \\ & -Q_1^{2Re}(\boldsymbol{k}')\sin(2\omega_g s)\big)\cos(2\omega_g t) + \big(Q_1^{2Re}(\boldsymbol{k}')\cos(2\omega_g s) + Q_1^{2i}(\boldsymbol{k}')\sin(2\omega_g s)\big)\sin(2\omega_g t)\big)\, ds \\ & - \int_0^\infty e^{-4\pi^2\left(k^2 s + k_1 k_2 s^2 + \frac{k_1^2 s^3}{3}\right)} \left(1 - \frac{2k_1^2}{k'^2}\right)\hat{u}_2^{ft}(\boldsymbol{k}', t, s+s')\, ds\end{aligned} \tag{5.105}$$

$$= \hat{u}_1^{ftcos}(\boldsymbol{k},t)\cos(2\omega_g t) + \hat{u}_1^{ftsin}(\boldsymbol{k},t)\sin(2\omega_g t), \tag{5.106}$$

$$\hat{u}_3^{f0}(\boldsymbol{k}) = \int_0^\infty e^{-4\pi^2\left(k^2 s + k_1 k_2 s^2 + \frac{k_1^2 s^3}{3}\right)} \left(Q_3^0(\boldsymbol{k}') + \frac{2k_1 k_3}{k'^2}\hat{u}_2^{f0}(\boldsymbol{k}')\right), ds \tag{5.107}$$

$$\begin{aligned}\hat{u}_3^{ft}(\boldsymbol{k},t) = \int_0^\infty & i2e^{-4\pi^2\left(k^2 s + k_1 k_2 s^2 + \frac{k_1^2 s^3}{3}\right)} \big(\big(Q_3^{2i}(\boldsymbol{k}')\cos(2\omega_g s) \\ & -Q_3^{2Re}(\boldsymbol{k}')\sin(2\omega_g s)\big)\cos(2\omega_g t) + \big(Q_3^{2Re}(\boldsymbol{k}')\cos(2\omega_g s) + Q_3^{2i}(\boldsymbol{k}')\sin(2\omega_g s)\big)\sin(2\omega_g t)\big)\, ds \\ & + \int_0^\infty e^{-4\pi^2\left(k^2 s + k_1 k_2 s^2 + \frac{k_1^2 s^3}{3}\right)} \left(\frac{2k_1 k_3}{k'^2}\right)\hat{u}_2^{ft}(\boldsymbol{k}', t, s+s')\, ds\end{aligned} \tag{5.108}$$

$$= \hat{u}_3^{ftcos}(\boldsymbol{k},t)\cos(2\omega_g t) + \hat{u}_3^{ftsin}(\boldsymbol{k},t)\sin(2\omega_g t), \tag{5.109}$$

where the terms Q_j^{2Re},Q_j^{2i} are given in (5.89)-(5.90), with 'j' denoting the component along the 1 ,2 and 3 directions. The coefficients of $\cos(2\omega_g t)$ and $\sin(2\omega_g t)$ in (5.102) and (5.108) are denoted by $\hat{u}^{ftcos}$ and $\hat{u}^{ftsin}$. The flow and vorticity components are coupled to the gradient component through $\hat{u}_2^{ft}(\boldsymbol{k'},t,s+s')$ and $\hat{u}_2^{f0}(\boldsymbol{k'})$ which are given by:

$$\begin{aligned}\hat{u}_2^{ft}(\boldsymbol{k'},t,s+s') = \int_0^\infty & i2e^{-4\pi^2\left(k'^2s'+k_1k_2's'^2+\frac{k_1^2s'^3}{3}\right)}\left(\frac{k'^2+k_1^2s'^2+2k_1k_2's'}{k'^2}\right)\\ &\left(\left(Q_2^{2i}(\boldsymbol{k''})\cos(2\omega_g(s+s'))-Q_2^{2Re}(\boldsymbol{k''})\sin(2\omega_g(s+s'))\right)\cos(2\omega_g t)\right.\\ &\left.+\left(Q_2^{2Re}(\boldsymbol{k''})\cos(2\omega_g(s+s'))+Q_2^{2i}(\boldsymbol{k''})\sin(2\omega_g(s+s'))\right)\sin(2\omega_g t)\right)ds', \qquad (5.110)\end{aligned}$$

and

$$\hat{u}_2^{f0}(\boldsymbol{k'}) = \int_0^\infty e^{-4\pi^2\left(k'^2s'+k_1k_2's'^2+\frac{k_1^2s^3}{3}\right)}\left(\frac{k'^2+k_1^2s^2+2k_1k_2's}{k'^2}\right)Q_2^0(\boldsymbol{k''})\,ds \qquad (5.111)$$

respectively. The primed variables in (5.110) and (5.111) are defined as $\boldsymbol{k}'' = k_1\mathbf{1}_1+(k_2+k_1(s+s'))\mathbf{1}_2+k_3\mathbf{1}_3$, $k_2' = k_2+k_1s$ and $k'' = |\boldsymbol{k''}|$. The coefficients of $\cos(2\omega_g t)$ and $\sin(2\omega_g t)$ in the time-dependent terms are defined as $\hat{u}_i^{ftcos}(\boldsymbol{k},t)$ and $\hat{u}_i^{ftsin}(\boldsymbol{k},t)$ respectively. The components along the flow and vorticity directions given in (5.104)-(5.109) is therefore a sum of one-dimensional integral and a two-dimensional integral. The two-dimensional integrals in (5.104)- (5.109) are coupled with the velocity in the gradient direction and are given by (5.110) and (5.111).

5.6.4 Evaluation of the integrals

The integral for the tumbling time period given in (5.66) is evaluated in this section. The inertial terms given in (5.80) along with the term involving the singularity in the test problem in (5.67), are substituted in (5.66) to obtain the final form of the integral as:

$$\begin{aligned}\Delta T_{Re^{3/2}}^{tumb} =& \frac{Re^{3/2}}{8\pi Y_c}\int\int_0^{T_{jeff}}\left[-4\pi^2k^2(\hat{u}_1^f\mathbf{1}_1+\hat{u}_2^f\mathbf{1}_2+\hat{u}_3^f\mathbf{1}_3)+\boldsymbol{R}_1+\boldsymbol{R}_2\cos(2\omega_g t)\right.\\ &\left.+\boldsymbol{R}_3\sin(2\omega_g t)\right]\cdot\left(\boldsymbol{T_1^{tumb}}+\boldsymbol{T_2^{tumb}}\cos(2\omega_g t)+\boldsymbol{T_3^{tumb}}\sin(2\omega_g t)\right)dtd\boldsymbol{k}. \qquad (5.112)\end{aligned}$$

where the components of $\hat{\boldsymbol{u}}^f$ are given in (5.98)-(5.100). The integration over time in (5.112) is straightforward and leads to:

$$\Delta T^{tumb}_{Re^{3/2}} = \frac{Re^{3/2}}{8\pi Y_C}\int \Bigg[\frac{2\pi}{\omega_g}\boldsymbol{T}^{tumb}_{\mathbf{1}}\cdot(\boldsymbol{R}_1 - 4\pi^2k^2(\hat{u}^{f0}_1\mathbf{1}_1 + \hat{u}^{f0}_2\mathbf{1}_2 + \hat{u}^{f0}_3\mathbf{1}_3))$$
$$+\frac{\pi}{\omega_g}\boldsymbol{T}^{tumb}_{\mathbf{2}}\cdot(\boldsymbol{R}_2 - 4\pi^2k^2(\hat{u}^{ftcos}_1\mathbf{1}_1 + \hat{u}^{ftcos}_2\mathbf{1}_2 + \hat{u}^{ftcos}_3\mathbf{1}_3))$$
$$+\frac{\pi}{\omega_g}\boldsymbol{T}^{tumb}_{\mathbf{3}}\cdot(\boldsymbol{R}_3 - 4\pi^2k^2(\hat{u}^{ftsin}_1\mathbf{1}_1 + \hat{u}^{ftsin}_2\mathbf{1}_2 + \hat{u}^{ftsin}_3\mathbf{1}_3))\Bigg]\,d\boldsymbol{k}. \tag{5.113}$$

The expressions for $\hat{u}^{fi}$ (i=‘0’,‘cos’,‘sin’) are given in (5.101)-(5.109). Each of the terms proportional to $\hat{u}^{fi}_1$ and $\hat{u}^{fi}_3$ (i=‘0’,‘cos’,‘sin’) in (5.113) is a sum of 4-dimensional and 5-dimensional integrals. The terms proportional to $\hat{u}^{fi}_2$ are 4-dimensional integrals and the terms proportional to $\boldsymbol{R}_1$,$\boldsymbol{R}_2$ and $\boldsymbol{R}_3$ involve 3-dimensional integrals.

The numerical evaluation of the integrals proceeds in a manner similar to that of the spinning case in section 5.5. First we express them in a spherical coordinate system. It will be seen that, individually, the 3-dimensional and the 4-dimensional integrals mentioned above are divergent in the integration over k in the spherical coordinate system. However the combination of these integrals are convergent, and proceeding in a manner similar to the spinning case, we could reduce the integral in (5.113) to a sum of 3-dimensional and 4-dimensional convergent integrals. These integrals are evaluated numerically to obtain the time period.

To illustrate the simplification of (5.113) to convergent integrals mentioned above, we focus on the evaluation of the integrals proportional to $\hat{u}^{f0}_1$, $\boldsymbol{R}_1$,$\boldsymbol{R}_2$ and $\boldsymbol{R}_3$. The simplification of the other terms in the integral follow the same method as presented below. We present the final simplified form of the integrals for the other terms in appendix C. We have written the 4-dimensional and 5-dimensional integrals for the term proportional to $\hat{u}^{f0}_1$ below:

$$\int(-4\pi^2k^2\,\hat{u}^{f0}_1(\boldsymbol{k})\,\mathbf{1}_1\cdot\boldsymbol{T}^{tumb}_1)d\boldsymbol{k} = -\int 4\pi^2k^2\left[-\frac{(\kappa^2+1)^2}{2\kappa^2}\frac{iB_3k_2}{2k^2\pi}+\frac{iB_1(k^2-2k_1^2)k_2}{2k^4\pi}\frac{(1-\kappa^4)}{2\kappa^2}\right]$$
$$\int_0^\infty e^{-4\pi^2\left(k^2s+k_1k_2s^2+\frac{k_1^2s^3}{3}\right)}Q^0_1(\boldsymbol{k'})dsd\boldsymbol{k}+\int 4\pi^2k^2\left[-\frac{(\kappa^2+1)^2}{2\kappa^2}\frac{iB_3k_2}{2k^2\pi}+\frac{iB_1(k^2-2k_1^2)k_2}{2k^4\pi}\frac{(1-\kappa^4)}{2\kappa^2}\right]$$
$$\int_0^\infty e^{-4\pi^2\left(k^2s+k_1k_2s^2+\frac{k_1^2s^3}{3}\right)}\left(1-\frac{2k_1^2}{k'^2}\right)\int_0^\infty e^{-4\pi^2\left(k'^2s'+k_1k'_2s'^2+\frac{k_1^2s'^3}{3}\right)}\left(\frac{k'^2+k_1^2s'^2+2k_1k'_2s'}{k'^2}\right)$$
$$Q^0_2(\boldsymbol{k''})ds'dsd\boldsymbol{k}. \tag{5.114}$$

The first and the second integral on the right-hand side are respectively the 4-dimensional and 5-dimensional integrals. Recall that the 5-dimensional integral arises due to the coupling with the velocity component in the gradient direction. While writing the 5-dimensional integral, we have used the definition of $\hat{u}_2^{f0}$ in (5.111) and substituted in (5.104). The term in the square brackets in (5.113) corresponds to the $\mathbf{1}_1$ component of $\boldsymbol{T}_{\mathbf{1}}^{tumb}$ and is obtained from (5.67). The integrals in (5.113) can be expressed in a spherical coordinate system with $k_1 = k\sin\theta\cos\phi$, $k_2 = k\sin\theta\sin\phi$, $k_3 = k\cos\theta$ and $d\boldsymbol{k} = k^2\sin\theta dk d\theta d\phi$. Rewriting (5.114) to isolate the k integral in the spherical coordinate system (again for brevity we have retained the notation k_1,k_2 and k_3), one gets:

$$\begin{aligned}
\int(-4\pi^2k^2\,\hat{u}_1^{f0}(\boldsymbol{k})\,\mathbf{1}_1\cdot\boldsymbol{T}_1^{tumb})d\boldsymbol{k} = &-\int_0^{2\pi}\int_0^{\pi}\int_0^{\infty}4\pi^2\left\{k^2Q_1^0(\boldsymbol{k}')\left[-\frac{(\kappa^2+1)^2}{2\kappa^2}\frac{iB_3k_2}{2k^2\pi}+\right.\right.\\
&\left.\left.\frac{iB_1(k^2-2k_1^2)k_2}{2k^4\pi}\frac{(1-\kappa^4)}{2\kappa^2}\right]\right\}\int_0^{\infty}k^2e^{-4\pi^2\left(k^2s+k_1k_2s^2+\frac{k_1^2s^3}{3}\right)}dk\,ds\,sin\theta\,d\theta\,d\phi\\
&+\int_0^{2\pi}\int_0^{\pi}\int_0^{\infty}\int_0^{\infty}\left\{4\pi^2k^2\left[-\frac{(\kappa^2+1)^2}{2\kappa^2}\frac{iB_3k_2}{2k^2\pi}+\frac{iB_1(k^2-2k_1^2)k_2}{2k^4\pi}\frac{(1-\kappa^4)}{2\kappa^2}\right]\right.\\
&\left.\left(1-\frac{2k_1^2}{k'^2}\right)Q_2^0(\boldsymbol{k}'')\left(\frac{k'^2+k_1^2s'^2+2k_1k_2's'}{k'^2}\right)\right\}\\
&\int_0^{\infty}e^{-4\pi^2\left(k^2s+k_1k_2s^2+\frac{k_1^2s^3}{3}\right)}e^{-4\pi^2\left(k'^2s'+k_1k_2's'^2+\frac{k_1^2s'^3}{3}\right)}k^2dk\,ds'\,ds\,\sin\theta\,d\theta\,d\phi, \qquad (5.115)
\end{aligned}$$

where the term in the curly brackets is independent of k because Q_1^0(the ‘1’ component of $\boldsymbol{Q}^0$, see (5.86)) and the term in the square brackets above are proportional to $1/k$. The k integrals above are evaluated for the 4-dimensional case, given by

$$\begin{aligned}
\int_0^{\infty}k^2e^{-4\pi^2\left(k^2s+k_1k_2s^2+\frac{k_1^2s^3}{3}\right)}dk &= \int_0^{\infty}k^2e^{-4\pi^2k^2(s+\sin^2\theta\cos\phi\sin\phi s^2+\sin^2\theta\cos^2\phi s^3/3)}dk\\
&= \frac{1}{32\pi^{5/2}(s+\sin^2\theta\cos\phi\sin\phi s^2+\sin^2\theta\cos^2\phi s^3/3)^{3/2}}, \qquad (5.116)
\end{aligned}$$

and the 5-dimensional case given by:

$$\begin{aligned}
&\int_0^{\infty}k^2e^{-4\pi^2\left(k^2s+k_1k_2s^2+\frac{k_1^2s^3}{3}\right)}e^{-4\pi^2\left(k'^2s'+k_1k_2's'^2+\frac{k_1^2s'^3}{3}\right)}dk = \int k^2e^{-4\pi^2k^2(s+\sin^2\theta\cos\phi\sin\phi s^2+\sin^2\theta\cos^2\phi s^3/3)}\\
&e^{-4k^2\pi^2\frac{sp}{3}\left(3\left(4+s^2-s^2cos2\theta+2s\sin^2\theta(s\cos2\phi+2\sin2\phi)\right)+4\cos\phi\sin^2\theta s'(3\sin\phi+\cos\phi(3s+s'))\right)}dk\\
&= \frac{1}{32\pi^{5/2}(f^{exp}(s,s',\theta,\phi))^{3/2}}, \qquad (5.117)
\end{aligned}$$

where f^{exp} is the function that multiplies '$-4\pi^2k^2$' in the exponent of the integrand. The result of the k-integration for the four-dimensional integral is proportional to $\frac{1}{s^{3/2}}$ and therefore diverges in the limit of $s \to 0$. The sum of all the four-dimensional divergent integrals in (5.115) and (C.1)-(C.9), and the three dimensional integral presented in (5.118) is however convergent. The reason for the emergence of this divergence is explained in section 5.5. Such a divergence is present in the 4-dimensional integrals proportional to $\hat{u}_2^{f0}$, $\hat{u}_2^{f0}$, $\hat{u}_j^{fi}$(j=1,2 and 3 and i='tcos','tsin') given in appendix (C.1)-(C.9) also. Further the k integrals in (C.1)-(C.9) are identical to that of (5.115).

The three-dimensional integral proportional to $\boldsymbol{R}_1$,$\boldsymbol{R}_2$ and $\boldsymbol{R}_3$ in (5.114) are given below:

$$\int \left[\frac{2\pi}{\omega_g}\boldsymbol{T}_{\boldsymbol{1}}^{tumb}\cdot(\boldsymbol{R}_1)+\frac{\pi}{\omega_g}\boldsymbol{T}_{\boldsymbol{2}}^{tumb}\cdot\boldsymbol{R}_2+\frac{\pi}{\omega_g}\boldsymbol{T}_{\boldsymbol{3}}^{tumb}\cdot\boldsymbol{R}_3\right]d\boldsymbol{k}. \tag{5.118}$$

$\boldsymbol{R}_1$, $\boldsymbol{R}_2$, $\boldsymbol{R}_3$, $\boldsymbol{T}_1^{tumb}$, $\boldsymbol{T}_2^{tumb}$ and $\boldsymbol{T}_3^{tumb}$ (see (5.81)-(5.83) and (5.67)-(5.70)) are proportional to (1/k) and $d\boldsymbol{k}$ is proportional to k^2dk in (5.118) making the k integral divergent as $k \to \infty$. The divergence here can again be isolated by introducing an integral over a dummy variable 's'. Noting that $\int_0^\infty 4\pi^2k^2exp(-4\pi^2k^2s) = 1$ for $s \neq 0$ and is divergent as $s \to 0$, the integrals proportional to $\boldsymbol{R}_1$,$\boldsymbol{R}_2$ and $\boldsymbol{R}_3$ are written as

$$4\pi^2\int_0^{2\pi}\int_0^{\pi}\int_0^{\infty}\int_0^{\infty}\left[\frac{2\pi}{\omega_g}\boldsymbol{T}_{\boldsymbol{1}}^{tumb}\cdot\boldsymbol{R}_1+\frac{\pi}{\omega_g}\boldsymbol{T}_{\boldsymbol{2}}^{tumb}\cdot\boldsymbol{R}_2+\frac{\pi}{\omega_g}\boldsymbol{T}_{\boldsymbol{3}}^{tumb}\cdot\boldsymbol{R}_3\right]k^2e^{-4\pi^2k^2s}dsk^2dk\sin\theta d\theta d\phi, \tag{5.119}$$

where we have added an additional 's' integral to isolate the divergence. The k integral can be readily evaluated and (5.119) becomes:

$$4\pi^2\int_0^{2\pi}\int_0^{\pi}\int_0^{\infty}\left\{\left[\frac{2\pi}{\omega_g}\boldsymbol{T}_{\boldsymbol{1}}^{tumb}\cdot\boldsymbol{R}_1+\frac{\pi}{\omega_g}\boldsymbol{T}_{\boldsymbol{2}}^{tumb}\cdot\boldsymbol{R}_2+\frac{\pi}{\omega_g}\boldsymbol{T}_{\boldsymbol{3}}^{tumb}\cdot\boldsymbol{R}_3\right]k^2\right\}\frac{1}{32\pi^{5/2}s^{3/2}}ds\sin\theta d\theta d\phi, \tag{5.120}$$

where the term in the curly brackets above is independent of k.

In (5.115) and (C.1)-(C.9), the results of k integration from (5.116) and (5.117) are substituted, and they are combined with (5.120), to obtain the final integral for the time period. The final integral is evaluated numerically using Gaussian quadrature. The numerical integration has to be carried out for each of the aspect ratios. This is unlike the spinning case, where the aspect ratio dependent term factored out from the integral(see 5.63). However in the limit of extreme aspect ratios($\kappa- > 0$ for an oblate spheroid and $\kappa- > \infty$ for a prolate spheroid), one can pull out aspect ratio dependence and obtain the asymptotic limit. This is discussed in section 5.6.5. The correction for the tumbling orbit obtained from the numerical integration is presented in section 5.7.

5.6.5 Extreme aspect ratio analysis

In this section, we evaluate the inertial correction to the time period for spheroids with extreme aspect ratios ($\kappa << 1$ or $\kappa >> 1$) rotating in the tumbling orbit. An oblate (prolate) spheroid spends a time of O(κ) ($1/\kappa$) in the aligned phase and O(1) time in the non-aligned phase. The aligned phase of a thin prolate spheroid (slender fiber) corresponds to $\boldsymbol{p}$ close to the flow axis ($\phi_j = 0$), while that of for a thin oblate spheroid (flat disk) corresponds to $\boldsymbol{p}$ being close to the gradient axis ($\phi_j = \pi/2$). One would then expect the inertia to primarily alter the time period during the aligned phase, that is, when ϕ_j is close to $\pi/2$ or $3\pi/2$ (0 or π) for an oblate (prolate) spheroid. The integral when expressed in terms of ϕ_j takes the form:

$$\Delta T_{c2}^{tumb} = -Re^{3/2}\int_{\pi}^{-\pi}\frac{\dot{\phi}_{c2}d\phi_j}{\dot{\phi}_{jeff}^2} = \int_{\pi}^{-\pi}\frac{1}{8\pi Y_c}\int\left[4\pi^2k^2\hat{\boldsymbol{u}}^f + \frac{\partial\hat{\boldsymbol{u}}^{match}}{\partial t} - (\boldsymbol{\Gamma}^{\dagger}\cdot\boldsymbol{k})\cdot\nabla_{\boldsymbol{k}}\hat{\boldsymbol{u}}^{match}\right.$$
$$\left.+\boldsymbol{\Gamma}\cdot\hat{\boldsymbol{u}}^{match}\right]\cdot\left\{\frac{i\,(\boldsymbol{S}^{(2t)}\cdot\boldsymbol{k})\cdot\boldsymbol{1}_3}{2\pi k^2}\cdot\left(\boldsymbol{I}-\frac{\boldsymbol{kk}}{k^2}\right)\right\}\frac{1}{\dot{\phi}_{jeff}^2}d\boldsymbol{k}d\phi_j. \tag{5.121}$$

Noting that $\dot{\phi}_{jeff}$ (5.26) in the extreme aspect ratio limit is zero when the spheroid is perfectly aligned , one can see that the above integral diverges in the aligned phase. This suggests that the contribution comes from region close to the aligned phase. One can then use a boundary layer analysis, to isolate the contribution to the integral in (5.121).

We will first estimate the contribution from the aligned phase for a flat disk. Defining the boundary layer variable as $\hat{\phi} = (-\pi/2 + \phi_j)/\kappa$, one can rewrite (5.121) in the boundary layer variable as:

$$\Delta T_{c2}^{tumb} = \int_{\infty}^{-\infty}\frac{1}{8\pi Y_c}\int\left[4\pi^2k^2\hat{\boldsymbol{u}}^f + \frac{\partial\hat{\boldsymbol{u}}^{match}}{\partial t} - (\boldsymbol{\Gamma}^{\dagger}\cdot\boldsymbol{k})\cdot\nabla_{\boldsymbol{k}}\hat{\boldsymbol{u}}^{match}\right.$$
$$\left.+\boldsymbol{\Gamma}\cdot\hat{\boldsymbol{u}}^{match}\right]\cdot\left\{\frac{i\,(\boldsymbol{S}^{(2t)}\cdot\boldsymbol{k})\cdot\boldsymbol{1}_3}{2\pi k^2}\cdot\left(\boldsymbol{I}-\frac{\boldsymbol{kk}}{k^2}\right)\right\}\frac{1}{\kappa^3(\hat{\phi}^2+1)^2}d\boldsymbol{k}d\hat{\phi}. \tag{5.122}$$

At the leading order in κ, the term within braces in (5.122) becomes:

$$\left\{ \frac{i\,(\boldsymbol{S}^{(2t)} \cdot \boldsymbol{k}) \cdot \mathbf{1}_3}{2\pi k^2} \cdot \left(\boldsymbol{I} - \frac{\boldsymbol{kk}}{k^2} \right) \right\} = \boldsymbol{T}_1 - \boldsymbol{T}_2, \tag{5.123}$$

where T_1,T_2 and are defined in (5.68-5.69) and $B_1 = B_3 = -16/3$. The term proportional to the singularity in the test problem is therefore independent of κ. The leading order term in the $\hat{\boldsymbol{u}}^{match}$ takes the form:

$$\hat{\boldsymbol{u}}^{match} = -\frac{i\left(k^2 - 2\mathrm{k1}^2\right) A_2 k_2}{4k^4\pi}\mathbf{1}_1 - \frac{i\mathrm{k1}A_2\left(k^2 - 2k_2^2\right)}{4k^4\pi}\mathbf{1}_2 + \frac{i\mathrm{k1}A_2 k_2 k_3}{2k^4\pi}\mathbf{1}_3 \tag{5.124}$$

Recall that A_2 is the coefficient of the longitudinal extension and is equal to $-8\pi\kappa/3$ in the flat disk limit. The inertial terms in the square bracket in (5.122) is therefore proportional to κ. Although the inertial terms involving the singularities in the axisymmetric extension and transverse extensions come at O(κ), these contributions are also proportional to the boundary layer variable $\hat{\phi}$, and the integration over $\hat{\phi}$ in (5.122) is zero for these contributions. The evaluation of the integral in (5.122) leads to:

$$\Delta T_{c2}^{tumb} = Re^{3/2} 0.1763/\kappa^2 \tag{5.125}$$

for a flat disk.

The estimation of the correction for the slender fiber case is slightly nontrivial. If one proceeds in a manner similar as that of the flat disk given above, one can see that the scaling of the leading order term of the integrand in the time period integral, when expressed in the boundary layer variable($\hat{\phi}$) is $\kappa^2/\log\kappa$. However, it turns out that the leading order term is an odd function of the boundary layer variable, and therefore the integral over $\hat{\phi}$ is zero. To evaluate the integral at the next order($\kappa/\log\kappa$) is difficult and not pursued here.

5.7 Results: Time period - O($Re^{\frac{3}{2}}$)

In this section we summarize the numerical results obtained using the analytical expressions derived in the previous two sections. The scaled correction to the tumbling time period is plotted against eccentricity(e) for a prolate spheroid in figure 5.4a. For a sphere ($e = 0$) the correction is 1.355, and it first decreases with increasing eccentricity (increasing aspect ratio) till an e of about 0.75, shown in the inset plot, before eventually diverging in the slender fiber limit. The correction normalized with the Jeffery period, which diverges as κ as $\kappa \to \infty$, is

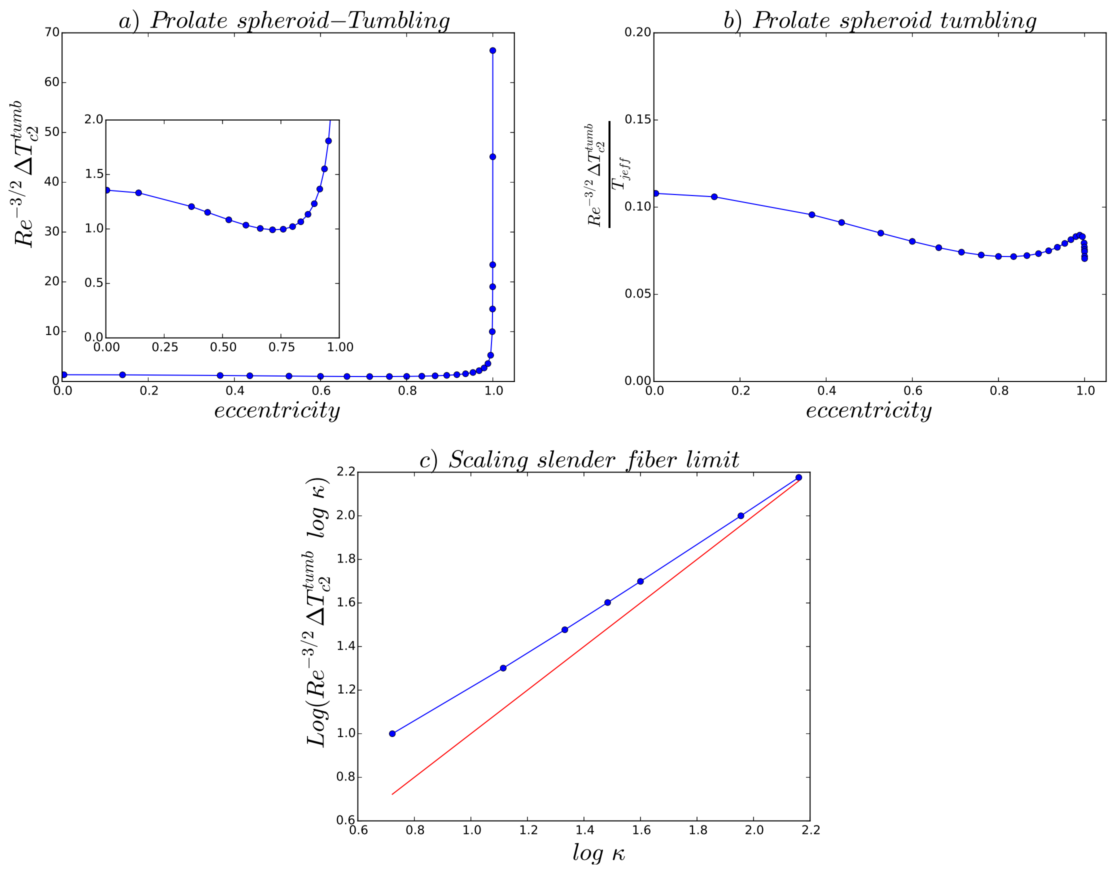

Fig. 5.4 (a) The correction at O($Re^{3/2}$) is plotted against eccentricity for prolate spheroid in tumbling orbit. The inset plot shows a zoomed view of eccentricity$<$ 0.8. (b) The correction at O($Re^{3/2}$) scaled with the Jeffery period is plotted against eccentricity for the same. (c) The correction is plotted on a log-log scale. The red line has a slope 1.

plotted against eccentricity in figure 5.4b. As is clear from the dip in the plot for large κ, the divergence of the inertial correction is slower than O(κ) for $\kappa \to \infty$. To obtain the scaling for the divergence we have plotted it on a log-log scale in figure 5.4c. together with a line of slope 1 (red) for purposes of comparison. The plot suggests a scaling of approximately O($\kappa/\log\kappa$) consistent with the arguments at the end of section 5.6.5.

The correction to the time period is plotted against eccentricity, for an oblate spheroid in the tumbling orbit in figure 5.5a. The correction starts again from that for the sphere ($e = 0$) and, to begin with, decreases slightly with increasing eccentricity(decreasing aspect ratio), as shown in the inset plot, before eventually diverging in the limit of a flat disk. The correction scaled with the Jeffery period(which diverges as $1/\kappa$ as $\kappa \to 0$) is plotted in figure 5.5b, and

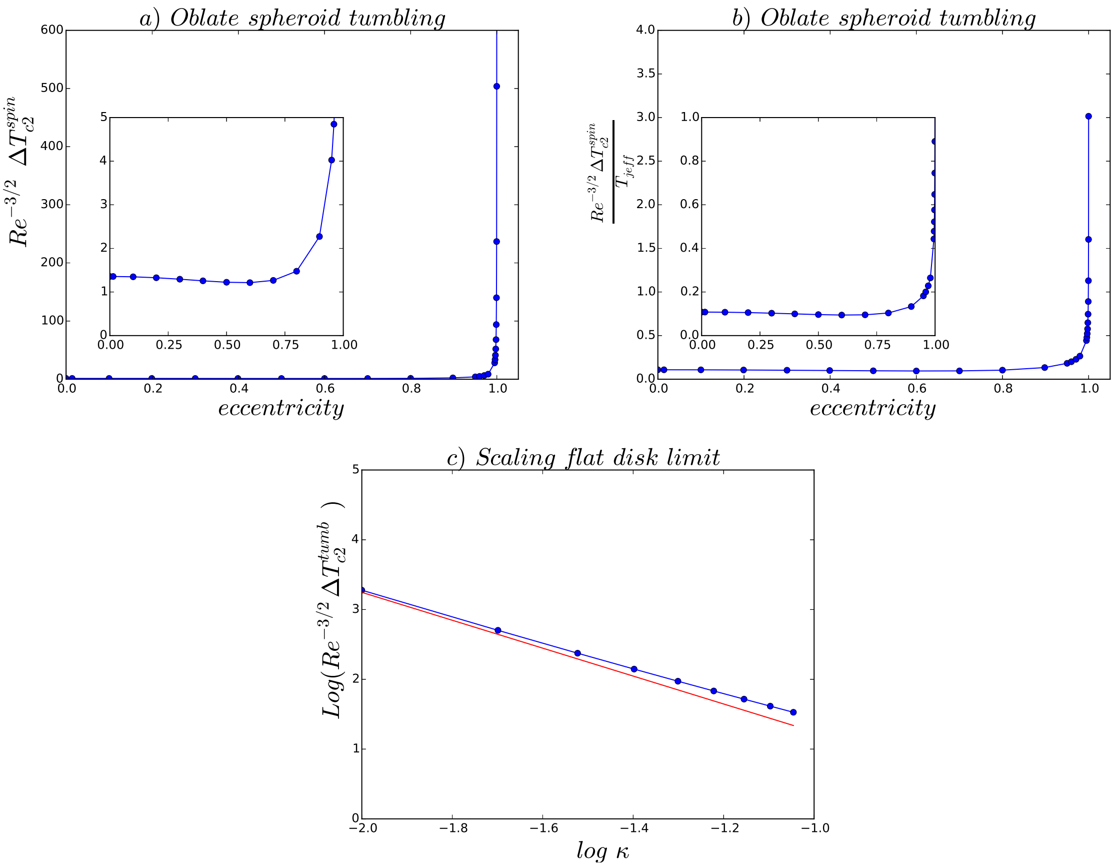

Fig. 5.5 (a) The correction at O($Re^{3/2}$) is plotted against eccentricity for oblate spheroid in tumbling orbit. The inset plot shows the zoomed view for eccentricity < 0.8. (b) The correction at O($Re^{3/2}$) scaled with the Jeffery period is plotted against eccentricity for the same. (c)The correction is plotted on a log-log scale. The red line is the asymptote obtained from an analysis for flat disk.

in contrast to the prolate case continues to diverge in the limit of $\kappa \to 0$. We have plotted the flat-disk asymptote (red) given by (5.125) as well as the numerical results on a log-log scale in figure 5.5c; the asymptotes compare well to the numerical results, and validates the predicted O(κ^{-2}) divergence. In figure 5.6 we have plotted the correction against eccentricity for an oblate spheroid in spinning orbit, which was given in (5.63). In the spinning case the correction to time period decreases with increasing eccentricity and approaches a finite value 0.47 for the flat disk.

The O($Re^{3/2}$) time period corrections for both the prolate and oblate spheroids have been found to be positive, implying an increase in the time period of rotation due to inertia. This is consistent with what has been observed in the simulations.

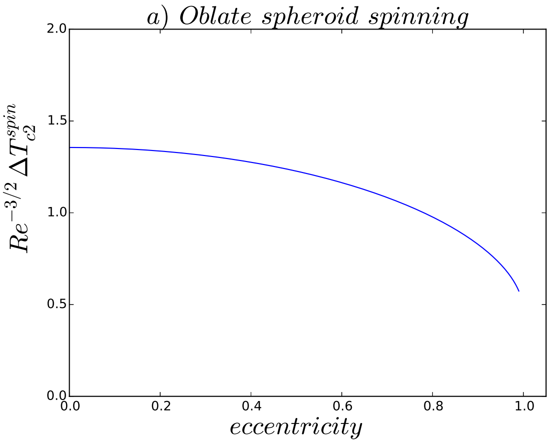

Fig. 5.6 The correction at $O(Re^{3/2})$ is plotted against eccentricity for oblate spheroid in spinning orbit.

5.8 Conclusions and future work

In this chapter we have evaluated the leading order fluid inertial correction, at $O(Re^{3/2})$, and the particle inertial correction, at $O(St^2)$, to the time period of rotation of a spheroid, in simple shear flow, in the tumbling and the spinning orbits. The first effects of fluid inertia occur at $O(Re)$, but at this order inertia acts to stabilize either one of two Jeffrey orbits depending on the spheroid aspect ratio and its initial orientation. Specifically it has been shown in chapter 2 that the stable orbit for a prolate spheroid of any aspect ratio is tumbling and an oblate spheroid with $\kappa > 0.142$ is spinning. The stable orbit for an oblate spheroid with $\kappa < 0.142$ is spinning or tumbling depending on the initial orientation. The first effects of particle inertia occur at $O(St)$ and it stabilizes the tumbling orbit for a prolate spheroid and the spinning orbit for an oblate spheroid. In the stabilized orbits, it is shown that the correction to the time period at $O(Re)$ and $O(St)$ is zero.

The calculation of the correction to the angular velocity at $O(St^2)$ for a spheroid is straightforward and is presented in section 5.4. The correction to the angular velocity at $O(Re^{3/2})$ is formulated as an integral in Fourier space, based on a reciprocal theorem formulation, the details of which are given in section 5.2. The disturbance velocity field around a spinning spheroid is steady and therefore, the correction to angular velocity at $O(Re^{3/2})$ is trivially related to the correction to time period through (5.40). The calculation proceeds in a manner similar to earlier ones for a sphere(Stone *et al.* (2000); Subramanian *et al.* (2011)), and the result is given in (5.63). The disturbance velocity field around a spheroid is unsteady in the tumbling orbit, and the evaluation of the time period correction is therefore not trivial. However, we show in section 5.6 that by expanding the integrand in the reciprocal theorem as a Fourier series in time one can evaluate this correction. The numerical results for both the tumbling and spinning orbits are given in section 5.7. The results conclude that the time period of rotation increases with fluid inertia in both tumbling and spinning orbits consistent with earlier simulations. We find that the scaling for the correction for a flat disk rotating in the tumbling orbit is $1/\kappa^2$ both from the plot of the arbitrary aspect ratio oblate spheroid presented in section 5.7 as well as an asymptotic analysis presented in section 5.6.5. For a slender fiber we obtain the scaling as approximately $\kappa/\log\kappa$ from the plot of the arbitrary aspect ratio prolate spheroid presented in section 5.7. The stronger divergence of the inertial correction, for thin oblate spheroids, evidently implies a breakdown of the analysis here. This will be taken up for future work.

Chapter 6

Conclusions and future work

This thesis has tried to answer the four questions that are raised in chapter 1.

In chapter 2, we address the first question, that is, whether weak inertial effects at O(Re) and O(St) eliminate the indeterminacy associated with the Stokes limit. The indeterminacy, as explained in chapter 1, arises due to the reversibility of the Stokes flow, which makes a spheroid rotate in any of a one parameter family of closed orbits, known as Jeffery orbits, in planar linear flows with $\lambda < \lambda_{crit}$. The investigations in chapter 2 concluded that for certain regions in the $\lambda - \kappa$ plane, the weak inertial effects stabilize either of the two orbits, namely the tumbling and the spinning orbits. However, there are regions in the $\lambda - \kappa$ plane, where the orbit that is stabilized by inertia, depends on the initial orientation of the spheroid. To be precise, in this region, a repeller divides the orientation unit-hemisphere into two basins of attractions, with the attractors being the tumbling and the spinning orbits. In particular, for a neutrally buoyant spheroid in simple shear flow ($\lambda = 0$), this region corresponds to $\kappa < 0.137$. This finding for simple shear flow in chapter 2, is utilized in chapter 3, to address the second question, that is about calculating the viscosity of a dilute suspension of neutrally buoyant spheroids. The viscosity of a suspension of neutrally buoyant spheroids, which include prolate spheroids of any aspect ratio as well as oblate spheroids with $\kappa > 0.137$, is calculated based on the distribution that is set up by inertia alone. To calculate the viscosity of a suspension of oblate spheroids with $\kappa < 0.137$, an additional orientation decorrelation mechanism in the form of rotary Brownian motion is considered. The orientation distribution that is set up by weak inertial effects together with weak Brownian motion is, interestingly, a distribution of the Boltzmann form, with a potential that depends on C, κ, and a dimensionless shear rate ($RePe_r$), and therefore lends itself to a novel thermodynamic interpretation in $C - \kappa - RePe_r$ space. The transition of this potential between a single-welled and a double-welled structure is interpreted as a phase transition, and the small-C and large-C minima identified with spinning and tumbling phases. A phase diagram is plotted in $C-\kappa-RePe_r$ space to identify the two-phase region and its envelope. The phase transition named the 'tumbling-spinning' transition, results in hysteretic dynamics within the two-phase envelope, making the viscosity sensitively dependent on the precise shear rate history. In this sense, the tumbling-spinning transition is analogous to the well known coil-stretch transition for polymer solutions, in that it endows an inertial suspension of thin oblate spheroids with a memory that far exceeds the nominal microstructural relaxation times.

The third question is addressed in chapter 4, by investigating the effects of inertia on a spheroid sedimenting in a simple shear flow using a reciprocal theorem formulation. The combined effect of the torque due to sedimentation, and that due to inertial forces are analyzed therein, for three canonical cases, where the sedimenting force is aligned with any of the gradient, vorticity and flow axes of the simple shear flow. Interestingly, depending on the non-dimensional parameter Re_{sed}/Re, the torque due to sedimentation may result in the emergence of a repeller in the orientation space, in cases where there were no repellers in the limit of $Re_{sed}/Re = 0$. The final question is addressed in chapter 5, where an investigation is carried out to understand the effect of inertia on the time period of rotation of a spheroid in a simple shear flow. As mentioned in chapter 1, simulations have observed that in the tumbling and the spinning orbits, the effect of fluid inertia is to increase the time period from its leading order value, and that of particle inertia is to decrease it. It is shown in chapter 5 that in these orbits, the O(Re) and O(St) angular velocities calculated in chapter 2, do not alter the time period from its leading order value. The next correction due to particle inertia comes at O(St^2), and the calculation of this is straightforward due to the regular nature of the problem. On account of being a singular problem , the correction due to fluid inertia comes at O($Re^{3/2}$), and from the outer region ($L >> Re^{-1/2}$). A Fourier space based formulation is used to calculate the correction. The corrections to the time period at O(St^2) and O($Re^{3/2}$) are calculated and the qualitative change in time period predicted by the analysis, is consistent with simulations. It is important to note that for the case of a neutrally buoyant spheroid the correction comes at O($Re^{3/2}$) and the effect of fluid inertia is therefore dominant.

Several new questions have emerged from this thesis and are given below.

In chapter 2, the solution to the Stokes equations around a spheroid in simple shear flow, is presented in terms of a vector spheroidal harmonics formalism . This formalism, together with addition theorems, readily generalizes to the case of an N-body problem, and is thus a powerful one, and can be extended to problems of a greater complexity. As mentioned in chapter 3, in an experiment with an inertial suspension of spheroids, hydrodynamic interaction might be the easiest accessible orientation decorrelation mechanism. If one could solve the two body problem for a spheroid in a shear flow, the results can be used to understand the combined effect of inertia and hydrodynamic interaction, and the resulting phase diagram may be different from that presented in chapter 3 for the Brownian motion. More importantly in an experiment, it will be easier to access the different regions of the resulting phase diagram. The spheroidal harmonics formalism may also be used to understand the effect of viscoelasticity, on the orientation dynamics of a spheroid of arbitrary aspect ratio, rotating in a planar linear flow. Again in an experiment, it is fairly straightforward to realize the effects of viscoelasticity, and therefore it is important to understand the orientation dynamics of a spheroid in a viscoelastic fluid. The orientation dynamics of a spheroid sedimenting in random linear flow is a question that can be pursued due to its importance in geophysical situations such as the orientation distribution of ice crystals in clouds, which in turn contributes to the scattering albedo of the earth-atmospheric system.

References

AIDUN, C., LU, Y. & DING, E.-J. 1998 Direct analysis of particulate suspensions with inertia using the discrete boltzmann equation. *J. Fluid Mech.* **373**, 287–311.

AMINI, H., LEE, W. & CARLO, D. 2014 Inertial microfluidic physics. *Lab Chip* **14**, 2739–2761.

ARFKEN, G. B., WEBER, H. J. & HARRIS, F. E. 2011 *Mathematical methods for physicists: a comprehensive guide*. Academic press.

AUER JR, A. H. & VEAL, D. L. 1970 The dimension of ice crystals in natural clouds. *Journal of the Atmospheric Sciences* **27** (6), 919–926.

BATCHELOR, G. 1977 Developments in microhydrodynamics. *Theor. and Appl. Mechanics: Proc. Fourteenth Int. Cong., Delft, Netherlands* **83**, 33–55.

BATCHELOR, G. K. 1970*a* Slender-body theory for particles of arbitrary cross-section in stokes flow. *J. Fluid Mech.* **44**, 791–810.

BATCHELOR, G. K. 1970*b* The stress system in a suspension of force-free particles. *J. Fluid Mech.* **41**, 545–570.

BATCHELOR, G. K. 1972 Sedimentation in a dillute dispersion of spheres. *J. Fluid Mech.* **52**, 245–268.

BATCHELOR, G. K. & GREEN, J. 1972*a* The determination of the bulk stress in a suspension of spherical particles to order c^2. *J. Fluid Mech.* **56**, 401–427.

BATCHELOR, G. K. & GREEN, J. 1972*b* The hydrodynamic interaction of two small freely-moving spheres in a linear flow field. *J. Fluid Mech.* **56**, 375–400.

BECK, V. & SHAQFEH, E. 2006 Ergodicity breaking and conformational hysteresis in the dynamics of a polymer tethered at a surface stagnation point. *J. Chem. Phys.* **124**, 094902.

BENDER, C. M. & ORSZAG, S. A. 1999 *Advanced mathematical methods for scientists and engineers I*. Springer Science & Business Media.

BENTLEY, B. & LEAL, L. 1986 An experimental investigation of drop deformation and breakup in steady, two-dimensional linear flows. *Journal of Fluid Mechanics* **167**, 241–283.

BRADY, J. F. & MORRIS, J. F. 1997 Microstructure of strongly sheared suspensions and its impact on rheology and diffusion. *Journal of Fluid Mechanics* **348**, 103–139.

BRENNER, H. 1974 Rheology of a dilute suspension of axisymmetric brownian particles. *International journal of multiphase flow* **1** (2), 195–341.

BRETHERTON, F. P. 1962 The motion of rigid particles in a shear flow at low reynolds number. *Journal of Fluid Mechanics* **14** (02), 284–304.

BROWN, A. B. D. & RENNIE, A. R. 2001 Images of shear-induced phase separation in a dispersion of hard nanoscale discs. *Chem. Engg. Sci.* **56**, 2999–3004.

CANDELIER, F., EINARSSON, J., LUNDELL, F., MEHLIG, B. & ANGILELLA, J.-R. 2015 Role of inertia for the rotation of a nearly spherical particle in a general linear flow. *Physical Review E* **91** (5), 053023.

CARO, C., PEDLEY, T., SCHROTER, R. & SEED, W. 2012 *The Mechanics of the circulation*. Cambridge University Press.

CHALLABOTLA, N., NILSEN, C. & ANDERSSON, H. 2015 On rotational dynamics of inertial disks in creeping shear flow. *Phys. Lett. A* **379**, 011704.

CHANDRASEKHAR, S. 1943 Stochastic problems in physics and astronomy. *Reviews of modern physics* **15** (1), 1.

CHENG, X., MCCOY, J. H., ISRAELACHVILI, J. N. & COHEN, I. 2011 Imaging the microscopic structure of shear thinning and thickening colloidal suspensions. *Science* **333** (6047), 1276–1279.

CHILDRESS, S. 1964 The slow motion of a sphere in a rotating, viscous fluid. *Journal of Fluid Mechanics* **20** (02), 305–314.

CHWANG, A. T. & WU, T.-T. 1974 Hydromechanics of low-reynolds-number flow.part 1. rotation of axisymmetric prolate bodies. *J. Fluid Mech.* **63**, 607–622.

CHWANG, A. T. & WU, T. Y.-T. 1975 Hydromechanics of low-reynolds-number flow.part 2. singularity method for stokes flows. *J. Fluid Mech.* **67**, 787–815.

DABADE, V., MARATH, N. K. & SUBRAMANIAN, G. 2015 Effects of inertia and viscoelasticity on sedimenting anisotropic particles. *Journal of Fluid Mechanics* **778**, 133–188.

DE GENNES, P. 1974 Coil-stretch transition of dilute flexible polymers under ultrahigh velocity gradients. *The Journal of Chemical Physics* **60** (12), 5030–5042.

DERAKHSHANDEH, B., KEREKES, R. J., HATZIKIRIAKOS, S. G. & BENNINGTON, C. P. J. 2011 Rheology of pulp fibre suspensions: A critical review. *Chem. Engg. Sci.* **66**, 3460–3470.

DING, E.-J. & AIDUN, C. 2000 The dynamics and scaling law for particles suspended in shear flow with inertia. *J. Fluid Mech.* **423**, 317–344.

DWIVEDI, R. 2016 Effect of the brownian motion on thetransient dynamics of anisotropic particles in simple shear flow. *JNCASR Report* .

EINARSSON, J., ANGILELLA, J. & MEHLIG, B. 2014 Orientational dynamics of weakly inertial axisymmetric particles in steady viscous flows. *Physica D: Nonlinear Phenomena* **278**, 79–85.

EINARSSON, J., CANDELIER, F., LUNDELL, F., ANGILELLA, J. & MEHLIG, B. 2015*a* Effect of weak fluid inertia upon jeffery orbits. *Physical Review E* **91** (4), 041002.

EINARSSON, J., CANDELIER, F., LUNDELL, F., ANGILELLA, J. R. & MEHLIG, B. 2015*b* Rotation of a spheroid in a simple shear at small reynolds number. *Physics of Fluids* **27** (6).

ENNIS, G. J., OKAGAWA, A. & MASON, S. G. 1978 Memory impairment in flowing suspensions. ii. experimental results. *Canadian Journal of Chemistry* **56** (22), 2824–2832.

GAUTHIER, G., GONDRET, P. & RABAUD, M. 1998 Motions of anisotropic particles: application to visualization of three-dimensional flows. *Physics of Fluids (1994-present)* **10** (9), 2147–2154.

GOLDSTEIN, H. 1962 *Classical mechanics*, , vol. 4. Pearson Education India.

GOTO, S., KIDA, S. & FUJIWARA, S. 2011 Flow visualization using reflective flakes. *Journal of Fluid Mechanics* **683**, 417–429.

GRADSHTEYN, I. & RYZHIK, I. 2007 *Table of integrals, series and products*. Academic Press.

HARLEN, O. G. & KOCH, D. L. 1997 Orientational drift of a fibre suspended in a dilute polymer solution during oscillatory shear flow. *Journal of non-newtonian fluid mechanics* **73** (1), 81–93.

HARPER, E. & CHANG, I.-D. 1968 Maximum dissipation resulting from lift in a slow viscous shear flow. *Journal of Fluid Mechanics* **33** (02), 209–225.

HINCH, E. 1974 Mechanical models of dilute polymer solutions for strong flows with large polymer deformations. *Polymères et Lubrification* pp. 351–372.

HINCH, E. 1977 An averaged-equation approach to particle interactions in a fluid suspension. *J. Fluid Mech.* **83**, 695–720.

HINCH, E. & LEAL, L. 1972 The effect of brownian motion on the rheological properties of a suspension of non-spherical particles. *J. Fluid Mech* **52**, 683–712.

HINCH, E. J. 1991 *Perturbation methods*. Cambridge university press.

HUANG, H., YANG, X., KRAFCZYK, M. & LU, X.-Y. 2012 Rotation of spheroidal particles in couette flows. *Journal of Fluid Mechanics* **692**, 369–394.

JEFFERY, G. 1922 The motion of ellipsoidal particles immersed in a viscous fluid. *Proc. Roy. Soc. Lond* **A102**, 161–179.

KAO, S., COX, R. & MASON, S. 1977*a* Streamlines around single spheres and trajectories of pairs of spheres in two-dimensional creeping flows. *Chem. Engng. Sci.* **32**, 1505.

KAO, S. V., COX, R. G. & MASON, S. G. 1977*b* Streamlines around single spheres and trajectories of pairs of spheres in two-dimensional creeping flows. *Chem. Engg. Sci.* **32**, 1505–1515.

KARNIS, A., GOLDSMITH, H. & MASON, S. 1966 The flow of suspensions through tubes: V. inertial effects. *The Canadian Journal of Chemical Engineering* **44** (4), 181–193.

KIM, S. & KARRILA, S. J. 1991 Microhydrodynamics: Principles and selected applications. *Butterworth-Heinemann* .

KRISHNAMURTHY, D. 2014 Heat transfer from drops in shearing flows and collective motion in micro-scale swimmer suspensions. Master's thesis, Jawaharlal Nehru Centre for Advanced Scientific Research, Bangalore, India.

KUSHCH, V. I. 1997 Microstresses and effective elastic moduli of a solid reinforced by periodically distributed spheroidal particles. *Int J. of Solid Structures* **34**, 1353–1366.

KUSHCH, V. I. 1998 Elastic equilibrium of a medium containing a finite number of arbitrarily oriented spheroidal inclusions. *Int J. of Solid Structures* **35**, 1187–1198.

KUSHCH, V. I. & SANGANI, A. S. 2003 The complete solutions for stokes interactions of spheroidal particles by the mutipole expansion method. *Preprint, Int J. of Mutiphase Flow.* **34**, 1353–1366.

LARSON, R. G. 1988 Constitutive equations for polymer melts and solutions. *Butterworths* .

LARSON, R. G. 2005 The rheology of dilute solutions of flexible polymers: Progress and problems. *Journal of Rheology* **49** (1), 1–70.

LEAHY, B. D., CHENG, X., ONG, D. C., LIDDELL-WATSON, C. & COHEN, I. 2013 Enhancing rotational diffusion using oscillatory shear. *Physical review letters* **110** (22), 228301.

LEAL, L. 1979 The motion of small particles in non-newtonian fluids. *J. non-Newt. Fluid Mech.* **5**, 33–78.

LEAL, L. & HINCH, E. 1971 The effect of weak brownian rotations on particles in shear flow. *J. Fluid Mech* **46**, 685–703.

LEAL, L. G. 1975 The slow motion of slender rod-like particles in a second-order fluid. *J. Fluid Mech.* **69**, 305–337.

LEAL, L. G. 1992 Laminar flow and convective transport processes, scaling principles and asymptotic analysis. *Butterworth-Heinemann Series in Chemical Engineering* .

LEE, J. S., SHAQFEH, E. S. & MULLER, S. J. 2007 Dynamics of dna tumbling in shear to rotational mixed flows: Pathways and periods. *Physical Review E* **75** (4), 040802.

LEKKERKERKER, H. N. W. & VROEGE, G. J. 2012 Liquid crystal phase transitions in suspensions of mineral colloids: new life from old roots. *Phil. trans. R Soc. A* **371**, 263.

LIN, C.-J., PEERY, J. & SCHOWALTER, W. 1970*a* Simple shear flow round a rigid sphere: inertial effects and suspension rheology. *J. Fluid Mech.* **44**, 1–17.

LIN, C.-J., PEERY, J. H. & SCHOWALTER, W. 1970*b* Simple shear flow round a rigid sphere: inertial effects and suspension rheology. *Journal of Fluid Mechanics* **44** (01), 1–17.

LIOU, K.-N. 1986 Influence of cirrus clouds on weather and climate processes: A global perspective. *Monthly Weather Review* **114** (6), 1167–1199.

LLEWELLIN, E., MADER, H. & WILSON, S. 2002 The constitutive equation and flow dynamics of bubbly magmas. *Geophys. Res. Lett.* **29**, 23–1.

LUNDELL, F. 2011 The effect of particle inertia on triaxial ellipsoids in creeping shear: From drift toward chaos to a single periodic solution. *Physics of Fluids (1994-present)* **23** (1), 011704.

LUNDELL, F. & CARLSSON, A. 2010 Heavy ellipsoids in creeping shear flow: Transitions of the particle rotation rate and orbit shape. *Physical Review E* **81** (1), 016323.

LUNDELL, F. & CARLSSON, A. 2011 The effect of particle inertia on triaxial ellipsoids in creeping shear: From drift toward chaos to a single periodic solution. *Phys. Fluids* **23**, 011704.

LUNDELL, F., SÖDERBERG, L. D. & ALFREDSSON, P. H. 2011 Fluid mechanics of papermaking. *Annual Review of Fluid Mechanics* **43**, 195–217.

MANGA, M., CASTRO, J., CASHMAN, K. & LOEWENBERG, M. 1998 Rheology of bubble bearing magmas. *J. Volcanology Geothermal Res.* **87**, 15–28.

MAO, W. & ALEXEEV, A. 2014 Motion of spheroid particles in shear flow with inertia. *J. Fluid Mech.* **749**, 145–166.

MEIBOHM, J., CANDELIER, F., ROSEN, T., EINARSSON, J., LUNDELL, F. & MEHLIG, F. 2016 Angular velocity of a spheroid log rolling in a simple shear at small reynolds number. *arxiv* **1606.02665v2**.

MICHOT, L., BIHANNIC, I., MADDI, S., FUNARI, S. S., BARAVIAN, C., LEVITZ, P. & DAVISON, P. 2006 Liquid-crystalline aqueous clay suspensions. *Proc. Nat. Acad. Sci.* **103**, 16101–16104.

MIKULENCAK, D. R. & MORRIS, J. F. 2004 Stationary shear flow around fixed and free bodies at finite reynolds number. *Journal of Fluid Mechanics* **520**, 215–242.

MORRIS, J. & BRADY, J. 1997 Microstructure of strongly sheared suspensions and its impact on rheology and diffusion. *J. Fluid Mech* **348**, 103–139.

MORRIS, J., YAN, Y. & KOPLIK, J. 2007 Hydrodynamic interaction of two particles in confined linear shear flow at finite reynolds number. *Phys. Fluids* **19** (11), 113305.

MORSE, P. M. & FESHBACH, H. 1953 Methods of theoretical physics. *McGraw-Hill book company, Inc* .

MUELLER, S., LLEWELLIN, E. W. & MADER, H. M. 2011 The effect of particle shape on suspension viscosity and implications for magmatic flows. *Geophys. Res. Lett* **38**, L13316.

OKAGAWA, A., COX, R. & MASON, S. 1973*a* The kinetics of flowing dispersinos. vi. transient orientation and rheological phenomena of rods and discs in shear flow. *J. Coll. Int. Sci.* **45**, 303–329.

OKAGAWA, A., COX, R. & MASON, S. 1973*b* The kinetics of flowing dispersions. vii. oscillatory behavior of rods and discs in shear flow. *J. Coll. Int. Sci.* **45**, 303–329.

OKAGAWA, A. & MASON, S. G. 1974 Particle behavior in shear and electric fields. vii. orientation distributions of cylinders. *Journal of Colloid and Interface Science* **47** (2), 568–587.

VAN OLPHEN, H. 1963 *An introduction to clay colloid chemistry*. Wiley, New York.

PRAGER, S. 1957 Stress-strain relations in a suspension of dumbbells. *Transactions of The Society of Rheology (1957-1977)* **1** (1), 53–62.

QI, D. & LUO, L.-S. 2003 Rotational and orientational behaviour of three-dimensional spheroidal particles in couette flows. *Journal of Fluid Mechanics* **477**, 201–213.

RAHNAMA, M., KOCH, D. & SHAQFEH, E. 1995 The effect of hydrodynamic interactions on the orientation distribution in a fiber suspension subject to simple shear flow. *Phys. Fluids* **7**, 487–506.

ROSEN, T., DO-QUANG, M., AIDUN, C. & LUNDELL, F. 2015 The dynamical states of a prolate spheroid suspended in shear flow as a consequence of particle and fluid inertia. *J. Fluid Mech.* **771**, 115–158.

ROSEN, T., LUNDELL, F. & AIDUN, C. 2014 Effect of fluid inertia on the dynamics and scaling of neutrally buoyant particles in shear flow. *J. Fluid Mech.* **738**, 563–590.

SAFFMAN, P. 1956 On the motion of small spheroidal particles in a viscous liquid. *Journal of Fluid Mechanics* **1** (05), 540–553.

SAFFMAN, P. 1965 The lift on a small sphere in a slow shear flow. *Journal of fluid mechanics* **22** (02), 385–400.

SAVAS, Ö. 1985 On flow visualization using reflective flakes. *Journal of Fluid Mechanics* **152**, 235–248.

SCHROEDER, C., SHAQFEH, E. & CHU, S. 2004 Effect of hydrodynamic interactions on dna dynamics in extesional flow: simulation and single molecule experiment. *Macromol.* **37**, 9242–9256.

SCHROEDER, C. M., BABCOCK, H. P., SHAQFEH, E. S. & CHU, S. 2003 Observation of polymer conformation hysteresis in extensional flow. *Science* **301** (5639), 1515–1519.

SHAQFEH, E. S. G. 2005 The dynamics of single-molecule dna in flow. *Journal of Non-Newtonian Fluid Mechanics* **130** (1), 1–28.

STONE, H., JOHN, B. & LOVALENTI, P. M. 2000 Inertial effects on the rheology of suspensions and on the motion of individual particles. *unpublished* .

SUBRAMANIAN, G. & BRADY, J. 2004 Multiple scales analysis of the fokker–planck equation for simple shear flow. *Physica A: Statistical Mechanics and its Applications* **334** (3), 343–384.

SUBRAMANIAN, G. & BRADY, J. F. 2006 Trajectory analysis for non-brownian inertial suspensions in simple shear flow. *J. Fluid Mech.* **559**, 151–203.

SUBRAMANIAN, G. & KOCH, D. 2006*a* Centrifugal forces alter streamline topology and greatly enhance the rate of heat and mass transfer from neutrally buoyant particles to a shear flow. *Physical review letters* **96** (13), 134503.

SUBRAMANIAN, G. & KOCH, D. L. 2005 Inertial effects on fibre motion in simple shear flow. *J. Fluid Mech.* **535**, 383–414.

SUBRAMANIAN, G. & KOCH, D. L. 2006*b* Inertial effects on the orientation of nearly spherical particles in simple shear flow. *J. Fluid Mech.* **557**, 257–296.

SUBRAMANIAN, G. & KOCH, D. L. 2006*c* Inertial effects on the transfer of heat or mass from neutrally buoyant spheres in a steady linear velocity field. *Phys. Fluids* **18** (7), 073302.

SUBRAMANIAN, G. & KOCH, D. L. 2007 Heat transfer from a neutrally buoyant sphere in a second-order fluid. *J. Non-Newtonian Fluid Mech.* **144** (1), 49–57.

SUBRAMANIAN, G., KOCH, D. L., ZHANG, J. & YANG, C. 2011 The influence of the inertially dominated outer region on the rheology of a dilute dispersion of low-reynolds-number drops or rigid particles. *Journal of Fluid Mechanics* **674**, 307–358.

TAYLOR, G. 1923 The motion of ellipsoidal particles in a viscous fluid. *Proceedings of the Royal Society of London. Series A, Containing Papers of a Mathematical and Physical Character* pp. 58–61.

THORODDSEN, S. T. & BAUER, J. 1999 Qualitative flow visualization using colored lights and reflective flakes. *Physics of Fluids (1994-present)* **11** (7), 1702–1704.

TREVELYAN, B. & MASON, S. 1951 Particle motions in sheared suspensions. i. rotations. *J. Coll. Sci.* **6** (4), 354–367.

VROEGE, G. J. & LEKKERKERKER, H. N. W. 1992 Phase transitions in lyotropic colloidal and polymer liquid crystals. *Rep. Prog. Phys.* **55**, 1241–1309.

YU, Z., PHAN-THIEN, N. & TANNER, R. I. 2007 Rotation of a spheroid in a couette flow at moderate reynolds numbers. *Physical Review E* **76** (2), 026310.

Appendix A

Expressions for the functions I_i's and J_i's

$$I_1 = 2\pi \tag{A.1}$$

$$I_2 = 2\pi(\kappa_{eq}-1)(\kappa_{eq}+1)^{-1} \tag{A.2}$$

$$I_3 = 2\pi\left(2\left(\left(C^2+1\right)\left(C^2\kappa_{eq}^2+1\right)\right)^{-1/2}-1\right) \tag{A.3}$$

$$I_4 = 2\pi(\kappa_{eq}-1)^2(\kappa_{eq}+1)^{-2} \tag{A.4}$$

$$\begin{aligned} I_5+I_6 = &-\left(4\pi\left(2\kappa_{eq}^2\left(3\sqrt{\left(C^2+1\right)\left(C^2\kappa_{eq}^2+1\right)}-8C^2-6\right)+4\kappa_{eq}\sqrt{\left(C^2+1\right)\left(C^2\kappa_{eq}^2+1\right)}\right.\right.\\ &+\sqrt{\left(C^2+1\right)\left(C^2\kappa_{eq}^2+1\right)}+4\left(4C^2+1\right)\kappa_{eq}^3\sqrt{\left(C^2+1\right)\left(C^2\kappa_{eq}^2+1\right)}\\ &\left.\left.+\kappa_{eq}^4\left(\sqrt{\left(C^2+1\right)\left(C^2\kappa_{eq}^2+1\right)}-16\left(C^4+C^2\right)-2\right)-2\right)\right)\\ &\left(\left(\kappa_{eq}^2-1\right)^2\sqrt{\left(C^2+1\right)\left(C^2\kappa_{eq}^2+1\right)}\right)^{-1} \end{aligned} \tag{A.5}$$

$$J_1 = \pi(\kappa_{eq}^2 - 1)(\kappa_{eq} + 1)^{-2} \tag{A.6}$$

$$J_2 = -\pi(\kappa_{eq}^2 - 1)\left(-4\sqrt{(C^2+1)\left(C^2\kappa_{eq}^2+1\right)} + C^2(\kappa_{eq}+1)^2 + 4\right)C^{-2}\left(\kappa_{eq}^2 - 1\right)^{-2} \tag{A.7}$$

$$J_3 = \pi(\kappa_{eq}^2 - 1)(\kappa_{eq} - 1)(\kappa_{eq} + 1)^{-3} \tag{A.8}$$

$$\begin{aligned} J_4 = &-\pi(\kappa_{eq}^2 - 1)\left(8C^4\kappa_{eq}^3 + C^2\left((\kappa_{eq}+1)^4 - 8\kappa_{eq}^2\sqrt{(C^2+1)\left(C^2\kappa_{eq}^2+1\right)}\right)\right. \\ &\left. -4\left(\kappa_{eq}^2+1\right)\left(\sqrt{(C^2+1)\left(C^2\kappa_{eq}^2+1\right)} - 1\right)\right)C^{-2}\left(\kappa_{eq}^2 - 1\right)^{-3} \end{aligned} \tag{A.9}$$

Note that only $I_5 + I_6$ matters since $F_5^p(\xi_0, \lambda) = F_6^p(\xi_0, \lambda)$ (see (2.82)) and $F_5^f(\xi_0) = F_6^f(\xi_0)$ (see 2.99).

Appendix B

The $C-\tau$ coordiante system

The details of the (C,τ) coordinate system are given below. The orbital coordinates (C,τ) are related to spherical coordinate angles, θ_j and ϕ_j, as $C=\frac{\tan\theta_j(\kappa_{eq}^2\sin^2\phi_j+\cos^2\phi_j)^{1/2}}{\kappa_{eq}}$ and $\tan\tau=1/(\kappa_{eq}\tan\phi_j)$. The unit vectors $\hat{\boldsymbol{C}}$ and $\hat{\boldsymbol{\tau}}$ are given by $\frac{\partial\hat{\boldsymbol{r}}}{\partial C}/|\frac{\partial\hat{\boldsymbol{r}}}{\partial C}|$ and $\frac{\partial\hat{\boldsymbol{r}}}{\partial\tau}/|\frac{\partial\hat{\boldsymbol{r}}}{\partial\tau}|$ respectively, where $\hat{\boldsymbol{r}}$ is the unit radial vector in spherical coordinates ($\hat{\boldsymbol{r}}=\sin\theta_j\cos\phi_j\mathbf{1}'_x+\sin\theta_j\sin\phi_j\mathbf{1}'_y+\cos\theta_j\mathbf{1}'_z$). The metric factors h_C and h_τ are given by $|\frac{\partial\hat{\boldsymbol{r}}}{\partial C}|$ and $|\frac{\partial\hat{\boldsymbol{r}}}{\partial\tau}|$ respectively. Simplifying, one gets:

$$\hat{\boldsymbol{C}}=\cos\theta_j\cos\phi_j\mathbf{1}'_x+\cos\theta_j\sin\phi_j\mathbf{1}'_y-\sin\theta_j\mathbf{1}'_z=\hat{\boldsymbol{\theta}}_{\boldsymbol{j}}, \tag{B.1}$$

$$\hat{\boldsymbol{\tau}}=\frac{\frac{\partial\theta_j}{\partial\tau}}{\sqrt{\left(\frac{\partial\theta_j}{\partial\tau}\right)^2+\left(\frac{\partial\phi_j}{\partial\tau}\right)^2\sin^2\theta_j}}\hat{\boldsymbol{\theta}}_{\boldsymbol{j}}+\frac{\frac{\partial\phi_j}{\partial\tau}\sin\theta_j}{\sqrt{\left(\frac{\partial\theta_j}{\partial\tau}\right)^2+\left(\frac{\partial\phi_j}{\partial\tau}\right)^2\sin^2\theta_j}}\hat{\boldsymbol{\phi}}_{\boldsymbol{j}}, \tag{B.2}$$

$$h_C=\frac{\partial\theta_j}{\partial C}, \tag{B.3}$$

$$h_\tau=\sqrt{\left(\frac{\partial\theta_j}{\partial\tau}\right)^2+\left(\frac{\partial\phi_j}{\partial\tau}\right)^2\sin^2\theta_j}, \tag{B.4}$$

where $\hat{\boldsymbol{\theta}}_{\boldsymbol{j}}$ and $\hat{\boldsymbol{\phi}}_{\boldsymbol{j}}=-\sin(\phi_j)\mathbf{1}'_x+\cos(\phi_j)\mathbf{1}'_y$ are the polar and azimuthal unit vectors in spherical coordinate system, and $\hat{\boldsymbol{\tau}}$ is tangent to a Jeffery orbit. The (C,τ) is a non-orthogonal coordinate system and the angle(α) between the unit vectors $\hat{\boldsymbol{C}}$ and $\hat{\boldsymbol{\tau}}$ is given by:

$$\cos\alpha=\frac{\frac{\partial\theta_j}{\partial\tau}}{\sqrt{\left(\frac{\partial\theta_j}{\partial\tau}\right)^2+\left(\frac{\partial\phi_j}{\partial\tau}\right)^2\sin^2\theta_j}}. \tag{B.5}$$

The $\hat{\boldsymbol{\tau}}$ can then be written as $\cos\alpha\,\hat{\boldsymbol{\theta}}_{\boldsymbol{j}}+\sin\alpha\,\hat{\boldsymbol{\phi}}_{\boldsymbol{j}}$.

The divergence operator in the (C,τ) coordinate system is given by:

$$\nabla.\boldsymbol{f}=\frac{1}{h_C h_\tau\sin\alpha}\frac{\partial}{\partial C}\left(h_\tau\sin\alpha\,\boldsymbol{f}.\hat{\boldsymbol{C}}\right)+\frac{1}{h_C h_\tau\sin\alpha}\frac{\partial}{\partial\tau}\left(h_C\sin\alpha\,\boldsymbol{f}.\hat{\boldsymbol{\tau}}\right). \tag{B.6}$$

The gradient operator in the (C,τ) coordinate system is given by:

$$\nabla f=\left(\frac{1}{h_C\sin^2\alpha}\frac{\partial f}{\partial C}-\frac{\cot\alpha}{h_\tau\sin\alpha}\frac{\partial f}{\partial\tau}\right)\hat{\boldsymbol{C}}+\left(\frac{1}{h_\tau\sin^2\alpha}\frac{\partial f}{\partial\tau}-\frac{\cot\alpha}{h_C\sin\alpha}\frac{\partial f}{\partial C}\right)\hat{\boldsymbol{\tau}}. \tag{B.7}$$

Appendix C

The integrals in (5.113)

The 4-dimensional and 5-dimensional integrals for the terms proportional to $\hat{u}_1^{fi}$(i=‘0’,‘tcos’,‘tsin’), $\hat{u}_3^{fi}$ (i=‘0’,‘tcos’,‘tsin’) and the 4-dimensional integral for $\hat{u}_2^{fi}$ (‘tcos’,‘tsin’) in (5.113) are given below in the spherical coordinate system.
The integral proportional to $\hat{u}_2^{f0}$ is written using (5.101) and (5.67),

$$\begin{aligned}\int(-4\pi^2k^2\,\hat{u}_2^{f0}(\boldsymbol{k})\,\mathbf{1}_2\cdot\boldsymbol{T}_1^{tumb})d\boldsymbol{k} = -\int_0^{2\pi}\int_0^{\pi}\int_0^{\infty}4\pi^2\left\{k^2\left[\frac{iB_3k_1}{2k^2\pi}\frac{(1+\kappa^2)^2}{2\kappa^2}\right.\right.\\ \left.\left.+\frac{iB_1k_1(k^2-2k_2^2)}{2k^4\pi}\frac{(1-\kappa^4)}{2\kappa^2}\right]\frac{k^2+k_1^2s^2+2k_1k_2s}{k^2}Q_2^0(\boldsymbol{k}')\right\}\\ \int_0^{\infty}k^2e^{-4\pi^2\left(k^2s+k_1k_2s^2+\frac{k_1^2s^3}{3}\right)}dk\,ds\,\sin\theta d\theta d\phi.\end{aligned} \tag{C.1}$$

The integral proportional to $\hat{u}_3^{f0}$ is written using (5.107) and (5.67):

$$\begin{aligned}\int(-4\pi^2k^2\,\hat{u}_3^{f0}(\boldsymbol{k})\,\mathbf{1}_3\cdot\boldsymbol{T}_1^{tumb})d\boldsymbol{k} = -\int_0^{2\pi}\int_0^{\pi}\int_0^{\infty}4\pi^2\left\{k^2\left[-\frac{iB_1k_1k_2k_3}{k^4\pi}\frac{(1-\kappa^4)}{2\kappa^2}\right]\right.\\ \left.Q_3^0(\boldsymbol{k}')\right\}\int_0^{\infty}k^2e^{-4\pi^2\left(k^2s+k_1k_2s^2+\frac{k_1^2s^3}{3}\right)}dk\,ds\,\sin\theta d\theta d\phi-\int_0^{2\pi}\int_0^{\pi}\int_0^{\infty}\int_0^{\infty}4\pi^2\left\{k^2\right.\\ \left.\left[-\frac{iB_1k_1k_2k_3}{k^4\pi}\frac{(1-\kappa^4)}{2\kappa^2}\right]\frac{2k_1k_3}{k'^2}\left(\frac{k'^2+k_1^2s'^2+2k_1k_2's'}{k'^2}\right)Q_2^0(\boldsymbol{k}'')\right\}\\ \int_0^{\infty}e^{-4\pi^2\left(k^2s+k_1k_2s^2+\frac{k_1^2s^3}{3}\right)}e^{-4\pi^2\left(k'^2s'+k_1k_2's'^2+\frac{k_1^2s'^3}{3}\right)}k^2dk\,ds\,ds'\,\sin\theta d\theta d\phi.\end{aligned} \tag{C.2}$$

The integral proportional to $\hat{u}_1^{ftcos}$ is written using (5.105) and (5.67):

$$\begin{aligned}
&\int (-4\pi^2 k^2\, \hat{u}_1^{ftcos}(\boldsymbol{k})\, \mathbf{1}_1 \cdot \boldsymbol{T}_2^{tumb}) d\boldsymbol{k} = -\int_0^{2\pi} \int_0^{\pi} \int_0^{\infty} 4\pi^2 \Bigg\{ k^2 \left[\frac{(\kappa^4-1)}{2\kappa^2} \frac{iB_3 k_2}{2k^2\pi} \right. \\
&\quad \left. + \frac{iB_1(k^2-2k_1^2)k_2}{2k^4\pi} \frac{(1+\kappa^2)^2}{2\kappa^2} \right] \left(Q_1^{2i}(\boldsymbol{k'}) \cos(2\omega_g s) - Q_1^{2Re}(\boldsymbol{k'}) \sin(2\omega_g s) \right) \Bigg\} \\
&\quad \int_0^{\infty} i2k^2 e^{-4\pi^2 \left(k^2 s + k_1 k_2 s^2 + \frac{k_1^2 s^3}{3} \right)} dk\, ds\, sin\theta\, d\theta\, d\phi + \int_0^{2\pi} \int_0^{\pi} \int_0^{\infty} \int_0^{\infty} 4\pi^2 k^2 \Bigg\{ \\
&\quad \left[\frac{(\kappa^4-1)}{2\kappa^2} \frac{iB_3 k_2}{2k^2\pi} + \frac{iB_1(k^2-2k_1^2)k_2}{2k^4\pi} \frac{(1+\kappa^2)^2}{2\kappa^2} \right] \left(1 - \frac{2k_1^2}{k'^2} \right) \left(Q_2^{2i}(\boldsymbol{k''}) \cos(2\omega_g(s+s')) \right. \\
&\quad \left. - Q_2^{2Re}(\boldsymbol{k''})\ sin(2\omega_g(s+s')) \right) \left(\frac{k'^2 + k_1^2 s'^2 + 2k_1 k_2' s'}{k'^2} \right) \Bigg\} \int_0^{\infty} e^{-4\pi^2 \left(k^2 s + k_1 k_2 s^2 + \frac{k_1^2 s^3}{3} \right)} \\
&\quad i2e^{-4\pi^2 \left(k'^2 s + k_1 k_2' s^2 + \frac{k_1^2 s^3}{3} \right)} k^2 dk ds'\, ds\, \sin\theta d\theta d\phi. \qquad \text{(C.3)}
\end{aligned}$$

The integral proportional to $\hat{u}_2^{ftcos}$ is written using (5.102) and (5.67):

$$\begin{aligned}
&\int (-4\pi^2 k^2\, \hat{u}_2^{ftcos}(\boldsymbol{k})\, \mathbf{1}_2 \cdot \boldsymbol{T}_2^{tumb}) d\boldsymbol{k} = -\int_0^{2\pi} \int_0^{\pi} \int_0^{\infty} 4\pi^2 \Bigg\{ k^2 \left[\frac{-iB_3 k_1}{2k^2\pi} \frac{(\kappa^4-1)}{2\kappa^2} \right. \\
&\quad \left. + \frac{iB_1 k_1(k^2-2k_2^2)}{2k^4\pi} \frac{(1+\kappa^2)^2}{2\kappa^2} \right] \left(\frac{k^2 + k_1^2 s^2 + 2k_1 k_2 s}{k^2} \right) \left(Q_2^{2i}(\boldsymbol{k'}) \cos(2\omega_g s) \right. \\
&\quad \left. - Q_2^{2Re}(\boldsymbol{k'}) \sin(2\omega_g s) \right) \Bigg\} \int_0^{\infty} i2e^{-4\pi^2 \left(k^2 s + k_1 k_2 s^2 + \frac{k_1^2 s^3}{3} \right)} k^2 dk\, ds\, \sin\theta d\theta d\phi. \qquad \text{(C.4)}
\end{aligned}$$

The integral proportional to $\hat{u}_3^{ftcos}$ is written using (5.108) and (5.69):

$$\begin{aligned}
&\int (-4\pi^2 k^2\, \hat{u}_3^{ftcos}(\boldsymbol{k})\, \mathbf{1}_3 \cdot \boldsymbol{T}_2^{tumb}) d\boldsymbol{k} = -\int_0^{2\pi}\int_0^{\pi}\int_0^{\infty} 4\pi^2 \left\{ k^2 \left[-\frac{iB_1 k_1 k_2 k_3}{k^4 \pi} \frac{(1+\kappa^2)^2}{2\kappa^2} \right] \right.\\
&\quad \left. \left(Q_3^{2i}(\boldsymbol{k'})\cos(2\omega_g s) - Q_3^{2Re}(\boldsymbol{k'})\sin(2\omega_g s)\right) \right\} \int_0^{\infty} i2e^{-4\pi^2\left(k^2 s + k_1 k_2 s^2 + \frac{k_1^2 s^3}{3}\right)} k^2\, dk\, ds \\
&\quad \sin\theta\, d\theta\, d\phi - \int_0^{2\pi}\int_0^{\pi}\int_0^{\infty}\int_0^{\infty} \left\{ 4\pi^2 k^2 \left[-\frac{iB_1 k_1 k_2 k_3}{k^4 \pi} \frac{(1+\kappa^2)^2}{2\kappa^2} \right] \left(\frac{2k_1 k_3}{k'^2} \right) \right.\\
&\quad \left. \left(\frac{k'^2 + k_1^2 s'^2 + 2k_1 k_2' s'}{k'^2} \right) \left(Q_2^{2i}(\boldsymbol{k''})\cos(2\omega_g (s+s')) - Q_2^{2Re}(\boldsymbol{k''})\sin(2\omega_g (s+s'))\right) \right\}
\end{aligned} \tag{C.5}$$

$$\int_0^{\infty} e^{-4\pi^2\left(k^2 s + k_1 k_2 s^2 + \frac{k_1^2 s^3}{3}\right)}\, i2e^{-4\pi^2\left(k'^2 s + k_1 k_2' s^2 + \frac{k_1^2 s^3}{3}\right)} k^2 dk ds'\, ds\, \sin\theta\, d\theta\, d\phi. \tag{C.6}$$

The integral proportional to $\hat{u}_1^{ftsin}$ is written using (5.105) and (5.67):

$$\begin{aligned}
&\int (-4\pi^2 k^2\, \hat{u}_1^{ftsin}(\boldsymbol{k})\, \mathbf{1}_1 \cdot \boldsymbol{T}_3^{tumb}) d\boldsymbol{k} = -\int_0^{2\pi}\int_0^{\pi}\int_0^{\infty} 4\pi^2 \left\{ k^2 \left[\frac{iB_1 (k^2 - k_1^2 + k_2^2) k_1}{2k^4 \pi} \right. \right.\\
&\quad \left. \left. \left(\frac{\kappa^2 + 1}{\kappa} \right) \right] \left(Q_1^{2Re}(\boldsymbol{k'})\cos(2\omega_g s) + Q_1^{2i}(\boldsymbol{k'})\sin(2\omega_g s)\right) \right\} \int_0^{\infty} i2e^{-4\pi^2\left(k^2 s + k_1 k_2 s^2 + \frac{k_1^2 s^3}{3}\right)} \\
&\quad k^2\, dk\, ds\, \sin\theta\, d\theta\, d\phi + \int_0^{2\pi}\int_0^{\pi}\int_0^{\infty}\int_0^{\infty} 4\pi^2 \left\{ k^2 \left[\frac{iB_1 (k^2 - k_1^2 + k_2^2) k_1}{2k^4 \pi} \left(\frac{\kappa^2 + 1}{\kappa} \right) \right] \right.\\
&\quad \left. \left(1 - \frac{2k_1^2}{k'^2} \right) \left(\frac{k'^2 + k_1^2 s'^2 + 2k_1 k_2' s'}{k'^2} \right) \left(Q_2^{2Re}(\boldsymbol{k''})\cos(2\omega_g (s+s')) + Q_2^{2i}(\boldsymbol{k''})\sin(2\omega_g (s+s'))\right) \right\} \\
&\quad \int_0^{\infty} e^{-4\pi^2\left(k^2 s + k_1 k_2 s^2 + \frac{k_1^2 s^3}{3}\right)}\, i2e^{-4\pi^2\left(k'^2 s + k_1 k_2' s^2 + \frac{k_1^2 s^3}{3}\right)} k^2 dk ds'\, ds\, \sin\theta\, d\theta\, d\phi.
\end{aligned} \tag{C.7}$$

The integral proportional to $\hat{u}_2^{ftsin}$ is written using (5.102) and (5.67):

$$\int(-4\pi^2k^2\,\hat{u}_2^{f0}(\boldsymbol{k})\,\mathbf{1}_2\cdot\boldsymbol{T}_3^{tumb})d\boldsymbol{k} = -\int_0^{2\pi}\int_0^{\pi}\int_0^{\infty}4\pi^2\left\{k^2\left[-\left(\frac{\kappa^2+1}{\kappa}\right)\frac{iB_1k_2(k^2+k_1^2-k_2^2)}{2k^4\pi}\right]\right.$$
$$\left.\left(\frac{k^2+k_1^2s^2+2k_1k_2s}{k^2}\right)\left(Q_2^{2Re}(\boldsymbol{k}')\cos(2\omega_g s)+Q_2^{2i}(\boldsymbol{k}')\sin(2\omega_g s)\right)\right\}$$
$$\int_0^{\infty} i2e^{-4\pi^2\left(k^2s+k_1k_2s^2+\frac{k_1^2s^3}{3}\right)}k^2\,dk\,ds\,\sin\theta\,d\theta\,d\phi. \tag{C.8}$$

The integral proportional to $\hat{u}_3^{ftsin}$ is written using (5.108) and (5.67):

$$\int(-4\pi^2k^2\,\hat{u}_3^{ftsin}(\boldsymbol{k})\,\mathbf{1}_3\cdot\boldsymbol{T}_3^{tumb})d\boldsymbol{k} = -\int_0^{2\pi}\int_0^{\pi}\int_0^{\infty}4\pi^2\left\{k^2\left[-\left(\frac{\kappa^2+1}{\kappa}\right)\frac{iB_1(k_1^2-k_2^2)k_3}{2k^4\pi}\right]\right.$$
$$\left.\left(Q_3^{2Re}(\boldsymbol{k}')\cos(2\omega_g s)+Q_3^{2i}(\boldsymbol{k}')\sin(2\omega_g s)\right)\right\}\int_0^{\infty} i2e^{-4\pi^2\left(k^2s+k_1k_2s^2+\frac{k_1^2s^3}{3}\right)}$$
$$k^2\,dk\,ds\,\sin\theta\,d\theta\,d\phi - \int_0^{2\pi}\int_0^{\pi}\int_0^{\infty}\int_0^{\infty}4\pi^2\left\{k^2\left[-\left(\frac{\kappa^2+1}{\kappa}\right)\frac{iB_1(k_1^2-k_2^2)k_3}{2k^4\pi}\right]\right.$$
$$\left.\left(\frac{2k_1k_3}{k'^2}\right)\left(Q_2^{2Re}(\boldsymbol{k}'')\cos(2\omega_g(s+s'))+Q_2^{2i}(\boldsymbol{k}'')\sin(2\omega_g(s+s'))\right)\left(\frac{k'^2+k_1^2s'^2+2k_1k_2's'}{k'^2}\right)\right\}$$
$$\int_0^{\infty} e^{-4\pi^2\left(k^2s+k_1k_2s^2+\frac{k_1^2s^3}{3}\right)}\,i2e^{-4\ pi^2\left(k'^2s+k_1k_2's^2+\frac{k_1^2s^3}{3}\right)}k^2dkds'\,ds\,\sin\theta\,d\theta\,d\phi. \tag{C.9}$$